Studies on hyperthermia in magnetic fluids: Effects of particle loading, medium viscosity, size polydispersity, orientational ordering and thermal losses on heating efficiency

By

BARID BARAN LAHIRI

Enrolment No: PHYS 02 2011 04 015

Indira Gandhi Centre for Atomic Research, Kalpakkam,

Tamil Nadu, India 603 102

A Thesis submitted to the

Board of Studies in Physical Sciences

In partial fulfillment of requirements

for the degree of

DOCTOR OF PHILOSOPHY

of

HOMI BHABHA NATIONAL INSTITUTE

November, 2017

Homi Bhabha National Institute

Recommendations of the Viva Voce Board

As members of the Viva Voce Board, we certify that we have read the dissertation prepared by **BARID BARAN LAHIRI** entitled "**Studies on hyperthermia in magnetic fluids: Effects of particle loading, medium viscosity, size polydispersity, orientational ordering and thermal losses on heating efficiency**" and recommend that it may be accepted as fulfilling the thesis requirement for the award of Degree of Doctor of Philosophy.

S. Sai — **Date:** 22/03/2018

Chairman-**Dr. Saroja Saibaba**

John Philip — **Date:** 22/03/2018

Convener/Guide-**Dr. John Philip**

J L N — **Date:** 22/03/2018

Member 1-Examiner

T R Ravindran — **Date:** 22.3.2018

Member 2- **Dr. T. R. Ravindran**

R Ramaseshan — **Date:** 22/3/18

Member 3- **Dr. R. Ramaseshan**

Final approval and acceptance of this thesis is contingent upon the candidate's submission of the final copies of the thesis to HBNI.

I hereby certify that I have read this thesis prepared under my direction and recommend that it may be accepted as fulfilling the thesis requirement.

John Philip

Date: 22/03/2018

Place: Kalpakkam

Dr. John Philip

(Guide)

CERTIFICATE

I hereby certify that I have read this thesis prepared under my direction and recommend that it may be accepted as fulfilling the thesis requirement.

Date: 04/11/2017

Place: Kalpakkam

Dr. John Philip

(Guide)

STATEMENT BY AUTHOR

This dissertation has been submitted in partial fulfillment of the requirements for an advanced degree at Homi Bhabha National Institute (HBNI) and is deposited in the library to be made available to the borrowers under the rules of HBNI.

Brief quotations from this dissertation are allowable without special permission, provided that accurate acknowledgement of the source is made. Requests for permission for extended quotation from or reproduction of this manuscript in whole or in part may be granted by the Competent Authority of HBNI when in his or her judgment the proposed use of the material is in the interest of scholarship. In all other instances, however, permission must be obtained from the author.



(Barid Baran Lahiri)

DECLARATION

I, hereby declare that the investigation presented in this thesis has been carried out by me. The work is original and has not been submitted earlier, as a whole or in part, for a degree/diploma at this or any other Institution/University.



(Barid Baran Lahiri)

List of Publications arising from the thesis

Journals

1. "Magnetic hyperthermia in phosphate coated iron oxide nanofluids", **B. B. Lahiri**, T. Muthukumaran and John Philip, *J. Magn. Magn. Mater.*, **2016**, *407*, 101-113.

2. "Infrared thermography based magnetic hyperthermia study in Fe_3O_4 based magnetic fluids", **B. B. Lahiri**, Surojit Ranoo and John Philip, *Infrared Phys. Technol.*, **2016**, *78*, 173-184.

3. "Magnetic hyperthermia study in water based magnetic fluids containing TMAOH coated Fe_3O_4 using infrared thermography", **B. B. Lahiri**, Surojit Ranoo and John Philip, *Infrared Phys. Technol.*, **2017**, *80*, 71-82.

4. "Magnetic hyperthermia in magnetic nanoemulsions: effects of polydispersity, particle concentration and medium viscosity", **B. B. Lahiri**, Surojit Ranoo, A. W. Zaibudeen and John Philip, *J. Magn. Magn. Mater.*, **2017**, *441*, 310-327.

5. "Uncertainties in the estimation of specific absorption rate during radiofrequency alternating magnetic field induced non-adiabatic heating of ferrofluids", **B. B. Lahiri**, Surojit Ranoo and John Philip, *J. Phys. D Appl. Phys.*, **2017**, *50*, 455005.

6. "Effect of orientational ordering of magnetic nanoemulsions immobilized in agar gel on magnetic hyperthermia", **B. B. Lahiri**, Surojit Ranoo and John Philip, *J. Magn. Magn. Mater.*, **2018**, *451*, 254-268.

Conferences

1. **B. B. Lahiri**, Surojit Ranoo and John Philip, "*Infrared thermography for studying field induced heating during magnetic fluid hyperthermia: a convection correction approach*", National Conference on Non-destructive Evaluation, ISNT, Thiruvananthapuram, India, December 15-17, **2016**, pp 100-101.

2. **B. B. Lahiri**, Surojit Ranoo and John Philip, "*Probing of radiofrequency alternating magnetic field induced heating in surfactant capped iron oxide nanoparticles using infrared thermography for hyperthermia aided cancer treatment*", National Symposium on Nano Science and Technology, Centre for Nano Science and Engineering (CeNSE), IISC, Bangalore, India, July 2-4, **2017**, pp 8-9.

3. **B. B. Lahiri**, J. Sangeetha, Surojit Ranoo, A.W. Zaibudeen and John Philip, "*Atomic force microscopy based studies on the field induced orientation of magnetic nanoemulsions*", International Conference on Electron Microscopy and Allied Techniques, EMSI, Mamallapuram, India, July 17-19, **2017**, pp 131-133.

4. **B. B. Lahiri**, Surojit Ranoo and John Philip, "*Effect of surface area to volume ratio on thermal losses during radio-frequency magnetic field induced non-*

adiabatic heating in magnetic nanofluids: A lumped system analysis", 9th National Conference on Thermophysical Properties, NCTP, Kalpakkam, India, November 6-8, **2017**, P-15.

5. Surojit Ranoo, **B. B. Lahiri** and John Philip, "*Monitoring of magnetically triggered heating in a water based magnetic fluid using infrared thermography: Effects of convection*", 9th National Conference on Thermophysical Properties, NCTP, Kalpakkam, India, November 6-8, **2017**, P-16.

6. **B. B. Lahiri**, Surojit Ranoo and John Philip, "*Magnetic nanoemulsions for multimodal hyperthermia*", 2nd Annual Conference of Indian Society of Nanomedicine, NanoBioTek-2017, Thiruvananthapuram, Kerala, December 6-8, **2017**, P-104.

7. **B. B. Lahiri**, Surojit Ranoo, T. Muthukumaran and John Philip, "*Magnetic hyperthermia in water based ferrofluids: effects of initial susceptibility and size polydispersity on heating efficiency*", 62nd DAE Solid State Physics Symposium, Mumbai, India, December 26-30, **2017**, P-62.

Other Publications (not included in the thesis)

1. "Infrared thermography based studies on the effect of age on localized cold stress induced thermoregulation in human", **B. B. Lahiri**, S. Bagavathiappan, K. Nishanthi, K. Mohanalakshmi, L. Veni, Saumya, S. M. Yacin and John Philip, *Infrared Phys. Technol.*, **2016**, *76*, 592-602.

2. "Studies on temperature evolution during fatigue cycling of Ni-Al bronze (NAB) alloy using infrared thermography", **B. B. Lahiri**, A. Sarkar, S. Bagavathiappan, A. Nagesha, T. Saravanan, R. Sandhya, T. Jayakumar and John Philip, *Insight*, **2016**, *58*, 70-81.

3. "Infrared thermography-based studies on hydrotesting of stainless steel pressure vessels", **B. B. Lahiri**, T. K. Haneef, S. Bagavathiappan, N. Kulasegaran, C. K. Mukhopadhyay, T. Jayakumar and John Philip, *Insight*, **2015**, *57*, 406-413.

4. "Infrared thermography based studies on mobile phone induced heating", **B. B. Lahiri**, S. Bagavathiappan, C. Soumya, T. Jayakumar and John Philip, *Infrared Phys. Technol.*, **2015**, *71*, 242-251.

5. "Effect of non-magnetic inclusions in magnetic specimens on defect detection sensitivity using active infrared thermography", **B. B. Lahiri**, S. Bagavathiappan, Libins T. Sebastian, John Philip and T. Jayakumar, *Infrared Phys. Technol.*, **2015**, *68*, 52-60.

6. "Infrared thermography based defect detection in ferromagnetic specimens using a low frequency alternating magnetic field", **B. B. Lahiri**, S. Bagavathiappan, C. Soumya, V. Mahendran, V.P.M. Pillai, John Philip and T. Jayakumar, *Infrared Phys. Technol.*, **2014**, *64*, 125-133.

7. "Measurement of annular air-gap using active infrared thermography", **B. B. Lahiri**, S. Bagavathiappan, R. Shunmugasundaram, John Philip and T. Jayakumar, *Infrared Phys. Technol.*, **2013**, *61*, 192–199.

8. "Detection of pathogenic gram negative bacteria using infrared thermography", **B. B. Lahiri**, M. P. Divya, S. Bagavathiappan, S. Thomas and John Philip, *Infrared Phys. Technol.*, **2012**, *55*, 485–490.

9. "Medical applications of infrared thermography: A review", **B. B. Lahiri**, S. Bagavathiappan, T. Jayakumar and John Philip, *Infrared Phys. Technol.*, **2012**, *55*, 221–235.

10. "Quantification of defects in composites and rubber materials using active thermography", **B. B. Lahiri**, S. Bagavathiappan, P. R. Reshmi, John Philip, T. Jayakumar and Baldev Raj, *Infrared Phys. & Technol.*, **2012**, *55*, 191–199.

(Barid Baran Lahiri)

To the loving memory of my mother,

Late Mrs. Dola Ghosh Lahiri

ACKNOWLEDGEMENTS

At the onset, I express my deepest sense of gratitude to my esteemed guide, **Dr. John Philip**, for his thoughtful guidance, insightful advice, warm encouragement, critical comments and correction of the thesis. He has groomed me as a PhD student and his logical way of thinking on critical scientific problems, thought provoking discussions and generosity have been a great learning experience. I have been extremely lucky to have a guide who cared so much about my work and who always stood beside me, both on academic and personal fronts. I look forward to receive continued guidance from him in future.

I would like to extend my sincere gratitude towards my doctoral committee chairman, **Dr. Saroja Saibaba** and the committee members, **Dr. T. R. Ravindran** and **Dr. R. Ramaseshan** for their untiring support and valuable suggestions.

I thank **Dr. A. K. Bhaduri**, Director, IGCAR and **Dr. G. Amarendra**, Director, Metallurgy and Materials Group for allowing me to carry out the research work at Indira Gandhi Centre for Atomic Research (IGCAR). I also thank the former centre directors and group directors for their support.

I gratefully acknowledge the help received from **Mr. Surojit Ranoo**, towards carrying out the experiments, **Mr. T. Muthukumaran** and **Mr. A.W. Zaibudeen**, for helping me with the ferrofluid and ferroemulsion samples, **Mr. S. Kalyani**, for his help towards X-ray diffraction and magnetization measurements and **Mrs. Sangeetha Jayakumar**, for her help towards atomic force microscopy studies.

I express my sincere gratitude towards all the members of **Smart Materials Section (SMARTS)** for their support, kind assistance and help in numerous occasions. I also thank all members of **Corrosion Science and Technology Division (CSTD)**, **Non**

Destructive Evaluation Division (NDED) and **Materials Characterization Group (MCG)** for their support and encouragement.

I deeply acknowledge the help received from my **senior and junior colleagues**, **friends and batch-mates** who have supported me in one way or the other.

Last but not the least, I would like to express my sincere gratitude towards my **family members**, especially my beloved wife, **Sangeetha** and my dearest daughter, **Ananya** for their continued support, understanding, love and care in all aspects of my life.

CONTENTS

	Page no.
SYNOPSIS	i
LIST OF FIGURES	vi
LIST OF TABLES	xv
LIST OF ABBREVIATIONS	xvii
LIST OF SYMBOLS	xx
Chapter 1	
Introduction	
1.1 Magnetism in materials	1
1.2 Different types of magnetic materials	3
1.3 Magnetism in nanoparticles	11
1.3.1 Effects of size on magnetism in nanoparticles	12
1.3.2 Spinel ferrites	17
1.3.2.1 Structure of spinel ferrites	17
1.3.2.2 Super exchange interactions in spinel ferrites	19
1.3.3 Bio-medical applications of magnetic nanoparticles (MNP)	20
1.4 Magnetic fluids	23
1.4.1 Ferrofluids	24
1.4.2 Ferroemulsions	25
1.5 Hyperthermia using nanoparticles	27
1.6 Magnetic fluid hyperthermia (MFH)	30
1.6.1 Multimodal approaches involving MFH	36
1.7 Mechanisms of radio frequency alternating magnetic field (RF-AMF) induced heating in magnetic materials	38
1.7.1 Eddy current heating	39
1.7.2 Heating by viscous stirring in MNP	40
1.7.3 Heating by hysteresis losses	41
1.7.4 Neel-Brownian relaxation in superparamagnetic nanoparticles	41
1.7.5 RF-AMF induced heating in ferrofluids: Rosensweig's model	45
1.7.6 RF-AMF induced heating of oriented MNP	48
1.8 Motivation	52
1.9 Objectives	53
1.10 Overview of the thesis	54
Chapter 2	
Experimental methods	
2.1 Synthesis of magnetic nanoparticles (MNP)	56
2.1.1 Coprecipitation method	56
2.1.2 Synthesis of ferrofluids using coprecipitation method	57
2.1.2.1 Preparation of oil based ferrofluid containing oleic acid coated Fe_3O_4 MNP	57
2.1.2.2 Preparation of water based ferrofluids	58
2.1.3 Preparation of ferroemulsions	58
2.1.4 Preparation of agar based samples	60
2.1.4.1 Preparation of agar based samples loaded with $CoFe_2O_4$ and emulsion droplets	60
2.1.4.2 Preparation of agar based samples loaded with oriented emulsion droplets	60
2.2 Characterization techniques	61

2.2.1 Powder X-ray diffraction 62
2.2.2 Small angle X-ray scattering 63
2.2.3 Dynamic light scattering 64
2.2.4 Thermogravimetric analysis 66
2.2.5 Fourier transform infrared spectroscopy 66
2.2.6 Vibrating sample magnetometer 68
2.2.7 Atomic force microscopy and magnetic force microscopy 69
2.3 Radio frequency induction heating system 73
2.3.1 Parallel resonance tank circuit and heating coils 73
2.3.2 Calculation of magnetic field amplitudes 77
2.4 Sample temperature measurement during RF-AMF induced heating 79
2.4.1 Fiber optic temperature sensor 80
2.4.2 Infrared thermography 83
2.5 Protocols for SAR measurement 89
2.6 Uncertainties in SAR measurement 92
2.6.1 Peripheral heating 94
2.6.2 Delayed heating and initial rate determination methodology 96
2.6.3 Heat loss to sample holder 100
2.6.4 Spatial variation of temperature within sample 101
2.6.5 Linear loss approximation and effects of sample volume and surface area 102
2.6.6 Adiabatic reconstruction 109
2.7 Conclusions 113

Chapter 3
Infrared thermography based magnetic hyperthermia studies in Fe_3O_4 based magnetic fluids

3.1 Introduction 115
3.2 Infrared thermography (IRT) based MFH studies on water based ferrofluid containing tetramethyl ammonium hydroxide (TMAOH) coated Fe_3O_4 MNP 116
3.2.1 Experimental details and characterization studies 116
3.2.2 Results and discussions 118
3.2.2.1 IRT based temperature measurement during RF-AMF induced heating 118
3.2.2.2 Comparison of IRT and probe based temperature rise curves and convection correction 124
3.2.2.3 Variation of specific absorption rate (SAR) with sample concentration and RF-AMF amplitude 135
3.3 IRT based MFH studies on oil based ferrofluid containing oleic acid coated Fe_3O_4 MNP 137
3.3.1 Experimental details and characterization studies 138
3.3.2 Results and discussions 140
3.3.2.1 IRT based temperature measurement during RF-AMF induced heating 140
3.3.2.2 Comparison of IRT and probe based temperature rise curves and convection correction 147
3.3.2.3 Variation of SAR with sample concentration and RF-AMF amplitude 152
3.4 Conclusions 154

Chapter 4
Studies on magnetic fluid hyperthermia in water based magnetic nanofluids containing phosphate coated magnetic nanoparticles
4.1 Introduction 156
4.2 MFH in water based ferrofluid containing phosphate coated Fe_3O_4 MNP 157
4.2.1 Experimental details and characterization studies 157
4.2.2 Results and discussions 161
4.2.2.1 RF-AMF induced heating 161
4.2.2.2 Effects of sample concentration on RF-AMF induced heating efficiency 164
4.3 MFH in water based ferrofluid containing phosphate coated $CoFe_2O_4$ MNP 173
4.3.1 Experimental details and characterization studies 173
4.3.2 Results and discussions 177
4.3.2.1 RF-AMF induced heating 177
4.3.2.2 Effects of sample concentration and medium viscosity on RF-AMF induced heating efficiency 183
4.4 Conclusions 187
Chapter 5
Magnetic hyperthermia in magnetic nanoemulsions: Effects of polydispersity, particle concentration, medium viscosity and orientational ordering
5.1 Introduction 189
5.2 Effects of polydispersity, particle concentration and medium viscosity on RF-AMF induced heating efficiency 190
5.2.1 Experimental details and characterization studies 191
5.2.2 Results and discussions 197
5.2.2.1 RF-AMF induced heating of octane based ferrofluid 197
5.2.2.2 RF-AMF induced heating of magnetic nanoemulsion 200
5.2.2.3 Effects of polydispersity and MNP concentration on heating efficiency 205
5.2.2.4 Effects of medium viscosity on heating efficiency 208
5.3 Effects of orientational ordering on heating efficiency of magnetic nanoemulsions immobilized in an agar gel 213
5.3.1 Experimental details and characterization studies 214
5.3.2 Results and discussions 215
5.3.2.1 Atomic force microscopy based studies on orientational ordering 215
5.3.2.2 Effects of orientational ordering on RF-AMF induced heating efficiency 220
5.4 Conclusions 231
Chapter 6
Conclusions and recommendations for future work
6.1 Summary and conclusions 234
6.2 Recommendations for future work 237

List of References 239

LIST OF FIGURES

Figure no.	Figure caption	Page no.
Figure 1.1	Alignment of moments and the variation of inverse of susceptibility (χ^{-1}) as a function of temperature for different kinds of magnetism. Here, TC, TN and TB indicate Curie temperature (for ferro and ferrimagnetic materials), Neel temperature (for antiferromagnetic materials) and blocking temperature (for superparamagnetic materials), respectively. Typical shapes of the magnetization curves, as a function of applied magnetic field, is also shown for ferromagnetic, paramagnetic and superparamagnetic materials. The susceptibility and saturation magnetization of superparamagnetic materials are higher than those of paramagnetic materials due to macro-spin approximation.	4
Figure 1.2	Schematic diagram showing the hierarchical structure of different types of magnetism.	5
Figure 1.3	Schematic representation of variation of coercivity as a function of size for ferromagnetic/ferrimagnetic nanoparticles. The insets show the typical shapes of the magnetization curves, as a function of applied magnetic field for superparamagnetic and ferromagnetic materials. The saturation magnetization, remnant magnetization and coercive field are indicated in the ferromagnetic hysteresis loop.	15
Figure 1.4	Schematic diagram of a typical cubic spinel ferrite structure.	19
Figure 1.5	Bio-medical applications of magnetic nanoparticles (MNP).	22
Figure 1.6	Schematics of typical (a) ferrofluids and (b) ferroemulsions. Here, MNP indicates magnetic nanoparticle. The MNP are coated with a surfactant for steric stabilization in an oil medium, whereas, the emulsion droplets are coated with an anionic surfactant for electrostatic stabilization in aqueous medium.	25
Figure 1.7	Schematic illustration of some important applications of magnetic fluids (ferrofluids and ferroemulsions).	27
Figure 1.8	Schematic illustration of various nano-materials used in different types of hyperthermia. Here, NPTT, NFRA, NUH and MFH indicate nano-photo thermal therapy, nano-radio frequency ablation, nano-ultrasound hyperthermia and magnetic fluid hyperthermia, respectively.	28
Figure 1.9	Number of publications in MFH, as a function of year of publication. The data is tabulated on March 1st, 2017 using SciFinder (https:// www.cas.org/ products/ scifinder). (Inset) A typical scheme for MFH based cancer therapy (RF-AMF indicates radio frequency alternating magnetic field).	32
Figure 1.10	During RF-AMF induced heating, MNP act as efficient converters of magnetic energy to heat energy. Various factors (like size & polydispersity, anisotropy, orientational ordering, medium viscosity, saturation magnetization and coercivity) influencing RF-AMF induced heating efficiency in magnetic nanoparticles are schematically shown. Two major applications of RF-AMF induced heating of MNP, viz., magnetic fluid hyperthermia and magneto-thermally triggered drug delivery are also illustrated.	38
Figure 1.11	Schematic diagram representing the magnetic moment oriented (a) along easy axis (black dotted line) in the absence of an external magnetic field and (b) along the direction of external magnetic field (indicated by an arrow). (c) Neel relaxation of the magnetic moment on withdrawal of the external magnetic field. The magnetic moment relaxes back towards the easy direction. (d) Brownian relaxation of the magnetic moment on withdrawal of the external magnetic field. Relaxation is achieved by whole scale rotation of the MNP and	43

	the magnetic moment remains fixed with respect to the crystallographic direction (indicated by the red dotted line).	
Figure 1.12	Variation of Neel, Brownian and effective relaxation time as a function of MNP diameter for three different values of anisotropy energy density, viz., 25, 50 and 75 kJm^{-3}, respectively.	44
Figure 1.13	Variation of normalized total energy (E_t/k_BT) as a function of θ_m (angle between the anisotropy and magnetization axes) for different orientations of RF-AMF with respect to H_{DC}, viz., $\phi = 0^0$, 45^0 and 90^0. Variation of E_t/k_BT for H = 0 is also shown in the figure. (Inset) Schematic illustration of the system geometry with the angles θ_m and ϕ.	51
Figure 2.1	Characterization techniques used to investigate different physical properties of the magnetic nanoparticles (MNP), ferrofluids (FF) and ferroemulsions (FE). The physical properties probed by each technique and typical results are also shown in the figure.	62
Figure 2.2	Schematic diagram of a typical vibrating sample magnetometer (VSM), showing the essential components.	68
Figure 2.3	(a) Schematic diagram of a typical atomic force microscope (AFM). (b) Schematic illustration of the different modes of operation in an AFM.	70
Figure 2.4	(a) AFM tip surface profile (Y_{AFM}), as a function of distance along X-axis, obtained after tip-shape de-convolution of typical topography images. (b) First order (dY_{AFM}/dx) and (c) second order (d^2Y_{AFM}/dx^2) derivatives of the tip surface profile with respect to the distance along X-axis. The bending radius ($r_{bending}$) is estimated using the formula: $r_{bending} = [\{1+(dY_{AFM}/dx)^2\}^{3/2}]/(d^2Y_{AFM}/dx^2)$.	72
Figure 2.5	Schematic diagram of the radio frequency induction heating system, used in the present study, along with the essential components. The schematic diagram of the parallel resonance tank circuit is also shown, where, the heating coil acts as an inductor and the generator module indicates filters, chopper, inverter, auxiliary and upstream transformers.	76
Figure 2.6	Typical photographs of the heating coil used. The diameter and height of the coil, along with water inlet and outlet, are indicated in the photographs.	76
Figure 2.7	Axial distribution of magnetic field for a current (477.5 A) carrying coil with 6 number of turns. The sample is kept within ± 3.5 mm of the central location for ensuring minimum non-uniformity in field distribution. (Inset) Schematic illustration of the magnetic field at an on-axis point for a current carrying loop. The radial component (PT) cancels out due to circular symmetry of the on-axis point.	79
Figure 2.8	Schematic diagram of a typical fluorescence lifetime spectroscopy based fiber optic temperature sensor.	81
Figure 2.9	Typical photograph of the fiber optic temperature sensor (Osensa Innovations Corp., Canada) used in the present study.	83
Figure 2.10	Schematic illustration of the total radiance received by an infrared camera.	85
Figure 2.11	Typical photograph of the RF induction heating system used for magnetic fluid hyperthermia experiments. (a) Infrared camera, (b) fiber optic temperature sensor, (c) optical to electrical signal converter, (d) resonator tank, (e) high frequency generator, (f) heating coil, (g) tripod stand for infrared camera, (h-i) data, from fiber optic temperature senor and infrared camera, respectively, displayed on personal computers. The sample is placed at the centre of the heating coil.	87
Figure 2.12	Illustration of the three numerical techniques, viz., (a) Box-Lucas, (b) exponential regression and (c) linear regression of the initial data, used for determination of the initial rates of temperature rise under non-adiabatic limit,	91

	during RF-AMF induced heating (H = 57.3 kAm^{-1}) in a water based ferrofluid contacting 1.5 wt. % phosphate coated Fe_3O_4 MNP. The values of initial rate and adjusted R^2 are also shown in the corresponding figures.	
Figure 2.13	Schematic classification of various types of uncertainties involved in SAR estimation during RF-AMF induced heating. The major reasons behind each type of uncertainty and the probable solutions are also outlined.	93
Figure 2.14	(a) Temperature rise (ΔT) as a function of time during RF-AMF induced heating of four different base fluids (without any magnetic nanoparticles), viz., kerosene, hexadecane, ethylene glycol and water. (Inset) Maximum temperature rise (ΔT_{max}) as a function of $(\rho c)^{-1}$ for the base fluids. The adjusted R^2 and slope of the linear regression analysis are ~ 0.97 and 0.09 ± 0.01 Jm^{-3}, respectively. (b) ΔT as a function of time for the base fluids (water and kerosene) with and without PTFE shielding surrounding the sample holder, during RF-AMF induced heating under external field amplitudes of 63.0 and 51.4 kAm^{-1}. The maximum temperature rise with and without PTFE shielding are encircled in orange and blue, respectively.	95
Figure 2.15	ΔT as a function of time, measured using fiber optic temperature sensor and IRT for water and kerosene based samples during RF-AMF induced heating under external field amplitudes of (a) 63.0 kAm^{-1} and (b) 57.3 kAm^{-1}, respectively. The temperature rise curves obtained from fiber optic sensor are fitted with three linear regression analyses, viz., initial delay time (0-3 s), delay corrected time (3-10 s) and without delay corrected time (0-10 s). On the other hand, IRT based curves are fitted with a single linear regression analysis. (c) Calibration curve showing the variation in response time (t) as a function of probe diameter. The data is collected from specifications provided by the manufacturer. A schematic diagram of a typical fiber optic temperature sensor is also shown in the figure. (d) Delay time corrected initial rates of temperature rise as a function of initial rates of temperature rise without delay time correction, for the water based samples.	99
Figure 2.16	Variation of ΔT as a function of time, during RF-AMF induced heating of (a) water and (b) kerosene based magnetic fluid, containing Fe_3O_4 MNP, under external field amplitudes of 63.0 and 51.4 kAm^{-1} followed by natural cooling. Variation of (dT/dt) as a function of ΔT for the water based magnetic fluid during natural cooling after RF-AMF induced heating under external field amplitudes of (c) 63.0 kAm^{-1} and (d) 51.4 kAm^{-1}. Variation of (dT/dt) as a function of ΔT for the kerosene based magnetic fluid during natural cooling after RF-AMF induced heating under external field amplitudes of (e) 63.0 kAm^{-1} and (f) 51.4 kAm^{-1}. The 4^{th} order polynomial fits and linear regression analyses are also shown in the figures.	105
Figure 2.17	Variation of LR and ΔT_{LL} as a function of sample volume for the water and kerosene based sample in the cases of (a) 5 mL and (b) 1 mL sample vials, during natural cooling after RF-AMF induced heating under external field amplitude of 63.0 and 51.4 kAm^{-1}, respectively. LR and ΔT_{LL} as a function of external field amplitude for (c) water and (d) kerosene based magnetic fluids, when 1 mL and 5 mL sample vials are used. Variation of LR and ΔT_{LL} as a function of external field amplitude for (e) water and (f) kerosene based magnetic fluids, when temperature measurements are performed using IRT and fiber optic temperature sensor and the samples are kept in a 5 mL vial.	109
Figure 2.18	(a) Typical variation of ΔT as a function of time, during RF-AMF induced heating of a water based sample under a non-adiabatic experimental set-up. The rate of temperature rise, as a function of median time is calculated using several linear regression analyses (shown in the figure). (b) Variation of rate of	112

	temperature rise (measured), linear loss rate and adiabatically reconstructed rate of temperature rise as a function of median time. Variation of SAR calculated using adiabatic reconstruction method as a function of SAR calculated using slope corrected method, proposed by Wildeboer et al. [297], for (c) water and (d) kerosene based magnetic fluids of three different concentration under various external field amplitudes.	
Figure 3.1	(a) Powder X-ray diffraction pattern of the synthesized Fe_3O_4 MNP. (b) Room temperature M-H curve for the synthesized Fe_3O_4 MNP. The saturation magnetization is ~ 42 emu/g. (Inset) Variation of magnetization as a function of the inverse of magnetic field. The value of the inverse magnetic field ($1/H_0$) for zero magnetization is determined from linear regression analysis (also shown in the figure).	119
Figure 3.2	Typical infrared images of the sample W2 (6 wt. %) at time t = (a) 0, (b) 100, (c) 200, (d) 300, (e) 400, (f) 500, (g) 600, (h) 700, (i) 800, (j) 900 s, respectively, during RF-AMF induced heating under an external field amplitude of 63.0 kAm^{-1} at 126 kHz. The pseudo colour coded temperature scales are also shown along with the images.	120
Figure 3.3	Infrared thermography based temperature increase ($\Delta T = T-T_i$), as a function of time, for the magnetic nanofluids containing TMAOH coated Fe_3O_4 MNP, at five different sample concentrations, during RF-AMF induced heating under four different external field amplitudes, viz., (a) 63.0, (b) 57.0, (c) 51.4 and (d) 45.3 kAm^{-1}, respectively.	121
Figure 3.4	(a) Variation of maximum temperature rise (ΔT_{max}) at the end of the heating period (t = 900 s), as a function of external field amplitude for the water based magnetic fluids of five different concentrations. (b) Variation of ΔT_{max} as a function of sample concentration, during field induced heating under four different external field amplitudes. The variation of ΔT_{max} with sample concentration was fitted with Box-Lucas equation and the regression curves are also shown in the figure.	122
Figure 3.5	(a) Horizontal temperature profiles at various time intervals, during RF-AMF induced heating of the sample W2 (6 wt. %), under an external field amplitude of 63.0 kAm^{-1}. (b) 3-dimensional view of the surface temperature distribution of the sample W2 at t = 400 s, during RF-AMF induced heating under an external field amplitude of 63.0 kAm^{-1}.	125
Figure 3.6	RF-AMF induced temperature rise followed by natural temperature decay for three consecutive cycles, for the sample W2 (6 wt. %), at an external field amplitude of 57.0 kAm^{-1}. The square wave indicates the state of the RF-AMF.	126
Figure 3.7	Variation of initial rate of temperature rise as a function of sample concentration for the water based magnetic nanofluids, during RF-AMF induced heating under four different external field amplitudes.	126
Figure 3.8	Variation of ΔT, measured using IRT and conventional fiber optic temperature sensor, as a function of time, during RF-AMF induced heating of the samples (a) W3 and (b) W2, under four different external field amplitudes. Variation of (c) crossover temperature difference (ΔT_{cross}) and (d) crossover time (t_{cross}) as a function of sample concentration.	128
Figure 3.9	(a) Variation of $\Delta T_{IRT\text{-}Probe}$ as a function of time, during RF-AMF induced heating of the sample W1 under four different external field amplitudes. (b) Variation of the time corresponding to maximum error ($t_{error\text{-}max}$), as a function of RF-AMF amplitudes, for magnetic fluids of five different concentration. (c) Variation of $\Delta T_{IRT\text{-}Probe}$ as a function of ΔT_{IRT} during RF-AMF induced heating of the sample W1, under RF-AMF amplitudes of (c) 63.0 kAm^{-1} and (d) 57.0 kAm^{-1}. (e) Box-Lucas fitting of the increasing part of $\Delta T_{IRT\text{-}Probe}$ vs. ΔT_{IRT} curve	132

	for the sample W1, during RF-AMF induced heating under an external field amplitude of 57.0 kAm^{-1}. (f) Linear regression analyses of the decreasing part of $\Delta T_{IRT\text{-}Probe}$ vs. ΔT_{IRT} curve for the sample W1, during RF-AMF induced heating under an external field amplitude of 57.0 kAm^{-1}. Linear fits corresponding to single and dual slope correction procedures are shown in the figure.	
Figure 3.10	Empirical data correction protocol for ΔT vs. time curves, recorded using IRT and conventional fiber optic temperature sensor for the samples (a) W1 and (b) W2, during RF-AMF induced heating under external field amplitudes of 57.0 and 63.0 kAm^{-1}, respectively.	133
Figure 3.11	(a) Variation of convection corrected SAR as a function of sample concentration. SAR decreased with increasing sample concentration due to an enhancement of dipolar interaction. (b) Variation of convection corrected SAR as a function of square of the external field amplitudes for water based magnetic fluids of four different concentrations. SAR increased linearly with H^2 and the linear fits are shown by solid lines.	136
Figure 3.12	(a) Distance distribution function, P(r), obtained from SAXS, as a function of MNP diameter. (Inset) Variation of ln(I(q)) as a function of ln(q) for the synthesized MNP. The high q (Porod's region) data is fitted with a linear regression analysis (also shown in the figure). (b) Hydrodynamic size distribution of the MNP dispersed in kerosene. The data is fitted with a log-normal distribution (also shown in the figure). (c) FTIR spectra of the oleic acid coated MNP, where, the major absorption bands are indexed.	141
Figure 3.13	Typical infrared images of the sample K1 (23 wt. %) at time t = (a) 0, (b) 10, (c) 20, (d) 30, (e) 40, (f) 50, (g) 60, (h) 70, (i) 80, (j) 90, (k) 100, (l) 110, (m) 120, (n) 130 and (o) 140 s, respectively, during RF-AMF induced heating. The pseudo colour coded temperature scales are also shown along with the images. The RF-AMF amplitude was kept constant at 57.3 kAm^{-1}.	142
Figure 3.14	IRT based Temperature increase (ΔT) as a function of time, during RF-AMF induced heating under various RF-AMF amplitudes for four different sample concentrations, viz., (a) 23, (b) 16.5, (c) 11 and (d) 7.5 wt. %. Variation of ΔT_{max} as a function of (e) external field amplitude and (f) sample concentration, where, the horizontal lines indicate the hyperthermia limit (ΔT = 14 ^{0}C).	144
Figure 3.15	(a) Horizontal line scans across the top surface of the sample K1 at time t = 0-150 s, in steps of 10 s, during RF-AMF induced heating under an external field amplitude of 57.3 kAm^{-1}. (b) 3-dimensional surface plot at time t = 30 s, during RF-AMF induced heating of sample K1 under an external field amplitude of 57.3 kAm^{-1}.	145
Figure 3.16	(a) Temperature (measured using IRT) variation as a function of time for the sample K1 (23 wt. %), during RF-AMF induced heating under an external field amplitude of 57.3 kAm^{-1} followed by natural cooling for three consecutive cycles. The square wave indicates the state of the external RF-AMF, where, the upper and lower states represent 'on' and 'off' conditions, respectively. (b) RF-AMF induced temperature rise and natural temperature decay for the three consecutive heating cycles in the case of sample K1 (for H = 57.3 kAm^{-1}), under cyclic boundary conditions.	146
Figure 3.17	Variation of initial rate of temperature rise ($\left.\frac{dT}{dt}\right\|_{t=0}$) as a function of sample concentration, for five different external field amplitudes, in the case of oil based ferrofluid containing oleic acid coated Fe_3O_4 MNP.	147
Figure 3.18	Variation of ΔT, measured using IRT and fiber optic temperature sensor, as a function of time, during RF-AMF induced heating under various external field	149

	amplitudes for two samples, viz., (a) K2 (16.5 wt. %) and (b) K3 (11 wt. %). (c) Variation of crossover temperature difference (ΔT_{cross}) as a function of sample concentration, for five different external field amplitudes. (d) Variation of $t_{cross}/t_{heating}$ as a function of sample concentration, for five different external field amplitudes, where, t_{cross} and $t_{heating}$ indicate crossover time and heating time (period for which, RF-AMF is switched on), respectively.	
Figure 3.19	ΔT vs. time curves, recorded using IRT and conventional fiber optic temperature sensor for the sample K1 (23 wt. %), during RF-AMF induced heating under an external field amplitude of 57.3 kAm^{-1}. The convection corrected ΔT data are also shown in the figure and dual slope correction procedure is found to be more accurate.	151
Figure 3.20	(a) Variation of convection corrected SAR as a function of sample concentration, for the samples K1-K4, under five different external field amplitudes. SAR increased with sample concentration due to an enhancement of effective number of heat sources per unit volume. (b) Variation of SAR as a function of square of the external field amplitudes. The linear fits are shown as solid lines.	153
Figure 4.1	(a) Powder XRD pattern of the phosphate coated Fe_3O_4 MNP. The average crystallite size (~ 7.8 nm) is calculated from the strongest diffraction peak corresponding to the (311) plane. (b) Room temperature M-H curve for the phosphate coated Fe_3O_4 MNP. The saturation magnetization is ~ 52 emu/g. (c) Hydrodynamic size distribution of the phosphate coated MNP dispersed in water. (d) TEM image of the synthesized phosphate coated MNP. (Inset) Number distribution obtained from the TEM image. (e) Weight loss, as a function of temperature, for the phosphate coated MNP. (f) FTIR spectra of the phosphate coated MNP, where, the major absorption bands are indexed.	160
Figure 4.2	Temperature increase (ΔT) as a function of time for phosphate coated Fe_3O_4 MNP based ferrofluids at various external field amplitudes for six different sample concentrations, viz., (a) 0.5 (b) 1.0, (c) 1.5, (d) 2.0, (e) 2.5 and (f) 6.0 wt. %.	162
Figure 4.3	(a) Variation of ΔT_{max} as a function of external field amplitude, for six different sample concentrations, in the case of water based ferrofluid containing phosphate coated Fe_3O_4 MNP. The horizontal dotted line indicates a ΔT of 14 ^0C (hyperthermia limit). (b) Variation of ΔT_{max} as a function of sample concentration for five different external field amplitudes.	163
Figure 4.4	Variation of SAR as a function of square of the external field amplitude (H^2), for six different sample concentrations, viz., 0.5, 1.0, 1.5, 2.0, 2.5 and 6.0 wt. %. It can be seen that SAR varies linearly with H^2 and the linear regression curves are also shown in the figure.	165
Figure 4.5	(a) Variation of SAR as a function of sample concentration, for five different external field amplitudes. (Inset) The variation of ΔT as a function of time, for six different sample concentrations, at a fixed RF-AMF amplitude of 57.3 kAm^{-1}. The arrows are shown to aid in following the non-monotonic behaviour of the temperature rise with increasing sample concentration. (b) Schematic diagram, showing the lowering of anisotropy energy barrier due to enhancement of dipolar interaction at higher sample concentration. The vertical line separates the increasing and decreasing trend of the SAR values. The subscripts 'low' and 'high' indicate low and high concentration, respectively. C, BH, N_{flip} and E_{flip} indicate sample concentration, anisotropy barrier height, nos. of flip per unit time and energy release per flip, respectively.	167
Figure 4.6	Theoretical variation of heating power per sample volume as a function of sample concentration. Redrawn from (with permission) Haase and Nowak	172

	[280].	
Figure 4.7	(a) Distance distribution function (P(r)), obtained from SAXS, as a function of MNP diameter for the phosphate coated $CoFe_2O_4$ MNP. The data is fitted with a log-normal distribution (also shown in the figure). (b) Variation of ln(I(q)), as a function of ln(q), for the phosphate coated $CoFe_2O_4$ MNP. The high q region is fitted with a straight line (also shown in the figure).	175
Figure 4.8	Room temperature magnetization curve of the $CoFe_2O_4$ MNP. (Inset 1) Magnified region of the room temperature M-H curve, from H = 0 to ± 0.22T, where, the hysteresis loop is clearly discernible. (Inset 2) Low temperature (~ 5 K) M-H curve of the $CoFe_2O_4$ MNP, where, a wide hysteresis loop is clearly seen.	176
Figure 4.9	Typical infrared images of the sample C2 at time t = (a) 0, (b) 100, (c) 200 and (d) 300 s, during RF-AMF induced heating under an external field amplitude of 51.4 kAm^{-1}. The pseudo colour coded temperature scales are shown along with the images. The emissivity was optimized to reflect the true temperature of the fluid sample.	179
Figure 4.10	Variation of temperature rise (ΔT), as a function of time, for the phosphate coated $CoFe_2O_4$ nanofluids of five different concentrations, viz., (a) 1, (b) 2, (c) 3, (d) 4 and (e) 5 wt. %, during RF-AMF induced heating under four different external field amplitudes, viz., 51.4, 45.0, 36.7 and 26.0 kAm^{-1}. (f) RF-AMF induced temperature rise followed by natural temperature decay for three consecutive cycles, for the sample C5 (5 wt. % MNP concentration), under an external field amplitude of 51.4 kAm^{-1}. The square wave indicated the state of RF-AMF.	180
Figure 4.11	(a) Variation of ΔT_{max} as a function of H^2 for the samples C1-C5. ΔT_{max} increased linearly with H^2 and the linear regression analyses are also shown in the figure. (b) Variation of SAR as a function of H^2 for the samples C1-C5. SAR increased linearly with H^2 and the linear regression analyses are also shown in the figure.	181
Figure 4.12	(a) Variation of SAR as a function of sample concentration, for the samples C1-C5, during RF-AMF induced heating under four different external field amplitudes, viz., 51.4, 45.0, 36.7 and 26.0 kAm^{-1}. (b) Bar chart, showing the SAR values of the sample C2 and agar immobilized samples C2A1 and C2A2 containing 1 and 2 wt. % agar concentrations, respectively. Typical infrared images of the agar immobilized sample C2A2, at time t = 0 (Inset: I1) and 200 s (Inset: I2), respectively, during RF-AMF induced heating under an external field amplitude of 51.4 kAm^{-1}.	185
Figure 5.1	Temperature dependent magnetization (ZFC: zero field cooled and FC: field cooled) for the oleic acid coated Fe_3O_4 MNP, in the temperature range of 4-300 K. The blocking temperature (T_B) is obtained as ~ 191 K. (Inset) Magnetization as a function of applied magnetic field for the oleic acid coated Fe_3O_4 MNP at room temperature. The saturation magnetization is obtained as ~ 42 emu/g.	193
Figure 5.2	(a) Hydrodynamic size distributions of the emulsion samples E1, E2 and E3. (b) Zeta potential distributions for the emulsion samples. (c) Weight loss data for the emulsion samples, determined from thermogravimetric analysis (TGA). The MNP concentration for the samples E1, E2 and E3 are 4.7, 4.6 and 1.7 wt. %, respectively.	194
Figure 5.3	(a) AFM topography image of the agar immobilized magnetic nano-emulsion sample (EA1) on a mica substrate, where, the emulsion droplets can be clearly seen. The topography height scale and lateral dimensions are shown along with the image. (b) Magnified view of a 3 μm × 3 μm area (indicated by the red square in Fig. 5.3a). Dimensional analyses are performed and the intensity	196

	profiles as a function of size are shown in (c). The average droplet diameter is found to be ~ 200 nm.	
Figure 5.4	(a) ΔT as a function of time, for the sample O1, at a fixed frequency of 126 kHz and under five different external field amplitudes, viz., 57.3, 51.4, 45.0, 36.7 and 26.0 kAm^{-1}. The temperature rise as a function of time for the dispersion medium alone is also shown. (b) Linear variation (Adj. $R^2 = 0.96$) of SAR and ΔT_{max} as a function of H^2, for the sample O1. (c) Theoretically calculated SAR values, at 300 K, under five different external field amplitudes. (Inset) The variation of experimentally determined SAR values as a function of the theoretically calculated SAR values.	198
Figure 5.5	ΔT as a function of time, for the samples (a) E1, (b) E2 and (c) E3, during RF-AMF induced heating under four different external field amplitudes, viz., 63.0, 57.0, 51.4 and 45.3 kAm^{-1}. (d) Linear Variation of SAR (adjusted $R^2 = 0.9$, 0.97 and 0.93 for the samples E1, E2 and E3, respectively), as a function of H^2, for the emulsion samples. Linear variation of ΔT_{max}, as a function of H^2, for the samples E1 and E2.	204
Figure 5.6	Effect of size polydispersity on SAR. Theoretically calculated SAR for the emulsion samples E1, E2 and E3 with the most probable radii (r_{mp}) of 100, 80.3 and 90.8 nm, respectively, under an external field amplitude of 63.0 kAm^{-1}. The σ_{ln} values are 0.2, 0.4 and 0.3 for the samples E1, E2 and E3, respectively. The SAR variation of the hypothetical samples E1 (r_{mp} = 100 nm and $\sigma_{ln} = 0.4$) and E2 (r_{mp} = 100 nm and $\sigma_{ln} = 0.4$) are also shown. (Inset) Theoretically calculated SAR values for the samples E1 and E2 for external field amplitudes of 57.0, 51.4 and 45.3 kAm^{-1}, respectively.	206
Figure 5.7	(a) ΔT as a function of time, for the agar matrix alone (without any MNP loading), where, it can be seen that temperature rise is insignificant. Additionally, ΔT as a function of time, measured using fiber optic temperature sensor and IRT, for the agar based sample loaded with 0.5 wt. % MNP, under an external field amplitude of 26.0 kAm^{-1}, is shown. The convection corrected IRT based temperature rise profile is also shown in the figure. (b) ΔT as a function of time, for the agar based sample EA1, under four different external field amplitudes, viz., 63.0, 57.0, 51.4 and 45.3 kAm^{-1}. (d) Linear variation of SAR and ΔT_{max} as a function of H^2 for the sample EA1.	210
Figure 5.8	(a) Bar chart, showing the SAR values for the samples E1 and EA1 as a function of external field amplitude. SAR ratio (SAR-EA1/SAR-E1) between the samples EA1 and E1 is also shown. (b) SAR ratio (SAR-EA1/SAR-O1) of the agar based sample, EA1 and MNP based nanofluid, O1 as a function of external field amplitude.	212
Figure 5.9	(a) AFM topography image (90 μm × 90 μm) of the dried nanoemulsion droplets, drop casted on a freshly cleaved mica surface, under the influence of H_{DC} (direction of H_{DC} shown by an arrow). (b) A magnified view (10 μm × 10 μm) of a section (indicated by the green rectangle) of Fig. 5.9a. (c) 3D surface topography of Fig. 5.9b. (d) Magnified (1.5 μm × 1.5 μm) MFM topography view of a section (indicated by the orange rectangle) of the linear chain-like structure shown in Fig. 5.9b. (e) 3D surface topography of Fig. 5.9d. (f) MFM phase image (lift distance ~ 500 nm) of Fig. 5.9d.	218
Figure 5.10	(a) AFM topography image (10 μm × 10 μm) of the emulsion droplets immobilized in an agar matrix in the absence of H_{DC}, where, the emulsion droplets are found to be randomly oriented. (b) Magnified view (2.5 μm × 2.5 μm) of a section (indicated by the blue rectangle) of Fig. 5.10a. (c) 3D surface topography of Fig. 5.10b. (d) AFM topography image showing the formation of linear chain-like structures in agar immobilized emulsion droplets under the	219

	influence of H_{DC}. (e) Magnified view (3.5 μm × 10 μm) of a section (indicated by the orange rectangle) of Fig. 5.10d. (f) Magnified view (1.8 μm × 2.0 μm) of a section (indicated by green rectangle) of Fig. 5.10e.	
Figure 5.11	Typical infrared images of the emulsion sample (E) at time t = (a) 0, (b) 200, (c) 400 and (d) 600 s, respectively, during RF-AMF induced heating under an external field amplitude of 63.0 kAm^{-1}. The pseudo colour coded temperature scale is also shown. (e) Horizontal temperature profiles along the top surface of the sample E, during RF-AMF induced heating under an external field amplitude of 45.3 kAm^{-1} at time t = 0, 100, 200, 300, 400, 500 and 600 s.	221
Figure 5.12	Temperature rise (ΔT) as a function of time, for the samples (a) E, (b) EA, (c) EA_{para} and (d) EA_{per}, during field induced heating under external field amplitudes of 63.0, 57.0, 51.4 and 45.3 kAm^{-1}. (Insets) Adiabatically reconstructed temperature rise as a function of time, during RF-AMF induced heating under four different external field amplitudes, for the corresponding samples.	223
Figure 5.13	(a) Variation of SAR as a function of H^2, during RF-AMF induced heating of the agar based samples, viz., EA, EA_{para} and EA_{per}. (Inset) Linear variation of SAR as a function of H^2 for the sample E. (b) Variation of ΔT_{max} as a function of H^2, during RF-AMF induced heating of the samples EA, EA_{para} and EA_{per}. (Inset) Linear variation of ΔT_{max} as a function of H^2 for the sample E.	224
Figure 5.14	Bar chart of the SAR values, as a function of external field amplitude, for the agar based samples, viz., EA, EA_{para} and EA_{per}. It is observed that the maximum and minimum values of SAR are for the samples EA_{para} ($\phi = 0^0$) and EA_{per} ($\phi = 90^0$), respectively, and SAR values for the sample EA are intermediate in all the cases. The geometrical orientations of RF-AMF (H) and H_{DC} for the samples EA, EA_{para} and EA_{per} are schematically shown in the figure.	227
Figure 5.15	Variation of Neel, Brownian and effective relaxation time, as a function of MNP diameter, for $\phi = 0^0$ (H_{DC} parallel to H) and 90^0 (H_{DC} perpendicular to H).	228
Figure 5.16	(a) Variation of effective relaxation time (τ), as a function of MNP diameter, for two different orientation of RF-AMF with respect to H_{DC}, viz., $\phi = 0^0$ and 90^0. (Inset) Theoretically calculated normalized SAR, as a function of MNP diameter, for $\phi = 0^0$ and 90^0. (b) Variation of SAR ratios (EA_{para} to EA_{per} and EA_{para} to EA) as a function of external field amplitude for the agar based samples.	229

LIST OF TABLES

Table No.	Table Caption	Page No.
Table 1.1	Curie temperature, saturation magnetization and critical exponent of iron, cobalt and nickel. As T→T_C (from above), $\chi \propto (T - T_C)^{-\gamma_E}$. Mean field approximation yields $\gamma_E = 1$ [5].	7
Table 1.2	Blocking temperature for surfactant capped Fe_3O_4 MNP of different sizes.	11
Table 1.3	A few commercially available magnetic nanoparticles and specific ligands.	21
Table 1.4	A few typical *in vitro* and *in vivo* applications of NPTT, NFRA and NUH. Here, PEDOT-PSS-PEG = poly-(3, 4-ethylenedioxythiophene)–poly (4-styrenesulphonate) - polyethylene glycol, NGS-PEG-Cy7 = nano graphene sheet with polyethylene glycol coating labelled with Cy7, β-CD-capped HMSN = β cyclodextrin capped hydrophobic mesoporous silica nanoparticles.	29
Table 1.5	Comparison between different kinds of hyperthermia with respect to excitation source, excitation range, heat generation principle, target locations, advantages and drawbacks.	30
Table 1.6	Details of a few clinical trials carried out using MFH. Here, PC = prostate cancer, GM = glioblastoma multiforme, CT = concomitant treatment, BT = brachytherapy, RT = radiotherapy, Median T90 = temperature exceeded for 90 % of tumor volume, Median CEM 43 = cumulative equivalent minutes at 43 ^{0}C.	32
Table 1.7	Details of a few MFH based *in vivo* studies. Here, DMSA = dimercaptosuccinic acid, DOX = doxorubicin, N6L = nucant multivalent pseudopeptide, Chito-FION = chitosan oligosaccharide stabilized ferrimagnetic iron oxide nanocubes.	33
Table 1.8	Details of a few *in vitro* studies using MFH. Here, CEIO = carbon encapsulated iron oxide MNP, PEG = polyethylene glycol, FA = folic acid, DOX = doxorubicin, Her2 = anti-human epidermal growth factor receptor, CREKA = tumor homing peptide (Cys-Arg-Glu-Lys-Ala), m = mesoporous, dm = dual porus, 5-FU = 5-fluorouracil.	34
Table 1.9	A few MFH studies using different kinds of MNP. Sizes of the MNP, obtained SAR values, exposure conditions and the corresponding references are listed.	35
Table 2.1	Salient features of the radio frequency induction heating system (Five Celes, France), used in the present study.	75
Table 2.2	Salient features of the heating coil used in the present study.	76
Table 2.3	Calculated magnetic field amplitudes as a function of coil current in a few cases.	78
Table 2.4	Salient features of the fiber optic temperature sensor used in the present study.	82
Table 2.5	Salient features of FLIR SC 5000 series infrared camera.	87
Table 2.6	Linear loss rate (LR) and ΔT_{LL} for water and kerosene based samples of different volumes in 1 mL sample holder. W and K indicate water and kerosene based ferrofluids with 10 and 6.5 wt. % sample concentrations, respectively.	104
Table 2.7	Linear loss rate (LR) and ΔT_{LL} for water and kerosene based samples of	104

	different volumes in 5 mL sample holder. W and K indicate water and kerosene based ferrofluids with 10 and 6.5 wt. % sample concentrations, respectively.	
Table 2.8	Linear loss rate and ΔT_{LL} for water (W) and kerosene (K) based samples of 1000 µL volume, in 5 mL sample holder (BV), using infrared thermography (IRT) based temperature measurements.	108
Table 2.9	A summary of different types of thermodynamic uncertainties involved in non-adiabatic SAR estimation.	113
Table 3.1	Regression parameters for Box-Lucas fit of ΔT_{max} as a function of sample concentration.	122
Table 3.2	Parameters for linear regression analyses of the decreasing section of the $\Delta T_{IRT\text{-}Probe}$ vs. ΔT_{IRT} curve for the sample W1, during RF-AMF induced heating, under an external field amplitude of 57.0 kAm^{-1}.	133
Table 3.3	Comparison of SAR obtained using IRT (SAR-IRT) and fiber optic temperature sensor (SAR-FO), along with the convection corrected SAR values (SAR-IRT-CC).	134
Table 3.4	Comparison of SAR obtained using IRT (SAR-IRT) and fiber optic temperature sensor (SAR-FO), along with convection corrected SAR values (SAR-IRT-CC) for the samples K1-K4.	151
Table 4.1	Comparison of initial rates of temperature rise and SAR values calculated using three different data analysis techniques (Box-Lucas fit, exponential fit and linear regression analysis) for the sample A3, under five different external field amplitudes.	164
Table 4.2	Optimum sample concentration and maximum SAR and ΔT_{max} for the water based ferrofluids, containing phosphate coated Fe_3O_4 MNP, under five different RF-AMF amplitudes.	166
Table 4.3	ΔT_{max} (maximum temperature rise at the end of heating phase) and specific absorption rate (SAR) for the samples C1-C5, during RF-AMF induced heating, under four different external field amplitudes, viz., 51.4, 45.0, 36.7 and 26.0 kAm^{-1}.	182
Table 5.1	Details of the samples E1, E2 and E3.	195
Table 5.2	SAR and ΔT_{max} values of the samples E, EA, EA_{para} and EA_{per}, during RF-AMF induced heating, under four different external field amplitudes.	224

SYNOPSIS

Magnetic nanoparticles have widespread applications in the bio-medical field. Magnetic fluid hyperthermia (MFH) is one of the applications, where a fluid containing magnetic nanoparticles (MNP) is used for cancer therapy with the aid of a radio frequency alternating magnetic field (RF-AMF). The high surface to volume ratio of the surface modified MNP is found to be beneficial for preferential conjugation with the tumor cells and external magnetic field guided drug delivery. Multimodal hyperthermia therapy, using larger sized magnetic nano-carriers, enables synergistic coupling of MFH with drug delivery or photodynamic therapy. Owing to its immense clinical benefits, MFH is being considered as an alternate cancer treatment modality. Though RF-AMF induced heating of MNP is well studied, several challenges still remain, for e.g., the role of sample concentration, dipolar interaction, medium viscosity, size polydispersity and external DC magnetic field induced texturing on the RF-AMF induced heating efficiency are poorly understood. Also, there are several uncertainties involved in the calculations of specific absorption rate (SAR), which are rarely addressed. For real time *in vivo* applications of MFH in human, effective monitoring of temperature, preferably mapping, of the entire tumor region is required which warrants the need for developing a non-contact and wide area temperature mapping protocol. These served as motivation for undertaking the present problem. The major objectives of this thesis are i) to probe the role of size polydispersity, particle concentration and medium viscosity on RF-AMF induced heating efficiency in oil and water based ferrofluids; ii) to probe the thermal losses associated with RF-AMF induced non-adiabatic heating of magnetic fluids and to develop an adiabatic reconstruction protocol for the measured temperature rise curves; iii) to develop an effective temperature mapping methodology during RF-AMF

induced heating of magnetic fluids using infrared thermography (IRT) and to develop a convection corrected data analysis protocol for the accurate quantification of heating efficiency; iv) to probe RF-AMF induced heating in larger sized magnetic nanoemulsions from the perspective of multimodal therapy and (v) to study the effect of external DC magnetic field induced texturing on MFH efficiency of magnetic nanoemulsion. The thesis consists of six chapters and details of the chapters are summarized below.

Chapter 1 gives an introduction on magnetism in nanoparticles with a focus on ferrofluids (dispersions of single domain superparamagnetic MNP) and oil-in-water ferroemulsions (size ~ 200 nm). It is followed by a description on the Neel-Brownian relaxation mechanism and Rosensweig's model of RF-AMF induced heating in magnetic nanofluids. **Chapter 2** briefly discusses the experimental methods for synthesis of magnetic nanofluids and various characterization techniques used in the present study. This is followed by a discussion on radiofrequency induction heating system used for MFH studies, sample temperature measurement using radio frequency (RF) immune fiber optic temperature sensor (contact type) and non-contact infrared thermography (IRT) technique and SAR quantification protocols. Various thermodynamic uncertainties associated with peripheral heating, delayed heating, heat loss from sample and spatial variation in temperature profile within the sample are also discussed. This chapter also includes a description on an adiabatic reconstruction protocol, developed for the accurate estimation of SAR, which was found to decrease the uncertainties by a factor of ~ 3. **Chapter 3** discusses MFH studies in water and oil based ferrofluids containing tetramethyl ammonium hydroxide (TMAOH) and oleic acid coated Fe_3O_4 MNP, respectively, using IRT and the results are compared with those obtained from conventional fiber optic temperature sensor. The temperature rise

curves measured using both the techniques were found to be very similar. Nevertheless, it was found that the IRT based measurements indicated higher temperature up to a certain time and beyond that, the temperature obtained from IRT was lower than the fiber optic temperature sensor based data. These observations were attributed to the internal and external convection phenomena during RF-AMF induced heating. An empirical data analysis protocol was developed for incorporating the convection effects. It was observed that the convection corrected SAR values were in good agreement with those obtained from the conventional fiber optic temperature sensor (within a maximum error of ± 5 %). For the water based ferrofluid, it was observed that SAR decreased with increasing sample concentration due to an enhancement in dipolar interaction. On the other hand, for the oil based ferrofluids, in the absence of agglomeration, SAR was found to increase with sample concentration due to an increase in the effective number of heat sources per unit volume. **Chapter 4** presents the results of MFH studies in water based ferrofluids containing phosphate coated Fe_3O_4 and $CoFe_2O_4$ MNP of different concentrations. The SAR was found to vary linearly with square of the field amplitudes. For the phosphate coated Fe_3O_4 ferrofluids, SAR initially increased with sample concentration, attained a maximum at an optimum concentration and, thereafter, decreased with increasing sample concentration. During Neel relaxation, the magnetic moments of the individual nanoparticles flip direction across the anisotropy energy barrier and the dissipated power during this process is directly proportional to the product of number of flips per unit time and energy released per flip. For lower sample concentration, the dipolar interaction is less significant and hence, the anisotropy energy barrier is higher, which leads to a larger value of energy release per flip. On the other hand, probability of such flipping is lower for higher anisotropy energy barrier, resulting in a

comparatively lower number of flips per unit time. With increase in sample concentration, the height of the anisotropy energy barrier reduces due to an increase in dipolar interaction, resulting in larger number of flips per unit time, albeit with lower energy release per flip. This causes the SAR to peak at an optimum sample concentration, where the product of energy release per flip and number of flips per unit time is maximum. Beyond the optimum concentration, SAR decreased with increasing sample concentration due to the enhanced dipolar interaction, which caused the Neel relaxation time and ensemble averaged equilibrium susceptibility to decrease. Experiments on water based ferrofluids, containing phosphate coated $CoFe_2O_4$ MNP, showed no substantial variation in SAR with increasing sample concentration. This was attributed to the significant contribution from hysteresis loss to the global SAR, owing to the ferromagnetic nature of $CoFe_2O_4$. **Chapter 5** discusses the MFH studies on magnetically polarizable oil-in-water nanoemulsions, containing single domain superparamagnetic nanoparticles in the oil phase, where the effects of size polydispersity of the droplets, MNP concentration, medium viscosity and external DC magnetic field induced orientational ordering on MFH efficiency was probed. The magnetic nanoemulsion with lower polydispersity (σ_{ln} = 0.2) exhibited ~ 3.3 times higher SAR, as compared to the sample with larger polydispersity (σ_{ln} = 0.4). The SAR values of the nanoemulsions with 4.6 wt. % MNP loading (with σ_{ln} = 0.4) and 1.7 wt. % MNP loading (with σ_{ln} = 0.3) were found to be comparable, suggesting a higher heating efficiency for nanoemulsions with lower MNP loading and reduced polydispersity. The emulsion droplets, immobilized in an agar matrix, exhibited a ~ 40-50% drop in SAR due to abrogation of whole scale Brownian relaxation of the emulsion droplets in the agar medium. Further, for a fixed RF-AMF amplitude, the highest SAR was obtained for the sample oriented parallel to

the direction of RF-AMF, which was attributed to the enhancement of effective uniaxial anisotropy energy density and increased effective relaxation time. Magnetic force microscopy (MFM) studies revealed an extremely weak remnant volume magnetization of the oriented emulsion droplets, indicating superparamagnetic nature of the droplets, which is essential for practical applications. **Chapter 6** presents a summary of the results obtained, along with the conclusions drawn and recommendations for future work.

Chapter 1

Introduction

Chapter 1 Introduction

1.1 Magnetism in materials

The attempts to understand natural phenomena, in ancient times, were driven by curiosity, fantasy and imagination. Our understanding of mysterious phenomena like fire, electricity, magnetism, etc. invariably changed the life of mankind with everlasting benefits. Magnetism, as per the most popular accounts, was an accidental discovery around 600 BC by a shepherd named Magnes, who lived in Magnesia near Mount Ida in ancient Greece, from observation of sudden sticking of the ferrule of his stick and nails of his footwear. Loadstones (containing magnetite: Fe_3O_4) is one of the most abundant natural magnetic materials. The word magnet is derived from the Greek word 'magnetis lithos' which means stones of magnesia. The term 'loadstone', on the other hand, has an Anglo-Saxon meaning: leading stone.

Many ancient scientists and engineers (Peter Peregrinus, Roger Bacon and Robert Norman to name a few [1]) contributed to the initial understanding of magnetism; but it was William Gilbert, in 1600, who is truly credited for advancing magnetism out of the realm of superstitions, mystery and mythology with sound scientific understating, backed by experimental evidences [1, 2]. The modern concept of electromagnetism was introduced by Hans Cristian Oersted, in 1819-1820, which was further extended by Andre Ampere in 1820-1821. 1825 witnessed the advent of a working electromagnet. This was followed by the monumental contributions of Carl Friedrich Gauss, Jean-Baptiste Biot, Felix Savart, Michael Faraday and Joseph Henry during the years 1820-1832 and James Clerk Maxwell, in 1865, introduced analytical understanding of electromagnetic induction and classical theories of electromagnetic fields and radiations [3]. The insightful Maxwell's equations were used by Albert Einstein, 1905, for developing special theory of relativity. The field of electromagnetism has latter been incorporated into several modern advanced fundamental

theories like gauge theory, quantum electrodynamics, electroweak theory and standard model of particle physics.

Magnetism in materials can arise from two different sources, viz., electron magnetic moment and spin magnetic moment of nucleons [3-5]. The magnetic moment of the nucleons are several times (typically ~ 10^{-3} times) smaller than the electron magnetic moment and hence, insignificant for magnetic properties of materials [4]. Nevertheless, magnetic moments of nucleons are extremely useful for nuclear magnetic resonance (NMR), magnetic resonance imaging (MRI), Mossbauer spectroscopy and neutron magnetic scattering studies [4, 5]. Magnetic dipole moment ($\vec{\mu}_e$) of an electron rotating about its axis (considering electron as classical charged particle) with an angular momentum $\vec{I}$, is given by the following equation [4, 6].

$$\vec{\mu}_e = \frac{-e}{m_e}\vec{I} \tag{1.1}$$

Here, e and m_e indicate charge and mass of the electron, respectively. The angular momentum in Eq. 1.1, depending on the actual scenario, can be either spin angular momentum ($\vec{S}$), orbital angular momentum ($\vec{L}$) or the total angular momentum ($\vec{J} = \vec{L} + \vec{S}$). For incorporating the quantum effects and addition of angular momenta, the classical results are corrected by a dimensionless quantity, known as g-factor and magnetic dipole moment of an electron is expressed by the following equation [4, 6].

$$\vec{\mu}_e = g\frac{-e}{m_e}\vec{A} = -2\pi g\mu_B\frac{\vec{I}}{h_p} \tag{1.2}$$

Here, $\vec{A}$, μ_B and h_p indicate area vector, Bohr magneton (9.27×10^{-24} JT^{-1}) and Planck's constant (6.62×10^{-34} m^2kgs^{-1}), respectively. The magnetic moments are quantized in units of Bohn magneton and magnetization of a material is defined as magnetic moment per unit

volume of the material. Nevertheless, the true origin of magnetism is quantum mechanical in nature, as proved by Bohr-van Leeuwen theorem [7, 8] and can be simplistically explained on the basis of Heitler-London theory [9] of two-body molecular orbital where the combined wave function [$\Psi(r_1,r_2)$] of two electrons at positions r_1 and r_2, can be represented by the following equation [10].

$$\psi(r_1, r_2) = \frac{1}{\sqrt{2}}[u_A(r_1)u_B(r_2) \pm u_A(r_2)u_B(r_1)] \tag{1.3}$$

Here, u_A and u_B are the two atomic orbitals centred on nuclei A and B, respectively, and the last product in Eq. 1.3, indicates that the first electron is in an atomic orbital centred on the second nucleus and vice versa giving rise to an exchange interaction. This exchange interaction is fundamental to the understanding of magnetism (especially for co-operative magnetism) and is much stronger (~ 10^4 times) than the dipole-dipole interaction [5, 10].

1.2 Different types of magnetic materials

The magnetic behaviour of materials depends on their electronic configurations and temperature. The ferromagnetic, antiferromagnetic and ferrimagnetic materials exhibit collective magnetic interactions and have long range magnetic ordering below a certain critical temperature, known as Curie temperature for ferro and ferrimagnets [4, 5]. On the other hand, paramagnetic and diamagnetic materials do not have long range magnetic ordering. Magnetic materials are characterized according to the variation of magnetization (M) as function of magnetic field (H_{DC}) and the ratio of these two quantities is called as magnetic susceptibility ($\chi = M/H_{DC}$). Principal types of magnetism are briefly described below. **Fig. 1.1** shows the spin alignments and variation of inverse of susceptibility (χ^{-1}) as a function of temperature for different kinds of magnetism. Typical shapes of the magnetization curves, as a function of applied magnetic field, for ferromagnetic,

paramagnetic and superparamagnetic materials are also shown in **Fig. 1.1**. **Fig. 1.2** schematically shows the hierarchical structure [11] of different types of magnetism.

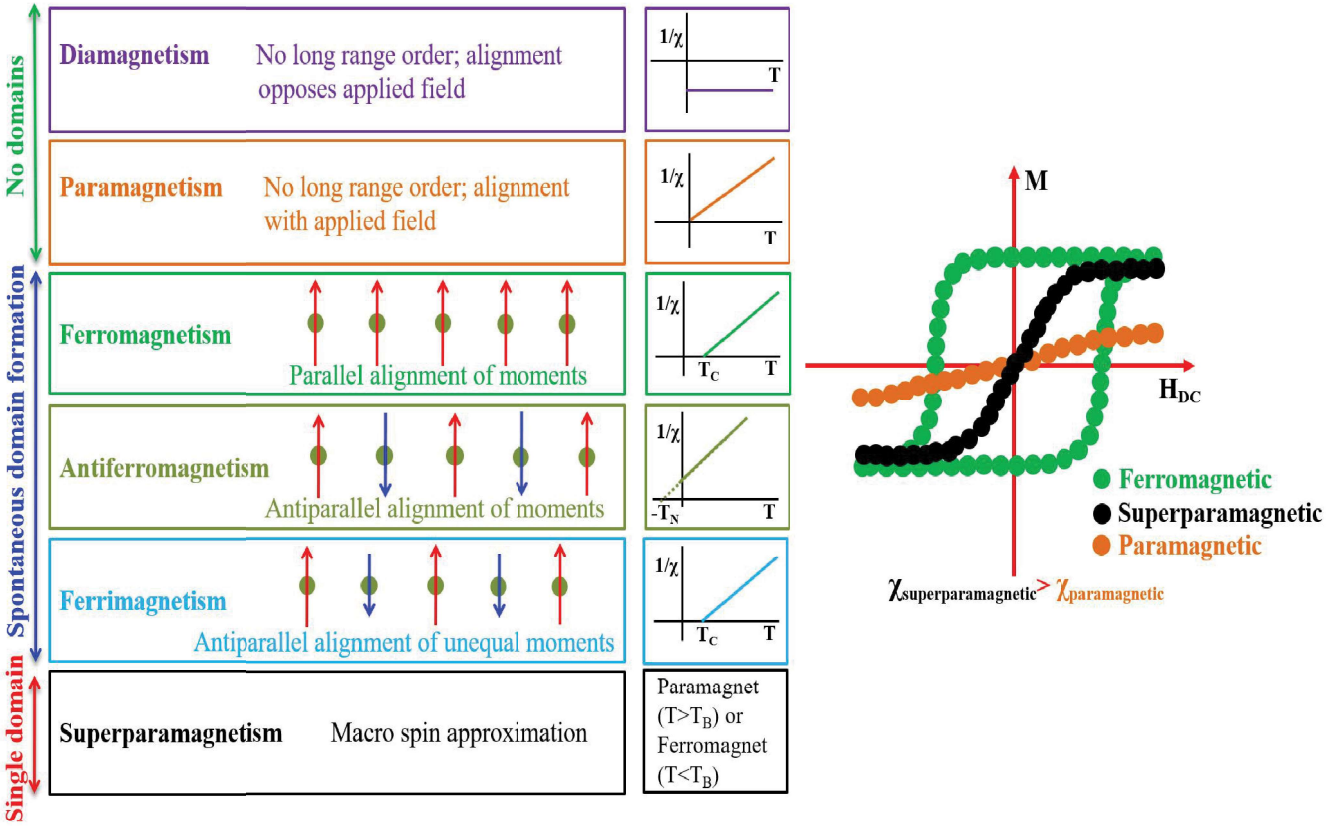


Figure 1.1: Alignment of moments and the variation of inverse of susceptibility (χ^{-1}) as a function of temperature for different kinds of magnetism. Here, T_C, T_N and T_B indicate Curie temperature (for ferro and ferrimagnetic materials), Neel temperature (for antiferromagnetic materials) and blocking temperature (for superparamagnetic materials), respectively. Typical shapes of the magnetization curves, as a function of applied magnetic field, is also shown for ferromagnetic, paramagnetic and superparamagnetic materials. The susceptibility and saturation magnetization of superparamagnetic materials are higher than those of paramagnetic materials due to macro-spin approximation.

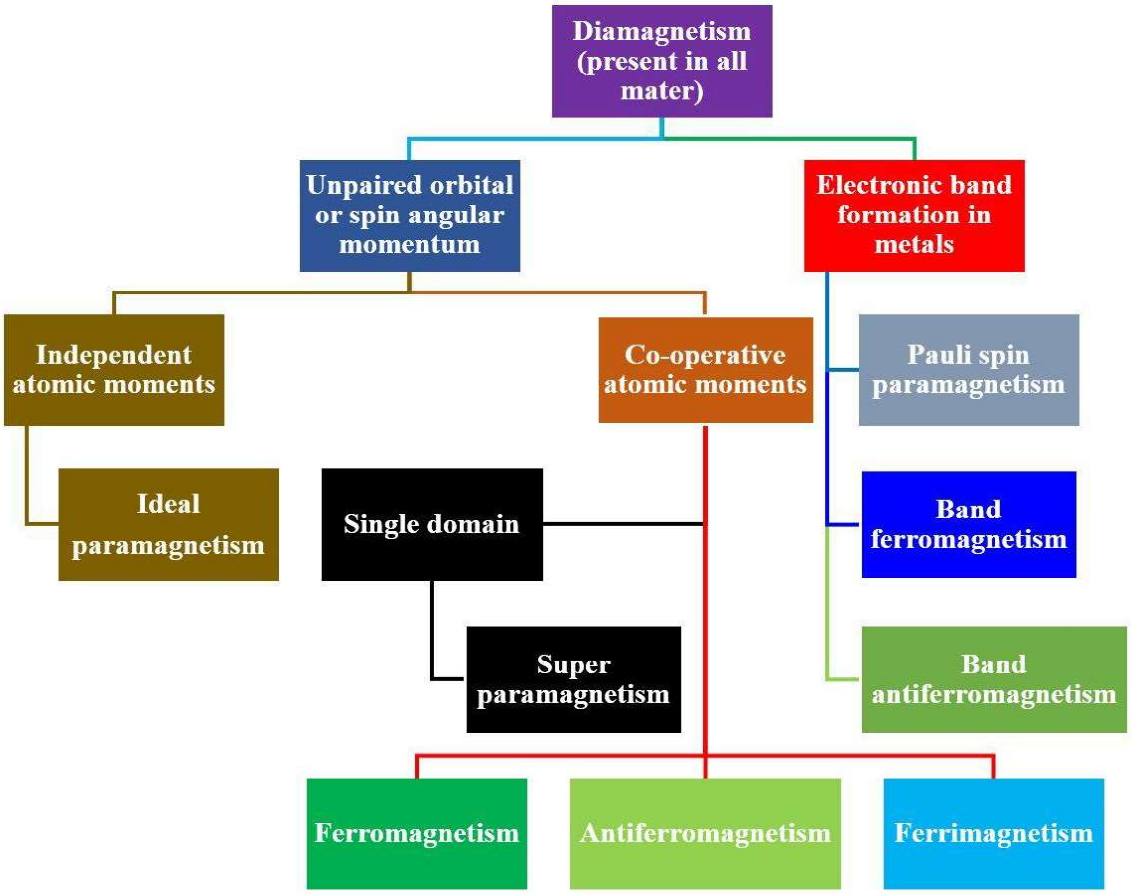


Figure 1.2: Schematic diagram showing the hierarchical structure of different types of magnetism.

Diamagnetism: Diamagnetism is due to the orbital motion of electrons and is present in all materials. For materials with unpaired electrons, diamagnetism is superseded by other types of magnetism and materials with no unpaired electrons or completely filled orbitals exhibit diamagnetic properties. For diamagnetic materials, application of a magnetic field results in negative magnetization leading to a negative value of susceptibility (shown in **Fig. 1.1**) which is independent of temperature. Monoatomic rare-earth gases like He, Ne, Ar and most poly-atomic gases like H_2, N_2, etc. are diamagnetic due to closed shell electronic configuration.

Paramagnetism: Paramagnetism occurs in materials with unpaired electrons in partially filled orbitals. In the absence of an external magnetic field, the dipole moments are randomly oriented leading to a net zero magnetization. However, in the presence of an external magnetic field, the moments orient themselves along the magnetic field, resulting in a net positive magnetization and susceptibility for the paramagnetic materials. On the other hand, the ability of the external magnetic field for orienting the magnetic moment is opposed by the randomizing effect of material temperature leading to a hyperbolic variation of susceptibility with temperature: $\chi = C_m/T$ (i.e., χ^{-1} varies linearly with T as shown in **Fig. 1.1**), which is known as Curies' law and C_m is a material dependent constant known as Curie constant. Oxygen molecule (O_2) and co-ordination complexes of d- and f-block elements are a few examples of paramagnets.

Ferromagnetism: Ferromagnetic materials have spontaneous magnetization, below a certain critical temperature, even in the absence of an external magnetic field. Under the Weiss molecular field approximation [12], each magnetic moment experiences an exchange field that is proportional to the average magnetization of all other moments (self-consistent mean field approximation) and can be expressed as $B_E=\lambda_E M$, where, B_E and λ_E indicate exchange field and exchange parameter, respectively. Curie temperature (T_C) is a critical temperature above which the spontaneous magnetization vanishes and it separates the ordered ferromagnetic phase (for $T<T_C$) from the disordered paramagnetic phase ($T>T_C$). The ferromagnetic susceptibility varies as: $\chi = C_m/(T-T_C)$ and at $T = T_C = C_m\lambda_E$, the susceptibility experiences a singularity due to phase transition from ferromagnetic to paramagnetic ordering (second order phase transition with infinite correlation length near criticality) [13]. The exchange parameter (λ_E) can be expressed in terms of Curie constant and Curie temperature: $\lambda_E = T_C/C_m = 3k_BT_C/[Ng^2\mu_B^2S(S+1)]$ and for iron, considering $T_C \sim 1000$ K, $g \sim 2$ and $S \sim 1$,

the value of λ_E is ~ 5000 indicating an exchange field of ~ 10^3 T as compared to ~ 0.1 T of the dipolar magnetic field at a neighbouring lattice point [5]. **Table 1.1** shows the T_C, saturation magnetization (M_s) and critical exponents for the three most commonly encountered ferromagnetic materials, viz., iron, cobalt and nickel.

Table 1.1: Curie temperature, saturation magnetization and critical exponent of iron, cobalt and nickel. As T→T_C (from above), $\chi \propto (T - T_C)^{-\gamma_E}$. Mean field approximation yields $\gamma_E = 1$ [5].

Material	T_C (K)	M_s (Gauss) (at room temperature)	M_s (Gauss) (at 4.2 K)	γ_E (dimensionless)
Iron (Fe)	1043	1707	1740	1.33 ± 0.02
Cobalt (Co)	1388	1400	1446	1.21 ± 0.04
Nickel (Ni)	627	485	510	1.35 ± 0.02

The exchange field approximately represents the quantum mechanical exchange interaction, as discussed earlier, and the exchange interaction between two atoms located at i and j and having spins $\vec{S}_i$ and $\vec{S}_j$ can be written as $H_E = -2J_{i,j}\vec{S}_i.\vec{S}_j$, which is known as Heisenberg model of exchange interaction [14]. Here, $J_{i,j}$ is the exchange integral which originates from overlapping of wave functions and for ferromagnetic materials, $J_{i,j}$ is positive ($J_{i,j}>0$) indicating that exchange energy is minimum for parallel spin alignment (below Curie temperature).

Each electron contributes to a saturation magnetic moment of 1 Bohr magneton (μ_B) and hence, theoretically, the magnetic moments of iron, cobalt and nickel atoms should be 4, 3 and 2 μ_B, respectively, on the basis of the fact that iron, cobalt and nickel have 4, 3 and 2 unpaired electrons in 3d shell, respectively. But the experimentally observed values for iron, cobalt and nickel are 2.22, 1.72 and 0.54 μ_B, respectively. These discrepancies and non-

integral values of effective number of magnetic carriers are explained on the basis of band or itinerant electron model which considers the delocalization of 3d electrons in metallic solids [5, 14].

Microscopically, the ferromagnetic materials below Curie temperature are composed of small regions, called magnetic domains, within each of which the magnetic moments are saturated. But the magnetization directions of the individual domains are not parallel and hence, an external magnetic field is required to achieve saturation magnetization at a macroscopic level. Under the application of an external field, the increase in magnetization of a ferromagnetic material occurs via three mechanisms, viz., reversible displacement of domain boundaries at low field, irreversible displacements of domain boundaries at moderate field and magnetization rotation at high field. Variation of magnetization as a function of applied magnetic field shows a typical hysteresis behaviour for ferromagnetic materials (shown in **Fig. 1.1**). The hysteresis loop is characterized by the saturation magnetization (maximum value of magnetization at high field), remnant magnetization (residual magnetization at zero field) and coercive field (the field required to demagnetize the sample). The positions of saturation magnetization, remnant magnetization and coercive field are indicated in the **inset of Fig. 1.3**. Ferromagnetic materials with low coercive field are called soft magnets, whereas, hard magnets require a comparatively larger coercive field for complete demagnetization.

Antiferromagnetism: Antiferromagnetic materials have antiparallel spin alignment ($J_{i,j}<0$) with net zero magnetization below the ordering temperature known as Neel temperature (T_N). In this case, the susceptibility does not diverge at T_N but shows a maximum at T_N ($\chi \propto \frac{1}{T+T_N}$) [4]. Antiferromagnetism is observed below T_N and above T_N the material

shows paramagnetic behaviour ($\chi \propto \frac{1}{T}$). Below T_N, antiferromagnetic materials show different values for parallel and perpendicular susceptibilities, where, the parallel susceptibility monotonically decreases with decreasing temperature. Typical examples of antiferromagnetic materials are MnO, NiO, FeMn, FeO, Cr, $FeCl_2$, etc.

Ferrimagnetism: Ferrimagnetic materials have effective antiparallel alignment of unequal magnetic moments leading to a substantial spontaneous magnetization at room temperature. Incomplete cancellation of magnetic moments within a domain leads to spontaneous magnetization (though lower than pure ferromagnets) in ferrimagnetic materials, which vanishes above Curie temperature leading to paramagnetic behaviour. Using self-consistent mean field approximation, it can be shown that coupling of two antiferromagnetic exchange interactions can lead to a ferrimagnetic ordering [4]. Like ferromagnetic materials, they have magnetic domains and exhibit magnetic saturation and hysteresis. Most common examples of ferromagnets include Fe_3O_4, $CoFe_2O_4$ and other types of ferrites.

Superparamagnetism: Superparamagnetism is a special form of magnetism, which occurs in single domain ferromagnetic or ferrimagnetic materials. The magnetic moment in such single domain magnetic nanoparticles can randomly flip due to thermal energy and hence, when the observation time for magnetization measurement is significantly larger than the time required for flipping of the moment, the magnetization appears to be zero in the absence of an external magnetic field [4, 5, 15]. When an external magnetic field is applied, superparamagnetic nanoparticles are magnetized and saturated at higher field values at a much faster rate as compared to paramagnetic materials. This is because of the fact that magnetic moment of a superparamagnetic nanoparticle is a single macro-spin which is a sum of the magnetic

moments of all the atoms present within the single domain. This phenomenon is known as macro-spin or giant-spin approximation in superparamagnetic nanoparticles [4]. Therefore, magnetization curves of superparamagnets are similar to that of paramagnets, but much steeper, i.e., superparamagnets have higher susceptibility as compared to paramagnets (shown in **Fig. 1.1**). This is the reason for the name 'superparamagnetism'. But this scenario is true above a certain critical temperature, known as blocking temperature (T_B). Below the blocking temperature, thermal energy is not sufficient to cause random flipping of magnetic moments and the superparamagnets are said to be in blocked state, i.e., they exhibit non-zero spontaneous magnetization in the absence of an external magnetic field [4, 5]. Below blocking temperature superparamagnetism resembles ferromagnetism and exhibits hysteresis loops.

Due to the presence of an anisotropy energy barrier, the magnetic moment of a superparamagnetic nanoparticle has two easy directions (most stable configurations) which are antiparallel to each other and separated by the anisotropy energy barrier. At a finite temperature, there exist a finite probability for flipping of magnetic moments against the anisotropy energy barrier and the time required for flipping ($\tau_{flipping}$) is, in general, expressed by a Neel-Arrhenious equation [16] of the form: $\tau_{flipping} = \tau_0 \exp(KV_p / k_B T)$, where, τ_0, K, V_p and k_B indicate attempt time, anisotropy energy density, particle volume and Boltzmann's constant, respectively. For measurement time ($\tau_{measurement}$) larger than $\tau_{flipping}$, the average magnetization is zero (superparamagnetic state). On the other hand, for $\tau_{measurement} < \tau_{flipping}$, a net non-zero magnetization exist (blocked state) and the blocking temperature (T_B) is defined by the equality of measurement and flipping time, which leads to $T_B = \frac{KV_p}{k_B \ln(\frac{\tau_{measurement}}{\tau_0})}$.

Table 1.2 shows the blocking temperature (T_B) of Fe_3O_4 MNP of four different sizes along

with the MNP volume (V_p), saturation magnetization (M_s) and anisotropy energy density (K) [17]. The anisotropy energy densities were calculated using the expression, $K=25k_BT_B/V_p$, where, k_B indicate Boltzmann's constant [18].

Table 1.2: Blocking temperature for surfactant capped Fe_3O_4 MNP of different sizes.

MNP size (nm)	MNP volume (m^3)	T_B (K)	M_s (emu/g)	K (kJ/m^3)
2.8	1.149×10^{-26}	28	14.2	841
3.7	2.652×10^{-26}	37	25.6	481
4.6	5.096×10^{-26}	41	33.5	278
6.8	1.646×10^{-25}	50	39	105

Single domain superparamagnetic nanoparticles have found wide spread applications in magnetic data recording, magnetic fluids and bio-medical fields [4, 19].

1.3 Magnetism in nanoparticles

The word 'nano' has been derived from the Greek word 'nanos', meaning dwarf. Nano scale (10^{-9} m) is intermediate between atomic (10^{-10} m) and meso (10^{-6} m) scales. Nanotechnology is the science, engineering and technology, which is conducted at the nano scale and is focused on fundamental understating and application of such nano-entities across the fields of physics, chemistry, material science, biology and engineering. Nanoscience, on the other hand, has been liberally understood as the fundamental science of materials at nano scale that enables the fruitful employment of nanotechnology. The concept of nanotechnology was first introduced in 1959 by Richard Feynman in his celebrated lecture: "There's plenty of room at bottom" [20]. In his epoch-making lecture, Richard Feynman indicated the possibility of miniaturization by manipulation at nano scale.

"I want to build a billion tiny factories, models of each other, which are manufacturing simultaneously. ... The principles of physics, as far as I can see, do not speak against the

possibility of manoeuvring things atom by atom. It is not an attempt to violate any laws; it is something, in principle, that can be done; but in practice, it has not been done because we are too big."

---- Richard P. Feynman (1918-1988)

The word nanotechnology was coined and popularized by Norio Taniguchi [21]. Large surface area to volume ratio of nanomaterials leads to several interesting features like high surface reactivity, improved electrical, optical and magnetic properties, possibility of band-gap engineering and profound quantum effects due to similarity of the sizes of these nanomaterials with their de Broglie wavelengths [22]. Nanoscience and nanotechnology has revolutionized the fate of human life forever and has found widespread applications in almost all aspects of technology ranging from bio-medical, aerospace, communication, defence, structural, automobile, energy, clean water, environmental, data storage and computation [23-25].

Magnetism in nanomaterials has been a topic of intense research for the last few decades due to its paramount importance in data recording and bio-medical applications [26]. Nanomagnetism is poised to produce continued strategic breakthroughs of future and the ability to manipulate magnetic materials at atomic/molecular level opens up huge vistas in the related fields from fundamental as well as application points of view. Apart from magnetic nanoparticles and thin films (layered magnetic structures), magnetic nanorings [27] and nanoplates [28] have also drawn considerable attention due to their unique magnetic properties.

1.3.1 Effects of size on magnetism in nanoparticles

Magnetic properties of nanoparticles are distinctly different from bulk magnetic (ferro or ferrimagnets) properties due to the following major reasons [29].

i) Due to smaller size of the magnetic nanoparticles (MNP), a large fraction of the atoms resides on the surface with broken translational symmetry, leading to specific sites with reduced coordination number, broken exchange bond and frustration [30, 31].

ii) The size of the MNP are comparable to their domain sizes and other critical length scales, leading to macro-spin approximation and quantum confinement effects [32, 33].

iii) The spin wave energy is comparable to the thermal energy, leading to changes in spin wave spectrum [34].

iv) In the cases of surfactant capped MNP, the close contact with the surfactant layer leads to changes in electron density and related magnetic effects [35, 36].

The magnetic behaviour of MNP are highly dependent on anisotropy energy density and dipole-dipole interaction energy between more than one MNP. If the anisotropy energy is stronger than the dipole-dipole interaction energy, the MNP exhibit superparamagnetism, whereas, enhanced dipole-dipole interaction energy leads to super spin glass-like behaviour [37, 38]. Spin glasses are disordered and frustrated (approximately equal number of ferromagnetic and antiferromagnetic bonds) magnetic system with random alignment of the magnetic moments of the component atoms in a metastable state, which exhibit time dependent magnetic behaviour [39, 40].

The coercivity is one of the most important parameters for selection of a magnetic material for practical applications. **Fig. 1.3** schematically shows the variation of coercive field (H_c) as a function of MNP size along with the relevant models used in each range for theoretical understanding. Typical shapes of the magnetization curves, as a function of applied magnetic field, for ferro and superparamagnetic materials are also illustrated in the inset of **Fig. 1.3**. The salient features of **Fig. 1.3** are described below.

i) The multi-domain state at larger size is energetically favourable when the energy required for formation of a domain wall is lower than the difference between

magnetostatic energies of single and multi-domain states [4]. As the particle size is reduced, the movement of the domain walls are restricted leading to an increasing trend in coercivity in the multidomain state [41]. Theoretical calculations based on Rayleigh loops are used to understand the magnetic properties in the multi-domain states [42]. According to Rayleigh loop theory, in the vicinity of the demagnetized state, the magnetization caused by the application of a weak magnetic field is expressed as $M = \chi_i H_{DC} + \eta_R H_{DC}^2$, where, M, H_{DC}, χ_i and η_R indicate magnetization, applied magnetic field, initial susceptibility and Rayleigh constant, respectively [43-45]. For small value of H_{DC} (in the reversible magnetization region), the magnetization can be approximated by the first term only, whereas, for higher values of magnetic field, the second term becomes significant due to irreversible magnetization [44]. η_R changes sign on inversion of magnetic field, resulting in a magnetization loop as a function of applied magnetic field [43].

ii) With further decrease in MNP size, enhancement in surface energy of the domain walls occur and single domain states are energetically more favourable than multi-domain states [46]. The critical size (D_s) for the formation of single domain MNP is expressed as, $D_s = \frac{72\sqrt{a_s K}}{\mu_0 M_s^2}$, where, a_s is the exchange stiffness constant related to the width of the domain walls [26]. Typical values of D_s for iron, cobalt and nickel are ~ 19.0, 96.4 and 53.6 nm, respectively [47]. In the vicinity of D_s, incoherent spin reversals occur and coercivity decreases with increasing MNP size due to vortex-like magnetic state. Several interesting phenomena (like curling, buckling and fanning of magnetization) occur in this size range, which is beyond the exchange length ($L_E = \sqrt{\frac{2a_s}{\mu_0 M_s^2}}$, typical

values are ~ 3.28, 4.70 and 7.64 nm for iron, cobalt and nickel, respectively) but in the vicinity of single-multi domain boundary [26].

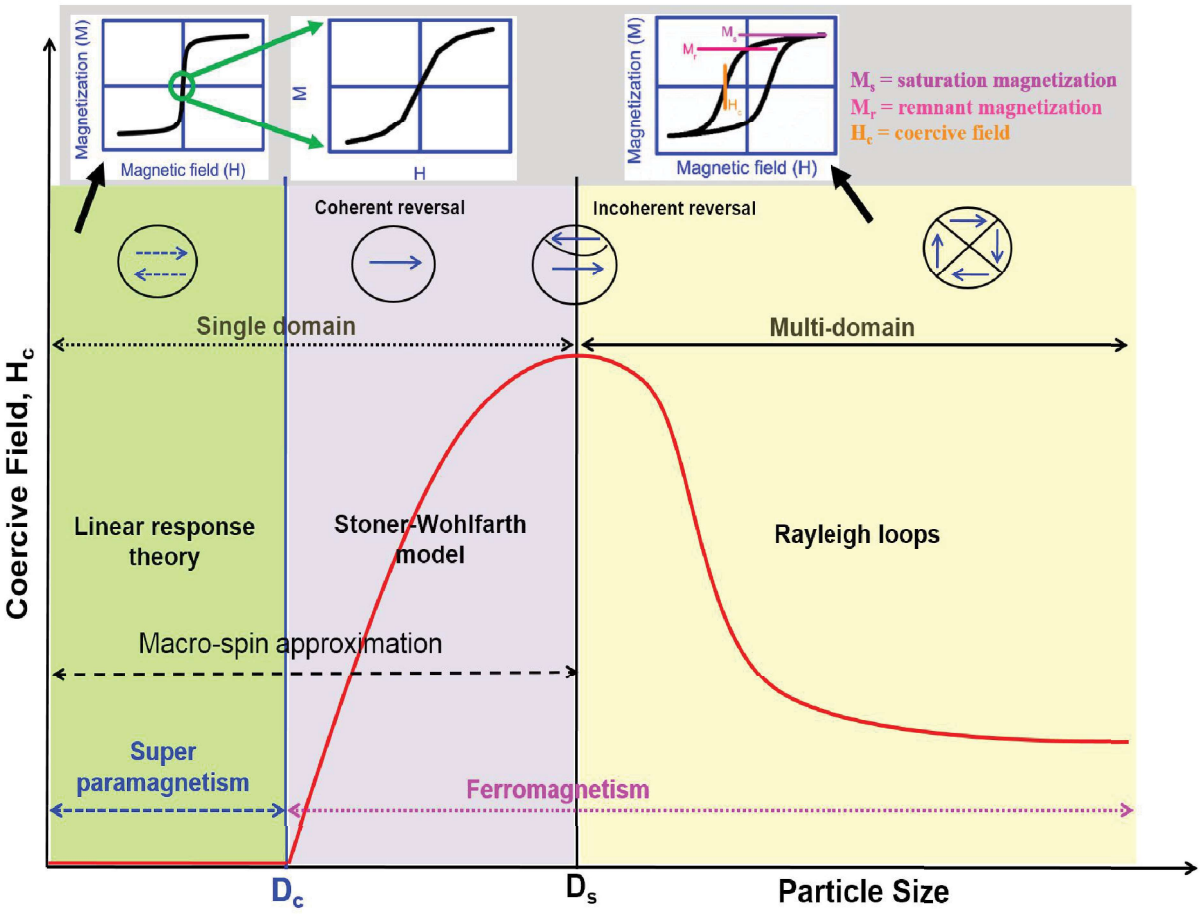


Figure 1.3: Schematic representation of variation of coercivity as a function of size for ferromagnetic/ferrimagnetic nanoparticles. The insets show the typical shapes of the magnetization curves, as a function of applied magnetic field for superparamagnetic and ferromagnetic materials. The saturation magnetization, remnant magnetization and coercive field are indicated in the ferromagnetic hysteresis loop.

iii) Below D_s, surface spin contribution increases with decreasing MNP size and coercivity decreases with decreasing MNP size. The configuration of magnetic moment in a single domain MNP depends on the contributions from magnetocrystalline anisotropy and

shape anisotropy energies [41]. In this region, coherent spin reversals occur and the theoretical calculations are based on Stoner-Wohlfarth model [42, 48]. The basic assumptions of this static model are single domain MNP, spheroidal geometry and uniaxial anisotropy energy density along the axis of symmetry (rotational) [48]. Variation of magnetization within the ferromagnetic material is neglected in this model and magnetization rotation with changing magnetic field (positive or negative in opposite directions along a single axis only) is calculated [49].

iv) With further decrease of MNP size, the thermal energy becomes sufficient to cause random flipping of the magnetic moments and beyond the critical size ($D_c = (\frac{150 k_B T}{\pi K})^{1/3}$, typical values are 16, 8 and 35 nm for iron, cobalt and nickel, respectively [26]), the MNP exhibit superparamagnetic properties with zero coercivity. Calculations based on linear response theory [16, 50, 51] are used for analysing the magnetic behaviour of superparamagnetic MNP. Considering K = 25 kJm^{-3} [52], the critical size of Fe_3O_4 for superparamagnetic behaviour at T = 300 K is ~ 20 nm. On the other hand, for $CoFe_2O_4$ MNP, superparamagnetic transition occur for sizes below ~ 10 nm [53, 54].

The saturation magnetization and Curie temperature of superparamagnetic MNP strongly varies with size due to significant contributions from surface spin disorder and fluctuations in the correlated magnetic moments confined in a small volume. Using a magnetic dead layer theory [55], it was shown that saturation magnetization of MNP (M_s) varies as $M_s=M_{sb}(1-6t_{coating}/d_{mnp})$, where, M_{sb}, $t_{coating}$ and d_{MNP} indicate saturation magnetization in multi-domain (bulk) state, coating thickness and MNP diameter, respectively [56]. On the other hand, T_C varies according to the following equation [26, 57, 58].

$$\frac{T_C(bulk) - T_C(MNP)}{T_C(bulk)} = \left(\frac{\xi_O}{d_{MNP}}\right)^{\lambda_s} \quad (1.4)$$

Here, λ_s and ξ_O are the shift exponent and order parameter, respectively. The estimated values of λ_s are 1, 1.42 and 1.1 from mean field approximation, Heisenberg's model and experimental analyses, respectively [26].

1.3.2 Spinel ferrites

Cubic spinel ferrites are a very important class of ferrimagnetic material due to their interesting physical properties and widespread technological applications. Hard ferrites (like cobalt and barium ferrite) with large coercivity and remnant magnetization are essential for permanent magnets due to their inherent resistance to demagnetization. On the other hand, soft ferrites (like manganese zinc ferrite or nickel zinc ferrites) can easily reverse their magnetization direction without much energy loss at high frequency which paved the way for their applications in the core of radio frequency transformers, switched-mode power supply and industrial inductors. Superparamagnetic ferrite nanoparticles and their dispersions have been a topic of intense research in the last few decades due to their diverse applications in the fields of bio-medical applications [59-63], heat transfer [64-69], magneto-rheological fluids [70-73] and sensors [74-77].

1.3.2.1 Structure of spinel ferrites

The general formulae for cubic spinel ferrites of transition metals is $[M_{\delta}^{2+}Fe_{1-\delta}^{3+}]_A[M_{1-\delta}^{2+}Fe_{1+\delta}^{3+}]_B O_4$, where, A and B indicate tetrahedral and octahedral sites, respectively, δ is the inversion parameter and M^{2+} indicate the divalent metal ions (for e.g., Fe^{2+}, Co^{2+}, Ni^{2+}, Mn^{2+}, Zn^{2+} etc.) [78]. The larger oxygen ions (ionic radius ~ 1.3 Å) are closely packed in a face-centred cubic structure and the smaller metal ions (ionic radii ~ 0.7-

0.8 Å) are placed in the spaces in-between them. The crystallographic arrangements are different for the tetrahedral and octahedral sites. In the tetrahedral A site, the metal ions are located at the centre of a tetrahedron whose corners are occupied by the oxygen ions, whereas, in the octahedral B site, the metal ion is surrounded by oxygen ions at the corner of an octahedron. A cubic spinel ferrite has 64 tetrahedral (A) and 32 octahedral (B) sites among which only 8 A sites (1/8 times) and 16 B sites (1/2 times) are occupied. **Fig. 1.4** schematically shows the structure of a cubic spinel ferrite along with the tetragonal and octahedral sites.

For δ = 1, the general formula becomes $[M^{2+}]_A[Fe_2^{3+}]_B O_4$ and in this case the tetrahedral and octahedral sites are complete filled by the divalent metal ions and trivalent Fe^{3+} ions, respectively. These are called ***normal spinels*** and typical examples are zinc ferrite and cadmium ferrite. For δ = 0, the general formula becomes $[Fe^{3+}]_A[M^{2+}Fe^{3+}]_B O_4$ and in this case the tetrahedral sites are fully occupied by trivalent Fe^{3+} ions, whereas, the octahedral sites are shared between divalent metal ions and trivalent Fe^{3+} ions. These are called ***inverse spinels*** and most popular examples include Fe_3O_4 and $CoFe_2O_4$. For $0<\delta<1$, both the tetrahedral and octahedral sites are shared between divalent metal ions and trivalent Fe^{3+} ions and such structures are called ***mixed spinels***. Typical examples of mixed spinel are manganese ferrite and nickel zinc ferrite. An inverse spinel ferrite is formed when the divalent metallic ions has more crystal field stabilization energy (CFSE) gain in the octahedral site as compared to the trivalent Fe^{3+} ions [79].

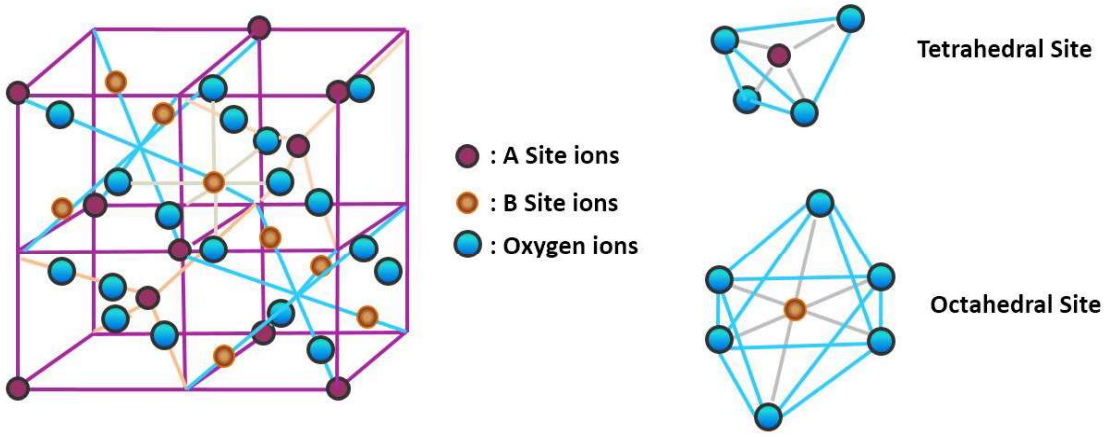


Figure 1.4: Schematic diagram of a typical cubic spinel ferrite structure.

1.3.2.2 Super exchange interactions in spinel ferrites

Super exchange or Kramers-Anderson exchange interaction leads to antiferromagnetic coupling between two next to nearest neighbour cations through a bridging non-magnetic anion [80, 81]. Super exchange interaction differs from direct exchange interaction due to the involvement of a non-magnetic anion and next to nearest neighbour atoms. In spinel ferrites, three kinds of magnetic interactions are possible between the metal cations located at tetrahedral (A) and octahedral (B) sites due to super exchange interaction through the bridging oxygen anion: A-A, A-B and B-B. The super exchange interactions are mediated through non-stationary transfer of one oxygen 2p electron to a neighbouring metal cation. The interaction energy for all three modes are negative leading to antiparallel alignment of the moments. Nevertheless, A-B interaction is the strongest in cubic spinel ferrites, followed by B-B and A-A interactions [4, 5]. In Fe_3O_4 MNP, this leads to an antiparallel alignment of Fe^{3+} ions in the tetrahedral (A) and octahedral (B) sites, resulting in complete cancellation of magnetic moments of Fe^{3+} ions and the magnetism of Fe_3O_4 is due to the uncompensated moments of Fe^{2+} ions in octahedral (B) sites [4, 5]. Hence, effective total magnetic moment

per formula unit of Fe_3O_4 = $(+5_{3+\text{ in A}}-5_{3+\text{ in B}}+4_{2+\text{ in B}})\ \mu_B = 4\ \mu_B$ which is in good agreement with the experimental value of 4.1 and the data obtained from neutron diffraction studies [5].

1.3.3 Bio-medical applications of magnetic nanoparticles (MNP)

MNP have found widespread application in the bio-medical field due to various factors, viz., high surface to volume ratio is found to be beneficial for promoting biological contact, easy escape from vasculature, preferential conjugation with specific cells for surface modified MNP and distal magnetic field controlled drug delivery or therapy [82, 83]. For biomedical applications, cytotoxicity and biocompatibility play an important role and magnetic iron oxide nanoparticles are found to be highly biocompatible as the iron-cell homeostasis is found to be well controlled by uptake, excretion and storage mechanisms and excess iron is easily removed from the body [60, 82]. Studies show that iron oxide MNP are biocompatible up to high doses (ferrofluids up to 5 % of blood volume with 1.5 wt. % MNP concentration) [84] and does not give rise to oxidative stress or long term change in the level of liver-enzymes in rats [85]. Biomedical applications of MNP include protein purification, isolation of nucleic acid, cell sorting, nucleic acid transfer and gene therapy, magnetic fluid hyperthermia, drug delivery and magnetic resonance imaging [60, 86-88]. A few examples of commercially available MNP along with the most common specific ligands are shown in **Table 1.3** [60, 89]. **Fig. 1.5** schematically shows the various bio-medical applications of MNP.

In protein purification, MNP functionalized with specific proteins are used for the separation of proteins, which eliminates the need for pre-treatment steps such as centrifugation and allow quick and efficient purification from crude samples [60, 90]. MNP also find applications in the isolation and detection of nucleic acids [91, 92].

Table 1.3: A few commercially available magnetic nanoparticles and specific ligands.

Category	**Type**	**Application**	**Product (representative)**	**Distributor (refers specifically to the product, other distributors also exist)**
Ferrofluids	Starch coated	Isolation of lysozymes, MRI-diagnostic, covalent coupling of biomolecules	FluidMAG-D	**Chemicell** (http://www.chemicell.com)
	Chitosan coated	Linear, bio-degradable polymer with amino group	FluidMAG-Chitosan	**Chemicell** (http://www.chemicell.com)
	Iron oxide in dextran matrix. Surface functionalized with hydroxide, carboxy (COOH) or amine (NH_2) groups. Surface coated with avidin, streptavidin, protein A, albumin, etc.	Magnetic resonance imaging (MRI), magneto-immuno assays. Good candidates for magnetic fluid hyperthermia.	Nanomag-D-spio	**Micromod Partikeltechnologie, GmbH** (https://www.micromod.de)
Coupled ligands	Streptavidin	Capture of biotinylated molecules	Sera-Mag Magnetic Speed Beads Streptavidin	**GE Healthcare Life Sciences** (http://www.gelifesciences.com)
	Protein G	Immunoglobulin G (IgG) purification	BioMag Plus Protein G Particles	**Polysciences, Inc.** (www.polysciences.com)
	Glutathione	Purification of glutathione S-transferase (GST) fusion proteins	GST MagBeads	**GenScript Corporation** (www.genscript.com)
	Amylose	Maltose-binding protein (MBP) fusion proteins isolation	Amylose Magnetic Beads	**New England Biolabs** (www.neb.com)
	Monoclonal antibodies	Selection of cells presenting specific antigens	Human Whole Blood CD4 (cluster of differentiation 4: a type of glycoprotein) selection Kit (positive selection)	**Stem Cell Technologies** (www.stemcell.com)

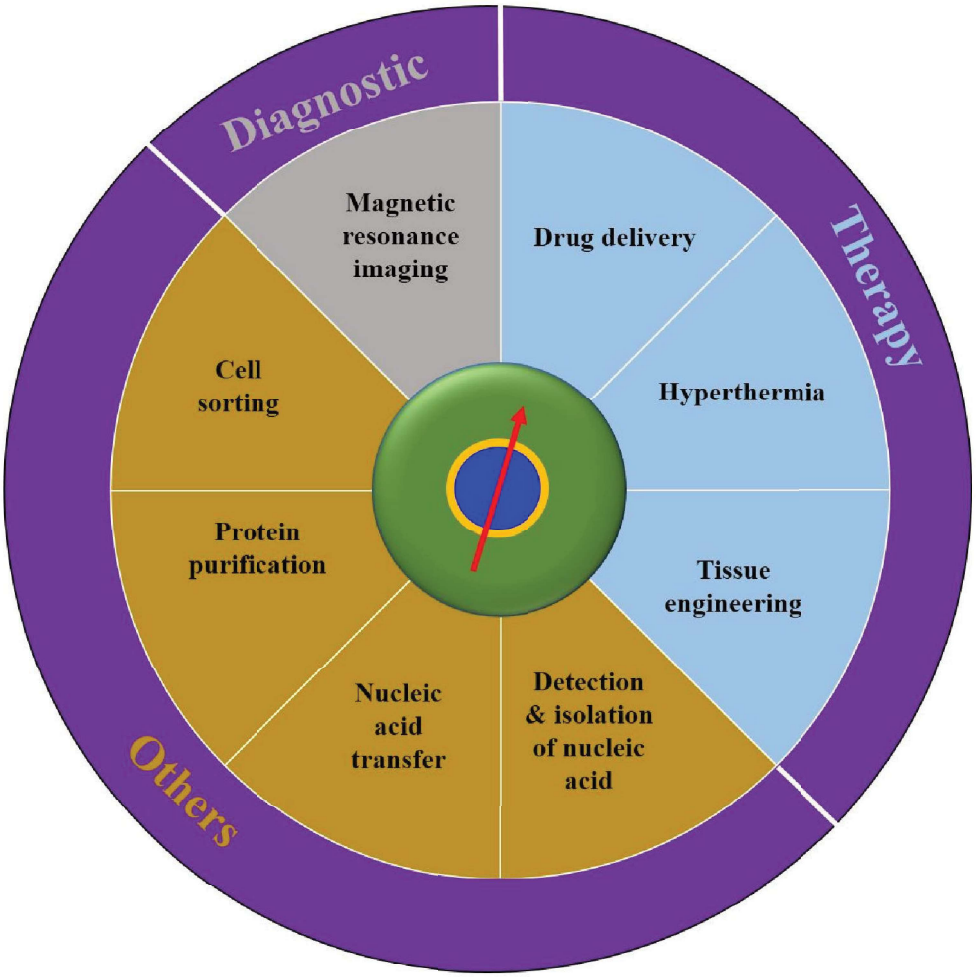


Figure 1.5: Bio-medical applications of magnetic nanoparticles (MNP).

Similarly, MNP are widely used in cell sorting, to isolate specific cell type or to deplete undesired cell types. It is also used for the detection of pathogens, beyond the detection limits of traditional analytical methods [93-95]. The application of MNP in nucleic acid transfer involves the use of magnetic force on nucleic acid attached with MNP for target specific uptake in cells [96, 97]. Further, magnetically enhanced gene therapy involves coupling of superparamagnetic nanoparticles to lipofectamine or liposomes for a multi-fold enhancement in gene expression [60, 98]. The use of MNP in targeted drug delivery involves a distally controlled magnetic field directed accumulation of MNP, associated with the drug of interest,

and subsequent release of drug at the targeted site [99-102]. Tissue engineering is yet another emerging field of application of MNP, where, magnetically labelled cells are organized using a magnetic force [103]. MNP as contrast agents facilitates the imaging of targeted cells, atherosclerotic plague, cell inflammation, tumor vascular imaging, etc. [104, 105]. Further, MNP are also used in magnetically fluid hyperthermia [51, 52] which is discussed in detail in this thesis.

1.4 Magnetic fluids

Though ferromagnetism in a homogeneous liquid is theoretically possible, there exist no material with Curie temperature beyond their melting point [106]. Magnetic fluids, on the other hand, are dispersion of magnetic particles in a medium like water or oil. Depending on the size of the dispersed phase, magnetic fluids can be grouped into two major categories, viz., magneto-rheological fluids with micron sized magnetic particles dispersed in the base fluid and ferrofluids with superparamagnetic nanoparticles (typical size ~ 3-15 nm) dispersed in water or oil medium [106]. Magneto-rheological (MR) fluids were first developed by Jacob Rabinow in 1948 [107]. Viscosity of such fluids increase under the influence of an external magnetic field and they exhibit very fast reversible transitions from liquid to solid-like phase on application of an external magnetic field, leading to several technologically important applications such as magneto-rheological dampers, seismic dampers, torque transduces, body armours for military applications, shock absorbers, clutches, brakes, magneto-rheological polishing of optical elements, etc. [108, 109]. Due to the larger size of the suspended magnetic particles, Brownian motion is not sufficient to prevent agglomeration or settling in magneto-rheological fluids [110-112]. Ferrofluid was discovered by Stephen Papell in 1963, at National Aeronautics and Space Administration (NASA), for external magnetic field guided liquid rocket fuel under weightless environments for space applications

[113]. Basic physical properties and various applications of ferrofluids are discussed in the following sections.

1.4.1 Ferrofluids

Ferrofluids are suspensions of superparamagnetic nanoparticles in a continuous medium of base fluid. Such ferrofluids are composed of single domain MNP with a molecular layer of dispersant coating and suspended in a suitable liquid medium, where, thermal agitation induced Brownian motion keeps the particles suspended and presence of coating prevents agglomeration [106]. To have a stable ferrofluid, certain stability requirements must be satisfied, such as i) stability against a magnetic field gradient (ratio of thermal energy to magnetic energy must be significantly higher than 1, i.e., $k_BT/\mu_0MH_{DC}V_p$ >1); ii) stability against gravitational field; iii) stability against magnetic agglomeration (ratio of thermal energy to dipole-dipole interaction energy must be higher than 1, i.e., $12k_BT/\mu_0M^2V_p$ >1) and iv) stability against attractive van der Waals force due to large surface area to volume ratio of the MNP by coating with suitable surfactants to provide electrostatic or steric repulsion [106]. The most commonly used MNP in ferrofluids are Fe_3O_4, γ-Fe_2O_3, $CoFe_2O_4$ and other types of spinel ferrites. **Fig. 1.6a** shows the schematic representation of a ferrofluid.

Due to their magnetic response, ferrofluids can be manipulated using an external magnetic field, leading to tunable physical properties like thermal [66, 68], rheological [71, 72] and optical [114, 115]. Such tunable properties of ferrofluids have been exploited in a huge number of practical applications, some of which are biosensors [77, 116, 117], cell separation [118], ultrasound contrast agent [119], magnetic resonance imaging [120], quantification of agglutination of biomolecules [121], detection of single nucleotide polymorphism [122], magnetic fluid hyperthermia [51, 123-126], diagnostic applications [127], drug delivery [128], magnetic field activated gels [129], optical filters [115, 130], optical gratings [131],

defect sensors [74, 75], leak free seals [132], lubricants [133], clutches [134], tunable dampers [135], rheological applications [70-73], density separation [136], ink jet printer [137], refrigeration [106, 138] and tunable heat transfer applications [64-66, 68, 69]. The technological applications of ferrofluids span over bio-medical field to aerospace and defence industries [137].

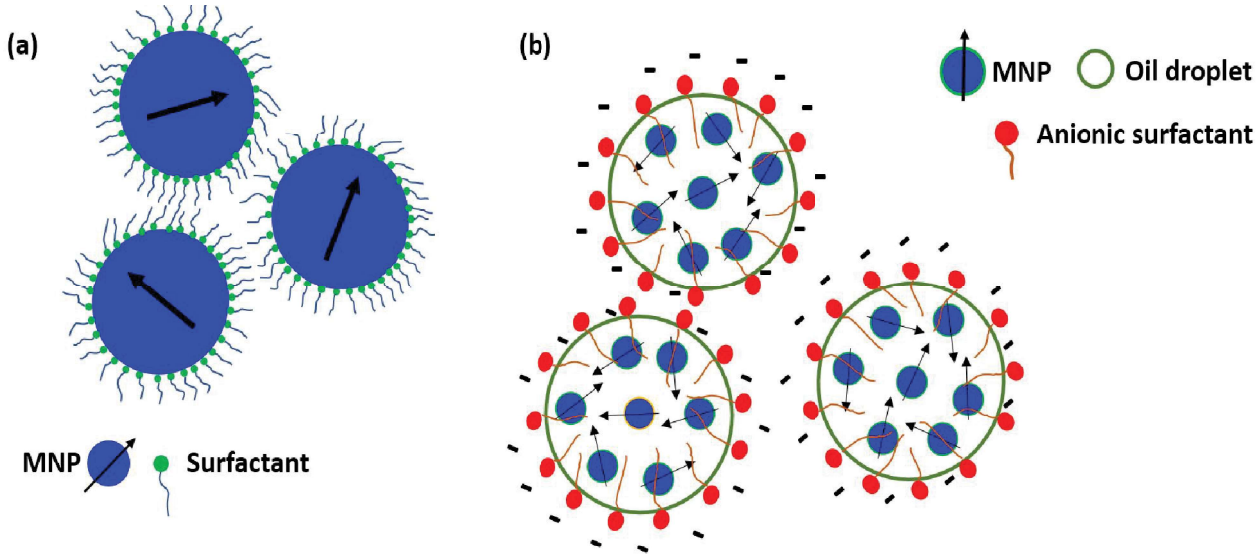


Figure 1.6: Schematics of typical (a) ferrofluids and (b) ferroemulsions. Here, MNP indicates magnetic nanoparticle. The MNP are coated with a surfactant for steric stabilization in an oil medium, whereas, the emulsion droplets are coated with an anionic surfactant for electrostatic stabilization in aqueous medium.

1.4.2 Ferroemulsions

Emulsions are a mixture of two or more immiscible liquids. Emulsions with droplet size in the range of 20-200 nm are known as nanoemulsions [139]. Instability of nanoemulsions are mediated through aggregation induced growth of droplet size, Ostwald ripening and coalescence of droplets [140]. The total interaction energy between the nanoemulsion

droplets is a sum of van der Waals, electrostatic, hydrophobic and steric interactions. The total interaction energy must be minimal for a stable nanoemulsion [141]. The Ostwald ripening is reduced by manipulating the internal osmotic pressure of the trapped phase to counter the Laplace pressure [142]. The coalescence, on the other hand, can be avoided by using a more hydrophilic surfactant to form a thicker hydration layer around the interface or by using electrostatic stabilization [140]. Thermodynamic, pH-dependent and rheological stabilities are also essential for the formulation of stable nanoemulsions [140]. Depending on the nature of dispersed phases and base fluids, nanoemulsions can be of two types: oil-in-water (O/W) [143-145] or water-in-oil (W/O) [146, 147]. Major applications of nanoemulsions involve nano-reactors for polymerization [148, 149], cosmetic formulations [139], DNA vaccine carriers through pulmonary route [150], delivery of DNA plasmid through skin [151], parenteral [152, 153], oral [154], intranasal [155] and topical [156, 157] drug delivery.

Magnetically polarizable oil-in-water nanoemulsions or ferroemulsions are a special kind of nanoemulsions with single domain superparamagnetic nanoparticles loaded in the oil phase. **Fig. 1.6b** shows the schematic representation of a ferroemulsion. They exhibit tunable optical and physical properties in response to an external magnetic field, which has been exploited for various applications, viz., optical filters [158-161], chemical sensor [76, 162], glucose sensor [77] and nano-scale mechanical probes as actuators in complex fluids and biological systems [163]. Ferroemulsions have also found widespread applications in the bio-medical field for drug delivery [164, 165], magnetic resonance imaging [166, 167] and multimodal hyperthermia [168-173].

In general, the term magnetic nanofluids indicates ferrofluids and ferroemulsions and **Fig. 1.7** summarizes the most important applications of magnetic nanofluids.

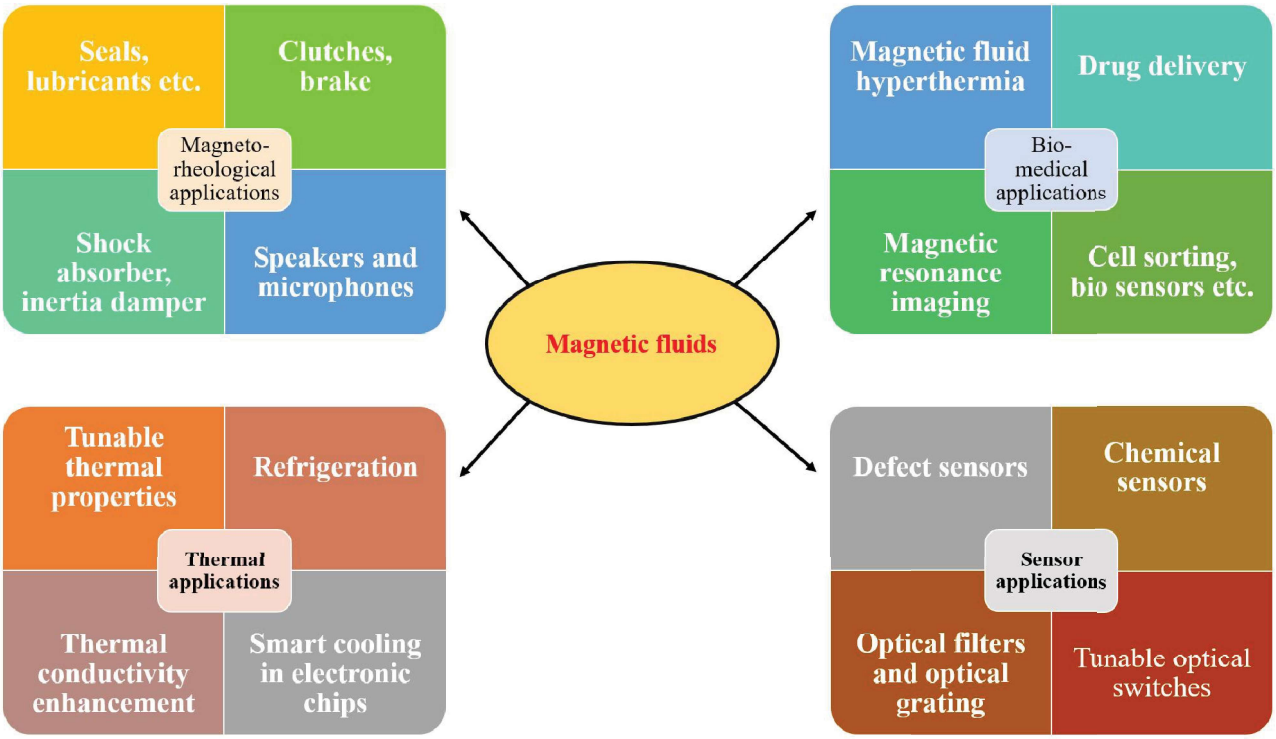


Figure 1.7: Schematic illustration of some important applications of magnetic fluids (ferrofluids and ferroemulsions).

1.5 Hyperthermia using nanoparticles

Cancer is one of the most potent cause of mortality worldwide. Several conventional (like surgery, chemotherapy and radiotherapy) and modern (like immunotherapy, gene therapy, hormone therapy) approaches have been attempted to fight cancer [174]. Hyperthermia is a relatively new and alternate cancer therapy, where, the cancerous tissues are exposed to a higher temperature leading to cellular degradation and therapy. Nanoparticles have found widespread application in hyperthermia, where, the nanoparticles absorb energy from the external source and enhance the effects of hyperthermia at cell locations. Based on the type of energy sources, nanoparticle mediated hyperthermia can be divided into four major types, viz., i) nano-photo thermal therapy (NPTT) using nano-photo-sensitizer and a laser source; ii)

nano-radio frequency ablation (NRFA) using radio frequency (RF) waves and RF absorbing nanoparticles; iii) nano-ultrasound hyperthermia (NUH) using high intensity focussed ultrasound (HIFU) and suitable nanoparticles and iv) magnetic fluid hyperthermia (MFH), where, radio frequency alternating magnetic field (RF-AMF) induced heating of MNP is used for cancer therapy [174]. Detailed description of the fundamental principles and applications for each type of hyperthermia can be found elsewhere [174]. **Fig. 1.8** schematically shows various types of nano-materials used for different kinds of hyperthermia [174]. **Table 1.4** shows a few *in vitro* and *in vivo* studies involving nano-photo thermal therapy (NPTT), nano-radio frequency ablation (NRFA) and nano-ultrasound hyperthermia (NUH) [174].

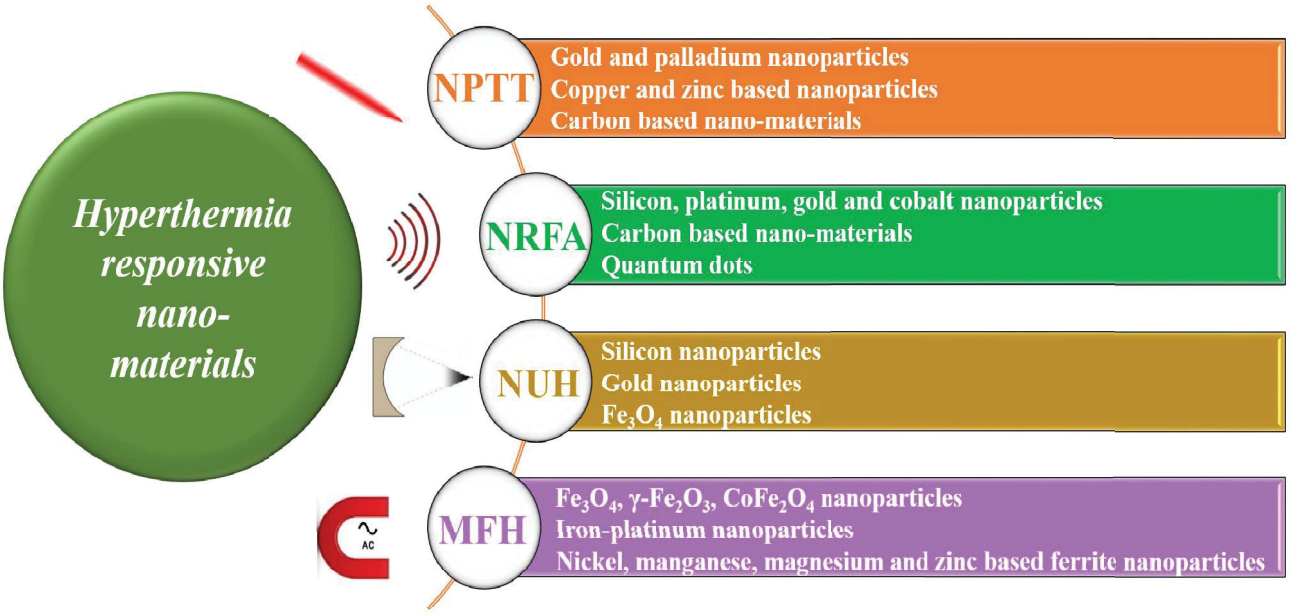


Figure 1.8: Schematic illustration of various nano-materials used in different types of hyperthermia. Here, NPTT, NFRA, NUH and MFH indicate nano-photo thermal therapy, nano-radio frequency ablation, nano-ultrasound hyperthermia and magnetic fluid hyperthermia, respectively.

Table 1.4: A few typical *in vitro* and *in vivo* applications of NPTT, NFRA and NUH. Here, PEDOT-PSS-PEG = poly-(3,4-ethylenedioxythiophene)–poly (4-styrenesulphonate) - polyethylene glycol, NGS-PEG-Cy7 = nano graphene sheet with polyethylene glycol coating labelled with Cy7, β-CD-capped HMSN = β cyclodextrin capped hydrophobic mesoporous silica nanoparticles.

Type of hyperthermia	**Class**	**Nanoparticle (size)**	**Concentration/ Dose**	**Exposure conditions**	**Cell death (*in vitro*) Tumor growth inhibition (*in vivo*)**	**Reference**
NPTT	*in vitro*	Peptide graphene oxide (20 nm)	6.6 μg/mL	808 nm, 15.3 W/cm^2, 480 s	> 90 %	Robinson et al. [175]
		Copper sulphide (3 nm)	36.5 μg/mL	808 nm, 40 W/cm^2, 300 s	79 %	Li et al. [176]
	in vivo (Breast)	PEDOT-PSS-PEG (80 nm)	10 mg/kg (intravenous)	808 nm, 0.5 W/cm^2, 300 s	100 %	Cheng et al. [177]
		NGS-PEG-Cy7 (30 nm)	20 mg/kg (intravenous)	808 nm, 2 W/cm^2, 5 s	100 %	Yang et al. [178]
NRFA	*in vitro*	Au-Cetuximab (20 nm)	0.020 μg/mL	13.56 MHz, 200 W, 300 s	~ 55 %	Glazer et al. [179]
		Au (10 nm)	0.591 μg/mL	13.56 MHz, 100 W, 60 s	~ 75 %	Kruse et al. [180]
	in vivo (pancreas)	Au-Cetuximab (10 nm)	10 mg/kg (intraperitoneal)	13.56 MHz, 600 W, 600 s	> 85 %	Glazer et al. [181]
	in vivo (lung)	Porous Si (50 nm)	~ 15 mg/kg (intratumoral)	27 MHz, 56 W, 120 s	25 %	Tamarov et al. [182]
NUH	*in vitro*	Si-dextran (80 nm)	250 μg/mL	0.88 MHz, 0.25 W/cm^2, 600 s	80 %	Osminkina et al. [183]
		AgCu-phenanthroline (23 nm)	0.9 μg/mL	1 MHz, 1 W/cm^2, 600 s	~ 80 %	Bernard et al. [184]
	in vivo (Melanoma)	Si-dextran (80 nm)	10 mg/kg (intravenous)	2.64 MHz, 2 W/cm^2, 360 s	~ 60 %	Osminkina et al. [183]
	in vivo (Breast)	β-CD-capped HMSN (220 nm)	~ 0.02 mg/kg (intratumoral)	1 MHz, 0.8 W/cm^2, 5 s	55 %	Zhao et al. [185]

Among various types of hyperthermia, magnetic fluid hyperthermia (MFH) is one of the most promising approaches due to its non-invasiveness and treatment capability for deep tumors.

The use of MNP also opens up several interesting opportunities in simultaneous use of MFH along with external magnetic field guided drug delivery and theranostic applications using bio-compatible MNP. **Table 1.5** shows a comparison between various kinds of hyperthermia [174]. The subsequent sections discuss the fundamental principles behind MFH and its various applications in detail.

Table 1.5: Comparison between different kinds of hyperthermia with respect to excitation source, excitation range, heat generation principle, target locations, advantages and drawbacks.

Category	NPTT	NRFA	NUH	MFH
Excitation source	Laser	RF waves	High intensity focussed ultrasound (HIFU) waves	Radio frequency alternating magnetic field
Excitation range	380-780 nm & 700-1100 nm	13.56 MHz (< 300 MHz)	~ 0.5-5 MHz	~ 100-400 kHz
Heat generation principle	Plasmonic resonance	Ohmic losses	Thermo-mechanical effects of HIFU	Neel-Brown relaxation and hysteresis losses
Target location	Head and neck cancers	Pelvis, abdomen, liver, lung tumors	Deep tumors	Deep tumors, brain, prostate, liver, cervix and esophagus tumors
Advantages	High safety and controlled heating	High penetration, non-invasive	High penetration with focussing. No fat over heating	High safety. No surface heating. Repeatable therapy with a single dose
Drawbacks	Low penetration, invasive fiber required for deep targets	Non-uniform heating, over-heating of fat tissues	Limited by air or bone interfaces, lack of experimental data.	Non-uniform heating, MNP concentration effects and optimization of MNP is an issue

1.6 Magnetic fluid hyperthermia (MFH)

Magnetic fluid hyperthermia (MFH) is a therapeutic procedure, where a magnetic fluid is injected into tissues containing cancerous cells and, thereafter, exposed to a RF-AMF,

resulting in a rise in fluid/tissue temperature due to various inherent loss mechanisms like Neel-Brownian relaxation and hysteresis [51]. The **inset of Fig. 1.9** shows a typical scheme of MFH based cancer treatment. It has been reported that a rise in tissue temperature beyond 42 ^{0}C (known as hyperthermia limit) causes cellular degradation and apoptosis of cancerous cells, thereby, aiding in cancer treatment [52, 186]. The various mechanisms of hyperthermia induced cell death involving thermally induced protein unfolding, thermal disruptions of cell physiology, intra-cellular thermal mechanisms in the temperature range of 40-46 ^{0}C and impairment of DNA repair pathways leading to preferential degradation of cancer cells have been studied in the past [187, 188]. Studies also indicate that an exposure beyond 46 ^{0}C makes the cancerous cells mores susceptible towards conventional treatment modalities like radiotherapy or chemotherapy [87, 88, 187]. MFH, as a therapeutic procedure, was first proposed by Gilchrist et al. [189], in 1957, for selective inductive heating of lymph nodes. *In vivo* studies show good efficacy of MFH in curing various types of cancer modes like melanoma, breast tumors and prostate cancer [190-194]. Recently, MagForce Nanotechnologies AG, Germany has obtained the approval of European Association for MFH therapy in human using superparamagnetic iron oxide nanoparticles [195, 196].

Owing to its immense clinical benefits, MFH is being actively pursued as an alternate cancer treatment modality, where, the research is primarily focussed on the effects of MNP size, saturation magnetization, anisotropy, shape, medium viscosity and sample concentration [89, 197-203]. **Fig. 1.9** shows a bibliographic database, where, it can be seen that the interest in MFH has steadily increased in recent years. Non-invasiveness, selective and tissue specific localized heating with reduced collateral damages to the healthy cells and possible theranostic (therapy + diagnosis using MRI) applications are the major advantages of MFH [204, 205]. **Tables 1.6, 1.7 and 1.8** show a few clinical trials, *in vivo* and *in vitro* studies using MFH, respectively [174].

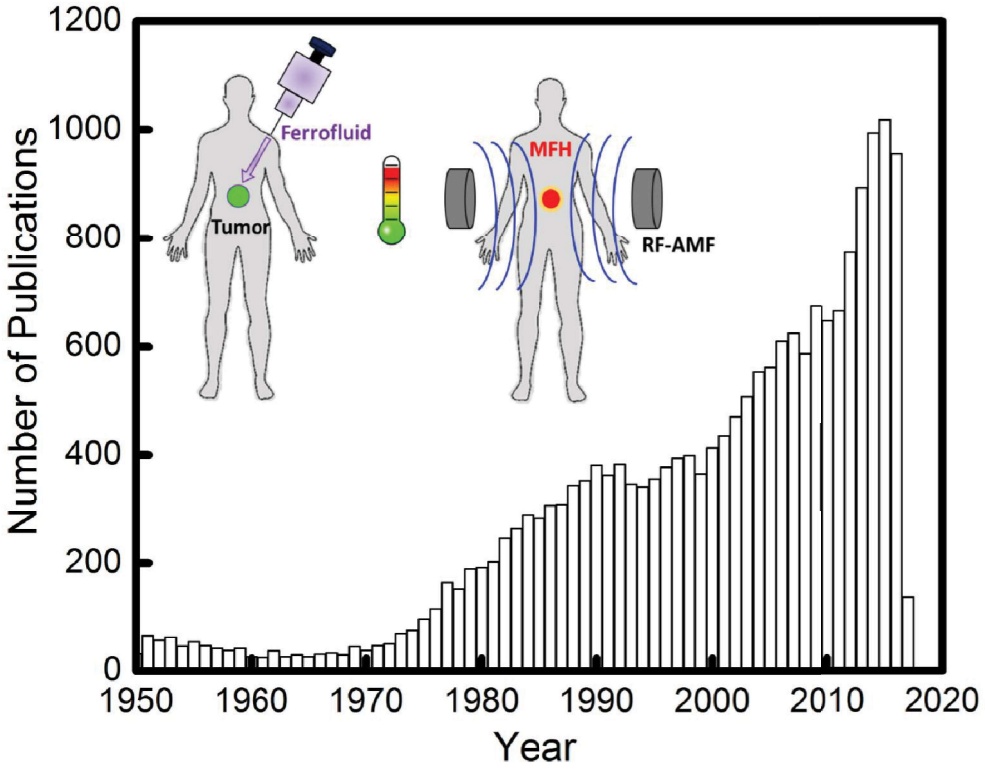


Figure 1.9: Number of publications in MFH, as a function of year of publication. The data is tabulated on March 1st, 2017 using SciFinder (https://www.cas.org/products/scifinder). (Inset) A typical scheme for MFH based cancer therapy (RF-AMF indicates radio frequency alternating magnetic field).

Table 1.6: Details of a few clinical trials carried out using MFH. Here, PC = prostate cancer, GM = glioblastoma multiforme, CT = concomitant treatment, BT = brachytherapy, RT = radiotherapy, Median T90 = temperature exceeded for 90 % of tumor volume, Median CEM 43 = cumulative equivalent minutes at 43 ^{0}C.

Type of cancer	Trial phase	MNP size (in nm)	Exposure conditions	Treatment type (CT)	Median T90 (^{0}C)	Median CEM 43 (min.)	Survival for CT (months)	Survival for MFH + CT (months)	Reference
GM	I	15	100 kHz, 8.5 kAm^{-1}, 3600 s	RT	40.5	7.7	2.7-11.5	14.5	Maier-Hauff et al. [206] & [174]
GM	II	12	100 kHz, 15 kAm^{-1}, 3600 s	RT	-	-	6.2	13.4	Maier-Hauff et al. [196] & [174]
PC	I	15	100 kHz, 18 kAm^{-1}, 3600 s	-	40.1	7.8	-	-	Johannsen et al. [207] & [174]
PC	I	<20	100 kHz, 15 kAm^{-1}, 3600 s	BT	39.9	5.8	-	-	Johannsen et al. [194] & [174]

Table 1.7: Details of a few MFH based *in vivo* studies. Here, DMSA = dimercaptosuccinic acid, DOX = doxorubicin, N6L = nucant multivalent pseudopeptide, Chito-FION = chitosan oligosaccharide stabilized ferrimagnetic iron oxide nanocubes.

Tumor type	MNP (size in nm)	Dose (mg/kg)	Exposure conditions	Tumor inhibition index (%)	Reference
Breast	Fe_3O_4-DMSA (12)	8 (intratumoral)	435 kHz, 15.4 kAm^{-1}, 3600 s	> 80	Kossatz et al. [208] & [174]
Breast	Fe_3O_4-DMSA-DOX –N6L (12)	8 (intratumoral)	435 kHz, 15.4 kAm^{-1}, 3600 s	~ 85	Kossatz et al. [209] & [174]
Breast	-	-(intratumoral)	400 kHz, 6.5 kAm^{-1}, 240 s	-	Hilger et al. [192]
Lung	Chito-FION (103)	0.4 (intratumoral)	1000 kHz, 0.208 kAm^{-1}, 1200 s	~ 70	Bae et al. [210] & [174]
Melanoma	Fe_3O_4-Porphyrin (12)	5 (intratumoral)	366 kHz, 5 kAm^{-1}, 600 s	> 75	Balivada et al. [211] & [174]
Melanoma	Fe_3O_4 (10)	10 (intratumoral)	118 kHz, -, 1800 s	~ 75	Ito et al. [190]
Melanoma	Fe-Fe_3O_4-Porphyrin (25)	- (intratumoral)	366 kHz, 5 kAm^{-1}, 600 s	~ 40	Rachakatla et al. [212] & [174]
Lymph nodes	Fe_2O_3 (20-100)	-	-	-	Gilchrist et al. [189]
Prostate	Fe_3O_4 (15)	1.8 (intratumoral)	100 kHz, 12.6 kAm^{-1}, 1800 s	~ 50	Johannsen et al. [213] & [174]
Pyriform sinus carcinoma	Fe_3O_4 (20)	- (intratumoral)	-, -, 2700 s	5 time higher apoptosis	Wang et al. [214] & [174]
Glioma	Fe_3O_4-Aminosilane (15)	20 (intratumoral)	100 kHz, 18 kAm^{-1}, 1800 s	4.5 times increase in survival	Jordan et al. [215] & [174]

Superparamagnetic Fe_3O_4 and γ-Fe_2O_3 are the most widely used MNP for hyperthermia applications because of their superior bio-compatibility (metabolization through heme oxygenase-1 [60]), high saturation magnetization, ease of synthesis and long term stability [216-218]. Apart from iron ferrite systems, several other spinel ferrites, like cobalt, manganese, nickel, zinc ferrites, either in uncoated form or coated with suitable organic (temperature responsive polymer [219] in some instances) or inorganic moieties like gold, silver, silica, polyethylene glycol, dextran, chitosan, etc. have been used for MFH [126]. Fe-Pt [220, 221], Lanthanum manganese perovskite [222], lanthanum-strontium manganite [223]

and strontium doped lanthanum manganite [224, 225] have also been used for MFH studies. To limit the heating beyond the desired limits, self-controlled MFH with large magnetization and Curie temperature around 40-45 ^{0}C has been studied theoretically [226, 227] and experimentally using zinc doped manganese ferrite, gadolinium (Gd) based materials and Fe-Co-Cr nanocomposites [228-230]. Inhalable superparamagnetic iron oxide [epidermal growth factor receptor (EGFR) targeted) for MFH therapy of lung cancer has also been demonstrated [231].

Table 1.8: Details of a few *in vitro* studies using MFH. Here, CEIO = carbon encapsulated iron oxide MNP, PEG = polyethylene glycol, FA = folic acid, DOX = doxorubicin, Her2 = anti-human epidermal growth factor receptor, CREKA = tumor homing peptide (Cys-Arg-Glu-Lys-Ala), m = mesoporous, dm = dual porus, 5-FU = 5-fluorouracil.

Medium cells	**MNP (size in nm)**	**MNP concentration (mg/mL)**	**Exposure conditions**	**Cell death (%)**	**Reference**
Lung cancer	Fe_3O_4-dextran-CREKA-Cisplatin (52)	3	292 kHz, 58 kAm^{-1}, 1800 s	> 75	Kruse et al. [232] & [174]
Glioblastoma	Fe_3O_4 (20-30)	7.93	297 kHz, 25 kAm^{-1}, 300 s	> 90	Meenach et al. [233] & [174]
Glioma	Fe_3O_4 - cationic liposome (35)	7.2	118 kHz, 30.6 kAm^{-1}, 3600 s	100	Shinkai et al. [234] & [174]
Adenocarcinoma	γ-Fe_2O_3-dextran-Her2 (10)	0.011	280 kHz, -, 3600 s	60	Pala et al. [235] & [174]
Gastric carcinoma	M-Fe3O4/dm-SiO_2/5-FU	0.1	55 kHz, 4.5 kAm^{-1}, 800 s	~ 90	Lu et al. [236]
Hepatocellular carcinoma	Fe_3O_4-alginate-galactosamine (128)	0.5	780 kHz, 19 kAm^{-1}, 1200 s	95	Liao et al. [237] & [174]
Hepatocellular carcinoma	γ-Fe_2O_3 (10-20)	8	200 kHz, -, 3600 s	~ 82	Yan et al. [238] & [174]
Cervical cancer	Bi-magnetic core-shell	0.2	1950 kHz, -, 100 s	-	Hammad et al. [239]
Cervical cancer	CEIO-PEG-FA (74)	0.5	750 kHz, 0.8 kAm^{-1}, 600 s	> 75	Sadhasivam et al. [240] & [174]
Cervical cancer	DOX-magnetic nanocomposite (65)	2	250 kHz, 36.6 kAm^{-1}, 1500 s	> 80	Sahu et al. [241] & [174]

During RF-AMF induced heating, the heating efficiency of magnetic fluid is expressed in terms of a dosimetric quantity known as specific absorption rate (SAR), which is defined as the power absorption per unit mass of magnetic sample (W/g). Some of the very high values of SAR, reported in literature, include 2452 W/g (H = 29 kAm^{-1} and f = 52 kHz) for iron oxide nanocubes [201]; 1661 W/g (H = 23.9 kAm^{-1} and f = 717 kHz) for manganese ferrite MNP [242]; 1650 W/g (H = 24.8 kAm^{-1} and f = 700 kHz) for maghemite MNP [243]; 960 W/g (H = 10 kAm^{-1} and f = 410 kHz) for bacterial magnetosomes [89, 244] and 720 W/g (H = 10 kAm^{-1} and f = 410 kHz) for metallic cobalt MNP [245]. A few MFH studies using different kinds of MNP along with the exposure conditions and the obtained SAR values are shown in **Table 1.9**.

Table 1.9: A few MFH studies using different kinds of MNP. Sizes of the MNP, obtained SAR values, exposure conditions and the corresponding references are listed.

MNP	Size (nm)	SAR (W/g)	Exposure conditions (kHz, kAm^{-1})	Reference
Resovist (commercial: from Bayer Schering Pharma AG, Germany)	10.5	89.4	900 kHz, 5.66 kAm^{-1}	Kallumadil et al. [246]
Sugar coated iron oxide MNP	35	76	168 kHz, 21 kAm^{-1}	Lartigue et al. [247]
Iron oxide-gold nanocomposite	8-56	88.3	967 kHz, 6.6 kAm^{-1}	Bell et al. [248]
Neodymium (Nd) doped lanthanum strontium manganite	30-38	43	300 kHz, 9.5 kAm^{-1}	Shlapa et al. [223]
Fe_3O_4 magnetic nanoclusters	52	215	126 kHz, 63.0 kAm^{-1}	Sathya et al. [249]
$MgFe_2O_4/ZrO_2$	39	4.5	214 kHz, 0.796 kAm^{-1}	Rashid et al. [250]
$Ni_{0.43}Fe_{2.57}O_4$	11	204	872 kHz, 20 kAm^{-1}	Lasheras et al. [61]
$CoFe_2O_4$	10	91.84	265 kHz, 30.1 kAm^{-1}	Salunkhe et al. [251]
Fe_3O_4 nano-platelets	30-50	300	114 kHz, 50.9 kAm^{-1}	Kishimoto et al. [252]
ZnFe2O4	5	89	300 kHz, 7.7 kAm^{-1}	Yelenich et al. [253]
Manganese ferrite	10.5-19.0	148.4	1950 kHz, 4.5 kAm^{-1}	Doaga et al. [254]
Co doped magnetosomes	-	500	183 kHz, 15.9 kAm^{-1}	Alphandery et al. [255]

1.6.1 Multimodal approaches involving MFH

Kumar and Mohammed [217] broadened the definition of MFH to include magnetically modulated drug delivery, which opened up several interesting opportunities to use comparatively larger sized (~ 200 nm) nano-systems like, magnetic nano-composites [256, 257] and magnetic nanoemulsions [258]. Such approaches are designed to make these system multifunctional, e.g., specific anticancer drugs (like doxorubicin, paclitaxel or daunorubicin) attached to these materials for magnetically controlled drug delivery along with MFH [128] or use of photoactive chloroaluminum phthalocyanine (ClAlPc) agents with the MNP to combine photodynamic therapy and MFH [168-170].

Though superparamagnetic (SPM) nanoparticles are used in most of the MFH studies, larger size nanoparticles are favourable for many applications, especially for multimodal applications [259, 260]. Studies show that nano-carriers loaded with anticancer drugs in the size range ~ 100-200 nm, are beneficial for enhanced permeation and retention (EPR) in the local environment (consisting of leaky vasculature) of cancerous cells and to avoid uptake by macrophages, filtration at spleen or liver and human complement system which enhances the immunity against damaged cells and foreign inclusions [256, 261, 262]. Win and Feng [263] reported higher cellular uptake of larger sized nanoparticles, which was found to be beneficial for increasing the drug delivery ratio to the affected cells. A higher SAR for ~ 200 nm sized, encapsulated ultra-magnetic liposome particles has been reported by Bealle et al. [264]. Studies revealed that for doxorubicin loaded (loading efficiency ~ 80 %), polyethylene glycol coated and carboxyl enriched mesoporous $MgFe_2O_4$ samples, MFH in combination with drug therapy, results in ~ 90 % cell deaths *in vitro*, as compared to MFH only [265]. Iron oxide modified oil-in-water magnetic nanoemulsion, with the magnetic particles distributed in the water phase and the oil phase containing photodynamic agents like chloroaluminum phthalocyanine were used by Paula et al. [168, 169] for simultaneous photodynamic therapy

combined with MFH and an increase (~ 70 %) in cell death during multimodal MFH was reported. MNP loaded hybrid PNIPAM-chitosan microgels (size ~ 200-500 nm) [266] and multilayered MNPs, like MNP clusters covered with silica shell coated with bio-compatible bovine serum albumin (size ~ 147 ± 20 nm) are also found to be potential candidates for multi-modal MFH agents [267]. Hu et al. [164] reported the use of bio-compatible core-shell, water-in-oil-in-water double emulsion, containing iron oxide MNP and poly (vinyl alcohol) as surfactant, as a dual-drug carrier with controlled drug release. The above studies show that comparatively larger sized nano-carriers are suitable for achieving synergistic multimodal therapy. Recent studies indicate that a high macroscopic temperature rise is not a prerequisite for MFH induced drug delivery, thereby, opening up the possibilities of using nano-carriers with even lower concentration of magnetic loading as multi-modal MFH agents [268]. Over the years, MFH has evolved as a tool for cancer therapy, where, the modern-day applications are not limited to RF-AMF induced heating only but also precise magneto-thermal control of cellular activities and drug delivery coupled with localized heating at nano-scale and molecular level along with selective enhanced depth of penetration and non-invasive controllability [269]. **Fig. 1.10** schematically summarizes the various parameters influencing RF-AMF induced heating of MNP and its major applications, viz., magnetic fluid hyperthermia and magneto-thermally triggered drug delivery [269]. The theoretical framework behind the RF-AMF induced heating in MNP is discussed in the subsequent sections.

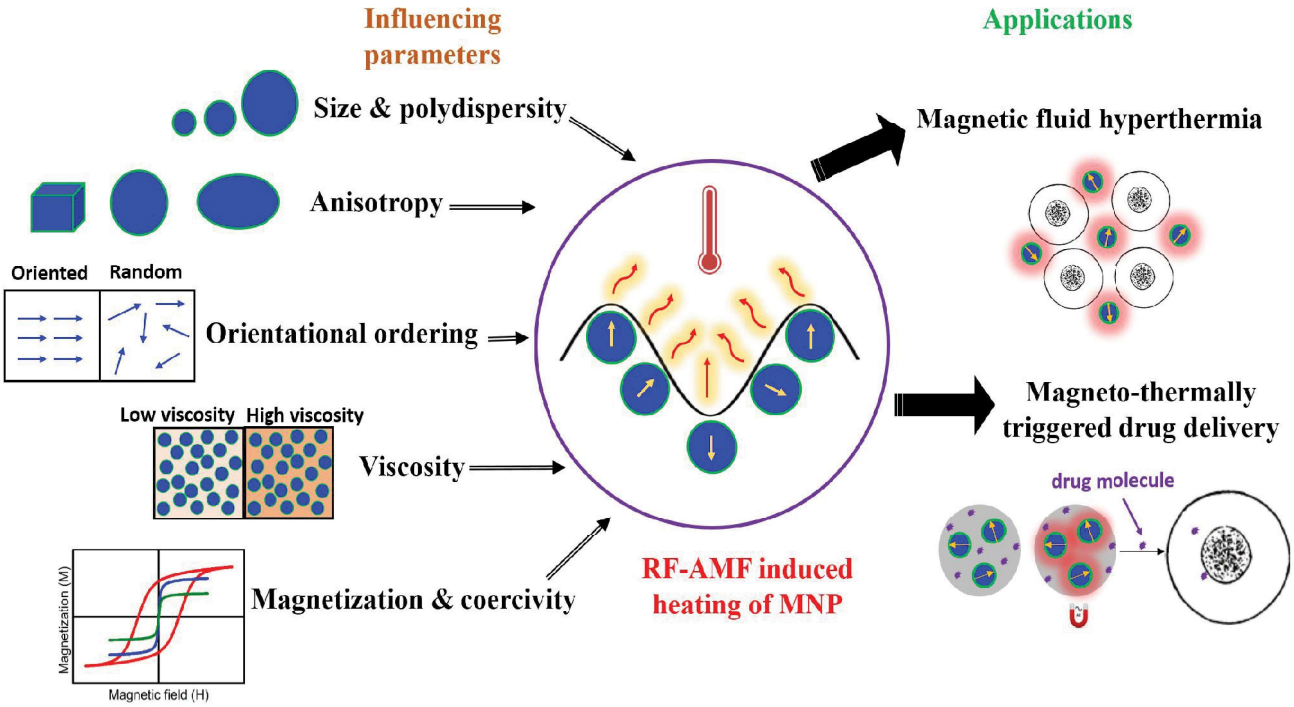


Figure 1.10: During RF-AMF induced heating, MNP act as efficient converters of magnetic energy to heat energy. Various factors (like size & polydispersity, anisotropy, orientational ordering, medium viscosity, saturation magnetization and coercivity) influencing RF-AMF induced heating efficiency in magnetic nanoparticles are schematically shown. Two major applications of RF-AMF induced heating of MNP, viz., magnetic fluid hyperthermia and magneto-thermally triggered drug delivery are also illustrated.

1.7 Mechanisms of radio frequency alternating magnetic field (RF-AMF) induced heating in magnetic materials

During radio frequency alternating magnetic field (RF-AMF) induced hyperthermia, heat transfer occurs in three different length scales, viz., i) 10-100 nm (governed by the size of the nano-carriers), ii) 1-20 μm (owing to the cell size) and iii) macro scale (influenced by the tissue dimensions, typical size ~ 20 mm) [270]. RF-AMF induced heating mechanism, on the other hand, depends on the magnetic materials used and can be classified into three major classes, viz., i) eddy current losses for macro-sized magnetic materials, ii) hysteresis losses (for multi-domain MNP) and iii) relaxation losses (for single domain MNP) [194]. A fourth

kind of heating mechanism, due to 'viscous stirring' of MNP with sizes beyond certain critical dimension has been proposed by Vallejo-Fernandez et al. [271].

1.7.1 Eddy current heating

When a conducting sample is subjected to a RF-AMF, the time dependent magnetic flux induces the flow of an eddy current in the sample in such a way that the induced magnetic field opposes the original magnetic field (in accordance with Faraday-Lenz's laws of electromagnetism). The resultant field attenuation depends on the frequency of the applied magnetic field, electrical conductivity and magnetic permeability of the material. The flow of eddy current results in temperature rise of the conducting sample due to Ohmic losses. The rate of heat production per unit volume, due to eddy current heating (P_{eddy}), is expressed by the following equation [272, 273].

$$P_{eddy} = G\pi^2\mu^2\sigma_E H^2 f^2 r^2 \tag{1.5}$$

Here, σ_E, μ, H, f, r and G indicate electrical conductivity of the material, magnetic permeability, amplitude and frequency of RF-AMF, radius of the exposed sample and a geometrical factor, respectively. Eddy current losses also occur in tissues, albeit resulting in lower temperature rise, as compared to metallic samples, due to low electrical conductivity of tissues [typical value ~ 0.6 $(\Omega m)^{-1}$] [274]. It has been reported that for frequencies up to 10 MHz, there is no significant attenuation of the magnetic field in a cylindrical muscle-equivalent structure with radius lower than or equal to that of a typical human torso [275].

Induced eddy current heating pose a safety hazard for practical *in vivo* applications of MFH in cancer therapy due to the unwanted heating of healthy or sub-cutaneous tissues [276]. Atkinson et al. [272] reported that for a coil diameter of 30 cm, test subjects were able to withstand the treatment for more than 1 hour without 'major discomfort' when the product of RF-AMF amplitude and frequency (H.f) was kept within 4.85×10^8 $Am^{-1}s^{-1}$, which is

generally known as Brezovich limit. Using a smaller coil diameter of 10 cm (typical tumor size), i.e., smaller radius of the exposed region, Dutz and Hergt [273] augmented the H.f limit to ~ 5 × 10^9 $Am^{-1}s^{-1}$. Due to the quadratic dependence on sample dimension (Eq. 1.5), the power generated per unit volume due to eddy current heating is insignificant for MNP and hence, is not considered for MFH. Considering the values of electrical conductivity of Fe_3O_4 as 3 ×10^{-6} S/m [277], magnetic permeability as 4π×10^{-7} H/m, geometrical factor as 1, amplitude and frequency of the RF-AMF as 63.0 kAm^{-1} and 126 kHz, respectively, the power generated per unit volume due to eddy current heating for hypothetical spheres of diameter 10 nm, 100 μm and 10 mm were found to be ~ 7.36 × 10^{-14} W/m^3, ~ 7.36 × 10^{-6} W/m^3 and ~ 7.36 × 10^{-2} W/m^3, respectively, which shows that the contribution from eddy current heating is insignificant for RF-AMF induced heating of MNP.

1.7.2 Heating by viscous stirring in MNP

Vallejo-Fernandez et al. [271] have proposed that for MNP with sizes beyond a critical value ($d_{c\text{-}V}(H)$), an additional heating mechanism is also mediated through viscous stirring within the dispersion medium, where, the frictional heating depends on the drag coefficient and turbulent flow of liquid in the vicinity of the MNP. The value of the critical diameter, $d_{c\text{-}V}(H)$, is given by the following equations [271].

$$d_{c-V}(H) = d_{MNP}(0)[1-\frac{H\times M_s}{0.96K}]^{-\frac{2}{3}} \tag{1.6}$$

$$d_{MNP}(0) = [\frac{6k_BT\ln(tf_0)}{\pi K}]^{\frac{1}{3}} \tag{1.7}$$

Here, t and f_o indicate measurement time and attempt frequency (= $1/\tau_0$), respectively.

1.7.3 Heating by hysteresis losses

Multi-domain MNP, when subjected to RF-AMF, show a nonlinear variation of magnetization as a function of applied field, which is represented by a hysteresis loop [4]. The power generated per unit volume during hysteresis loss (P_{hys}) is represented by the following equation [4].

$$P_{hys} = \mu_0 A \times f = \mu_0 f \oint M(H) dH \tag{1.8}$$

Here, μ_0, A, f, M and H indicate magnetic permeability of free space, hysteresis loop area, frequency of the applied magnetic field, magnetization and amplitude of the applied magnetic field, respectively.

During hysteresis cycling, two major processes contribute to P_{hys}, viz., displacement of domain walls (pinning and depinning at inhomogeneities) and rotation of magnetic moments within the domains [274]. Hysteresis loss is significant for MNP with sizes larger than the critical diameter ($d_c = (150 k_B T/\pi K)^{1/3}$), which is ~ 20 and 10 nm for Fe_3O_4 and $CoFe_2O_4$ MNP, respectively [52-54].

1.7.4 Neel-Brownian relaxation in superparamagnetic nanoparticles

The energy required for domain formation increases with decreasing particle size and beyond the critical size (d_c), domain formation is no longer energetically favourable. Moreover, with decreasing particle size, probability of spontaneous flipping of magnetization (due to thermal energy) increases and remnant magnetization (M_r) decreases exponentially according to the following equation [278].

$$M_r = M_{r0} \exp(-t/\tau) \tag{1.9}$$

Here, M_{r0} is the remnant magnetization for multi-domain state and τ indicate the effective relaxation time of the MNP. Under such conditions, the RF-AMF induced heating in single domain superparamagnetic MNP is achieved by Neel-Brownian relaxation losses [16, 50].

In the case of Neel relaxation, magnetic moments of the MNP follow the RF-AMF by rotating against the anisotropic energy barrier within the particle itself and the characteristic relaxation time, τ_N, is expressed by the following equation [16, 50, 52].

$$\tau_N = \frac{\tau_0}{2}\sqrt{\frac{\pi}{\sigma_{AT}}}e^{\sigma_{AT}} \tag{1.10}$$

Here, τ_0 is the attempt time (~ 1×10^{-9} s) and is related to the effective uniaxial anisotropy energy density (K), electron gyromagnetic ratio (γ_0), saturation magnetization (M_S) and linear damping factor (F_l) by the expression: $\tau_0 = \frac{M_s}{2\gamma_0 K}\frac{(1+F_l^2)}{F_l}$ [279]. σ_{AT} is the ratio of the magnetic anisotropy energy to thermal energy and is expressed as $\sigma_{AT} = KV_p/k_BT$, where V_p, k_B and T indicate MNP volume, Boltzmann's constant and absolute temperature, respectively.

In the absence of an applied magnetic field, the magnetic moments are randomly oriented along the individual magnetic easy axes of the MNP, determined by the individual particle's magneto-crystalline anisotropy. However, application of an external magnetic field breaks the inherent symmetry of the system by aligning the magnetic moments along the direction of the magnetic field which subsequently relax to the highest entropy state on withdrawal of the external field, thereby, releasing the stored magnetic energy, resulting in an increase in sample temperature.

On the other hand, in Brownian relaxation, heating is achieved by shear action during whole-scale rotation of the MNP within the base fluid, keeping the direction of the magnetic moments fixed with respect to the crystallographic orientations. Brownian relaxation mechanism is a viscosity dependent phenomena and the characteristic time scale (τ_B: Brownian relaxation time) is expressed by the following equation [50, 52].

$$\tau_B = \frac{3\eta V_h}{k_B T} \quad (1.11)$$

Here, η is the viscosity of the base fluid and V_h is the hydrodynamic volume of the dispersed MNP. **Fig. 1.11** schematically shows the Neel and Brownian relaxation mechanisms.

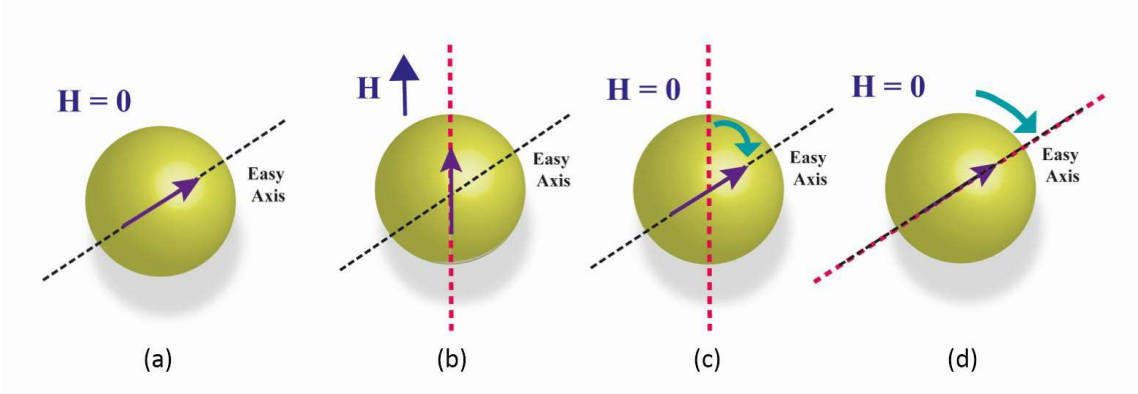


Figure 1.11: Schematic diagram representing the magnetic moment oriented (a) along easy axis (black dotted line) in the absence of an external magnetic field and (b) along the direction of external magnetic field (indicated by an arrow). (c) Neel relaxation of the magnetic moment on withdrawal of the external magnetic field. The magnetic moment relaxes back towards the easy direction. (d) Brownian relaxation of the magnetic moment on withdrawal of the external magnetic field. Relaxation is achieved by whole scale rotation of the MNP and the magnetic moment remains fixed with respect to the crystallographic direction (indicated by the red dotted line).

It is evident from Eq. 1.10 and 1.11 that τ_N increases exponentially with particle volume, whereas, τ_B scales linearly with hydrodynamic volume, indicating that for larger sized particles, Brownian relaxation is the dominant relaxation mechanism. As τ_N scales exponentially with anisotropy energy density, τ_N is significantly higher for MNP with higher anisotropy energy density (e.g., $CoFe_2O_4$). Both types of relaxation occur in parallel and the effective relaxation time (τ) is expressed by the following equation, which indicates that the effective relaxation time (τ) is the lowest among τ_N and τ_B.

$$\tau^{-1} = \tau_N^{-1} + \tau_B^{-1} \tag{1.12}$$

Figure 1.12 shows the variation of Neel relaxation time, Brownian relaxation time and effective relaxation time as a function of MNP diameter for three different values of anisotropy energy density, viz., 25, 50 and 75 kJm^{-3}, where, the coating thickness, system temperature, attempt time and medium viscosity were considered as 2 nm, 300 K, 1 $\times 10^{-9}$ s and 8.9 $\times$ 10^{-4} Pa.s, respectively.

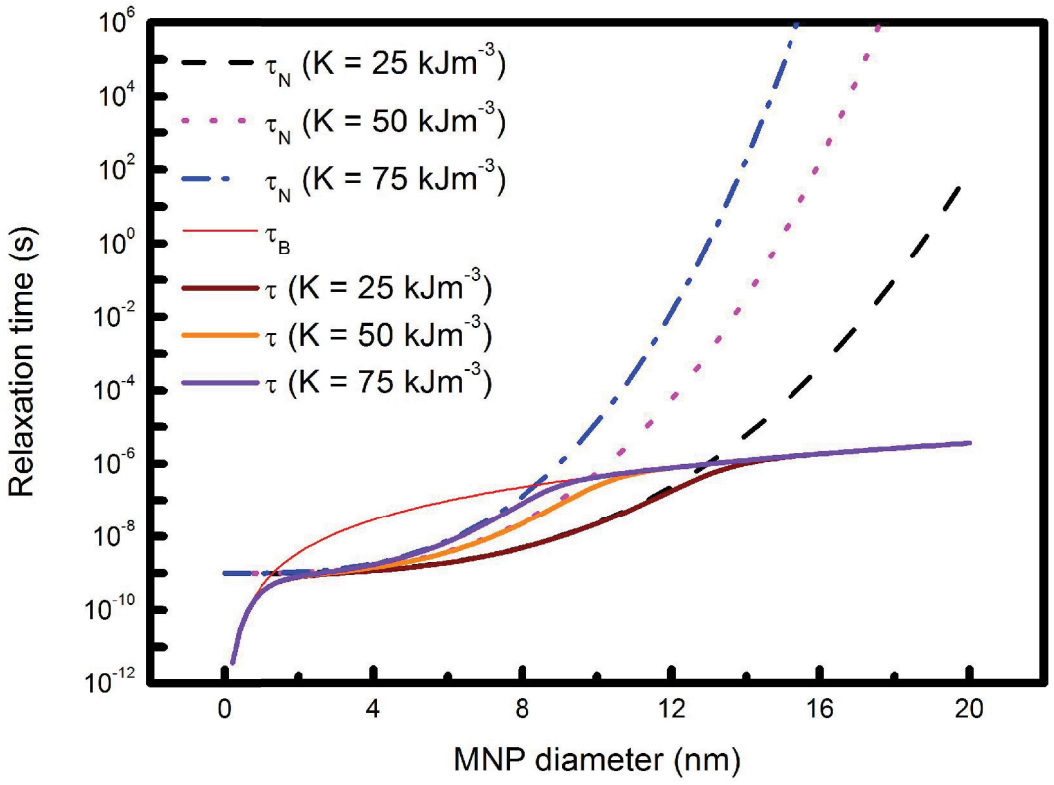


Figure 1.12: Variation of Neel, Brownian and effective relaxation time as a function of MNP diameter for three different values of anisotropy energy density, viz., 25, 50 and 75 kJm^{-3}, respectively.

Figure 1.12 clearly shows the effects of size and anisotropy energy density on effective relaxation time of superparamagnetic MNP. For a fixed value of anisotropy energy density, the Brownian contribution towards effective relaxation time increases with MNP diameter.

On the other hand, for MNP with higher anisotropy energy density (75 kJm^{-3}), Brownian relaxation becomes significant at ~ 8 nm, whereas, for lower anisotropy energy density (25 kJm^{-3}), Brownian contribution to effective relaxation time is significant only above 13 nm. Neel relaxation and hysteresis losses are mathematically equivalent [42, 280] and relaxation losses are manifestations of linear response approximation of high frequency hysteresis loops for single domain superparamagnetic MNP (without coherent reversal of macro-spin), under lower external field amplitudes ($\mu_0 M_S V_p H_{max} < k_B T$, where, H_{max} is the maximum amplitude of the applied RF-AMF) [42].

1.7.5 RF-AMF induced heating in ferrofluids: Rosensweig's model

For a constant density MNP system (non-interacting) subjected to a RF-AMF, the cyclic increase in internal energy (ΔU), under adiabatic conditions, can be expressed by the following equation [51]. Here, magnetization lags the applied field leading to a positive result of the integration, indicating conversion of magnetic work to internal energy.

$$\Delta U = -\mu_0 \oint M dH \tag{1.13}$$

Here, magnetization lags the applied field leading to a positive result of the integration, indicating conversion of magnetic work to internal energy. For a RF-AMF of the form: $H(t) = H\cos(\omega t) = \mathrm{Re}[He^{i\omega t}]$, the resulting magnetization is expressed by the following equation [51].

$$M(t) = \mathrm{Re}[\chi H e^{i\omega t}] = H(\chi' \cos\omega t + \chi'' \sin\omega t) \tag{1.14}$$

Here, χ' and χ'' indicate real and imaginary components of the complex susceptibility ($\chi = \chi' - i\chi''$, where $i^2 = -1$) of the magnetic fluid following the Debye model [51].

It can be seen from Eq. 1.14 that χ'' is the out-of-phase component of susceptibility, which indicates losses. For a motionless magnetic fluid subjected to a RF-AMF, the relaxation dynamics can be expressed by the following equation [51, 281].

$$\frac{\partial M(t)}{\partial t} = \frac{1}{\tau}[M_0(t) - M(t)] \tag{1.15}$$

Here, χ_0 and τ indicate ensemble averaged equilibrium susceptibility and effective relaxation time, respectively, and $M_0(t) = \chi_0 H\cos(\omega t)$ [51]. The solution of Eq. 1.15 provides the frequency dependence of ferrofluid susceptibility and its complex part ($\chi^{//}$) can be expressed as $\chi^{//} = \chi_0 \frac{\omega\tau}{1+\omega^2\tau^2}$. Substituting Eq. 1.14 and the form of χ// in Eq. 1.13 and multiplying the integrated result with frequency ($f = \omega/2\pi$), the following expression of power generated per unit volume is obtained [51].

$$P = \frac{1}{2}\omega\mu_0\chi_0 H^2 \frac{\omega\tau}{1+\omega^2\tau^2} \tag{1.16}$$

It is evident from Eq. 1.16 that the heating power is maximum at $\omega\tau = 1$, which indicates the critical frequency for optimal heating in a magnetic fluid [51]. For $\omega\tau << 1$, the factional term can be approximated as $1/[\omega\tau+(\omega\tau)^{-1}] = \omega\tau$ and $P \sim \omega^2H^2\tau$, i.e., heating power is linearly proportional to the square of frequency, effective relaxation time and square of applied field amplitude [52]. On the other hand, for $\omega\tau >> 1$, $P \sim H^2/\tau$, i.e., heating power is independent of frequency but directly proportional to the square of the applied field amplitude and inversely proportional to the effective relaxation time [52].

The ensemble averaged equilibrium susceptibility (χ_0) can be expressed in terms of the initial susceptibility (χ_i) and Langevin function $L(\xi)$ by the following relation [4, 51].

$$\chi_0 = \chi_i \frac{3}{\xi} L(\xi) = \chi_i \frac{3}{\xi} (\coth \xi - \xi^{-1}) \tag{1.17}$$

Here, $\xi = \mu_0 M_d V_p H/k_B T$, where M_d ($= M_s/\psi_s$) is the domain magnetization and ψ_s is the solid volume fraction. For $\xi << 1$, $(\coth \xi - \xi^{-1}) = \xi/3$ and it can be seen from Eq. 1.17 that under such conditions, $\chi_0 = \chi_i = (dM/dH)_i = \mu_0\psi_s M_d^2 V_p/3k_B T$. Hence, it is evident from the expression of χ_i and Eq. 1.16, that the power generated per unit volume is strongly dependent

on the particle size both explicitly (through particle volume) and implicitly (through effective relaxation time) [51, 256].

Moreover, Eq. 1.16 is valid for a perfectly monodisperse system and in reality, Eq. 1.16 is modified by integrating with a log-normal size distribution g(r) [$g(r) = \frac{1}{\sqrt{2\pi}\sigma_{\ln} r} \exp[\frac{-(\ln r / r_0)^2}{2\sigma_{\ln}^2}]$, where, r_0 is the median radius and $\sigma_{\ln}$ is the standard deviation (SD) in $\ln(r_0)$] to obtain the dissipated power per unit volume (P_{poly}) for a polydisperse system [51].

$$P_{poly} = \int_0^\infty P g(r) dr, \quad \text{where} \int_0^\infty g(r) dr = 1 \tag{1.18}$$

Experimentally, the RF-AMF induced heating efficiency of magnetic fluids is expressed in terms of specific absorption rate (SAR) [51, 52]. Eqs. 1.16 and 1.18 do not consider the concentration dependent effects, like dipolar interaction and aggregation and hence, SAR (= P/density) is experimentally determined by calorimetric measurements using the following equation [51, 52].

$$SAR = \frac{c_{samp}\rho_{samp}}{m_{Fe}} \left.\frac{dT}{dt}\right|_{t=0} \tag{1.19}$$

Here, c_{samp} and ρ_{samp} are the specific heat capacity and density of the magnetic fluid, respectively, $\left.\frac{dT}{dt}\right|_{t=0}$ indicates the initial rate of temperature rise under non-adiabatic limit and m_{Fe} signifies the weight of magnetic phase per unit volume of the sample [51].

It can be seen from Eqs. 1.16, 1.18 and 1.19 that SAR (or P) varies linearly with square of the applied field amplitude (H^2) and frequency (f) indicating a monotonic increase of SAR for higher values of field amplitude and frequency. To eliminate the dependence of SAR on extrinsic parameters and to enable a direct comparison between heating efficiencies, the SAR values are normalized with respect to the product of frequency and square of the field

amplitude [89]. The normalized SAR values are expressed in terms of intrinsic loss power (ILP = SAR/H^2f) which is a system independent parameter that directly indicates the efficiency of a magnetic fluid sample to convert electromagnetic energy to thermal energy [282]. Kallumadil et al. [89] have listed the ILP values for a number of commercial colloids, where, it was observed that the ILP values varied between 0.15 nHm^2kg^{-1} (BNF 01708 with carboxyl coating from Micromod Partikeltechnologie, GmbH, Germany) to 3.12 nHm^2kg^{-1} (Nanomag D-Spio with carboxyl coating from Micromod Partikeltechnologie, GmbH, Germany). A very high ILP value of 23.4 nHm^2kg^{-1} was reported for bacterial magnetosomes by Hergt et al. [244].

1.7.6 RF-AMF induced heating of oriented MNP

In the presence of an external DC field (H_{DC}), the MNP are oriented along the direction of the external DC field and under such condition the interaction strength between the MNP is described by the magnetic coupling constant (Λ), which is expressed as $\Lambda = \frac{\pi \mu_0 d_{MNP}^3 \chi^2 H^2}{72 k_B T}$, where d_{MNP} and χ indicate MNP diameter and ferrofluid susceptibility, respectively [159, 160]. When the magnetic coupling constant is much larger than unity ($\Lambda >> 1$), the MNP undergo disorder-order transition and form linear chain-like structures due to head-on aggregation along the direction of H_{DC} [283-285]. When subjected to a RF-AMF, such linear chains of MNP generate heat due to Neel-Brownian relaxation, which is strongly dependent on the angle between the direction of RF-AMF and axes of linear chains [286, 287].

For a system of identical and non-interacting MNP, external H_{DC} induced orientational ordering leads to parallel alignment of their anisotropy axes towards the field direction [288]. When such an aligned structure is subjected to a RF-AMF, then, according to Stoner-Wohlfarth model [48], the extent of magnetization rotation (under the action of RF-AMF)

depends on Zeeman and anisotropic energies and the effective total energy (E_t), is represented by the following equation [18, 289].

$$E_t = [KV_p \sin^2(\theta_m) + B_i] - \mu_0 M_s V_p H \cos(\phi - \theta_m) \quad (1.20)$$

Here, θ_m is the angle between the anisotropy axis and magnetization and ϕ is the angle between the anisotropy axis (direction of H_{DC}) and applied RF-AMF. K is the effective uniaxial anisotropy energy density and can be expressed as $K = K_b + (6/d_{MNP})K_s$, where, K_b and K_s indicate the bulk and surface anisotropy energy densities, respectively [18]. Assuming that surface anisotropy energy density is normal to the MNP surface and invoking symmetrical boundary conditions, Bodker et al. [290] demonstrated that for a perfect spherical MNP, the net contribution form surface anisotropy is non-existent and the effective anisotropy energy density is mainly due to contributions from bulk anisotropy energy density. According to Dormann-Bessais-Fiorani (DBF) model [18, 291, 292], B_i is an energy factor in the anisotropic energy term which describes the interparticle interactions (mainly dipolar interactions). For analytical simplicity, dipolar interactions are not considered in the present analyses. Substituting the expression of anisotropy magnetic field as $H_A = 2K/\mu_0 M_s$ in Eq. 1.20, the total energy (E_t) of the ensemble, normalized with respect to thermal energy, is expressed by the following equation [42, 288].

$$\frac{E_t}{k_B T} = \frac{KV_p}{k_B T}[\sin^2(\theta_m) - 2h\cos(\phi - \theta_m)] = \sigma_{AT}[\sin^2(\theta_m) - 2h\cos(\phi - \theta_m)] \quad (1.21)$$

Here, h (= H/H_A) is the normalized magnetic field and σ_{AT} (= KV_p/k_BT) is the ratio of the anisotropy energy to thermal energy. Equation 1.21 determines the total energy and effective uniaxial anisotropy energy density for an ensemble of non-interacting and identical MNP with orientational ordering. The angle ϕ, between H_{DC} and RF-AMF, has a strong influence on the effective uniaxial anisotropy energy density, Neel relaxation time and RF-AMF induced heating efficiency [52, 286].

It is evident from Eq. 1.21 that the expression of E_t/k_BT significantly varies with angle ϕ. The Eq. 1.21 for $\phi = 0$, 45 or 90^0 are given below.

$$\frac{E_t}{k_BT} = \sigma_{AT}[\sin^2(\theta_m) - 2h\cos(\theta_m)] \qquad (\text{for } \phi = 0^0) \qquad (1.22a)$$

$$\frac{E_t}{k_BT} = \sigma_{AT}[\sin^2(\theta_m) - 2h\cos(\theta_m - \pi/4)] \qquad (\text{for } \phi = 45^0) \qquad (1.22b)$$

$$\frac{E_t}{k_BT} = \sigma_{AT}[\sin^2(\theta_m) - 2h\sin(\theta_m)] \qquad (\text{for } \phi = 90^0) \qquad (1.22c)$$

Figure 1.13 shows the variation of E_t/k_BT as a function of θ_m (in the range -180 to $+180^0$) for typical oleic acid coated Fe_3O_4 MNP (with $\sigma_{AT} \sim 15.9$ and $d_{MNP} \sim 6.9$ nm) in the case of h = 0.4 (H = 63.0 kAm^{-1} and H_A = 160 kAm^{-1} [293]). The geometrical orientation involving H (RF-AMF), magnetization (M) and anisotropy axis (along H_{DC}) is schematically shown in the **inset of Fig. 1.13** for easy comparison.

Several interesting features can be observed from **Fig. 1.13** among which a few salient features are described below.

i) In the absence of a RF-AMF (H = 0), the energy curve is perfectly symmetrical around $\theta_m = 0^0$ and shows two distinct energy minima at $\theta_m = 0^0$ and $\pm\ 180^0$, i.e., along the easy axes of the MNP.

ii) On application of a RF-AMF along the anisotropy axis ($\phi = 0^0$), the symmetry of the energy profile is retained but the energy minima are non-degenerate and the primary minima around $\theta_m \sim 0^0$ is energetically favoured by RF-AMF [42].

iii) With further increase of ϕ (e.g., $\phi = 45^0$), the energy curve becomes completely asymmetric. For $\phi = 45^0$, the energy minima are non-degenerate and the energy difference between the primary and secondary minima is lower as compared to that in the case of $\phi = 0^0$.

iv) For $\phi = 90^0$, the energy minima are found to be degenerate and symmetrically located on either side of $\theta_m = 90^0$. This scenario can be physically explained from the distribution of magnetic moments within a cone of angle θ_m with cone axis along the direction of H_{DC} (anisotropy axis), which results in two degenerate energy minima for $\phi = 90^0$.

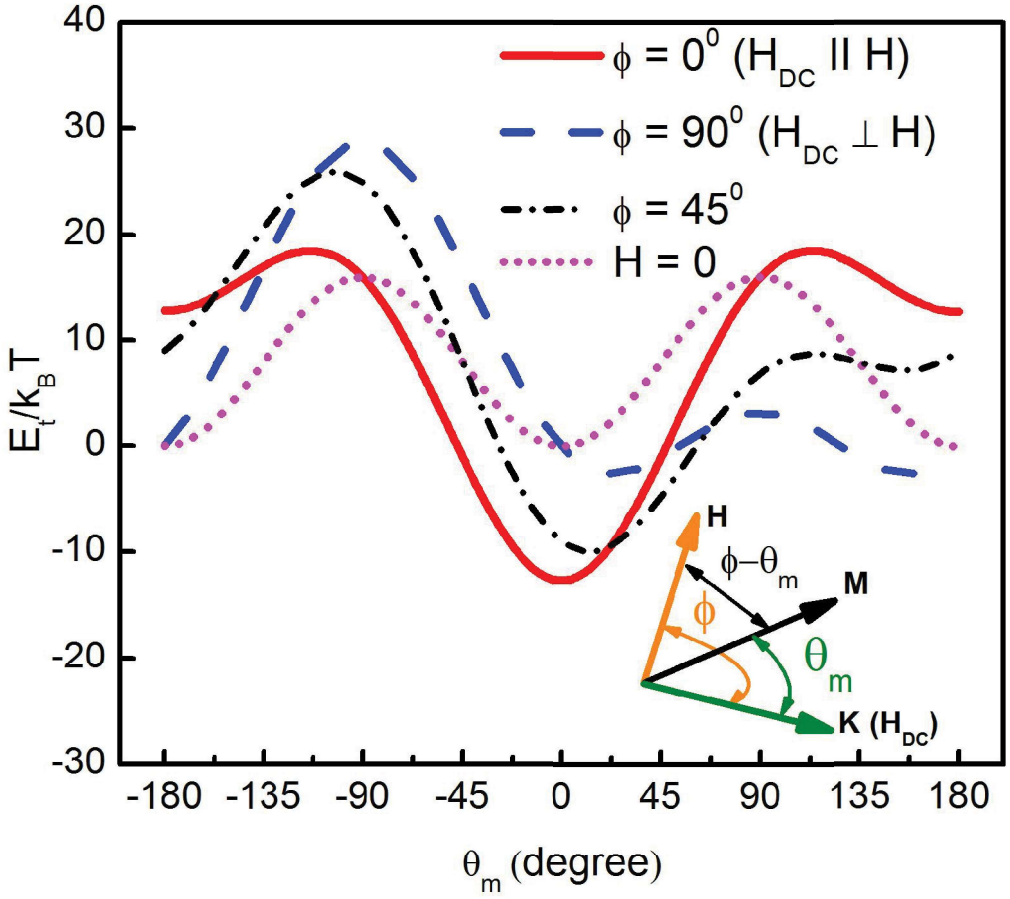


Figure 1.13: Variation of normalized total energy (E_t/k_BT) as a function of θ_m (angle between the anisotropy and magnetization axes) for different orientations of RF-AMF with respect to H_{DC}, viz., $\phi = 0^0$, 45^0 and 90^0. Variation of E_t/k_BT for H = 0 is also shown in the figure. (Inset) Schematic illustration of the system geometry with the angles θ_m and ϕ.

The normalized energy difference [$\Delta(E_t/k_BT)$] indicating the depth of the primary energy minima (around $\theta_m \sim 0^0$) was found to vary linearly with $(1+h)^2$, in accordance with the theoretical predictions [288], where, $h = H/H_A$.

The energy absorption in a system of identical MNP undergoing Neel relaxation, under RF-AMF, is directly proportional to the hysteresis loop area and using semi-analytical calculations, based on Stoner-Wohlfarth model [48], it was shown that the hysteresis loop areas for randomly oriented and aligned ($\phi = 0^0$) MNP varies according to the following equations (1.23a-b) and the parameter ε is defined by Eq. 1.24 [42].

$$A_{random} = 4M_s\mu_0 H_A(1-\varepsilon^{0.5}) \tag{1.23a}$$

$$A_{\phi=0} = 0.96M_s\mu_0 H_A(1-\varepsilon^{0.8}) \tag{1.23b}$$

$$\varepsilon = \frac{k_B T}{KV_p}\ln\left(\frac{k_B T}{4\mu_0 M_s H_{\max} V_p f\tau_0}\right) \tag{1.24}$$

Here, A_{random} and $A_{\phi=0}$ indicate hysteresis loop areas for random and oriented MNP, respectively. It is evident from Eqs. 1.23a-b that for intermediate to high dissipation limits, SAR of the aligned MNP are ~ 4.2 (= 4/0.96, neglecting the effect of ε) times higher than that of the randomly oriented MNP, which was experimentally confirmed by Beck et al. [294] in oriented MNP under a static 3T magnetic field. These results show that the heating efficiency of textured MNP, during MFH therapy, depends on the direction of orientation of the MNP with respect to the RF-AMF.

1.8 Motivation

Though field induced heating of MNP is well studied, several challenges still remain in the fundamental understanding of the mechanism involved and in the practical implementation of MFH. For e.g., the role of sample concentration, medium viscosity, size polydispersity and external DC magnetic field induced texturing, etc. on the MFH efficiency are poorly understood [273, 295, 296]. Another primary challenge lies in the understanding of collective behavior (like aggregation or agglomeration and dipolar interactions) and its effect on heating efficiency [52]. Also, there are several uncertainties involved in the non-adiabatic estimation

of SAR, which are rarely addressed [297]. Moreover, the effectiveness of MFH in tissue environment needs further studies for a better understanding [298, 299]. With respect to multimodal hyperthermia, the heating mechanism at different length scales and the effects of demagnetization field is not fully understood [300]. One of the major issues, with respect to real time *in vivo* application of MFH in human, is the effective monitoring of temperature, preferably mapping, at the tumor location during cancer therapy. Typically, a large number of fiber optic point sensors are required for this purpose which warrants the need for developing an effective non-invasive temperature mapping protocol for *in vivo* MFH based cancer therapy. The above-mentioned aspects served as motivation for undertaking the present study. This thesis attempts to provide a systematic study on the effects of particle loading, medium viscosity, size polydispersity, orientational ordering and thermal losses on heating efficiency in model ferrofluids and ferroemulsions synthesized and characterized in-house.

1.9 Objectives

The main goal of the thesis are (a) understanding various parameters influencing heating efficiency of magnetic fluids and achieving an optimal heating efficiency and b) understanding the uncertainties involved in SAR calculation and to evolve a non-contact temperature mapping protocol. The major objectives of this thesis are mentioned below.

i) To probe the role of particle concentration, medium viscosity and size polydispersity on RF-AMF induced heating efficiency in oil and water based ferrofluids.

ii) To probe the thermal losses associated with RF-AMF induced non-adiabatic heating of magnetic fluids and to develop an adiabatic reconstruction protocol for the measured temperature rise curves.

iii) To develop an effective temperature mapping methodology for MFH using infrared thermography and to develop a convection corrected data analyses protocol for accurate quantification of heating efficiency.

iv) To probe RF-AMF induced heating in larger sized magnetic nanoemulsions from the perspective of multimodal therapy.

v) To study the effect of external DC magnetic field induced texturing on MFH efficiency of magnetic nanoemulsion.

1.10 Overview of the thesis

The thesis consists of six chapters and details of the chapters are summarized below. **Chapter 1** gives an introduction to MNP with a focus on bio-medical applications of MNP, ferrofluids, ferroemulsions and MFH which is followed by a discussion of Neel-Brownian relaxation in superparamagnetic MNP and RF-AMF induced heating mechanism. **Chapter 2** briefly discusses the experimental methods for synthesis of ferrofluids and ferroemulsions, various characterization methods used and experimental protocols for MFH studies. This is followed by a detailed analyses of various thermodynamic uncertainties involved in SAR estimation due to non-adiabatic nature of the experimental set-up. **Chapter 3** discusses the MFH studies in water and oil based ferrofluids containing tetramethyl ammonium hydroxide (TMAOH) and oleic acid coated superparamagnetic Fe_3O_4 MNP, respectively, using IRT and the results are compared with those obtained from conventional fiber optic temperature sensor. It also presents an empirical data analysis methodology, developed for incorporating the external and internal convection effects. **Chapter 4** presents the results of MFH studies in a water based ferrofluid containing phosphate coated Fe_3O_4 and $CoFe_2O4$ MNP of varied concentration under different external field amplitudes. **Chapter 5** discusses MFH studies on magnetically polarizable oil-in-water nanoemulsions (size ~ 200 nm) containing single

domain superparamagnetic Fe_3O_4 MNP (size ~ 10 nm) in the oil phase. The effects of size polydispersity, MNP concentration, medium viscosity and external DC magnetic field induced orientational ordering on MFH efficiency is probed. **Chapter 6** presents a summary of the results obtained, along with the conclusions drawn and recommendations for future work.

Chapter 2

Experimental methods

Chapter 2 Experimental methods

2.1 Synthesis of magnetic nanoparticles (MNP)

Over the years various chemical methods have been developed for the synthesis of size and shape controlled, stable and monodispersed MNP, viz., coprecipitation [301], thermal decomposition [302], laser pyrolysis [303], microemulsion based [304, 305], sol-gel [306], solvothermal [307], microwave assisted [308] and microbial methods [309]. Among all the various methods, coprecipitation is one of the most widely used technique due to its advantages such as no requirement of toxic solvents, no precursor complexes and no high temperature. Moreover, chemical coprecipitation based techniques are eco-friendly, reproducible and can be easily scaled up [310].

2.1.1 Coprecipitation method

Though the formation and properties of crystalline precipitates during coprecipitation was theoretically discussed by Kolthoff [311] in 1932, the first coprecipitation based synthesis of ferrite MNP was reported by Massart [301], in 1981, where superparamagnetic iron oxide MNP was obtained by precipitating $FeCl_2$ and $FeCl_3$ using ammonium hydroxide as alkali. The simplified form of the chemical reaction is shown below.

$$Fe^{2+} + 2Fe^{3+} + 8OH^- = Fe_3O_4 \downarrow + 4H_2O \quad (2.1)$$

There are three major steps during coprecipitation, namely, inclusion, occlusion and adsorption. A close similarity between the ionic radii and charge of the reactants are essential prerequisites for coprecipitation. The formation pathways of Fe_3O_4 in coprecipitation depend on the rate of alkali addition (to achieve super-saturation), as a slow rate of alkali addition activates the most dominant pathway through transformation of akaganeite [β-FeO(OH)] to Fe_3O_4 via goethite [α- FeO(OH)] [312]. For faster rate of alkali addition, additional pathway

mediated through lepidocrocite [γ-FeO(OH)] gets activated and coexist with the former pathway [312]. The size and shape of the synthesized MNP using coprecipitation can be controlled by optimizing various parameters like pH, rate of alkali addition, stirring rate, stirring time and nature of salt solution [313, 314].

2.1.2 Synthesis of ferrofluids using coprecipitation method

In coprecipitation method, the respective salt solutions (Fe^{2+} and Fe^{3+} for Fe_3O_4) in stoichiometric ratio are mixed in a synthesis reactor, equipped with an external heater, stirrer (mechanical or magnetic), temperature and pH probes. The various experimental parameters, such as pH, temperature, rate of alkali addition, stirring rate, stirring time and nature of salt solutions are adjusted to achieve the desired particle size.

2.1.2.1 Preparation of oil based ferrofluid containing oleic acid coated Fe_3O_4 MNP

Fe_3O_4 MNP were synthesized by a chemical coprecipitation method using 1:1 acidic solution of 0.8 M $FeCl_3.6H_2O$ and 0.4 M $FeSO_4.7H_2O$ [66, 313]. The salt solutions were prepared in acidic solutions to avoid the formation of iron hydroxide and the solution was heated in a water bath to reach a temperature of 60 ^{0}C, followed by the addition of 25 % aqueous ammonia to the solution to rapidly increase the pH to ~ 10, accompanied by vigorous stirring. The rapid addition of ammonia resulted in super-saturation allowing the formation of excess number of nuclei and the vigorous stirring prevented coagulation of particles. At this stage the solution turned black indicating the formation of Fe_3O_4 MNP. Oleic acid was then added to the solution after digesting it for 30 minutes and the pH and temperature of the solution was adjusted to 9.5 and 70 ^{0}C, respectively, thus, resulting in formation of ammonium oleate salt. The higher temperature augmented the solubility and reduced the viscosity of the salt. The oleate anions, formed through the dissociation of ammonium oleate salt, replaced the

OH^- ions from the MNP surface (in alkaline medium MNP surface were decorated with OH^- ions) by ion-exchange adsorption phenomena. For the coating process to complete, the temperature, pH and stirring speed were maintained for further 30 minutes. The coated MNP were washed several times before further use and the oleic acid coated MNP were dispersed in an organic carrier fluid such as kerosene or octane. The oleic acid capping provided steric stabilization against van der Waals attraction, where, the carboxylic acid group of oleic acid was found to be attached to the surface of the MNP and the aliphatic chains extended into the nonpolar solvents [66].

2.1.2.2 Preparation of water based ferrofluids

Tetramethyl ammonium hydroxide (TMAOH) coated Fe_3O_4 MNP were prepared by chemical coprecipitation technique using 1:1 ratio of 0.8 M $FeCl_3.6H_2O$ and 0.4 M $FeSO_4.7H_2O$ as per the procedure discussed in section 2.1.2.1 [66]. The synthesized Fe_3O_4 MNP were later coated with TMAOH [$N(CH_3)_4OH$] surfactant to electrostatically stabilize the MNP in aqueous media.

Phosphate coated Fe_3O_4 MNP were synthesized by coprecipitation technique using 1:1 aqueous solution of 0.2 M $FeCl_3$. $6H_2O$ and 0.1 M $FeSO_4$. $7H_2O$ [315]. The synthesized MNP were coated with phosphate group by treating with 88 % orthophosphoric acid. Phosphate coated $CoFe_2O_4$ MNP were also synthesized using coprecipitation method. The coated phosphate layer provided electrostatic stability in aqueous media.

2.1.3 Preparation of ferroemulsions

Synthesis methods of nanoemulsions are characterized into three categories, viz., high energy, low energy and a combination of high energy and low energy methods [142, 316]. High energy emulsification methods involve high pressure homogenization using

ultrasonication [317], piston gap homogenizer [318] or a microfluidizer [317] to create a strong force for size reduction. On the other hand, low energy emulsification techniques include spontaneous emulsification [319], classical phase inversion [320] and catastrophic phase inversion [321] methods. The synthesis of nanoemulsion using low energy method involve fine tuning of several parameters like surfactants, co-surfactants, oil phase, temperature and hydrophilic-lipophilic balance, etc. [140, 322].

In the present study, oil-in-water stock emulsion (oleic acid coated single domain superparamagnetic Fe_3O_4 MNP dispersed in octane) of size ~ 0.1-1 μm was prepared using a classical phase inversion method by shearing ferrofluid oil, water and surfactant in the ratio of 5: 10: 5 using a homogenizer (IKA Werke, T25, Germany) [323]. Monodisperse emulsion with narrow size distribution was obtained from the stock emulsion using fractionation technique by adding excess surfactant in the continuous medium leading to depletion of micelles from the inter-droplet spacing [144]. The depleted micelles exerted an uncompensated osmotic pressure on the emulsion droplets leading to an attraction between them, resulting in a phase separation with the larger and smaller sized droplets being present in the denser and dilute phases, respectively. The process was repeated several times to achieve emulsion droplets of desired size and polydispersity.

The water dispersed oil droplets were stabilized using an anionic surfactant: sodium dodecyl sulphate (SDS) having a chemical formula $CH_3(CH_2)_{11}SO_4Na$. In aqueous solution, Na^+ dissociates and form counter ions around the negatively charged DS^- head group, which is hydrophilic in nature. The hydrophobic alkyl chain gets adsorbed on the emulsion interface and the hydrophilic DS^- is exposed to the aqueous medium. The dissociated Na^+ and DS^- formed an electrical double layer which provided electrostatic stabilization of the emulsion droplets in aqueous media.

2.1.4 Preparation of agar based samples

Agar consist of a neutral gel forming agarose polymer and agaropectin which is a charged polymer containing sulphate ions. It has been reported that gel with agar concentration less than 4 wt. % has a porosity similar to soft tissues, whereas, agar concentration beyond 4 wt. % changes the gel microstructure to resemble hard tissues [324]. Hence, agar gels were chosen to mimic tissue equivalent platform to load MNP or nanoemulsion droplets, using a protocol reported by Serantes et al. [286].

2.1.4.1 Preparation of agar based samples loaded with $CoFe_2O_4$ and emulsion droplets

Water based ferrofluid containing phosphate coated $CoFe_2O_4$ was collected in two sample vials (500 μL in each) and placed in a water bath sonicator at 70 ^{0}C for 1800 s. Thereafter, 5 and 10 mg of high melting point agar (as received from Sigma-Aldrich) was added to the hot ferrofluids for obtaining final agar concentration of 1 and 2 wt. %, respectively, without affecting the MNP concentrations. The prepared agar based samples were kept under sonication for additional 1800 s in order to obtain homogenous dispersions followed by prompt transfer to an ice bath to facilitate gel formation. Due to an increase in medium viscosity after gel formation, the MNP were immobilized in the agar matrix.

0.25 mL of the ferroemulsion in a sample holder was placed in a water bath sonicator at 70 ^{0}C for 600 s. Thereafter, 10 mg of agar was added to the emulsion for obtaining a final agar concentration of 4 wt. %. After sonication for an additional 1800 s, to obtain a homogeneous dispersion, the sample was promptly transferred to an ice bath for facilitating gel formation.

2.1.4.2 Preparation of agar based samples loaded with oriented emulsion droplets

0.34 mL of the ferroemulsion in a glass vial was placed in a water-bath sonicator at 70 ^{0}C for 10 minutes and thereafter, 4 mg of agar was added to the emulsion to obtain a final agar

concentration of 1.2 wt. %. The agar-based liquid sample was then subjected to sonication for an additional 30 minutes for obtaining a homogenous dispersion which was followed by prompt transfer to a custom made sample positioning stage located at the centre of a C-frame electromagnet (Ferro Chem, India) for cooling at ~ 22 ±2 ^{0}C and subsequent gel formation. During the cooling phase an external DC magnetic field (field amplitude, H_{DC} ~ 1485 ± 21 G) was applied for 30 minutes to orient the emulsion droplets along the field direction. Two different samples (EA_{para} and EA_{per}, respectively) were prepared by rotating the sample stage by 90^0. Though in both the samples, the orientational ordering was along the direction of H_{DC}, the sample rotation was performed in such a way that for the samples EA_{para} and EA_{per}, the direction of the applied RF-AMF, during field induced heating, was parallel and perpendicular to the direction of orientational ordering, respectively. For baseline data and comparison, a third sample (hereafter indicated as EA) was also prepared without applying an external DC magnetic field, where, the emulsion droplets were randomly oriented.

2.2 Characterization techniques

The prepared samples were characterized using various techniques, such as powder X-ray diffraction (XRD), small angle X-ray scattering (SAXS), dynamic light scattering (DLS), thermogravimetric analysis (TGA), Fourier transform infrared spectroscopy (FTIR), vibrating sample magnetometer (VSM), atomic force microscopy (AFM) and magnetic force microscopy (MFM), to obtain different physical properties of the MNP, ferrofluids and ferroemulsions. The various characterization techniques are categorized in **Fig. 2.1** and the basic working principle of each technique is briefly discussed in the subsequent sections.

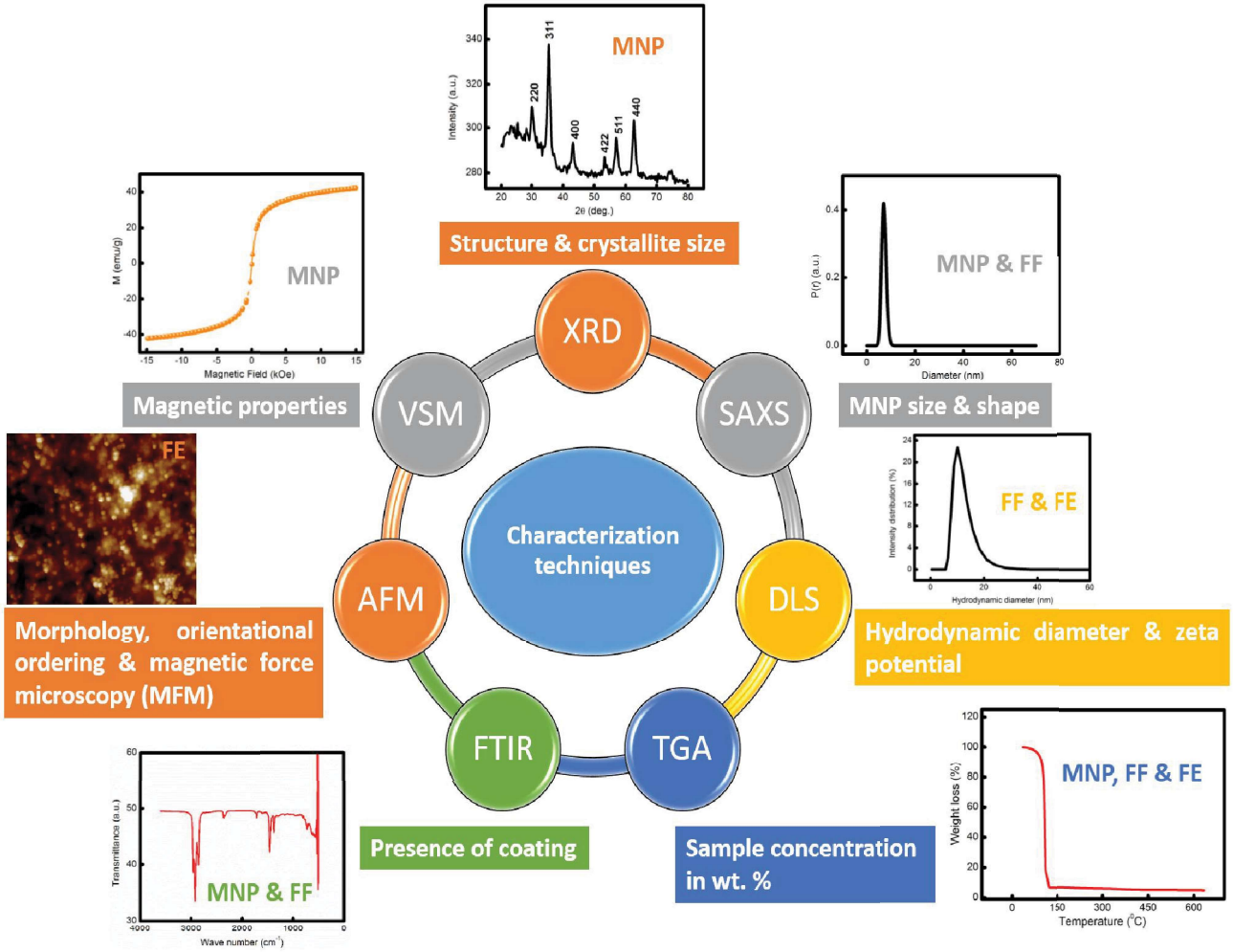


Figure 2.1: Characterization techniques used to investigate different physical properties of the magnetic nanoparticles (MNP), ferrofluids (FF) and ferroemulsions (FE). The physical properties probed by each technique and typical results are also shown in the figure.

2.2.1 Powder X-ray diffraction

Powder X-ray diffraction (XRD) is the most popular characterization tool for determining crystal structure, as the wavelength of the hard X-ray is similar to the size of the atoms. Apart from X-ray crystallography, XRD is also useful for chemical and phase analyses, stress measurements and studying crystal orientation and crystallite size [325].

The fundamental principle of XRD is the Bragg's law of diffraction [326], which is expressed as $2d_{hkl}\sin\theta = n\lambda_{X\text{-}ray}$, where d_{hkl} is the spacing between the crystallographic planes, θ is the

Bragg angle, n is the order of Bragg reflection and $\lambda_{X\text{-}ray}$ is the wavelength of the X-ray. During measurements, the X-ray source, sample and the detector lie on the circumference of a focussing circle and depending on the phase of the diffracted X-rays, constructive interference occurs at specific directions. The average crystallite size (d_{cryst}) is calculated from the broadening of the X-ray peak using Scherrer's equation of the form: $d_{cryst} = 0.89\lambda_{X\text{-}ray}/(FWHM \times \cos\theta)$, where, 0.89 is a proportionality constant for spherical particles and FWHM is the full width at half maxima of the maximum intensity peak measured in radian [327].

In the present study, powder XRD pattern of the synthesized MNP are recorded in the 2θ range of 20-80^0 using a Rigaku Ultima IV X-ray diffractometer which employs Cu-K_α radiation ($\lambda_{X\text{-}ray}$ = 1.5416 Å) in the Bragg-Brentano geometry. The scan rate and step size are fixed at 2^0 per minute and 0.02^0, respectively. The Cu-K_α is obtained by filtering out the other wavelengths using a monochromator and the monochromatic X-ray beam is collimated using solar slits which is then allowed to fall on the sample and the scattered X-ray are passed through an anti-scattering slit to improve the peak-to-background ratio. Data acquisition and preliminary analyses are performed using PDXL software, whereas, the obtained diffraction patterns are compared with the database of Joint Committee on Powder Diffraction Standards (JCPDS).

2.2.2 Small angle X-ray scattering

Small angle X-ray scattering (SAXS) is a characterization tool for obtaining information about size, shape and periodicity of structures ranging from ten to thousands of angstrom. Primary experimental requirements of SAXS are well collimated X-ray beam with small cross-sectional area and extended sample-detector distance to reduce X-ray background. In SAXS, the scattering intensity from a collection of objects I(q), where q is the scattering

wave vector ($q = 4\pi\sin\theta/\lambda_{X\text{-}ray}$), is expressed as $I(q) = N_{obj}F(q)S(q)$, where N_{obj}, F(q) and S(q) indicate number of objects, form factor (carries information on density distribution) and structure factor (carries information on spatial arrangement), respectively [328]. For length scales smaller than the primary particle size, S(q) becomes constant and I(q) is proportional to F(q) [328]. For a spherical particle of diameter d_{MNP}, the scattering intensity is expressed by the following equation [328, 329].

$$I(q) = (\Delta\rho_e)^2 V_p^{\,2}[3\frac{\sin(qd_{MNP}/2) - (qd_{MNP}/2)\cos(qd_{MNP}/2)}{(qd_{MNP}/2)^3}]^2 \quad (2.2)$$

Here $\Delta\rho_e$ and V_p indicate electron density difference between the particle and surrounding medium and particle volume, respectively. Equation 2.2 is oscillatory in nature and the first zero is located at $q \sim 9/d_{MNP}$ [330].

The distance distribution function [P(r)] is calculated by performing Fourier transform of the intensity profile using the equation: $P(r) = \frac{2}{\pi}\int_0^\infty I(q)qr\sin(qr)\exp(-B'q^2)dq$, where, B' is a numerical damping factor related to the termination effects of the Fourier transform [331]. For non-interacting spherical particles, SAXS intensity profile shows a Guiner region, followed by a Porod's region at high q, where, $I(q) \sim q^{-4}$, leading to a linear variation of ln[I(q)] as a function of ln(q) with a slope of -4 [332]. In the present study SAXS measurements are performed in transmission geometry (in the 2θ range of 0-2.2^0 in steps of 0.01^0) using a Rigaku Ultima IV instrument equipped with a Cu-K_α ($\lambda_{X\text{-}ray}$ = 1.5416 Å) source and scintillation detector. Data analysis is performed using NANO-solver software.

2.2.3 Dynamic light scattering

The hydrodynamic size (i.e., size of the hypothetical hard sphere that diffuses along with the dispersed particles) of the dispersed MNP is measured using dynamic light scattering (DLS),

which is also known as photon correlation spectroscopy. The spatial distribution of the dispersed MNP changes with time due to random Brownian motion giving rise to a continuously varying speckle pattern of the scattered light, which is analysed in real time using a time correlation function. The correlation function depends on the size of the MNP, i.e., for smaller particles, the correlation function decays faster due to their rapid motion as compared to the larger sized particles. The intensity-intensity auto correlation function for the scattered intensities at times t and t+δt is expressed by $g^{(2)}(q,t) = \frac{\langle I(q,t)I(q,t+\delta t)\rangle}{\langle I(q,t)\rangle^2}$, where q is the scattering vector and the intensity-intensity autocorrelation function is converted to an electric field auto correlation function, [$g^{(1)}(q,t)$], using the Siegert's relation, which is expressed as: $g^{(2)}(q,t) = 1 + \beta_{DLS}\left|g^{(1)}(q,t)\right|^2$, where, β_{DLS} is a correction factor depending on the scattering geometry and is roughly equal to the inverse of the number of speckle patterns used for analysis [333]. For monodisperse particles, the electric field auto correlation function is expressed by a single exponential function, i.e., $g^{(1)}(q,t) = \exp(-\Gamma t)$, where, Γ is the rate of relaxation and $\Gamma = D_{tran}q^2$, where D_{tran} is the translational diffusion coefficient of the particles. By measuring D_{tran}, hydrodynamic diameter (d_h) of the MNP is calculated using Strokes-Einstein's equation, which is expressed as $d_h = k_BT/3\pi\eta D_{tran}$, where η is the viscosity of the liquid medium.

In the present study, hydrodynamic diameter is measured by dynamic light scattering using Zetasizer Nano ZS (Malvern Instruments, UK) in the back-scattering geometry (178^0). The same instrument is also used for quantifying zeta potential of the suspended MNP (in water). The liquid layer surrounding the suspended particles can be divided into two regions, viz., an inner strongly bound region known as the Stern layer and a loosely bound outer region known as the diffused layer. There exist a notional boundary, called slipping plane, inside

which, the particles and ion form a stable entity and ions within the slipping plane travel along with the suspended particle. The potential at the slipping plane is called zeta potential, which indicates the colloidal stability of the suspended particles [334]. Here, zeta potential is calculated by measuring electrophoretic mobility (U_E) and using Henry's equation, which is expressed as $U_E = 2\varepsilon^E\xi_Z f(\kappa a)/3\eta$, where, ε^E, ξ_Z and $f(\kappa a)$ indicate dielectric constant, zeta potential and Henry's function, respectively. The thickness of the electrical double layer is expressed in terms of Debye length (κ^{-1}).

2.2.4 Thermogravimetric analysis

In thermogravimetric analysis (TGA) the amount and rate of change in the mass of a sample is monitored as a function of temperature or time under a controlled atmosphere using argon, nitrogen, oxygen, helium, etc. at controlled flow rates. Typical TGA instrumentation includes a sample pan attached to a high precision analytical balance and a furnace programmed for linear rise in temperature with time, which generates heat radially towards the centre [335]. TGA is used for characterizing sample with respect to their thermal and compositional stability and the MNP concentration is obtained from the weight loss curve as a function of temperature. In the present study, TGA on MNP or ferrofluids are performed using a Mettler Toledo TGA-DSC-1, 1100 LF (Switzerland) system under an inert atmosphere of argon in the temperature range of 30-600 ^{0}C at a heating rate of 10 ^{0}C per minute.

2.2.5 Fourier transform infrared spectroscopy

Infrared (IR) region spans from 10 to 12800 cm^{-1} and IR radiation is absorbed by a molecule if the frequency of the radiation matches with the vibrational frequency of the molecule. For a molecule to absorb the IR radiation, the vibrations or rotations within the molecule must cause a net change in dipole moment of the molecule [336]. Heteroatomic molecules or

molecules having non-symmetrical vibrational modes are IR active. Fourier transform infrared (FTIR) spectroscopy has several advantages over conventional IR spectroscopy, such as multiplexing, high signal-to-noise ratio, wavenumber precision and fast scanning. Typical FTIR spectrometer consists of a Michelson interferometer, where, the infrared source and a collimating mirror form the top arm of the interferometer and the bottom arm is equipped with a fixed mirror. The left arm of the interferometer contains sample and the IR detector, whereas, the moving mirror is located in the right arm of the interferometer. FTIR spectrometers use a broad spectrum glowing black-body as IR source and the collimated IR beam is fed into the interferometer, where an interferogram is formed, which is then transmitted through or reflected back from the sample allowing absorbance of radiation of certain wavenumber bands. The signal from the sample is finally measured using a suitable IR detector and displayed on a computer. For normalization, the background spectrum is also recorded.

In the present study, ABB Bomem MB 3000 FTIR spectrometer is used in the wavenumber range of 400-4000 cm^{-1}. The spectral resolution of the spectrometer is 4 cm^{-1}. The MNP are embedded in KBr pellets which are then used for FTIR studies. FTIR spectroscopy confirmed the presence of coating on the surface of the MNP.

For liquid samples (ferrofluids), FTIR spectroscopy is carried out in the attenuated total reflection (ATR) mode using a ZnSe crystal in the wavenumber range of 500-3600 cm^{-1}. ATR uses the property of total internal reflection, where, IR waves are allowed to pass through the ATR crystal in such a way that at least one reflection off the internal surface occurs, resulting in evanescent wave, which propagates into the sample (typical penetration depth is ~ 0.5-2 μm) [336]. The number of reflections and depth of penetration depend on several parameters, viz., the angle of incidence, wavelength, refractive indices of the crystal and medium, actual design and geometry of the crystal, etc.

2.2.6 Vibrating sample magnetometer

Vibrating sample magnetometer (VSM) is used for studying the magnetic properties of MNP. VSM operates on the basis of Faraday's law of induction, i.e., the induced electromotive force (EMF) in a circuit is proportional to the time rate of change of the magnetic flux (ϕ_m) linked to the circuit, i.e., EMF ~ $-d\phi_m/dt$. **Fig. 2.2** shows a schematic diagram of a typical VSM, where the essential components are shown.

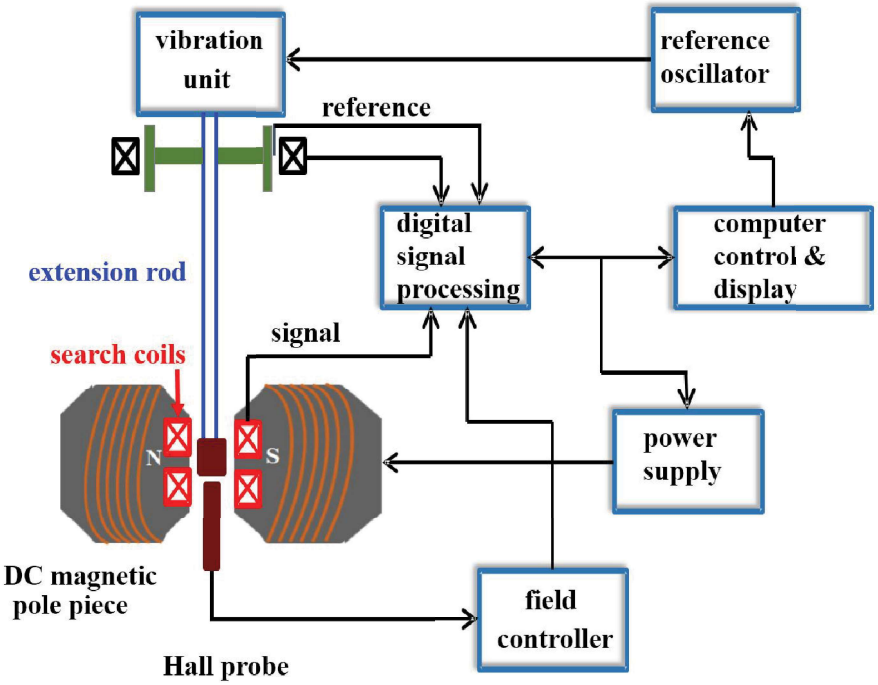


Figure 2.2: Schematic diagram of a typical vibrating sample magnetometer (VSM), showing the essential components.

The sample is first placed at the centre of a constant magnetic field, which magnetize the samples by alignment of magnetic domains or spins towards the field direction. The magnetization of the sample creates its own magnetic field around the sample and for vertical oscillation of the sample, this stray magnetic field varies with time, which is sensed by a set of pick-up coils. The induced electrical current in the pick-up coil is proportional to the

magnetization of the sample and the induced current is suitably amplified using digital signal processing unit typically consisting of trans-impedance and lock-in amplifiers. Assuming small dimension of the sample with respect to the distance of the sample from the pick-up coils, the magnetic induction, B is expressed by dipolar approximation and time variation of magnetic induction is expressed as $\frac{\partial B}{\partial t} = \frac{\partial B}{\partial z(t)} \frac{\partial z(t)}{\partial t}$, where, z(t) is the time dependent vertical displacement. The magnetic field variation, magnetization measurement protocols, sample temperature and signal processing are computer controlled and the final values of magnetization are represented in terms of emu/g. In the present study, a cryogen free VSM (M/s Cryogenics, UK) is used for magnetization measurements in the applied field range of ± 2.0 T. The temperature dependent magnetization measurements [zero field cooled (ZFC) and field cooled (FC)] are performed in the temperature range of 4-300 K under 100 G magnetic field. In the case of ZFC measurement, the sample is cooled down to 4 K in the absence of a magnetic field and then magnetization data is acquired during warming of the sample under the presence of 100 G field, whereas, for FC measurement, the magnetization data is acquired during cooling the sample up to 4 K in the presence of 100 G field.

2.2.7 Atomic force microscopy and magnetic force microscopy

Atomic force microscopy (AFM), invented by Binning, Quate and Gerber in 1986 [337], is one of the most versatile tool for imaging nanoparticles and studying their morphologies. In AFM, the interactive force between a tip and the sample surface is measured using a special kind of probe consisting of a cantilever with a sharp tip attached to its end. The force applied to the tip by the probing surface results in bending of the cantilever, which leads to a deflection in the reflected laser light that is measured using a position sensitive photo diode. By measuring the cantilever deflection, the tip-surface force is evaluated, from which, the

surface morphology is mapped in real space. **Fig. 2.3a** shows a schematic diagram of a typical AFM, where the essential instrumentations are highlighted. The sample is placed on a piezoelectric sensor with independent X, Y and Z motion controller, which are in-turn controlled by a robust feedback system that is driven by the output of the position-sensitive photo-diode indicating the deflection of the cantilever in real time. The set-point amplitude and gain of the phase-lock loop are optimized for each sample. **Fig. 2.3b** schematically shows a force-distance curve, where the three operating regions of AFM, viz., contact mode in repulsive regime, non-contact mode in attractive regime (large tip-surface separation) and tapping or semi-contact mode in the intermediate attractive regime are indicated.

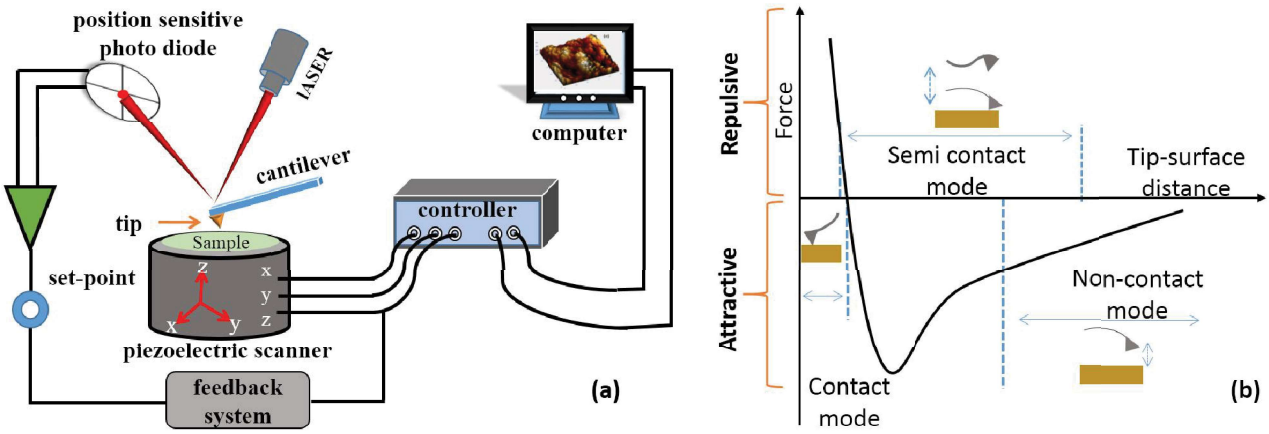


Figure 2.3: (a) Schematic diagram of a typical atomic force microscope (AFM). (b) Schematic illustration of the different modes of operation in an AFM.

In the present study, the surface morphology and external DC magnetic field induced orientational ordering of the magnetically polarizable oil-in-water nanoemulsion droplets are studied in the semi-contact mode using Ntegra Prima AFM (NT-MDT, Russia). For surface topography a commercial silicon tip (back surface is gold coated for superior reflection), with

bending radius ~ 10 nm and resonant frequency ~ 209.7 kHz, is used. The magnetic moment of the emulsion droplets is probed using magnetic force microscopy (MFM) using an aluminium coated silicon cantilever with CoCr coated tip (bending radius ~ 40 nm and resonant frequency ~ 67.4 kHz) under semi-contact topography guided lift mode with a typical lift distance (z) of ~ 500 nm. In MFM, the magnetic tip is under the additional influence of a magnetic force and for a lift distance of ~ 500 nm, the universal van der Waal's force is non-existent and the cantilever deflection is solely due to magnetic force experienced by the tip. The MFM data is analysed using classical point dipole approximations, i.e., the tip is approximated as a point magnetic dipole and the magnetic dipole fields of the sample and that of the tip are assumed to have the same vertical orientations [338, 339]. For a MFM cantilever oscillating at resonance frequency, the MFM phase difference ($\Delta\beta_{mag}$) is directly proportional to the gradient of magnetic force along Z-direction ($\partial F_z/\partial z$) and can be expressed by the following equation [338].

$$\Delta\beta_{mag} = -\frac{Q}{k_{spring}}\frac{\partial F_z}{\partial z} \tag{2.3}$$

Here, Q is the quality factor of the MFM cantilever (~ 500) and k_{spring} is the spring constant. Under classical point dipole approximation, the magnetic force gradient along Z-direction can be expressed as $\frac{\partial F_z}{\partial z} = \frac{24 m_{tip} m_{sample}}{z^5}$, where, m_{tip}, m_{sample} and z indicate magnetic moment of the MFM tip (~ 6×10^{-15} Am^2), magnetic moment of the sample and lift distance (~ 500 nm), respectively [339].

The obtained topography and phase images are analysed using Nova image processing software and tip shape de-convolution is performed before quantitative analyses of the topography images. **Fig. 2.4** shows a typical de-convoluted tip surface and the estimated

bending radius for a commercial silicon tip with a bending radius of 10 ± 1 nm. The estimated bending radius after de-convolution is found to be ~ 9 nm.

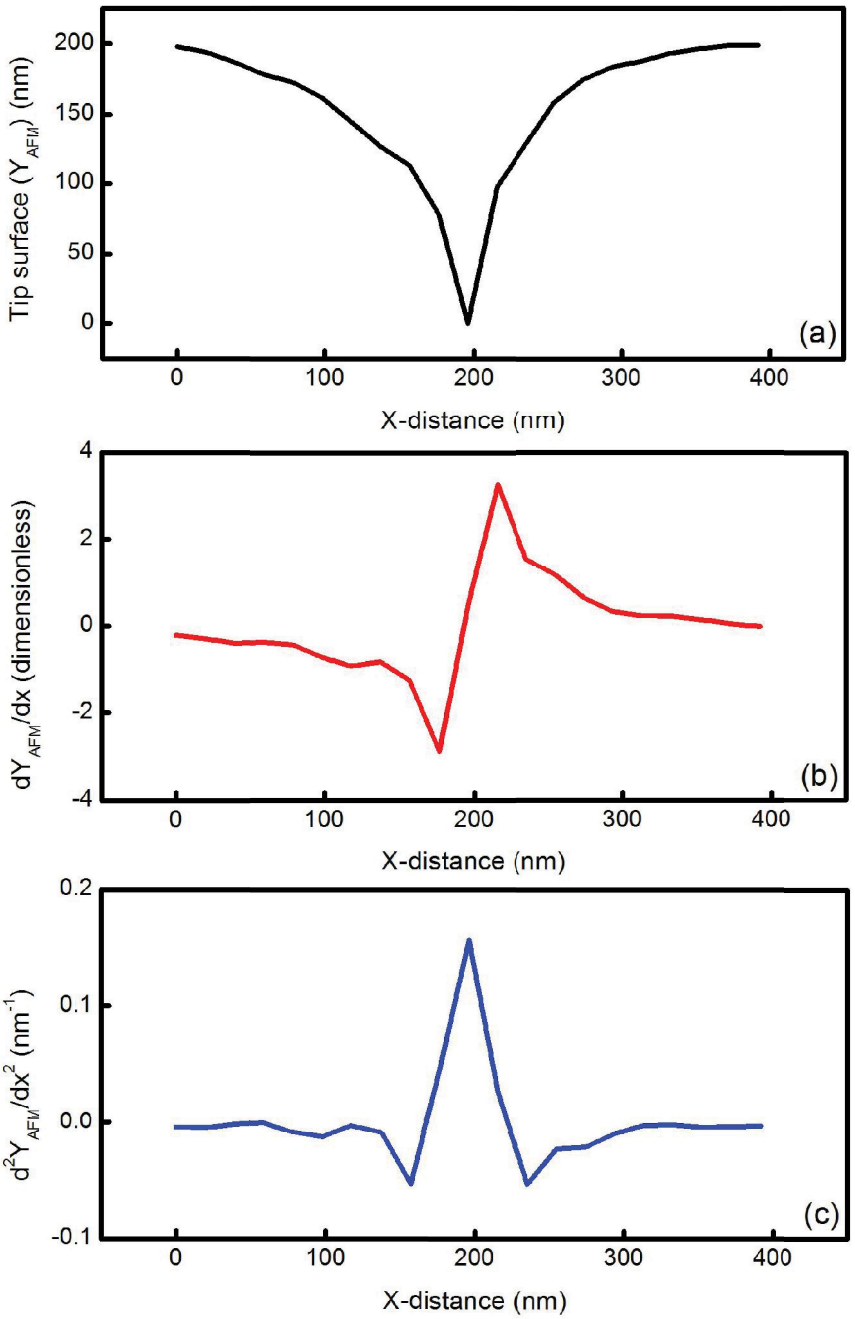


Figure 2.4: (a) AFM tip surface profile (Y_{AFM}), as a function of distance along X-axis, obtained after tip-shape de-convolution of typical topography images. (b) First order (dY_{AFM}/dx) and (c) second order (d^2Y_{AFM}/dx^2) derivatives of the tip surface profile with respect to the distance along X-axis. The bending radius ($r_{bending}$) is estimated using the formula: $r_{bending} = [\{1+(dY_{AFM}/dx)^2\}^{3/2}]/(d^2Y_{AFM}/dx^2)$.

2.3 Radio frequency induction heating system

A radio frequency (RF) induction system is used for exposing the magnetic fluids to a radio frequency alternating magnetic field (RF-AMF) for MFH studies. The induction heating system is equipped with a parallel resonance tank circuit driven by a solid state [metal-oxide-semiconductor field-effect transistor (MOSFET)] inverter and water cooled copper coils. The salient features of the induction heating system, heating coils and procedure for calculating magnetic field amplitudes are described below.

2.3.1 Parallel resonance tank circuit and heating coils

Parallel resonance occurs in an electrical circuit containing an inductive element in parallel to a capacitor element. Let us consider a resistance (R_p) in series with an inductance (L_p) and the L_p-R_p branch is in parallel to the capacitance (C_p). The resistance R_p accounts for the losses in the inductance, whereas, no such resistance is included in the capacitance branch as the resistive losses in capacitance are negligible. Let I_c and I_L indicate the phasors for current through the capacitance and inductance branches, respectively, whereas, I is the phasors for the total current. For small values of R_p, I_L and I_c are ~ 180^0 out-of-phase, as I_c leads the source voltage by 90^0 and I_L lags the source voltage by ~ 90^0. Using Kirchhoff's current law (KCL), the total current can be expressed as a sum of current through the inductor and capacitors, i.e., $I = I_L + I_c$. I_L and I_c can be expressed by the following set of equations [340].

$$I_L = \frac{V_{AC}}{R_p + i\omega_{AC} L_p} \tag{2.4a}$$

$$I_c = \frac{V_{AC}}{1/i\omega_{AC} c_p} = \mathrm{i}\omega_{AC}\mathrm{c_p V_{AC}} \tag{2.4b}$$

Hence, ω_{AC} is the circular frequency of the AC voltage (V_{AC}). The total impedance (Z_p) and admittance (Y_p), after rationalization, can be expressed by the following set of equations [340].

$$\frac{1}{Z_p} = \frac{1}{R_p + i\omega_{AC} L_p} + i\omega_{AC} c_p \tag{2.5a}$$

$$Y_p = \frac{1}{Z_p} = \frac{R_p + i(\omega_{AC} c_p R_p^2 + \omega_{AC}^3 L_p^2 c_p - \omega_{AC} L_p)}{R_p^2 + \omega_{AC}^2 L_p^2} \tag{2.5b}$$

The source current, I and source voltage, V_{AC} are in phase when the imaginary part of the admittance is zero, which is satisfied at resonance frequency (f_p) of the parallel resonance circuit and is expressed by the following equation [340].

$$f_p = \frac{\omega_p}{2\pi} = \frac{1}{2\pi}\sqrt{\frac{1}{L_p c_p} - \frac{R_p^2}{L_p^2}} \tag{2.6}$$

For small values of R_p, f_p is approximated as $f_p = \frac{1}{2\pi}\sqrt{\frac{1}{L_p c_p}}$ [340].

Parallel resonance circuits find numerous applications in constructions of radio receivers, tank circuits and electronic oscillators. The current circulating in a parallel resonance tank circuit is very large, i.e., Q_p times the supply current, where, Q_p is the ratio of capacitor current to the line current at resonance. Moreover, the factor, Q_p is also proportional to the ratio of maximum energy stored per cycle to energy dissipated per cycle in the parallel resonance tank circuit. As the circulating current is Q_p times higher than the supply current, parallel resonance tank circuits are ideal for radio frequency induction heating system, where a high value of coil current is desirable for generating large magnetic field amplitudes.

Induction heating system are, in general, built using two types of circuit topology, viz., voltage amplifier connected with a resonant circuit and using resonant inverters [341]. In the present study a high frequency induction heating system from Five Celes, France is used

which is built using a parallel resonant inverter topology. The salient features of the equipment are shown in **Table 2.1**.

Table 2.1: Salient features of the radio frequency induction heating system (Five Celes, France), used in the present study.

Parameters	**Values**
Input voltage	415 Volt (± 5 %)
Operating frequency range	100-400 KHz
Rated output power	12 kW
Type of control	Local, Remote (4-20 mA), programmable logic controller (PLC), Temperature feedback, recommended standard (RS)-432 communications
Other features	In-built PLC, proportional-integral-derivative (PID) controller Real time monitoring of current, voltage, power and frequency
In-built safety features	Power supply water failure Power module failure Capacitor box & Inductor water safety Power supply over temperature Output over current and output over voltage Output inductor short circuits

Figure 2.5 shows a schematic of the basic instrumentation of the induction heating system, where it can be seen that the major components of the system are radio frequency interference choke, radio frequency chopper, solid state (MOSFET) inverter and the parallel resonance tank circuit. **Fig. 2.5** also shows the schematic of the tank circuit, where it can be seen that four capacitor banks are in parallel to the heating coil, which acts as an inductor. The equivalent inductance and capacitance of the tank circuit are ~ 1.6 (± 5 %) μH and 1.32 (± 5 %) μF, respectively.

The parallel resonance tank circuit is equipped with water cooled (using a chiller unit) electrolytic copper coils of 50 mm diameter and 6 number of turns. **Fig. 2.6** shows typical photographs of the coil used in the present study. Salient features of the coil are indicated in **Table 2.2**.

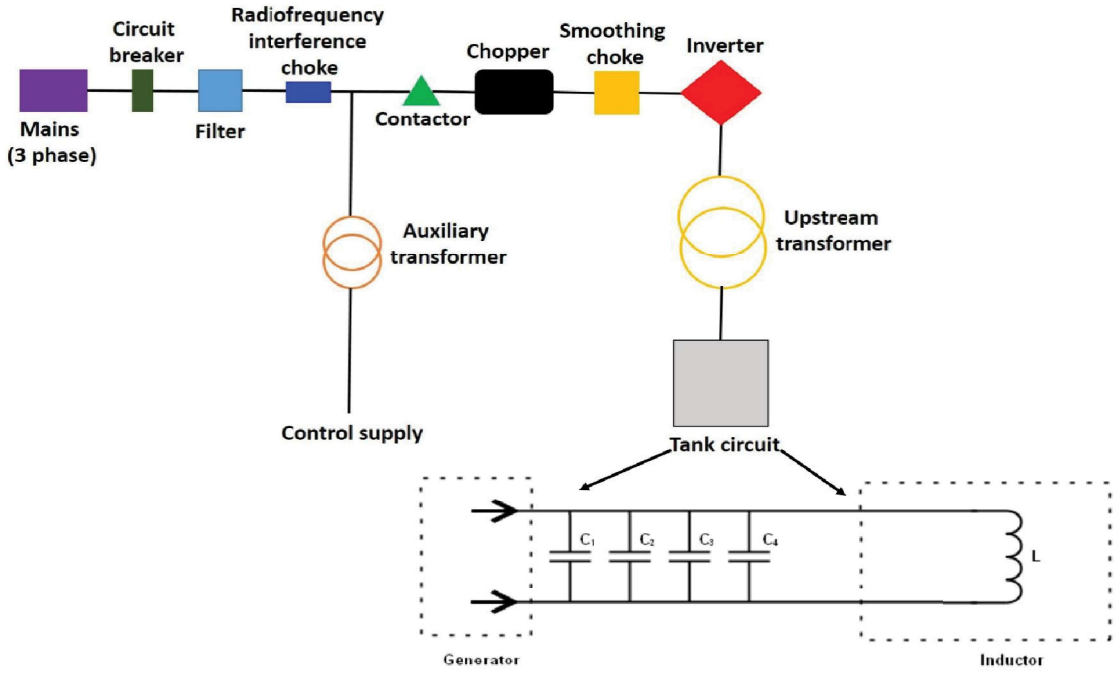


Figure 2.5: Schematic diagram of the radio frequency induction heating system, used in the present study, along with the essential components. The schematic diagram of the parallel resonance tank circuit is also shown, where, the heating coil acts as an inductor and the generator module indicates filters, chopper, inverter, auxiliary and upstream transformers.

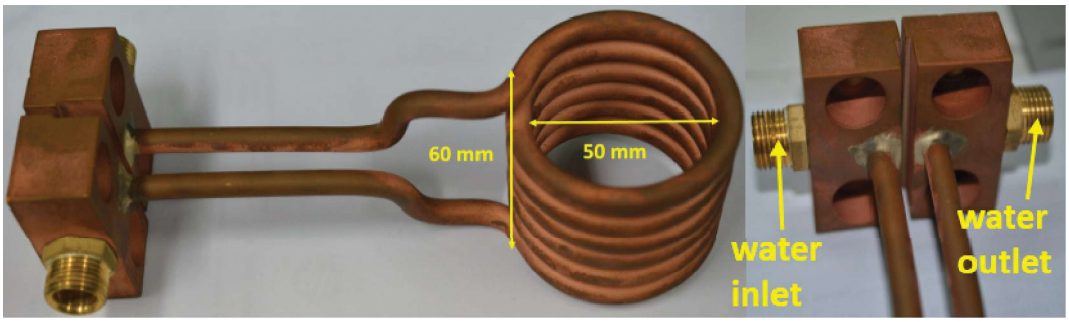


Figure 2.6: Typical photographs of the heating coil used. The diameter and height of the coil, along with water inlet and outlet, are indicated in the photographs.

Table 2.2: Salient features of the heating coil used in the present study.

Parameter	**Values**
Copper grade	Electrolytic copper
Inductance	1.6 (± 5 %) µH
Section	Rectangular tube
Type of cooling	Water forced
Geometry	Circular shape (diameter 50 mm), 6 number of turns

2.3.2 Calculation of magnetic field amplitudes

The magnetic induction at a generic off-axis point near a current carrying loop of radius, a_c, is calculated in cylindrical coordinate system (ρ, ϕ, z) using the following set of equations in terms of complete elliptical integrals [342, 343].

$$B_\rho = -\frac{\partial A_\phi}{\partial z} = \frac{\mu_0 I}{2\pi} \frac{z}{\rho[(a_c+\rho)^2+z^2]^{1/2}} [-K_{E1}(m_E) + \frac{a_c{}^2+\rho^2+z^2}{(a_c-\rho)^2+z^2} K_{E2}(m_E)] \quad (2.7a)$$

$$B_z = \frac{1}{\rho}\frac{\partial}{\partial \rho}(\rho A_\phi) = \frac{\mu_0 I}{2\pi} \frac{1}{[(a_c+\rho)^2+z^2]^{1/2}} [K_{E1}(m_E) + \frac{a_c{}^2-\rho^2-z^2}{(a_c-\rho)^2+z^2} K_{E2}(m_E)] \quad (2.7b)$$

$$B_\phi = \frac{\partial}{\partial z}(A_\rho) - \frac{\partial}{\partial \rho}(A_z) = 0 \quad (2.7c)$$

$$m_E = \frac{1-(1-\beta_E{}^2)^{1/2}}{1+(1-\beta_E{}^2)^{1/2}} \text{ and } \beta_E{}^2 = 4a_c\rho[(a_c+\rho)^2+z^2] \quad (2.7d)$$

Here, B_ρ, B_z, B_ϕ, A_ρ, A_z, A_ϕ, μ_0 and I indicate the ρ, z and ϕ components of magnetic induction and magnetic vector potential, magnetic permeability and current through the loop, respectively. K_{E1} and K_{E2} indicate complete elliptical integrals of first and second kinds, respectively. The numerical values of B_ρ and B_z can be computed for any values of ρ and z by evaluating β_E and m_E and finding the corresponding values of K_{E1} and K_{E2} from standard mathematical tables [344]. For an on-axis point, ρ = 0 = B_ρ (due to symmetry requirements as can be seen from the **inset of Fig. 2.7**) and B_z can be represented by the following simplified equation.

$$B_z = \frac{\mu_0 a_c{}^2 I}{2(z^2+a_c{}^2)^{3/2}} \quad (2.8)$$

For z = 0, i.e., at the centre of the current carrying coil, $B_z = \frac{\mu_0 I}{2a_c} = \frac{\mu_0 I}{d_{coil}}$, where, $d_{coil} = 2a_c$, is the diameter of the current carrying coil. For 6 number of turns, the total magnetic induction along z direction is $B_z = \frac{6\mu_0 I}{d_{coil}}$ and this equation is used for field calculation for varying coil

current in the present study (d_{coil} = 50 mm) [342, 345]. **Table 2.3** shows the calculated magnetic field values for a few cases. The magnetic field amplitude is found to increase linearly with reactive coil current and magnetic field amplitude is varied by suitably varying the coil current.

Table 2.3: Calculated magnetic field amplitudes as a function of coil current in a few cases.

Voltage (V)	Coil current (A)	Reflected direct current (A)	Calculated magnetic field amplitude (kAm^{-1})
457	477.5	6.8	57.3
410	428.4	6.1	51.4
359	375.1	5.3	45.0
293	306.2	4.3	36.7
207	216.3	3.0	26.0

Figure 2.7 shows the axial distribution of magnetic field (neglecting the radial variation) for each coil sections and the resultant magnetic field, where, the sample location is also highlighted. The sample is kept within ± 3.5 mm from the central location, where the axial variation in magnetic field is negligible, thereby, ensuring a homogenous magnetic field distribution inside the magnetic fluids. The sample location was optimized to reduce non-uniformity in magnetic field amplitude as specific absorption rate (SAR) varies significantly (SAR ~ H^2) due to the non-uniformity in magnetic field distribution due to the short length of the induction coil [342].

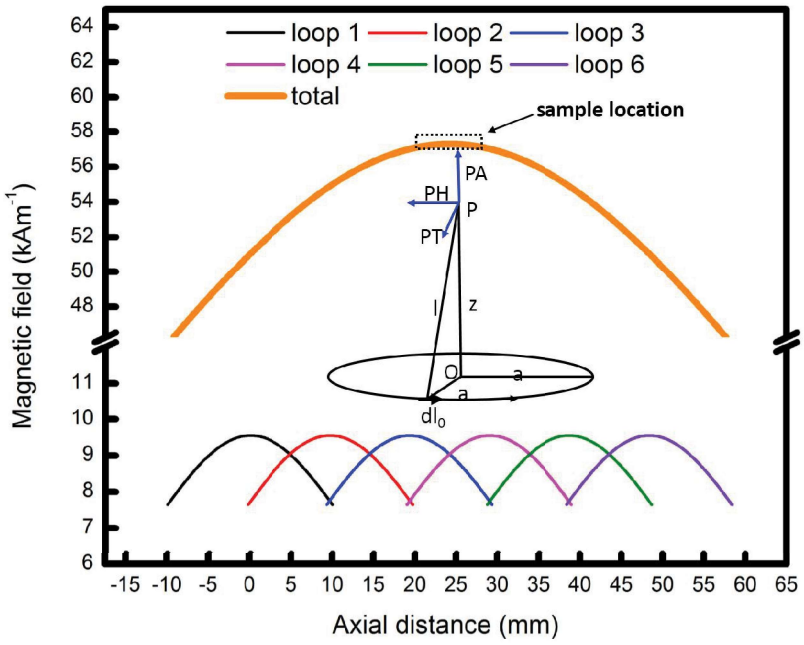


Figure 2.7: Axial distribution of magnetic field for a current (477.5 A) carrying coil with 6 number of turns. The sample is kept within ± 3.5 mm of the central location for ensuring minimum non-uniformity in field distribution. (Inset) Schematic illustration of the magnetic field at an on-axis point for a current carrying loop. The radial component (PT) cancels out due to circular symmetry of the on-axis point.

2.4 Sample temperature measurement during RF-AMF induced heating

Reliable estimation of SAR depends on the accurate measurement of temperature increase in magnetic nanofluids, as a function of time, during RF-AMF induced heating. The increase in sample temperature is measured at a single location using various techniques such as radio frequency (RF) immune fiber optic temperature sensor, infrared and liquid based thermometers, pyrometers and ultrasonic temperature sensors [345-348]. Though metallic thermometers are not suitable for temperature measurement under high frequency magnetic field, due to problems associated with self-heating by the induced eddy current, thin thermocouples have been used for measuring rise in sample temperature in MFH studies [348-350]. Recently, Skumiel et al. [348] have studied the usefulness and accuracy of pyrometer, thermocouples, fiber optic and ultrasonic temperature sensors during RF-AMF

induced heating of magnetic fluids and discussed the measurement errors associated with each type of sensors. Among the above mentioned techniques, RF immune fiber optic temperature sensor is the most popular contact type sensor due to its versatile applications (both *in vivo* and *in vitro*), ease of calibration and wide availability. Apart from contact type temperature measurement, infrared thermography (IRT) based non-contact temperature mapping is also used in the present study for temperature measurement. The basic working principles of these two techniques are discussed in the subsequent sections.

2.4.1 Fiber optic temperature sensor

Several types of fiber optic temperature sensor exist (like fluorescence based sensors [351], fiber Bragg grating sensors [352], chirped fiber Bragg grating sensors [353], Rayleigh scattering distributed sensors [354], Raman scattering distributed sensors [355], temperature dependent band gap type sensors [356], etc.), where, the basic working principle is based on change in optical properties of the sensor elements with change in temperature; for e.g., fluorescence lifetime, reflectivity due to change in grating periodicity, back scattering intensity, band gap, etc. [357]. In the present study, RF immune fiber optic temperature sensor from Osensa Innovation Corporation, Canada is used, which works on the principle of fluorescence lifetime measurement.

Fluorescence based fiber optic temperature sensors work on the principle of exponential decay of the fluorescence lifetime of phosphor type materials (like ruby, alexandrite, thulium or other rare-earth materials) [351, 358, 359]. **Fig.2.8** shows a schematic of a typical fluorescent lifetime based fiber optic temperature sensor. A square wave modulated light source, typically a light emitting diode (LED), is used to excite the fluorescent material, which is in contact with the object under investigation. A fast response photodiode is used for

measuring the fluorescence decay time and the time constant of exponential decay indicates the temperature of the object.

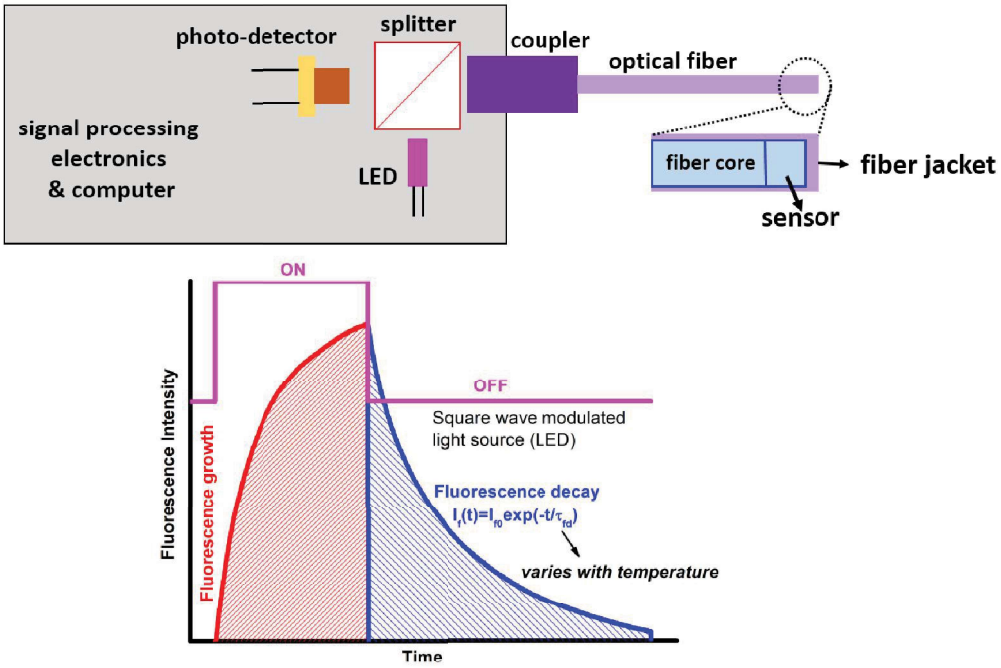


Figure 2.8: Schematic diagram of a typical fluorescence lifetime spectroscopy based fiber optic temperature sensor.

The decay in fluorescent intensity as a function of time can be expressed by the following equation [359].

$$I_f(t) = I_{f0}\exp(-\frac{t}{\tau_{fd}}) \tag{2.9}$$

Here $I_f(t)$, I_{f0} and τ_{fd} indicate fluorescence intensity at time t, initial fluorescence intensity (at time t = 0 upon excitation) and fluorescence decay life time, respectively. Fluorescence life time is defined as the time required for the intensity to drop to ~ 37 % of the initial intensity and is expressed in terms of decay rate constant (κ_f), using the following equation [359].

$$\kappa_f = \frac{1}{\tau_{fd}} = \kappa_{rad} + \kappa_{non-rad} = \frac{1}{\tau_{0\,fd}} + \kappa_{non-rad} \tag{2.10}$$

Here, κ_{rad}, $\kappa_{non\text{-}rad}$ and τ_{0fd} indicate radiative and non-radiative decay constants and the low temperature value of the fluorescence lifetime before quenching temperature, respectively [359]. The temperature dependence of the non-radiative quenching component can be expressed in terms of Boltzmann's statistics involving the relative population of the vibration states and according to Fonger and Struck model the following equation is obtained for the fluorescence life time [360].

$$\kappa_f = \frac{1}{\tau_{fd}} = \frac{1}{\tau_{0\,fd}} + A_f e^{-\frac{E_{CTS}}{k_B T}} \text{ or } \tau_{fd} = \frac{\tau_{0\,fd}}{[1 + \tau_{0\,fd} A_f e^{-\frac{E_{CTS}}{k_B T}}]} \tag{2.11}$$

Here, A_f is a material dependent constant and E_{CTS} indicate the energy of charge transfer states (CTS) [360]. The object temperature is measured by monitoring the changes in the fluorescence life time and using a suitable calibration chart. **Table 2.4** shows the salient features of the fiber optic temperature sensor used in the present study and **Fig. 2.9** shows a typical photograph of the same.

Table 2.4: Salient features of the fiber optic temperature sensor used in the present study.

Parameters	**Values**
Type	Fluorescence
Light source	Light emitting diode (LED)
Light source modulation	Square wave type
Temperature range	-40-100 ^{0}C
Shield material	Poly methyl methacrylate (PMMA)
Power supply	± 15 V, 50 W, SMPS (switched-mode power supply)
Signal conditioner output	Analogue: 4-20 mA, 16 bit digital
Resolution	0.01 ^{0}C
Accuracy	± 0.1 ^{0}C (typical standard deviation)
Update	10-1000 Hz (dynamic)
Connection	Universal serial bus (USB) 2.0

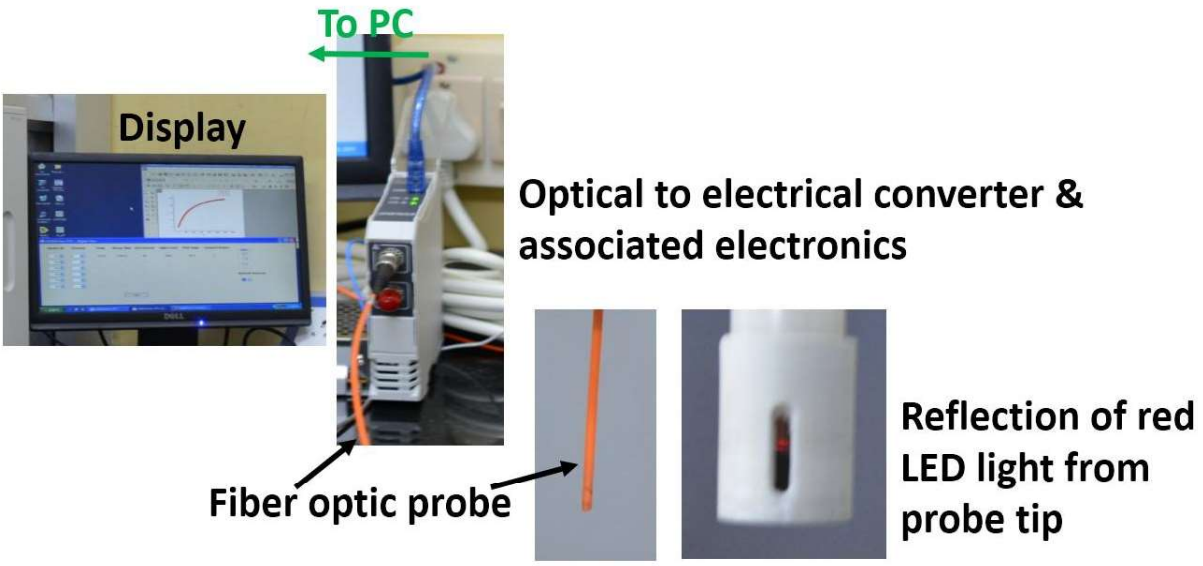


Figure 2.9: Typical photograph of the fiber optic temperature sensor (Osensa Innovations Corp., Canada) used in the present study.

2.4.2 Infrared thermography

Infrared thermography (IRT) is a non-contact temperature measurement methodology, where, the electromagnetic radiation emitted by the surface of an object under observation is detected using a suitable infrared detector and surface temperature of the object is obtained from the intensity of the radiation [361]. The infrared radiation (wavelength ranging from 0.75-1000 μm) lies in between the microwave and visible regions of the electromagnetic spectrum. This vast range is further subdivided into three categories, viz., far infrared or FIR (wavelength range: 5.6-1000 μm), medium infrared or MIR (wavelength range: 1.5-5.6 μm) and near infrared or NIR (wavelength range: 0.75-1.5 μm). Though the theoretical understanding about IRT was available from 1800, it took nearly 150-200 years for the technique to be available for routine use, due to lack of proper equipment and technical knowhow [362].

Blackbody is a hypothetical object, which absorbs all radiation incident on it and emits a continuous spectrum characteristic of its temperature and this continuous spectrum is governed by the well-known Planck's law and is expressed by the following equation [361].

$$L_\lambda = \frac{C_1}{\lambda^5[\exp(\frac{C_2}{\lambda T}) - 1]} \tag{2.12}$$

Here, λ is the wavelength (μm), L_λ is the power radiated by the blackbody per unit surface and per unit solid angle ($Wm^{-2}\mu m^{-1}sr^{-1}$), T is the temperature of the blackbody in absolute scale (K), C_1 and C_2 are the first and second radiation constants, respectively. Integrating Planck's law over all wavelength leads to the Stefan-Boltzmann's law which shows that the radiative power emitted per unit area is directly proportional to T^4 [361].

$$\frac{q_{IRT}}{A_{IRT}} = \sigma_{SB} T^4 \tag{2.13}$$

Here, q_{IRT} is the rate of energy emission (W), A_{IRT} is the area of the emitting surface (m^2) and σ_{SB} is the Stefan-Boltzmann's constant (σ_{SB} = 5.676×10-8 $Wm^{-2}K^{-4}$). For a real object, the Stefan-Boltzmann's law is modified as $\frac{q_{IRT}}{A_{IRT}} = \varepsilon_{IRT}\sigma_{SB}T^4$, where the parameter ε_{IRT} is known as emissivity, which is defined as the ratio of spectral power radiated by a real surface at a particular temperature to that of a hypothetical blackbody maintained at the same temperature. For a hypothetical blackbody, ε_{IRT} = 1 and for real surfaces, ε_{IRT}<1 [361]. The total thermal radiance received by the camera is from three independent sources, viz., radiance emitted from the object under investigation, reflected radiance from the object surface and self-radiance emitted from the atmosphere. Moreover, the presence of atmosphere attenuate the thermal radiances from all the three sources before detection by the infrared camera. **Fig. 2.10** schematically illustrates the situation and temperature of the object

under investigation is measured by the infrared camera using the following radiometric equation [361].

$$M_{cam} = \tau_{atm}\varepsilon_{IRT}M_{obj} + \tau_{atm}(1-\varepsilon_{IRT})M_{env} + (1-\tau_{atm})M_{atm} \quad (2.14)$$

Here, M_{cam} is the radiance received by the infrared camera. M_{obj}, M_{env} and M_{atm} are the radiance emitted by the surface of the object under investigation, surrounding environment and atmosphere, respectively. ε_{IRT} and τ_{atm} are the surface emissivity of the object under investigation and atmospheric transmittance, respectively.

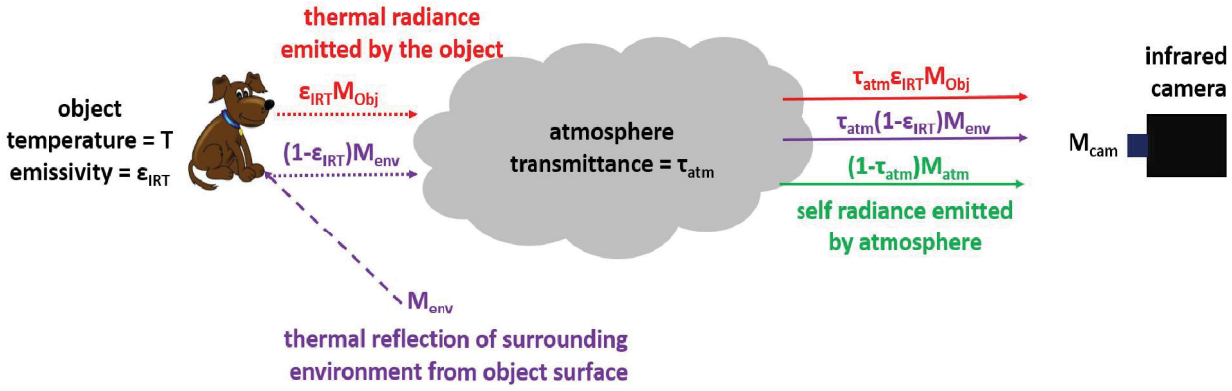


Figure 2.10: Schematic illustration of the total radiance received by an infrared camera.

Considering atmospheric transmittance to be nearly equal to unity for indoor measurements, Eq. 2.14 can be simplified to $M_{cam} = \varepsilon_{IRT}M_{obj} + (1-\varepsilon_{IRT})M_{env}$. Radiance received by the infrared camera is converted to an electrical signal by the infrared detector housed inside a camera casing and surface temperature of the object under investigation is obtained using suitable calibration curves [361]. Modern day infrared cameras have on-board image processing capabilities and show the surface temperature distribution as visual images, which

are pseudo colour coded, where, each pseudo colour indicates a range of temperature that aides in online visualization and faster analysis.

In the present study, FLIR SC 5000 series infrared camera is used for non-contact mapping of surface temperature during RF-AMF induced heating. This camera is equipped with an indium antimonide (InSb) based focal plane array detector with 320 × 256 elements. The detector elements are cooled using a Stirling cycle and the spectral range of the camera is 2.0-5.1 μm. Salient features of the camera is shown in **Table 2.5**. The camera is placed perpendicularly to the sample surface to avoid viewing angle error and the distance between the camera and the sample is maintained at 0.5 m for all cases. A 27 mm germanium made infrared transparent lens, with a field of view of $20^0 \times 16^0$, is used in the present study. At a distance of 0.5 m, the horizontal and vertical spatial resolutions of the recorded infrared images are found to be 0.69 and 0.44 mm/pixel, respectively. In the present study, for recording the infrared images, the value of atmospheric transmittance is considered as 1.0. On the other hand, the values of the surface emissivity and reflected background temperature are considered as (0.92 and 28.38 ^{0}C); (0.98 and 28.41 ^{0}C) and (0.96 and 28.46 ^{0}C) for oil based, water based and agar based samples, respectively. It has been reported that the emissivity of human skin is ~ 0.98 ± 0.01 in the wavelength range of 2-14 μm and does not vary with the colour or texture of the skin or the nature of experiments, i.e., *in vivo* or *in vitro* [363]. The acquired infrared images are later analysed using Altair software. The room temperature is kept constant at 28 (±1) ^{0}C throughout the experiments. Before applying the RF-AMF, the sample temperature is measured for 100 s to check thermal stability. **Fig. 2.11** shows a photograph of the experimental set-up, where, the RF induction heating system, heating coils, fiber optic temperature sensor and infrared camera are shown.

Table 2.5: Salient features of FLIR SC 5000 series infrared camera.

Parameters	**Values**
Detector	Indium Antimonide (InSb)
Spectral range	2.0-5.1µm
Resolution & pixel pitch	320×256 pixels and 30×30 µm
Temperature range	5-300 ^{0}C (standard) and 5-1500 ^{0}C (high temperature: additional)
Noise equivalent temperature difference (NETD)	<25 mk (20 mK typical) @ 25 ^{0}C
Sensor cooling	Stirling closed cycle cooler
f/# and input voltage	f/3.0 and 12 V (DC)
Integration time (electronic shutter speed)	3 µs to 20 ms
Read-out mode	Asynchronous integrate then read
Dynamic range and detector well capacity	14 bit and 7.1 M electrons

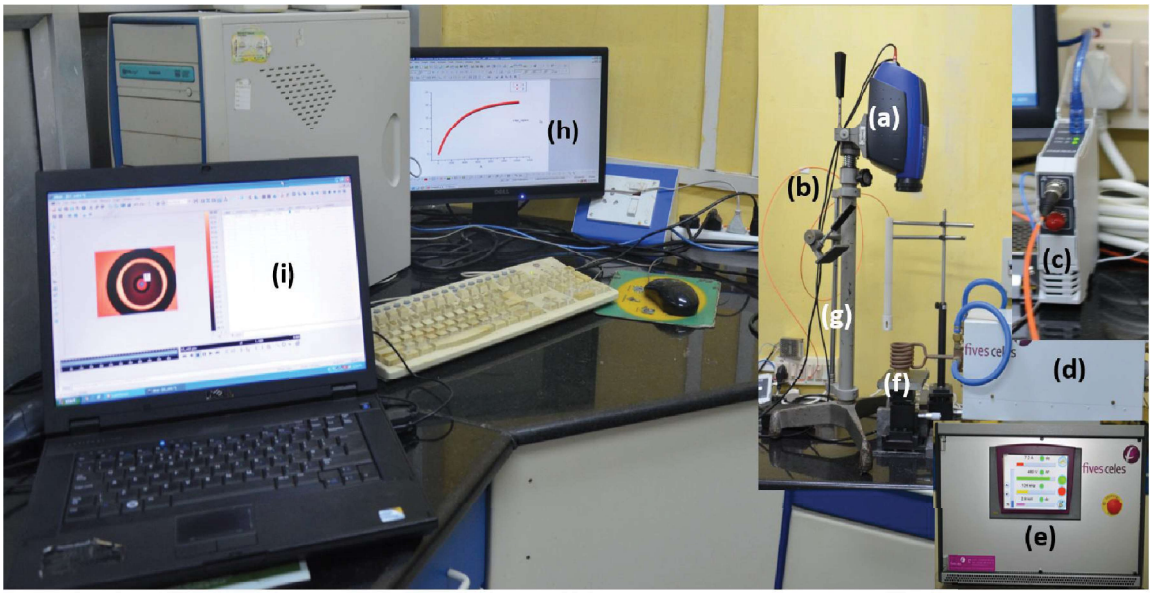


Figure 2.11: Typical photograph of the RF induction heating system used for magnetic fluid hyperthermia experiments. (a) Infrared camera, (b) fiber optic temperature sensor, (c) optical to electrical signal converter, (d) resonator tank, (e) high frequency generator, (f) heating coil, (g) tripod stand for infrared camera, (h-i) data, from fiber optic temperature senor and infrared camera, respectively, displayed on personal computer. The sample is placed at the centre of the heating coil.

IRT is routinely used for non-destructive evaluation, condition monitoring [361, 364, 365] and in the rapidly developing field of medical thermography [366-369]. Of late, IRT has also

found applications in the field of magnetic fluid hyperthermia. Boldor et al. [370] used IRT for measuring average temperature rise of multi-walled carbon nanotubes during selective photo-thermal hyperthermia using a near infrared laser radiation, where the samples were placed on a custom made brass stage and then irradiated with laser. Levy et al. [371] studied temperature evolution as a function of time in tumor phantoms during MFH using IRT. In this study the magnetic nanofluid sample was injected inside a tumor phantom and surface temperature was measured using IRT. Thereafter, heat conduction model was used to estimate the RF-AMF induced temperature rise in the magnetic nanofluid. Rodrigues et al. [372] used real time IRT for temperature measurement in murine models during MFH studies using citrate coated manganese ferrite samples and non-uniform field distribution, where the skin surface temperature was measured using IRT and later compared with intra-tumor temperature measured using a fiber optic sensor. Wildeboer et al. [297] studied the temperature distribution of a liquid sample placed inside a conical Eppendorf tube and flat bottom glass vial, where, the surface temperature of the sample holders was measured using IRT. Kim et al. [373] used lock-in micro-thermography for measuring thermal properties of MNP in polyacrylamide and agarose phantoms.

In all of the previous studies, IRT was used to measure temperature rise on surfaces and not directly on the magnetic nanofluid sample. In the present study, IRT is used to directly measure the fluid temperature during RF-AMF induced heating and a data analysis protocol is developed for incorporating external and internal convection corrections on the temperature rise curves measured using IRT for obtaining the exact sample temperature, which is further discussed in chapter 3.

2.5 Protocols for SAR measurement

Three different experimental techniques exist for calculating SAR of magnetic fluids, viz., dynamic hysteresis loop measurement, AC susceptibility measurement and calorimetric measurements [374, 375]. In dynamic hysteresis loop based measurements, the delay in magnetization with respect to the applied magnetic field is measured using a suitable instrument [in general, a vibrating sample magnetometer (VSM) or superconducting quantum interference device (SQUID)] [374] in quasistatic limit, i.e., the frequency of the applied magnetic field is significantly lower than that used for typical MFH applications. This technique is not suitable for superparamagnetic nanoparticles at room temperature due to thermally activated relaxation mechanisms. Apart from a few customized systems [376-378], there exist no commercially available systems for performing high frequency hysteresis measurements, which warrants data extrapolation that is often inaccurate due to inherent non-linearly of the magnetization dynamics. On the other hand, for AC susceptibility measurements, though several high frequency systems are available [376, 379, 380] the limiting factor is the applied magnetic field amplitude, which is often limited to < 0.5 kA/m and hence, requires data extrapolation at higher field amplitudes, leading to possible inaccuracies [374]. Though better systems are being developed [376], the uncertainties in both the above mentioned magnetic measurement techniques make the traditional calorimetric measurements the most widely used and universally accepted experimental technique for SAR determination using the initial rate of temperature rise under non adiabatic limit (using Eq. 1.19 in chapter 1).

Various techniques have been used for determining the initial rate of temperature rise during RF-AMF induced heating of magnetic fluids, which can be divided into two categories, viz., steady state and transient methods. Steady state methods make use of maximum temperature rise (ΔT_{max}) and time constant of temperature decay under isoperibol (the measurement set-

up is at constant temperature) conditions, where, SAR is calculated using an equation of the form: $SAR = \frac{c_{samp}\rho_{samp}}{m_{Fe}}\frac{\Delta T_{\max}}{\tau}$ and the values of ΔT_{max} and τ are obtained from exponential regression analyses of the experimental data [89, 379, 381, 382]. Pulsed heating method is yet another steady state method of SAR quantification, where, the equilibrium trend in temperature rise of the magnetic fluids between two consecutive RF-AMF pulses are measured (in general, using extrapolation techniques) [374, 383].

On the other hand, transient techniques are more popular due to easier data analyses and faster calculations during the transient regime without the requirement of establishing a steady state temperature of the sample. Among the various transient techniques, three different numerical methods for determining the initial rate of temperature rise have been widely reported in literature [89, 242, 384-386]. The first two of them, viz., phenomenological Box-Lucas [89, 123, 125] and exponential temperature rise [385] equations, rely on indirect methods of data fitting. The third one is a direct rate determination method using the slope of the linear regression analysis of the initial data set [242, 258, 384, 386]. The Box-Lucas and the exponential equations are described in Eqs. 2.15 and 2.16, respectively.

$$T(t) = m_{BL}(1 - e^{-n_{BL}t}) \quad \text{hence,} \left.\frac{dT}{dt}\right|_{t=0} = m_{BL}n_{BL} \tag{2.15}$$

$$T(t) = T_{0\exp} + M_{\exp}e^{\frac{t}{N_{\exp}}} \quad \text{hence,} \left.\frac{dT}{dt}\right|_{t=0} = \frac{M_{\exp}}{N_{\exp}} \tag{2.16}$$

Here, T is the time (t) dependent sample temperature and m_{BL}, n_{BL}, T_{0exp}, M_{exp} and N_{exp} are numerical constants, respectively. Box-Lucas and exponential temperature rise methods are whole field techniques, which also take into account the temperature losses due to convection at larger time scales leading to lower values of initial rate of temperature rise as compared to

the linear regression based analyses. **Fig. 2.12** illustrates the three methods for determining initial rate of temperature rise for a typical temperature rise curve during RF-AMF induced heating of a water based ferrofluid containing phosphate coated Fe_3O_4 MNP (concentration ~ 1.5 wt. %) at an external magnetic field amplitude of 57.3 kAm^{-1}. It can be seen from **Fig. 2.12** that the initial rates determined from the three techniques were similar. Nevertheless, the initial rates determined from the whole field methods were slightly lower as compared to the linear regression analysis due to losses. Variation in the range of linear regression analysis also leads to considerable uncertainties in SAR values which is discussed in section 2.6.2. In the present study, linear regression analysis and Box-Lucas methods were used for determining initial rates of temperature rise which were then used for SAR calculations.

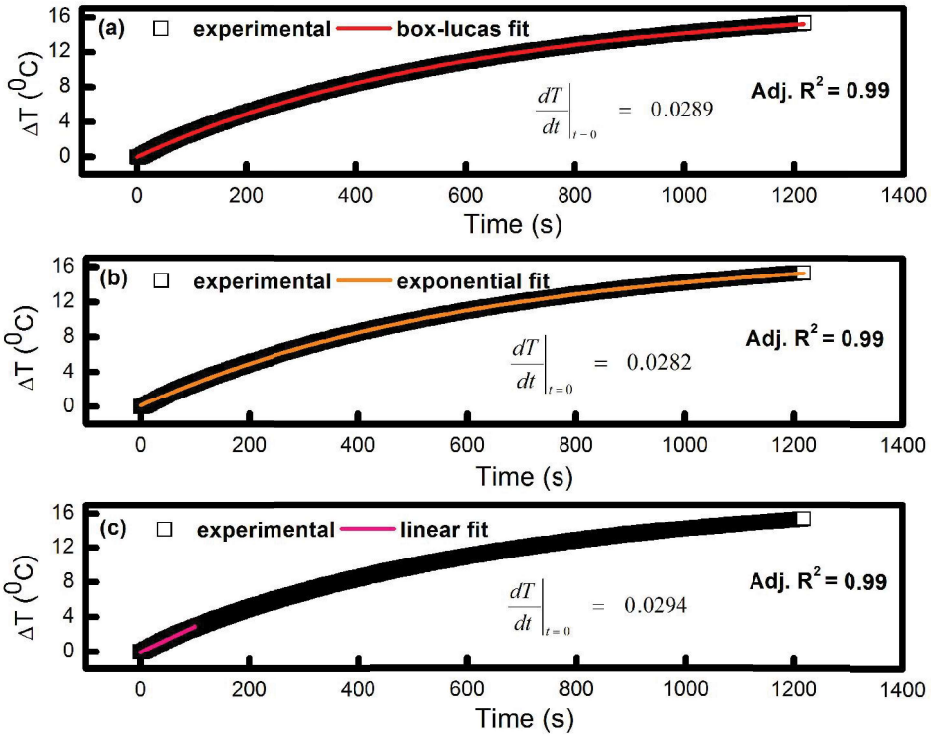


Figure 2.12: Illustration of the three numerical techniques, viz., (a) Box-Lucas, (b) exponential regression and (c) linear regression of the initial data, used for determination of the initial rates of temperature rise under non-adiabatic limit, during RF-AMF induced heating (H = 57.3 kAm^{-1}) in a water based ferrofluid contacting 1.5 wt. % phosphate coated Fe_3O_4 MNP. The values of initial rate and adjusted R^2 are also shown in the corresponding figures.

2.6 Uncertainties in SAR measurement

For safe, well tolerated and effective MFH based cancer treatment, robust, accurate and reliable estimation of heating efficiency of the magnetic fluids is a prerequisite [297]. For accurate determination of SAR using calorimetric measurements, at least from a theoretical point of view, an adiabatic experimental set-up is an absolute necessity [350], though it is seldom the case in practical applications [297]. Such adiabatic measurement systems are extremely complicated to build and the experiments are time consuming, apart from the necessity of a comparably large sample volume [89, 350, 374, 383]. Though the above issues have been circumvented with an adiabatic experimental set-up developed by Natividad et al. [350], as of now, such adiabatic systems (with vacuum and active adiabatic shielding) are expensive and not commercially available. As majority of the experimental studies on magnetic fluids for MFH applications are reported on calorimetric SAR determination, performed under non-adiabatic experimental conditions, a proper understanding of the uncertainties involved in such non-adiabatic measurements is very important. Based on the earlier studies by Andreu and Natividad [374], Wildeboer et al. [297], Huang et al. [342] and Wang et al. [387], the uncertainties in SAR measurement using a non-adiabatic experimental set-up are found to be due to various reasons ranging from inaccurate material properties to non-adiabatic heat losses and can be broadly classified into three categories, viz., i) material uncertainties, ii) thermodynamic uncertainties and iii) parametric uncertainties. **Fig. 2.13** schematically shows the three categories of uncertainties along with the probable causes and possible solutions. The material properties incorporate universal uncertainties in SAR, i.e., with or without adiabatic experimental set-up and hence, are categorized as level-1 uncertainties in **Fig. 2.13**, which can be minimized by accurate determination of these parameters. The parametric uncertainties are categorized as level-3 in **Fig. 2.13**, as they are due to a combination of inaccurate measurements of field amplitude and frequency and

wrong interpretations (extension of linear response theory beyond its validity, see section 1.7 in chapter 1 for details) and are present in calorimetric as well as magnetic measurements. On the other hand, thermodynamic uncertainties are due to non-adiabatic nature of the experimental set-up and there are various sources of thermodynamic uncertainties consisting of, but not limited to, peripheral heating, delayed heating, heat loss to the sample holder, spatial variation of sample temperature due to difference in probe position and heat loss to surrounding depending on the volume to surface area ratio of the magnetic fluids. Thermodynamic uncertainties are categorized as level-2 uncertainties, as they are only valid for calorimetric SAR measurements using a non-adiabatic experimental set-up and contribute most significantly to the errors associated with the measured SAR values.

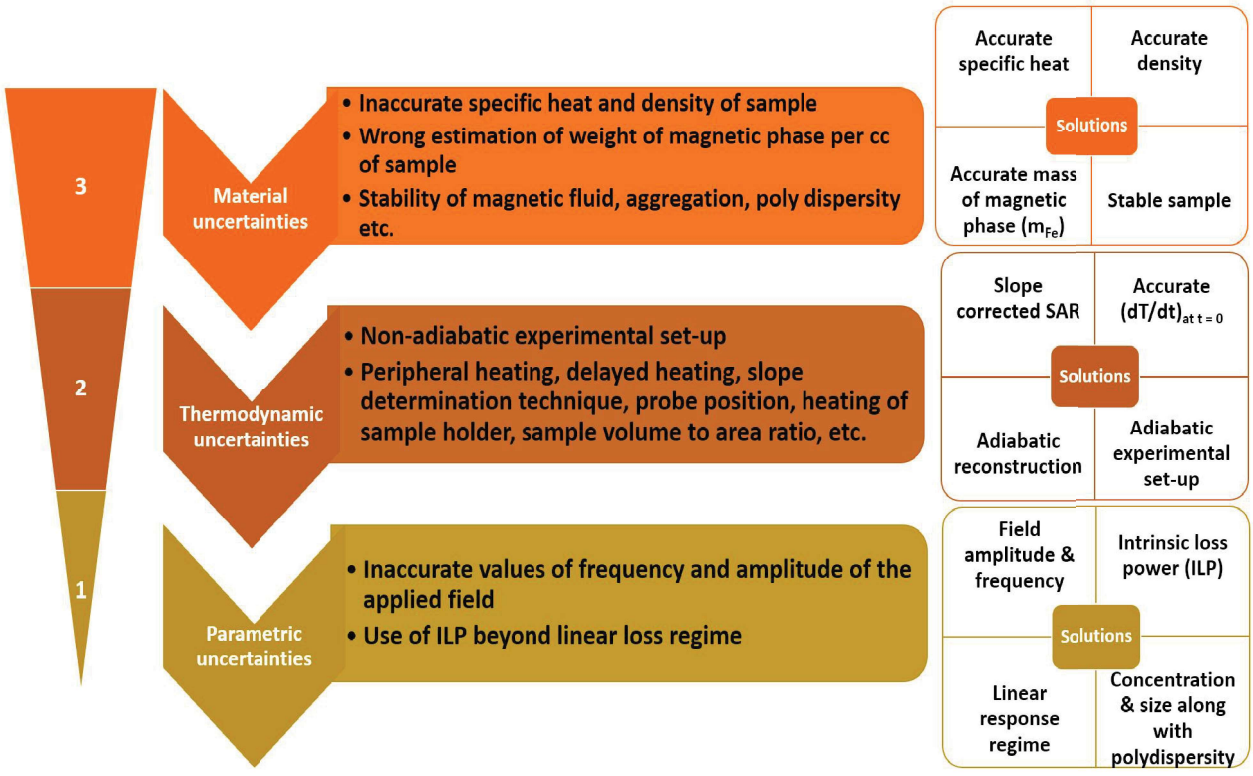


Figure 2.13: Schematic classification of various types of uncertainties involved in SAR estimation during RF-AMF induced heating. The major reasons behind each type of uncertainty and the probable solutions are also outlined.

2.6.1 Peripheral heating

The peripheral heating in non-adiabatic SAR measurements is due to heating of the base fluid (without any dispersed magnetic nanoparticles) inside the heating coil, where, the heating is reported to be due to a combination of induced eddy current and radiated heat from the coils [297]. To study the effects of eddy current induced heating, experiments were performed on four different base fluids, viz., kerosene (non-polar), hexadecane (non-polar), ethylene glycol (polar) and water (polar). **Fig. 2.14a** shows the variation of temperature rise (ΔT) as a function of time during RF-AMF induced heating of the different base fluids under an applied field amplitude of 63.0 kAm^{-1}. It was observed that the temperature rise was similar in all four fluids and the maximum temperature rise at the end of heating phase (t = 720 s) were ~ 3.42 (± 0.2), 3.32 (± 0.1), 3.11 (± 0.2) and 3.02 (± 0.1) ^0C for kerosene, hexadecane, ethylene glycol and water, respectively. As the temperature rise of the polar and non-polar fluids were essentially overlapping and maximum temperature rise were also similar, it was clear that induced eddy current heating had negligible effects on peripheral heating and hence, peripheral heating was predominantly due to radiated heat transfer from the coils.

The radiated heat flux ($\dot{q}_{rad}$) received by the fluid can be approximated as $\dot{q}_{rad} = \varepsilon_{coil}\sigma_{SB}A_{coil}(T_{coil} - T_{fluid})^4$, where ε_{coil}, σ_{SB}, A_{coil}, T_{coil} and T_{fluid} indicate coil surface emissivity, Stefan Boltzmann's constant, area, coil temperature and temperature of the fluid, respectively. The radiated heat flux is absorbed by the fluid leading to a rise in fluid temperature and under first order approximation, the following equation is proposed, where t-on and t-off indicate the time at which the RF-AMF is switched on and off, respectively.

$$\int_{t-on}^{t-off} \rho c V_{samp} \frac{dT}{dt} dt = \varepsilon_{coil}\sigma_{SB}A_{coil}(T_{coil} - T_{fluid})^4 \tag{2.17}$$

Here, ρ, c, V_{samp} and ΔT_{max} indicate the density, specific heat, volume and maximum temperature rise of the fluid, respectively. Neglecting the reduction in radiant heat flux with

increasing fluid temperature under first order approximation, it is evident from Eq. 2.17 that $\Delta T_{\max} \approx \frac{\varepsilon_{coil}\sigma_{SB}A_{coil}(T_{coil}-T_{fluid})^4}{\rho c V_{samp}}$, i.e., the maximum temperature rise is linearly proportional to the inverse of the product of density and specific heat for constant volume (750 µl in the present case) of the fluid.

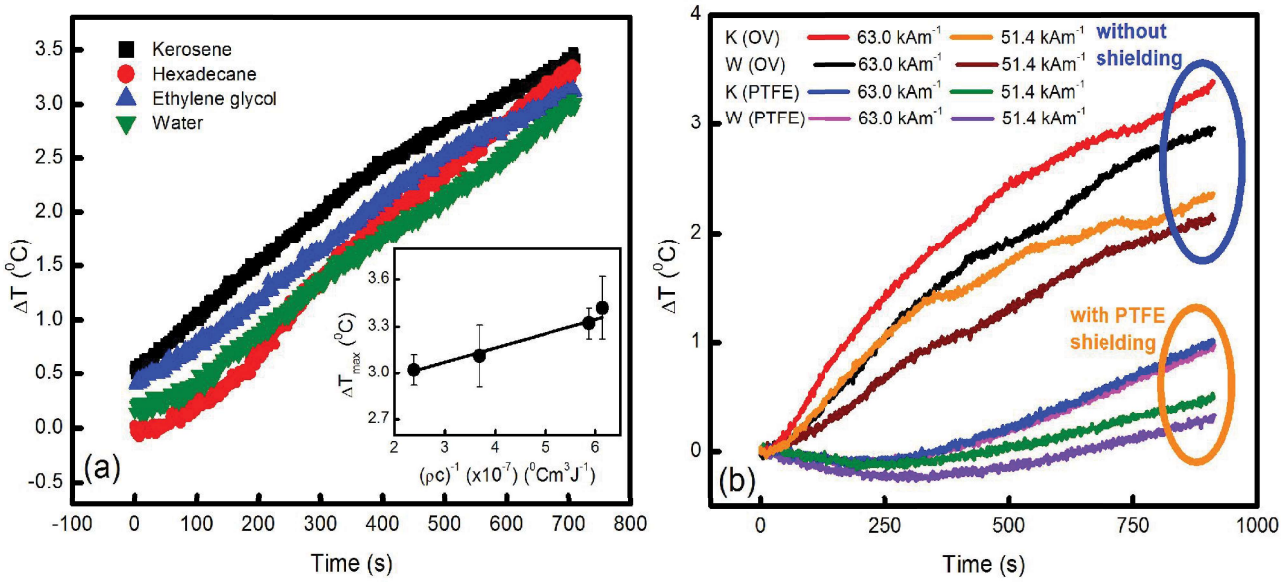


Figure 2.14: (a) Temperature rise (ΔT) as a function of time during RF-AMF induced heating of four different base fluids (without any magnetic nanoparticles), viz., kerosene, hexadecane, ethylene glycol and water. (Inset) Maximum temperature rise (ΔT_{max}) as a function of $(\rho c)^{-1}$ for the base fluids. The adjusted R^2 and slope of the linear regression analysis are ~ 0.97 and 0.09 ± 0.01 Jm^{-3}, respectively. (b) ΔT as a function of time for the base fluids (water and kerosene) with and without PTFE shielding surrounding the sample holder, during RF-AMF induced heating under external field amplitudes of 63.0 and 51.4 kAm^{-1}. The maximum temperature rise with and without PTFE shielding are encircled in orange and blue, respectively.

The **inset of Fig. 2.14a** shows the variation of ΔT_{max} as a function of $(\rho c)^{-1}$ and it can be seen that ΔT_{max} linearly increased with $(\rho c)^{-1}$. Further experiments were performed to analyse the peripheral heating with and without a polytetrafluoroethylene (PTFE) or Teflon (diamagnetic, $\chi \sim -10.25\times10^{-6}$ SI [388]) shielding around the glass-made sample holders with kerosene and

water. **Fig. 2.14b** shows the variation of ΔT, as a function of time, for both the cases with applied field amplitudes of 63.0 and 51.4 kAm^{-1}. It can be clearly seen that with PTFE shielding of the sample holder, ΔT_{max} decreased from 2.96 (± 0.3) to 0.96 (± 0.2) ^0C and 3.39 (± 0.4) to 1.01 (± 0.1) ^0C for water and kerosene, respectively for an applied field amplitude of 63.0 kAm^{-1}. In the absence of PTFE shielding, the radiant flux is completely absorbed by the base fluids leading to a substantial rise in fluid temperature during RF-AMF induced heating. On the other hand, in the presence of PTFE shielding, significant portion of the radiant heat is shielded by PTFE and hence, lower amount of the radiant heat flux reaches the base fluid leading to insignificant peripheral heating.

These experimental findings and theoretical analyses clearly prove that the cause of the peripheral heating is due to external radiant heat flux from the coils that can be significantly reduced by using a non-conducting and non-magnetic shielding around the sample holder.

2.6.2 Delayed heating and initial rate determination methodology

In majority of the MFH experiments, it is observed that there exists a time gap between applying the RF-AMF and the temperature rise of the magnetic nanofluids, which is known as delayed heating. In literature, three possible sources of delayed heating has been identified, viz., time constant associated with the induction heating system (i.e., the delay in establishing the required RF-AMF from the time of switching on the instrument), time associated with the thermal processes in the fluid (heat diffusion or convection) and response time of temperature measurement probe [297, 342, 387]. To further analyse the reasons behind the observed delayed heating, experiments were performed on water and kerosene based magnetic fluids of various sample concentrations under different magnetic field amplitudes using a conventional fiber optic temperature sensor and infrared thermography (IRT). **Figs. 2.15a-b** show the initial variation of ΔT (up to t = 10 s), as a function of time, for water (MNP concentration =

8 wt. %) and kerosene (MNP concentration = 23 wt. %) based samples for H = 63.0 and 57.3 kAm^{-1}, respectively. It can be observed that the fiber-optic sensor based data showed a delayed response (~ 3 s delay), whereas, no such delay was observed from the IRT based data. This clearly shows that the delayed heating is not due to time constant of induction heating system as the probe based and IRT based data were recorded using the same instrument. The 3 s delay in probe based measurements, observed in both water and kerosene based magnetic fluids, further rules out the possibility of delayed response due to thermal processes in the sample, as kerosene and water have widely varying thermal diffusivity (thermal diffusivity of water and kerosene are ~ 1.43×10^{-7} and 7.9×10^{-8} m^2s^{-1}, respectively) and Prandtl number (Prandtl number for water and kerosene varies between 1-10 (typical 7.56) and 18.3-25.7, respectively). These experimental findings clearly confirm that the delayed heating is predominantly due to the slower response time of the fiber optic temperature sensor. The average delay time (for probe based data) observed in the present case was ~ 3.1 ± 0.1 s (from 132 measurements).

To further analyse the response time of the fiber optic temperature sensor, a quadratic calibration curve (from scaling analysis of Fourier heat equation it can be shown that the square of distance is directly proportional to the product of thermal diffusivity and time) was drawn with known values of the response time and probe diameter as shown in **Fig. 2.15c**. Using the calibration curve, typical response time of the probe, used in the present study (diameter ~ 2100 ± 100 μm), was estimated as ~ 3.4 ± 0.4 s, which was found to be in very good agreement with the experimentally measured average delay time of 3.1 ± 0.1 s. This clearly shows that the finite time required for the heat wave to reach the core of the fiber optic temperature sensor is responsible for the delayed heating observed in hyperthermia studies. The delayed heating is not observed during temperature measurement using IRT as

the temperature measurement is real time in this case. It must be noted that by using a smaller diameter probe, the delay time can be significantly reduced.

It can be further seen from **Figs. 2.15a-b** that the IRT based data can be fitted with a single linear regression analysis, whereas, for probe based data, a single linear regression analysis leads to a wrong initial rate of temperature rise (from 0-10 s data) as compared to the linear regression analysis beyond the delay time (i.e., 3-10 s). The variations in slopes between the linear regression analyses performed on the initial data (0-3 s) and beyond the delay time (3-10 s data) are found to be very large (more than 100 %) which can lead to very high uncertainties in SAR computation, if not properly accounted for, i.e., data points beyond the delay time should only be considered for determination of the initial rate of temperature rise.

Several methods have been reported for determining the initial slope using linear regression analyses of initial data (first tens of second) [350, 389] or extended (10-100 s) data [387], direct calculation of ΔT over a time interval [342, 390, 391], numerical derivatives [392, 393] and extrapolated polynomial fit [394, 395]. It is evident that such a huge variation in data analysis methods for determining initial rate of temperature rise invariably contributes to significant uncertainties in the computed SAR values making them seldom comparable and poorly reproducible unless the exact method is known. Studies show different values of the initial rate of temperature rise using same experimental data sets (0-30 s data) [297], where, the initial rates were found to be 0.098, 0.12, 0.096, 0.1 and 0.16 $^{0}Cs^{-1}$ for linear regression, polynomial fit, direct, median and maximum numerical derivative methods, respectively. Considering the linear regression method as a baseline, this results in an uncertainty of 22.45, 2.04, 2.04, 63.27 % for the polynomial fit, direct, median and maximum numerical derivative methods, respectively. This shows that variations in the method used for initial rate estimation can lead up to ~ 63.27 % uncertainty in SAR estimation.

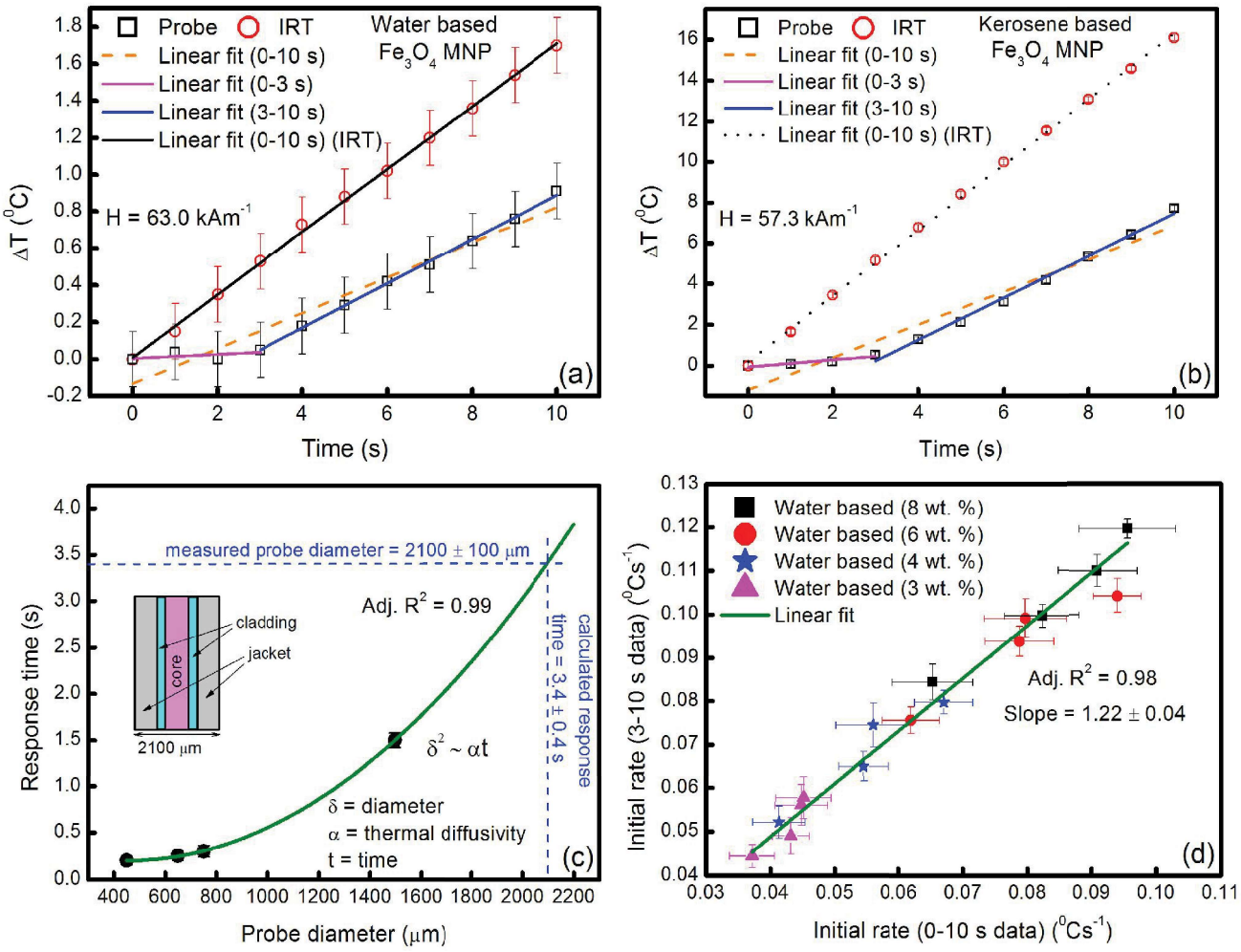


Figure 2.15: ΔT as a function of time, measured using fiber optic temperature sensor and IRT for water and kerosene based samples during RF-AMF induced heating under external field amplitudes of (a) 63.0 kAm^{-1} and (b) 57.3 kAm^{-1}, respectively. The temperature rise curves obtained from fiber optic sensor are fitted with three linear regression analyses, viz., initial delay time (0-3 s), delay corrected time (3-10 s) and without delay corrected time (0-10 s). On the other hand, IRT based curves are fitted with a single linear regression analysis. (c) Calibration curve showing the variation in response time (t) as a function of probe diameter. The data is collected from specifications provided by the manufacturer. A schematic diagram of a typical fiber optic temperature sensor is also shown in the figure. (d) Delay time corrected initial rates of temperature rise as a function of initial rates of temperature rise without delay time correction, for the water based samples.

Figure 2.15d shows the initial rates determined by linear regression analyses of the 3-10 s data as a function of the initial rates obtained by linear regression analyses of the 0-10 s data (i.e., neglecting the delayed heating) for water based ferrofluids. It can be seen that the initial

rates determined from both the methods were linearly correlated (adjusted $R^2 = 0.98$) and the slope of the linear regression analysis was ~ 1.22 ± 0.04. This shows the detrimental effects of delayed heating in SAR estimation, where, up to ~ 22-25 % undervaluation of SAR is possible, if not suitably accounted for.

2.6.3 Heat loss to sample holder

Though thermal losses from the magnetic nanofluid to the sample holder is negligible in an adiabatic experimental set-up due to the presence of active adiabatic shielding [350], temperature rise of the sample holder can be a potential source of error in non-adiabatic SAR measurements. Infrared thermography (IRT) was used to measure the temperature rise of the sample holder during RF-AMF induced heating of the water and kerosene based magnetic fluids of various concentrations under different external field amplitudes and the experimental findings indicated that the ratio of initial rate of temperature rise of the sample holder to that of the sample was higher for lower sample concentration and steadily decreased with increasing sample concentration, which was attributed to the faster heating of the magnetic nanofluids at higher concentrations. The temperature rise of the sample holder is predominantly due to conduction heat transfer (neglecting radiative losses) from the sample during RF-AMF induced heating and the corrected initial rates of temperature rise were estimated by summing the initial rates of temperature rise of the samples and the sample holder. The average uncertainties in initial rates were found to be 3 (± 2) and 3 (± 1) % for the water and kerosene based samples, respectively.

The interfacial temperature (at the fluid-glass interface) can be expressed as $T_{if} = T_f + (T_G - T_f)\frac{e_G}{e_G + e_f}$, where T_{if}, T_f, T_G, e_f and e_G indicate interfacial temperature, temperature of the fluid sample during field induced heating, bulk temperature

of the glass sample holder, effusivity [$e = (\rho ck)^{0.5}$, where k is thermal conductivity] of the fluid and glass, respectively [396]. Hence, the temperature difference between the interface and the fluids can be expressed by the following sets of equation.

$$T_{if} - T_W = \Delta T_{if-W} = \Delta T_{G-W} \frac{e_G}{e_G + e_W} \tag{2.18a}$$

$$T_{if} - T_K = \Delta T_{if-K} = \Delta T_{G-K} \frac{e_G}{e_G + e_K} \tag{2.18b}$$

It is evident from Eqs. 2.18a-b that $\Delta T_{if\text{-}W}/\Delta T_{if\text{-}K} = (e_G+e_K)/(e_G+e_W) \sim 0.3$. The conductive heat loss to the sample holder is expressed as $\dot{q}_{f-if} = \frac{k_f A^{if}}{l^{if}} \Delta T_{if-f}$, where, $\dot{q}_{f-if}$ indicates the heat flux from the fluid to the interface and k_f, A^{if} and l^{if} indicate thermal conductivity of the fluid, characteristic area and length, respectively. Considering the ratios of $\Delta T_{if\text{-}W}/\Delta T_{if\text{-}K}$ and thermal conductivity values of water and kerosene as ~ 0.3, 0.6 $Wm^{-1}k^{-1}$ and 0.2 $Wm^{-1}K^{-1}$, respectively it can be shown that $\dot{q}_{W-if} / \dot{q}_{K-if} \sim 0.9 \sim 1$, i.e., the heat loss to sample holder is approximately the same for water and kerosene based fluids leading to a similar value of uncertainty (~ 3 %) in SAR estimation.

2.6.4 Spatial variation of temperature within sample

Inhomogeneous temperature distribution in the magnetic nanofluids during RF-AMF induced heating under a non-adiabatic experimental condition leads to uncertainties in the measured initial rates of temperature rise. Flat bottom cylindrical sample holders or conical Eppendorf tubes are the most widely used sample vials for SAR measurements, and reports indicate that in the case of conical Eppendorf tubes, ~ 7.5 ^{0}C temperature difference could be observed between the top and bottom of a magnetic nanofluid sample, whereas, the temperature difference was limited within the 1-2 ^{0}C for flat bottom cylindrical sample holders indicating suitability of flat bottom cylindrical sample holders for SAR measurements [297].

Temperature measurements were performed during RF-AMF induced heating of water and kerosene based magnetic fluids, where, the probe location was varied radially and it was found that the uncertainty in SAR was within ~ 1 %. On the other hand, when the probe location was varied vertically for a fixed radial location, the highest SAR value was obtained just below the top surface and the maximum uncertainty in SAR estimation was ~ 0.3 % for probes located just below the top surface and centre of the sample (without touching the sample holder). This study confirmed that the uncertainties in SAR measurement due to spatial variation of the probe locations are not significant as long as a flat bottom cylindrical sample holder is used and the entire volume of the sample is exposed to a uniform field, provided that the sample is stable (free from rapid sedimentation).

2.6.5 Linear loss approximation and effects of sample volume and surface area

For an adiabatic experimental setup, the heat generated by the magnetic nanoparticles is entirely consumed towards raising the fluid temperature which can be expressed by the following equation.

$$P = c_{samp}\frac{dT(t)}{dt} \tag{2.19}$$

Here, P is the magnetically triggered heating power per unit volume. On the other hand, for a non-adiabatic set-up, Eq. 2.19 does not describe the situation adequately, as only a portion of the heat generated is utilized for raising the sample temperature. Under such non-adiabatic conditions, the increase in sample temperature can be described by the following equation, proposed by Andreu and Natividad [374] and later modified by Wildeboer et al. [297].

$$c_{samp}\frac{dT(t)}{dt} = P - P_{nl}(\Delta T) = P + (-LR)\times\Delta T + O(\Delta T^2) + O(\Delta T^3) + O(\Delta T^4) \tag{2.20}$$

Here, $P_{nl}(\Delta T)$ indicates non-linear heat losses from the sample to the surrounding which can be attributed to various mechanisms, viz., conduction, convection, radiation and phase

transition (like evaporation, melting, etc.). A 4th order polynomial was used in Eq. 2.20 to incorporate the effect of radiative losses [297]. For small values of ΔT, Eq. 2.20 can be approximated by the following equation [297].

$$c_{sample}\ \frac{dT(t)}{dt}\ =\ P\ +\ (-LR)\ \times\ \Delta T \tag{2.21}$$

Here, LR indicates linear loss rate which is determined from the temperature decay pattern during natural cooling [297]. **Figs. 2.16a-b** show the variation of ΔT as a function of time during RF-AMF induced heating under two different external field amplitudes (63.0 and 51.4 kAm^{-1}), followed by natural cooling for water and kerosene based samples, respectively. Here, 1000 μL of sample was used and the water and kerosene based samples were placed in vials of capacity 5 mL (bigger vial) and 1 mL (smaller vial), respectively. It can be clearly seen from **Figs. 2.16a-b** that sample temperature continuously increased during RF-AMF induced heating and started to decay when the field was switched off.

Figures 2.16c-d show the variation of the rate of temperature decay (dT/dt) as a function of temperature difference (ΔT) for the water based sample during natural cooling after RF-AMF induced heating under external field amplitudes of 63.0 and 51.4 kAm^{-1}, respectively. Following Eq. 2.20, the data was fitted with 4th order polynomial, as shown in the corresponding figures (**Figs. 2.16c-d**). The linearly varying region of the dT/dt vs. ΔT curves were analysed using linear regressions and the regression curves are also shown in **Figs. 2.16c-d**. The linear loss rates (LR) were found to be ~ 0.00295 (± 1 × 10^{-4}) and 0.00303 (± 1 × 10^{-4}) s^{-1} for the water based samples during RF-AMF induced heating under RF-AMF amplitudes of 63.0 and 51.4 kAm^{-1}, respectively, and the corresponding values of ΔT_{LL} (range of ΔT over which linear approximation was valid) were ~ 31.85 (± 0.5) and 28.18 (± 0.5) ^{0}C, respectively. Similar analyses were performed for the kerosene based sample and the results are shown in **Figs. 2.16e-f** for field amplitudes of 63.0 and 51.4 kAm^{-1}, respectively.

The corresponding values of LR and ΔT_{LL} were 0.00439 ($\pm$ 1 $\times$ 10^{-4}) s^{-1}, 0.00536 ($\pm$ 1 $\times$ 10^{-4}) s^{-1}, 15.82 ($\pm$ 0.5) ^{0}C and 15.08 ($\pm$ 0.5) ^{0}C, respectively. **Tables 2.6 and 2.7** show the summarized results for 1 mL and 5 mL capacity sample holders, respectively.

Table 2.6: Linear loss rate (LR) and ΔT_{LL} for water and kerosene based samples of different volumes in 1 mL sample holder. W and K indicate water and kerosene based ferrofluids with 10 and 6.5 wt. % sample concentrations, respectively.

Sample	Volume (µL)	RF-AMF amplitude (kAm^{-1})	LR (s^{-1}) ($\pm 1\times10^{-4}$ s^{-1})	ΔT_{LL} (^{0}C) ($\pm$0.5 ^{0}C)
W	1000	63.0	0.00342	24.28
W	500	63.0	0.00395	19.91
W	250	63.0	0.00454	13.26
W	1000	51.4	0.00352	23.19
W	500	51.4	0.00398	18.36
W	250	51.4	0.00501	12.35
K	1000	63.0	0.00439	15.82
K	500	63.0	0.00487	13.62
K	250	63.0	0.00851	8.55
K	1000	51.4	0.00536	15.08
K	500	51.4	0.00600	12.71
K	250	51.4	0.00860	7.09

Table 2.7: Linear loss rate (LR) and ΔT_{LL} for water and kerosene based samples of different volumes in 5 mL sample holder. W and K indicate water and kerosene based ferrofluids with 10 and 6.5 wt. % sample concentrations, respectively.

Sample	Volume (µL)	RF-AMF amplitude (kAm^{-1})	LR (s^{-1}) ($\pm 1\times10^{-4}$ s^{-1})	ΔT_{LL} (^{0}C) ($\pm$0.5 ^{0}C)
W	1000	63.0	0.00295	31.85
W	800	63.0	0.00301	28.02
W	600	63.0	0.00336	21.85
W	1000	51.4	0.00303	28.18
W	800	51.4	0.00322	26.98
W	600	51.4	0.00337	18.24
K	1000	63.0	0.00310	18.02
K	800	63.0	0.00344	15.55
K	600	63.0	0.00380	14.60
K	1000	51.4	0.00345	16.99
K	800	51.4	0.00362	13.75
K	600	51.4	0.00391	12.53

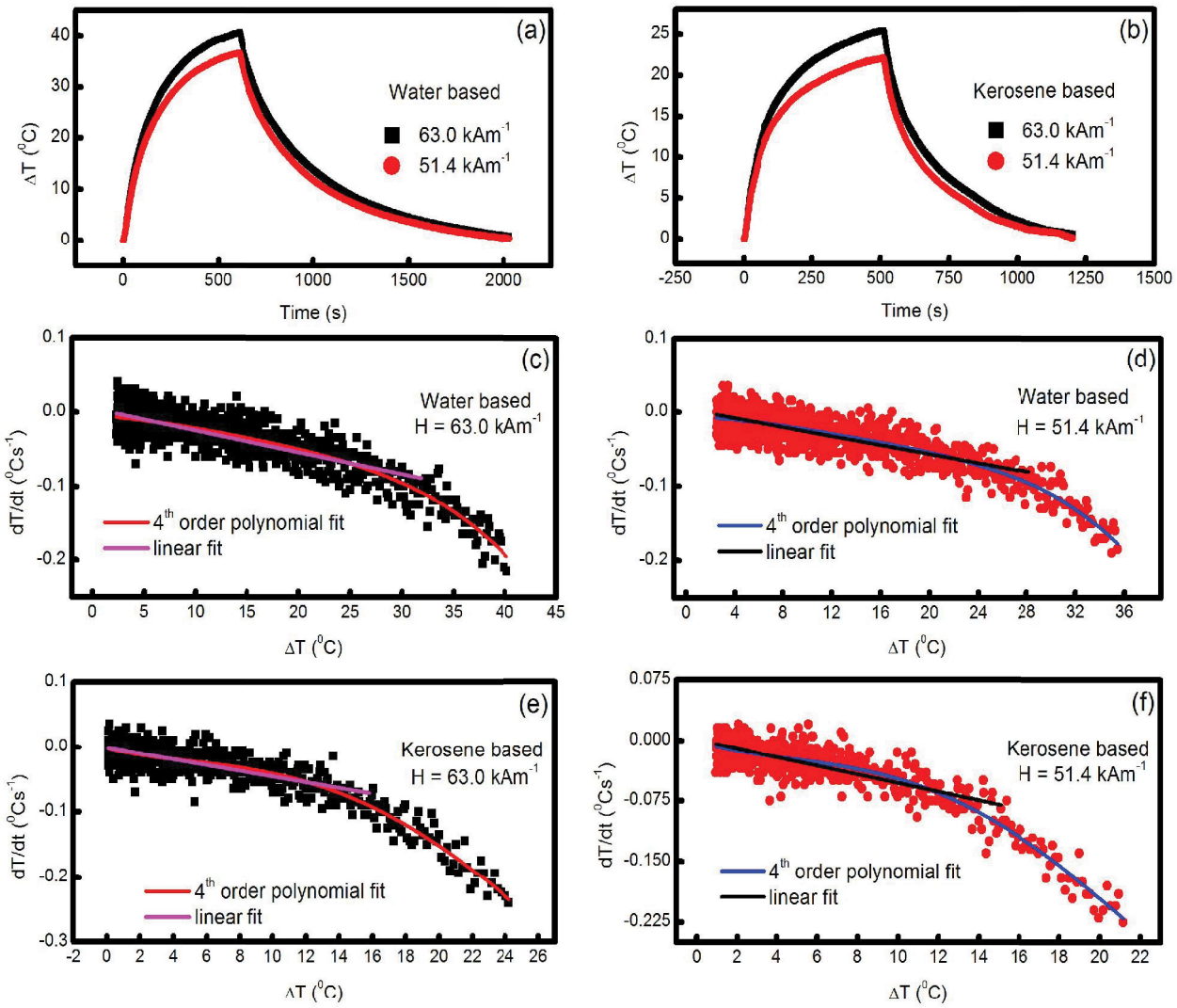


Figure 2.16: Variation of ΔT as a function of time, during RF-AMF induced heating of (a) water and (b) kerosene based magnetic fluid, containing Fe_3O_4 MNP, under external field amplitudes of 63.0 and 51.4 kAm^{-1} followed by natural cooling. Variation of (dT/dt) as a function of ΔT for the water based magnetic fluid during natural cooling after RF-AMF induced heating under external field amplitudes of (c) 63.0 kAm^{-1} and (d) 51.4 kAm^{-1}. Variation of (dT/dt) as a function of ΔT for the kerosene based magnetic fluid during natural cooling after RF-AMF induced heating under external field amplitudes of (e) 63.0 kAm^{-1} and (f) 51.4 kAm^{-1}. The 4th order polynomial fits and linear regression analyses are also shown in the figures.

A semi-analytic lumped system thermal model is used for understanding the observed variations in LR and ΔT_{LL} with sample volume and surface area. The temperature evolution of a lumped system during natural cooling can be described by the following equation [396, 397].

$$T - T_{amb} = (T_i - T_{amb})e^{-\frac{t}{\lambda_d}} \tag{2.22}$$

Here, T_{amb} and T_i indicate ambient and initial temperature of the system at the start of cooling phase, respectively. λ_d is the time constant of temperature decay and is defined as $\lambda_d = (\rho_{samp} c_{samp} V_{samp})/(h_{conv} A_{samp})$, where, h_{conv}, A_{samp} and V_{samp} indicate the convective heat transfer coefficient, surface area and volume of the sample, respectively. In linear loss approximation, Eq. 2.21 is analytically solvable and the generalized solution is of the form $\Delta T = \frac{P}{LR}(1 - e^{-\frac{\Delta t}{c/LR}})$, which is identical to the solution of lumped system, i.e., Eq. 2.22. In this analysis, the magnetic fluid along with the sample holder is assumed as a lumped system.

Using dimensional analyses (from Eq. 2.22), the rate of temperature decay is found to scale as ~ $1/\lambda_d$ and is directly proportional to the ratio of surface area to volume (A_{samp}/V_{samp}) of the sample and for magnetic fluids in cylindrical sample holders, rate of temperature decay ~ $2/r_{sh}$, where r_{sh} is the radius of the sample holder. This indicates three experimental possibilities, viz., i) using different volume of magnetic fluid in the same sample holder, i.e., varying V_{samp}, keeping A_{samp} fixed; ii) using the same volume of magnetic fluid in different sample holder, i.e., varying A_{samp}, keeping V_{samp} fixed and iii) using IRT for measuring only surface temperature distribution, thereby, allowing additional surface losses. All three possibilities were experimentally studied in detail and **Fig. 2.17** shows the variations of LR and ΔT_{LL} in different cases. The salient features of **Fig. 2.17** are discussed below.

i) Constant A_{samp} with varying V_{samp}

Figure 2.17a shows the variation of LR and ΔT_{LL} as a function of sample volume for the water and kerosene based sample in 5 mL sample holder (bigger vial: BV) during natural cooling after RF-AMF induced heating under external field amplitudes of 63.0 and 51.4

kAm^{-1}. It can be clearly seen from **Fig. 2.17a** that LR decreased with sample volume, whereas, ΔT_{LL} increased with increasing sample volume, which was found to be in agreement with the predictions of lumped system model (decay rate ~ (A_{samp}/V_{samp}). Higher values of LR indicated faster temperature decay and it can be seen from Eq. 2.22 that faster decay rate leads to a lower value of temperature difference for a fixed initial temperature dependence (T_i-T_{amb}), ultimately resulting in a narrower linearly varying region of dT/dt vs. ΔT curve, i.e., a lower value of ΔT_{LL}. **Fig. 2.17b** shows similar analyses for 1 mL sample holder (smaller vial: SV).

ii) Constant V_{samp} with varying A_{samp}

Figure 2.17c shows the variation of LR and ΔT_{LL} for a water based sample during natural cooling after RF-AMF induced heating under external field amplitudes of 63.0 and 51.4 kAm^{-1}, where 1 (SV) and 5 mL (BV) sample holders were used. It can be clearly seen from **Fig. 2.17c** that the values of LR were higher for the smaller vial, whereas, the values of ΔT_{LL} were higher for the bigger vials. For a fixed volume of sample (in this case 1000 μL), changing sample vials essentially leads to a change in the ratio of surface area to volume $(A_{samp}/V_{samp} = 2/r_{sh})$. The radii of the 5 mL and 1 mL sample holders were ~ 7.5 (±0.1) and 3.5 (±0.1) mm, respectively and hence, LR was lower (ΔT_{LL} showed an opposite trend) for the bigger sample holders for a constant volume of sample as the convective heat losses from the surface were lower as compared to the smaller vial. **Fig. 2.17d** shows similar analyses for a kerosene based ferrofluid.

iii) Surface temperature measurement using IRT and allowing additional surface losses

IRT based temperature measurement from the top surface of the fluid during RF-AMF induced heating is subjected to additional heat losses from the free surface, which is not the

case for bulk temperature measurement using a fiber optic probe. Due to additional surface losses, the rate of temperature decay, measured using IRT, can be expressed as $LR_{IRT} \sim [(A_{samp}/V_{samp}) + \delta_{top\text{-}surf}]$, where $\delta_{top\text{-}surf}$ indicate the additional losses from the top surface. Hence, linear loss rate measured from IRT based data was found to be higher (opposite trend for ΔT_{LL}) as compared to probe based data when other experimental parameters remained unchanged. **Fig. 2.17e** shows the variations of LR and ΔT_{LL} for a water based sample during natural cooling after RF-AMF induced heating at external field amplitudes of 63.0 and 51.4 kAm^{-1}, where, the temperature measurements were performed using fiber optic temperature sensor and IRT. It can be clearly seen from **Fig. 2.17e** that LR was higher, when temperature measurements were performed using IRT indicating the effect of additional heat losses. As the temperature decay was faster for IRT based measurements, the extent of ΔT over which linear approximation was valid (ΔT_{LL}) decreased significantly as compared to the probe based data. **Fig. 2.17f** shows the variation of LR and ΔT_{LL} for a kerosene based sample when the measurements were performed using IRT and fiber optic temperature sensor and it can be seen that for IRT based measurements, LR was higher but ΔT_{LL} was lower as compared to the probe based data. The detailed values of LR and ΔT_{LL} for IRT based measurements are shown in **Table 2.8**.

Table 2.8: Linear loss rate and ΔT_{LL} for water (W) and kerosene (K) based samples of 1000 µL volume, in 5 mL sample holder (BV), using infrared thermography (IRT) based temperature measurements.

Sample	Volume (µL)	RF-AMF amplitude (kAm^{-1})	Linear loss rate (LR) (s^{-1}) ($\pm 1\times10^{-4}$ s^{-1})	ΔT_{LL} (^0C) (± 0.5 ^0C)
W (10 wt. %)	1000	63.0	0.00298	28.65
W (10 wt. %)	1000	51.4	0.00318	25.75
K (6.5 wt. %)	1000	63.0	0.00359	16.29
K (6.5 wt. %)	1000	51.4	0.00355	14.38

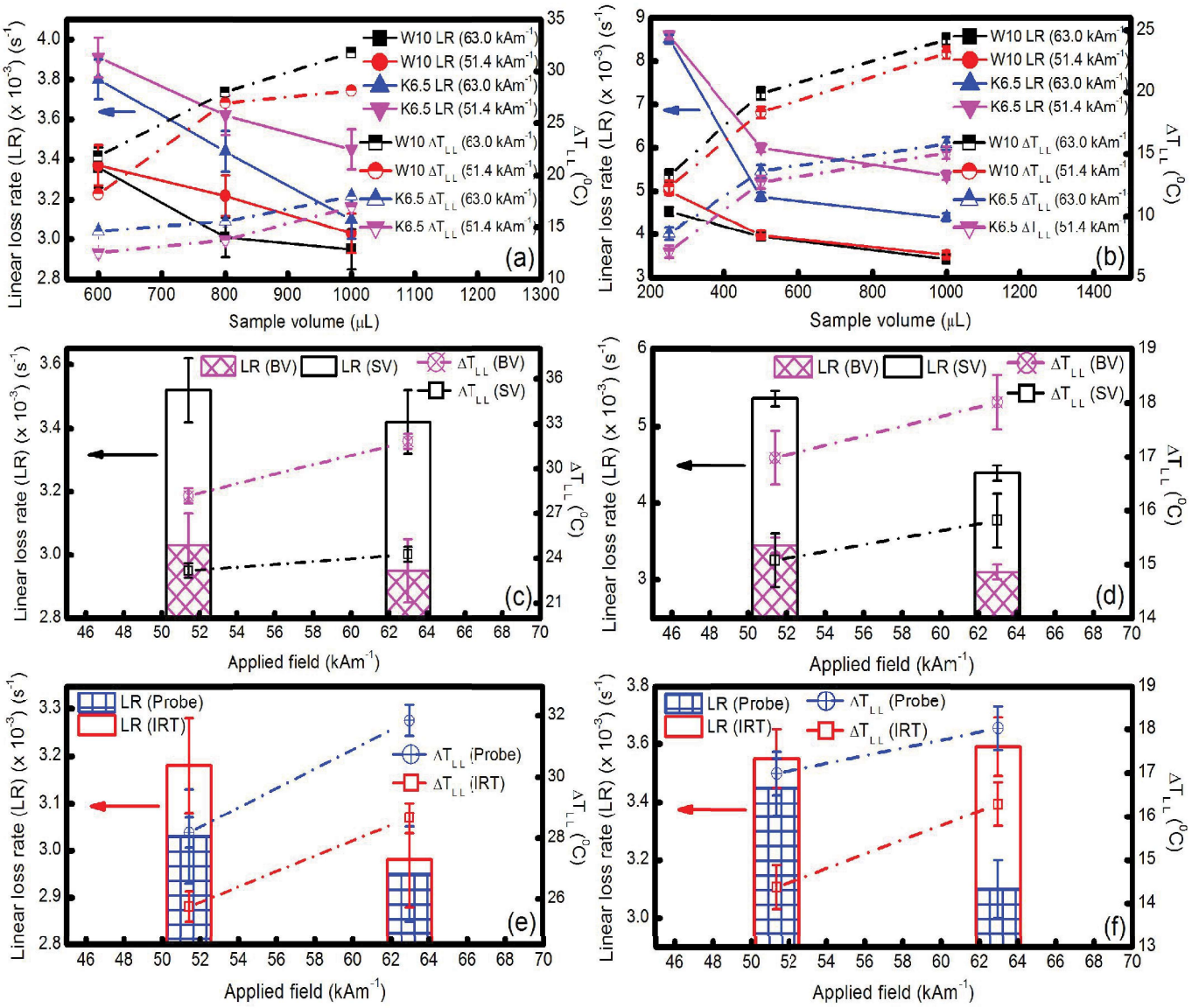


Figure 2.17: Variation of LR and ΔT_{LL} as a function of sample volume for the water and kerosene based sample in the cases of (a) 5 mL and (b) 1 mL sample vials, during natural cooling, after RF-AMF induced heating under external field amplitude of 63.0 and 51.4 kAm^{-1}, respectively. LR and ΔT_{LL} as a function of external field amplitude for (c) water and (d) kerosene based magnetic fluids, when 1 mL and 5 mL sample vials are used. Variation of LR and ΔT_{LL} as a function of external field amplitude for (e) water and (f) kerosene based magnetic fluids, when temperature measurements are performed using IRT and fiber optic temperature sensor and the samples are kept in a 5 mL vial.

2.6.6 Adiabatic reconstruction

Figure 2.18a shows the typical variation of ΔT as a function of time during RF-AMF induced heating of a water based magnetic fluid under an applied field amplitude of 63.0

kAm^{-1}. It can be seen that temperature increase was linear during the initial time but at higher time scales, the rate of temperature rise was slower due to heat losses from the sample to the surrounding due to non-adiabatic experimental conditions. The experimentally measured ΔT vs. time data was piecewise fitted with linear regression and the rates of temperature rise (dT/dt) at various median times were calculated. The median time for a linear regression analysis of 50-100 s data was selected as 75 s. **Fig. 2.18b** shows the variation of dT/dt as a function of median time, where dT/dt exponentially decayed with time. For an ideal adiabatic set-up, dT/dt should remain constant due to the absence of any heat loss but in practical experimental conditions, heat losses occur and hence, necessary rate corrections are performed to account for the effects of heat loss.

The linear loss rates (LR) were calculated from the temperature decay curves, as discussed in the preceding section and the variation of LR with median time is also shown in **Fig. 2.18b**. It can be seen that LR increased with median time and hence, for a time matched RF-AMF induced temperature rise followed by natural cooling experiment, adiabatic reconstruction of experimentally measured temperature rise curve is proposed using the following equation.

$$\Delta T_{adiabatic}^{ind} = \Delta T_{meas+corr}^{ind} + (LR) \times \Delta T_{meas+corr}^{ind} \times \Delta t^{ind} \tag{2.23}$$

Here, $\Delta T_{adiabatic}$, $\Delta T_{meas+corr}$, LR, Δt indicate adiabatically reconstructed temperature rise, experimentally measured and corrected (for peripheral heating, delayed heating and thermal losses to sample holder) temperature rise, linear loss rate and incremental time step (indicated by the index ind). The adiabatically reconstructed temperature rise rates are also shown in **Fig. 2.18b**, where, it can be seen that the variations are much lower as compared to the experimentally measured temperature rise rates.

The proposed adiabatic reconstruction protocol was found to decrease the uncertainties by a factor of ~ 3. **Figs. 2.18c-d** show the variation of adiabatically reconstructed SAR as a function of slope corrected SAR (using a technique proposed by Wildeboer et al. [297]) for

water and kerosene based magnetic fluids, respectively, where, it can be seen that the SAR values determined from both the techniques were linearly correlated. The adjusted R^2 of the linear regression analyses were ~ 0.99 in both the cases indicating accuracy of the linear model. The slopes of the linear regression analyses were ~ 0.997 (± 0.002) and 0.999 (± 0.003) for water and kerosene based samples, respectively, which indicated very good quantitative agreement between the two methods.

The slope corrected method is numerically involved and time consuming, as apart from determining the linear loss rate, the slope corrected SAR requires averaging over different time intervals (~ 30-60 s) of the temperature rise curves and performing an average over several segments within a specific time interval, where, the choice of optimum time interval and number of segments varies with experimental set-up and heating efficiency of the samples and often requires an iterative procedure for stabilization of the SAR values. On the other hand, the proposed adiabatic reconstruction methodology is simple, straight forward and is capable of SAR estimation with good accuracy.

Table 2.9 shows a summary of different types of thermodynamic uncertainties involved in non-adiabatic SAR estimation. In the present study, various experimental precautions (like optimizing sample location for minimum non-uniformity in field distribution, optimizing probe position, polytetrafluoroethylene (PTFE) shielding for reducing peripheral heating and optimizing sample volume) and data analysis protocols (like background subtraction, delayed heating correction and adiabatic reconstruction of experimental temperature rise curves) are adopted for accurate SAR estimation during RF-AMF induced heating of the magnetic fluids.

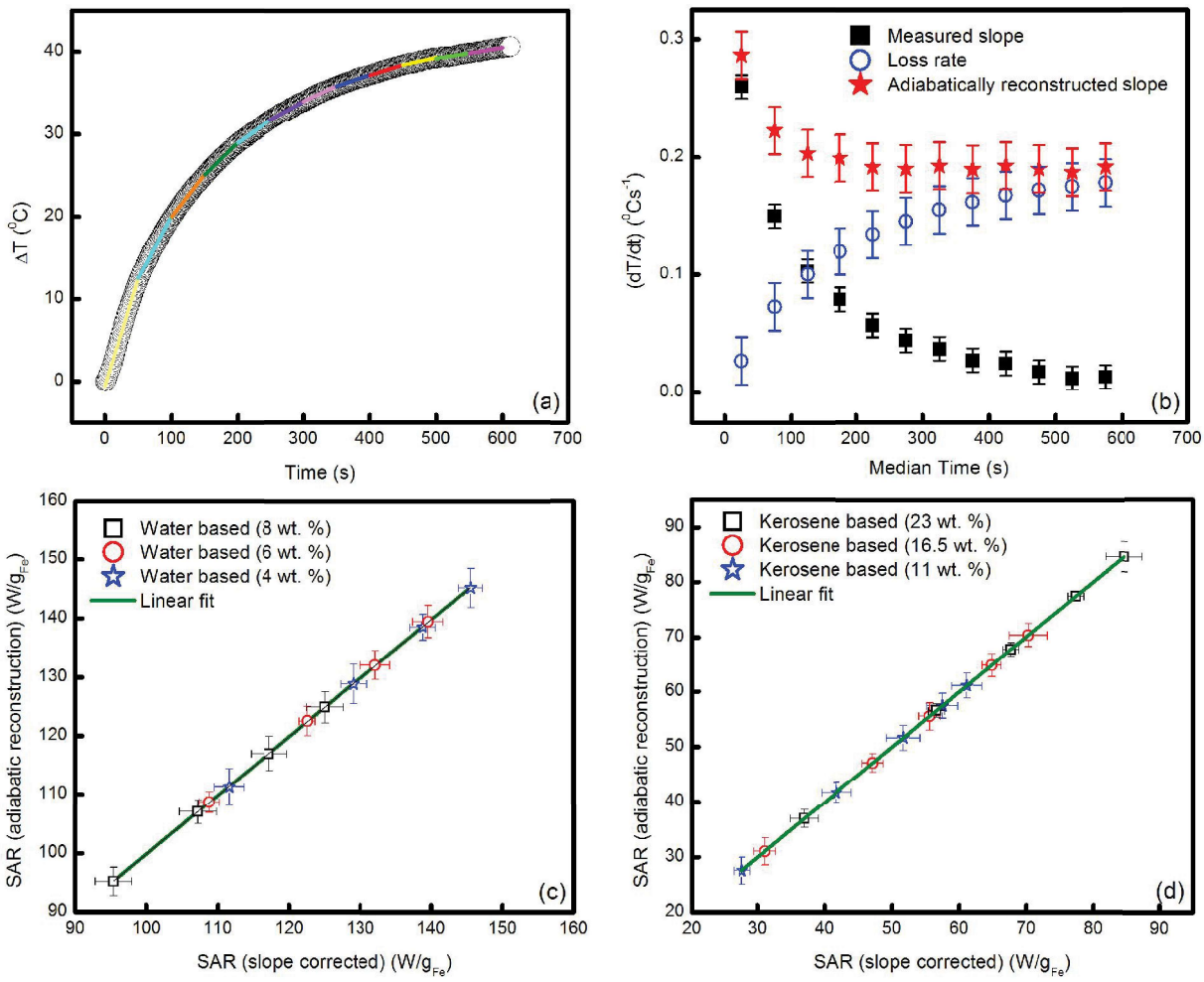


Figure 2.18: (a) Typical variation of ΔT as a function of time, during RF-AMF induced heating of a water based sample under a non-adiabatic experimental set-up. The rate of temperature rise, as a function of median time is calculated using several linear regression analyses (shown in the figure). (b) Variation of rate of temperature rise (measured), linear loss rate and adiabatically reconstructed rate of temperature rise as a function of median time. Variation of SAR calculated using adiabatic reconstruction method as a function of SAR calculated using slope corrected method, proposed by Wildeboer et al. [297], for (c) water and (d) kerosene based magnetic fluids of three different concentration under various external field amplitudes.

Table 2.9: A summary of different types of thermodynamic uncertainties involved in non-adiabatic SAR estimation.

Type of uncertainty	Uncertainty in SAR estimation	Solution
Peripheral heating	± 1.5 % & ± 4.3 % (with and without shielding)	• Using shielded sample holder and background subtraction.
Delayed heating	± 22-25 %	• Initial rate determination beyond delayed heating regime (typical ~ 3 s). Applicable for fiber optic temperature sensor.
Heat loss to sample holder and spatial variation of temperature within the sample	± 3 % & ± 1 %	• Data correction • Positioning of the temperature probe at the centre of the sample • Avoiding wall effects • Exposure of the entire sample to magnetic field.
Initial heating rate determination method and range of regression analysis	~ ± 23 %	• Proper selection of method and data range for initial rate determination.
Sample volume to area ratio	> ± 35 %	• Optimizing sample volume • Adopting adiabatic reconstruction.

2.7 Conclusions

This chapter describes the synthesis and characterization techniques for the magnetic nanoparticles and ferrofluids, experimental methods for hyperthermia studies, effects of thermal losses on RF-AMF induced heating efficiency and adiabatic reconstruction protocol for reducing uncertainties in quantification of SAR under non-adiabatic experimental conditions. The MNP were synthesized using coprecipitation method and the synthesized MNP were characterized using powder XRD, SAXS, DLS, TGA, FTIR, VSM and AFM techniques. The RF-AMF induced heating experiments were performed using a high frequency induction heating system and sample temperature measurements were carried out using a fiber optic temperature sensor and infrared thermography.

Various uncertainties involved in non-adiabatic measurement of SAR during RF-AMF induced heating of ferrofluids were studied and the uncertainties were classified into three categories, viz., material uncertainties (level-1), thermodynamic uncertainties (level-2) and

parametric uncertainties (level-3). The material and parametric uncertainties were found to influence the SAR values estimated using calorimetric and magnetic methods, whereas, the thermodynamic uncertainties were primarily responsible for the errors associated with SAR measurements using a non-adiabatic calorimetric set-up. Experimental findings clearly showed that the peripheral heating of the base fluid is primarily due to radiation heat transfer from the heating coils and decreased significantly when the sample was shielded due to reduced amount of radiant flux reaching the base fluid. The observed delayed heating was attributed to the slower response time of the fiber optic temperature sensor and no such delay was observed in the temperature rise curves measured using IRT. It was observed that the delayed heating can cause up to 22-25 % uncertainty in the estimated SAR values and determination of initial rate of temperature rise beyond the delay time was found to reduce the uncertainty. It was also confirmed that the spatial variation of the probe location caused an uncertainty of ~ 1 % for stable samples in cylindrical flat bottom sample holders when the entire sample was exposed to the RF-AMF and the probe was centrally located. Theoretical calculations showed that linear decay rate increased with sample area to volume ratio, which was experimentally confirmed using different volumes of the samples. The variation of linear decay rate was studied in detail and an adiabatic reconstruction protocol was developed for correcting the measured temperature rise curves, which was found to reduce the uncertainties by a factor of ~ 3. The corrected SAR values, obtained from the simple and easily adaptable adiabatic reconstruction protocol, were found to be in very good agreement with those obtained from the computationally intense slope corrected rate method.

Chapter 3

Infrared thermography based magnetic hyperthermia studies in Fe_3O_4 based magnetic fluids

Chapter 3 Infrared thermography based magnetic hyperthermia studies in Fe_3O_4 based magnetic fluids

3.1 Introduction

Real time *in vivo* application of MFH in human requires effective monitoring of temperature over tumor locations, which requires a large number of fiber optic temperature sensors. To avoid complexity of using multiple sensors, development of a non-contact and non-invasive wide area temperature measurement methodology for rapid adaptation is warranted for real time MFH aided cancer treatment. Here, infrared thermography (IRT) is demonstrated as an alternate non-contact and non-invasive temperature measurement methodology for quantification of SAR in magnetic nanofluids for MFH applications. Infrared thermography is routinely used for various bio-medical applications [366] like breast cancer detection [398, 399], diabetic neuropathy and vascular disorder [400-402], fever detection [403], quantification of viable bacterial count [368], thermoregulation monitoring [367, 404], etc. It is also used extensively in non-destructive evaluation [361, 364, 365]. Though the application of IRT during MFH is reported in a few studies by Rodrigues et al. [405], Levy et al. [371], and Rodrigues et al. [372]; such studies involved measurement of temperature rise on surfaces but not the direct measurement of temperature rise in magnetic nanofluids. Also, there is a lack of knowledge on associated convection losses.

Here an IRT based methodology is used for directly measuring the RF-AMF induced rise in fluid temperature. The major advantages of IRT based temperature measurement over the conventional fiber optic temperature sensor based measurements are listed below.

- Simultaneous temperature measurement on several locations (i.e., temperature mapping over a large area) as compared to a point measurement using fiber optic temperature sensor.

- Real time, non-contact and non-invasive temperature measurement.
- Data display as pseudo colour coded temperature map for easy interpretation.
- No sample contamination due to non-contact measurement approach.

The drawbacks of IRT based approach include the requirement of an unobstructed view of the sample surface and its inability to measure temperature deep inside the samples. In this study, the later concern is addressed by developing an empirical data correction protocol to incorporate the effects of internal and external convection phenomena.

For demonstrating the efficacy of IRT based temperature measurement procedure and for developing the convection corrected data analysis protocol, experiments were performed on water and oil based magnetic nanofluids.

3.2 Infrared thermography (IRT) based MFH studies on water based ferrofluid containing tetramethyl ammonium hydroxide (TMAOH) coated Fe_3O_4 MNP

IRT based temperature measurement during field induced heating of a water based stable ferrofluid containing Tetramethyl ammonium hydroxide (TMAOH) coated Fe_3O_4 MNP is systematically studied. Guller et al. [406] reported that TMAOH coated nanoparticles are non-cytotoxic to human dermal fibroblasts and slightly cytotoxic to HaCat keratinocytes, indicating the bio-compatibility of TMAOH coated MNP. A convection correction procedure is developed to match the IRT based temperature rise curves with those obtained using fiber optic temperature sensor. Variation of SAR with sample concentration and external field amplitude is also probed.

3.2.1 Experimental details and characterization studies

TMAOH coated Fe_3O_4 nanoparticles were prepared by a chemical coprecipitation technique as discussed in Section 2.1.2 in chapter 2. A master solution containing 8 wt. % MNP (hereafter indicated as W1) was diluted to obtain 6, 4, 3 and 2 wt. % samples that are

hereafter indicated as W2, W3, W4 and W5, respectively. The synthesized magnetic nanoparticles were characterized using XRD, DLS and VSM. The powder XRD pattern and room temperature M-H curve of the synthesized MNP are shown in **Figs. 3.1a-b**, respectively. XRD data indicated Bragg reflection peaks corresponding to (220), (311), (400), (422), (511) and (440) planes of cubic spinel structure of Fe_3O_4 (JCPDS file no. 19-0629). The average crystallite size determined from the highest intensity peak of (311) plane, using Scherrer's equation, was found to be ~ 8.0 (± 0.9) nm, whereas, DLS showed an average hydrodynamic size of ~ 10 (± 1) nm. The saturation magnetization, measured using VSM, was found to be ~ 42 emu/g (without correction to dead layer contribution) which is much lower than the saturation magnetization of bulk magnetite (92 emu/g). It can be seen from **Fig. 3.1b** that the M-H curve did not show hysteresis at room temperature indicating superparamagnetic (SPM) behaviour. It must be noted in this regard that the critical size $[D_c = (\frac{150 k_B T}{\pi K})^{1/3}]$ of Fe_3O_4 for SPM behaviour is ~ 20 nm (considering K = 25 kJm^{-3}), whereas, the average size of the synthesized MNP was much lower in the present study confirming SPM behaviour. It can be further seen from **Fig. 3.1b** that the magnetization curve showed a typical Langevin type behaviour and considering a polydisperse size distribution of the MNP, the field dependent magnetization was expressed as $M(H) = M_s \int_0^\infty Lf(y)dy$, where M_s, f(y) and L denote saturation magnetization, volume fraction distribution as a function of reduced diameter, $y = D/D_m$, where D_m is the mean diameter of the size distribution and Langevin function, respectively [407]. For a log-normal size distribution, the values of the mean diameter (D_m) and its standard deviation (σ_m) were calculated using the equations $D_m = \left[\frac{18 k_B T}{\pi M_s}\sqrt{\frac{\chi_i}{3\psi_s M_s}\frac{1}{H_0}}\right]^{1/3}$ and $\sigma_m = \frac{1}{3}[\ln\{\frac{3\chi_i}{\psi_s M_s . \frac{1}{H_0}}\}^{1/2}]$,

where χ_i is the initial susceptibility, $\psi_s = 1$ for solids and $1/H_0$ indicates the value of the inverse magnetic field for which magnetization is zero in the high field region. The **inset of Fig. 3.1b** shows the linear regression analyses for M vs. 1/H curve, from which the value of $1/H_0$ was obtained as 1.8958 kG^{-1}. For the MNP used in the present study, the $D_m \pm \sigma_m$ was found to be 11.3 ± 1.8 nm.

The ferrofluids in a glass vial was placed at the centre of the heating coil. Experiments were performed under a fixed frequency of 126 kHz at four different external field amplitudes, viz., 63.0, 57.0, 51.4 and 45.3 kAm^{-1}, using a radio frequency induction heating system. Sample temperature was measured using an infrared camera and the values were compared with the temperature obtained from a conventional radio frequency immune fiber optic temperature sensor. Detailed description of the experimental methods can be found in the sections 2.4 and 2.5 in chapter 2. SAR values were estimated in terms of W/g_{Fe}, where g_{Fe} indicates the mass of magnetic phase only [408]. The specific heat capacity and density of the base fluid (water in the present case) was considered as 4.18 $Jg^{-1}K^{-1}$ and 1 g/cc, respectively.

3.2.2 Results and discussions

3.2.2.1 IRT based temperature measurement during RF-AMF induced heating

Figures 3.2a-j show the typical infrared images at t = 0, 100, 200, 300, 400, 500, 600, 700, 800 and 900 s, respectively, during RF-AMF induced heating of the sample W2 (6 wt. %) under an external field amplitude of 63.0 kAm^{-1}. The pseudo colour coded temperature scales are also shown along with the individual images where the fluid sample is clearly discernible. Though the room temperature was maintained at 28 (± 1) ^{0}C, throughout the experiments, the sample holder and the glass vial appeared at a comparatively lower temperature in the IRT images due to the emissivity variations.

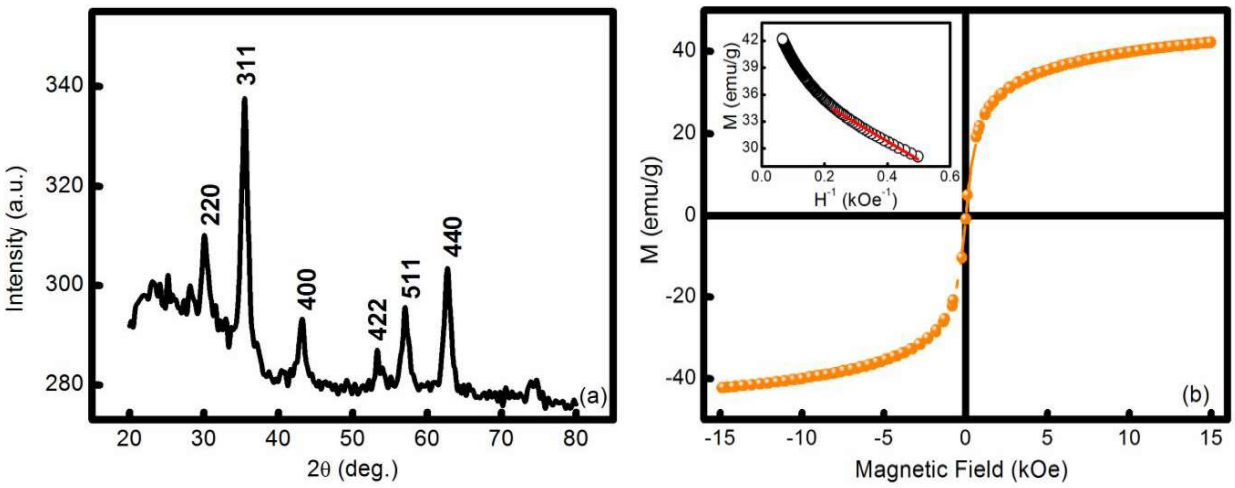


Figure 3.1: (a) Powder X-ray diffraction pattern of the synthesized Fe_3O_4 MNP. (b) Room temperature M-H curve for the synthesized Fe_3O_4 MNP. The saturation magnetization is ~ 42 emu/g. (Inset) Variation of magnetization as a function of the inverse of magnetic field. The value of the inverse magnetic field ($1/H_0$) for zero magnetization is determined from linear regression analysis (also shown in the figure).

Here, the emissivity was set to reflect the fluid temperature correctly. The lower temperature concentric shell (with a black pseudo colour) surrounding the fluid sample indicated the boundary of the glass vial. It can be clearly seen from the infrared images that the fluid temperature increased with time during RF-AMF induced heating. The average fluid temperature increased from 28.05 (± 0.2) ^{0}C at t = 0 s to 49.84 (± 0.7) ^{0}C at t = 900 s during RF-AMF induced heating, whereas, the glass vial temperature increased from 23.43 (± 0.3) ^{0}C to 29.59 (± 0.5) ^{0}C. This temperature rise (~ 6.2 ^{0}C) of the glass vial was attributed to the heat loss from the magnetic fluid sample, which is not normally detected using conventional fiber optic temperature sensor. Similar results were obtained for the other samples too.

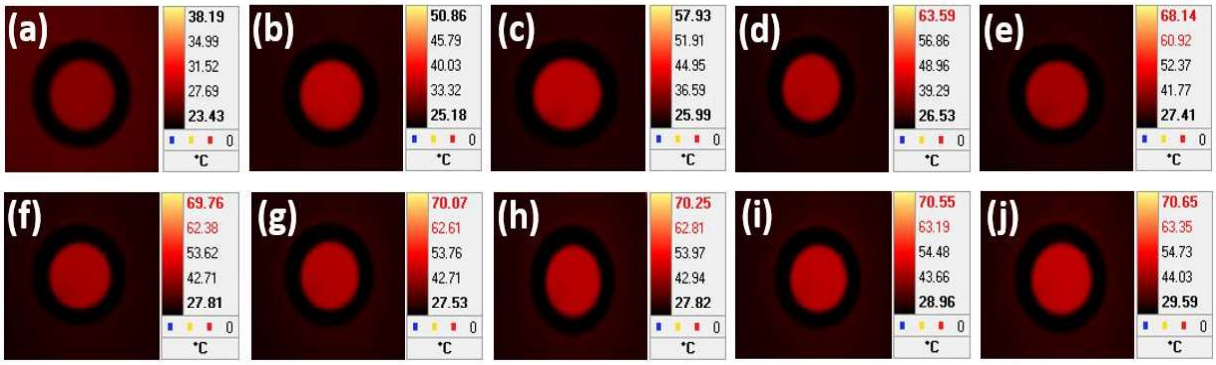


Figure 3.2: Typical infrared images of the sample W2 (6 wt. %) at time t = (a) 0, (b) 100, (c) 200, (d) 300, (e) 400, (f) 500, (g) 600, (h) 700, (i) 800, (j) 900 s, respectively, during RF-AMF induced heating under an external field amplitude of 63.0 kAm^{-1} at 126 kHz. The pseudo colour coded temperature scales are also shown along with the images.

The mean sample temperature was obtained by spatially averaging over a large number of pixels excluding the edge pixels to avoid the wall effect. **Figs. 3.3a-d** show the temperature rise ($\Delta T = T-T_i$, where, T_i is the initial temperature = 28 ^0C) as a function of time during RF-AMF induced heating of the magnetic fluids of 8, 6, 4, 3 and 2 wt. % concentrations and under four different field amplitudes, viz., 63.0, 57.0, 51.4 and 45.3 kAm^{-1}, respectively. It can be clearly seen from **Fig. 3.3** that the sample temperature continued to increase with time during RF-AMF induced heating which was in agreement with our earlier observations (**Fig. 3.2**). It was further observed that the nature of the temperature rise curves were similar and initially temperature increased monotonically and beyond certain time the rate of temperature rise deceased, which was attributed to the temperature loss from the magnetic fluid to the surrounding. For all values of the external field amplitude, the highest temperature rise was obtained for the magnetic fluid with the highest concentration. When the RF-AMF is switched on, the dispersed magnetic nanoparticles undergo Neel and Brownian relaxations as described in chapter 1 (sections 1.7.4 and 1.7.5). During the relaxation processes, the

magnetic nanoparticles transfer energy from the applied RF-AMF to the magnetic fluid causing the temperature of the later to increase with time.

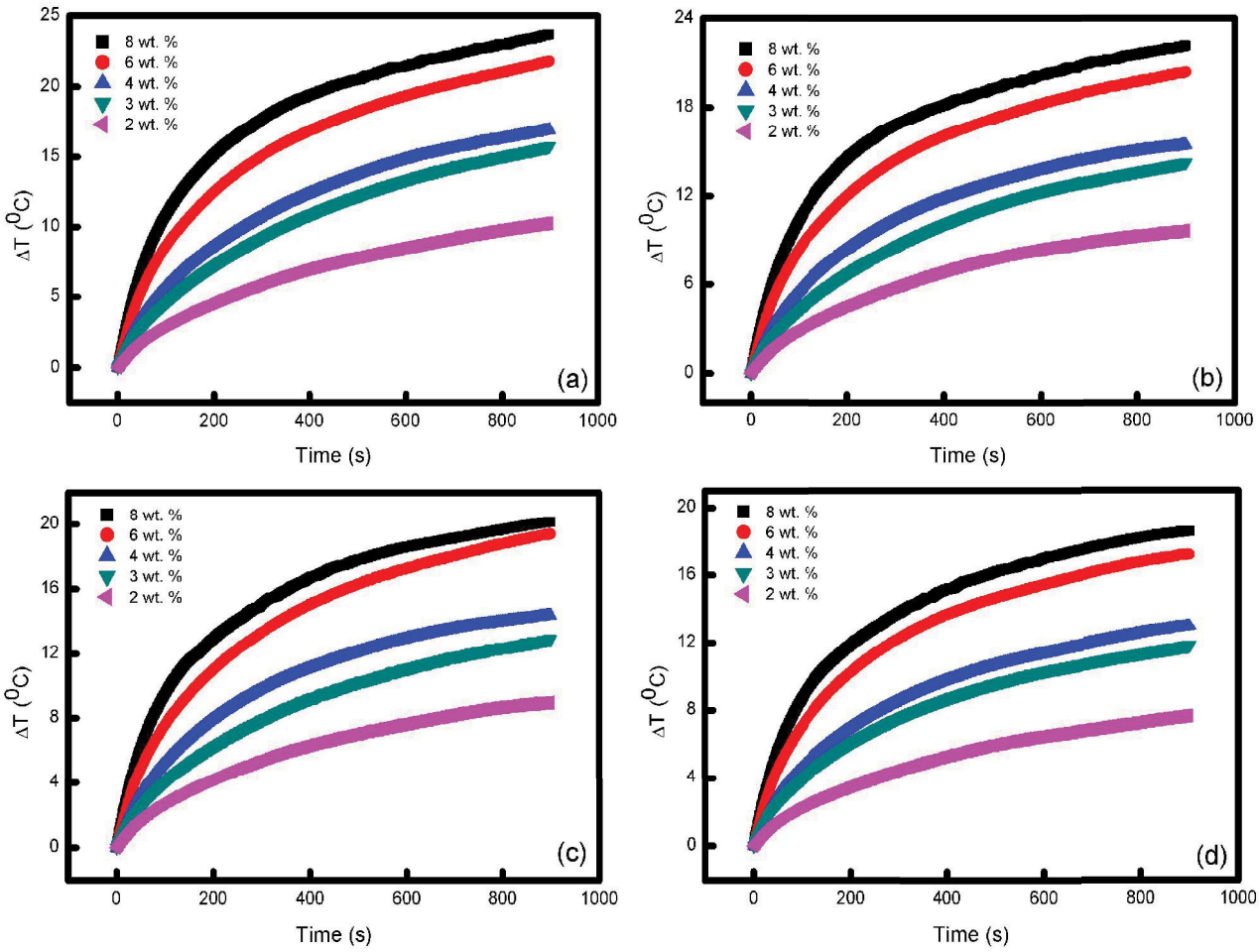


Figure 3.3 Infrared thermography based temperature increase ($\Delta T = T\text{-}T_i$), as a function of time, for the magnetic nanofluids containing TMAOH coated Fe_3O_4 MNP, at five different sample concentrations, during RF-AMF induced heating under four different external field amplitudes, viz., (a) 63.0, (b) 57.0, (c) 51.4 and (d) 45.3 kAm^{-1}, respectively.

Figure 3.4a shows the maximum temperature rise (ΔT_{max}) at the end of the heating period (t = 900 s) as a function of external field amplitude for the samples W1 (8 wt. %), W2 (6 wt. %), W3 (4 wt. %), W4 (3 wt. %) and W5 (2 wt. %). It can be clearly seen that ΔT_{max} increased with external field amplitude, which is also theoretically expected, as the RF-AMF

induced heating of magnetic nanofluids increases with applied magnetic field amplitude (dissipated power, P~H^2 from Eq. 1.16 in chapter 1). **Fig. 3.4b** shows the variation of ΔT_{max} with sample concentration for four different external field amplitudes where ΔT_{max} was found to increase with sample concentration and the values were significantly larger for higher external field amplitudes. The variation of ΔT_{max} with sample concentration (C) was empirically fitted using the phenomenological Box-Lucas equation of the form: $\Delta T_{max} = A_{conc}(1 - e^{-B_{conc}C})$, where A_{conc} and B_{conc} are numerical constants. The regression curves are also shown in **Fig. 3.4b** and **Table 3.1** shows the fit parameters in detail.

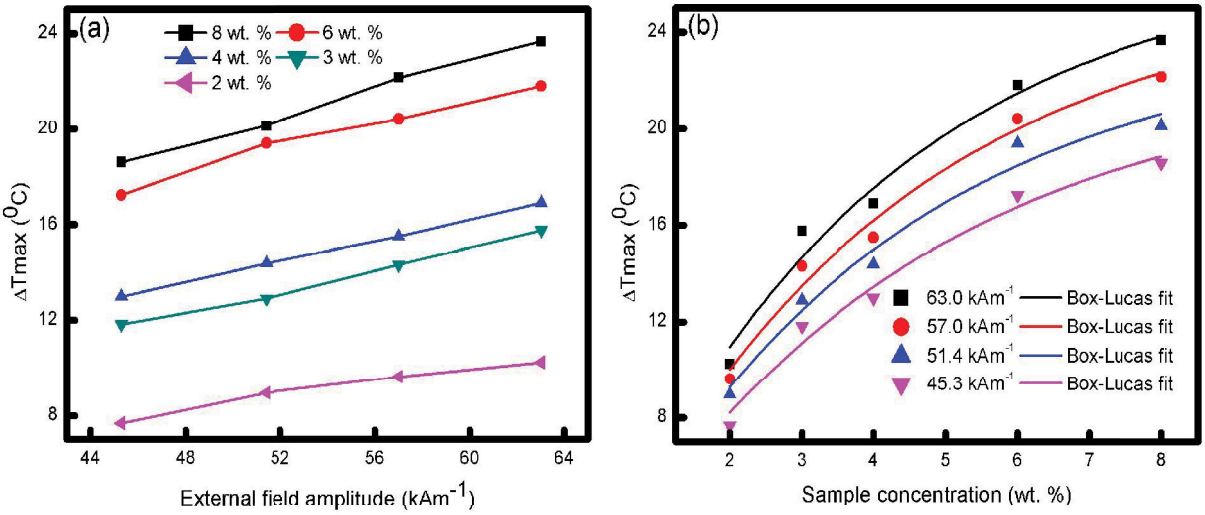


Figure 3.4: (a) Variation of maximum temperature rise (ΔT_{max}) at the end of the heating period (t = 900 s), as a function of external field amplitude for the water based magnetic fluids of five different concentrations. (b) Variation of ΔT_{max} as a function of sample concentration, during field induced heating under four different external field amplitudes. The variation of ΔT_{max} with sample concentration was fitted with Box-Lucas equation and the regression curves are also shown in the figure.

Table 3.1: Regression parameters for Box-Lucas fit of ΔT_{max} as a function of sample concentration.

RF-AMF amplitude (kAm^{-1})	**A_{conc} (^0C)**	**B_{conc} (dimensionless)**	**Adjusted R^2**
63.0	27.36 ± 1.86	0.26 ± 0.04	0.97
57.0	26.02 ± 1.65	0.24 ± 0.03	0.98
51.4	23.99 ± 1.74	0.24 ± 0.04	0.97
45.3	22.52 ± 1.69	0.23 ± 0.03	0.98

Figure 3.5a shows the horizontal temperature profiles across the sample W2 at various time intervals during RF-AMF induced heating under an external field amplitude of 63.0 kAm^{-1}. The surface temperature distribution was found to be extremely uniform in the magnetic fluids. **Fig. 3.5b** shows the 3-dimensional surface plot of the fluid temperature in the case of sample W2 at t = 400 s, at an external magnetic field amplitude of 63.0 kAm^{-1}. **Fig. 3.5b** clearly shows the uniformity of surface temperature distribution, which is essential in MFH based therapeutic procedure for ensuring uniform, homogenous and isotropic thermal dose to the target cells. Single point temperature measurement using a conventional fiber optic temperature sensor does not provide information on surface temperature distribution.

Figure 3.6 shows the IRT based temperature variation as a function of time for the sample W2, during RF-AMF induced heating under an external field amplitude of 57.0 kAm^{-1}, followed by natural cooling for three consecutive cycles. The reversible temperature rise and decay for all three cycles indicated very good thermal stability and repeatable thermal response of the magnetic fluid. Similar results were obtained for other samples under different external field amplitudes. The square wave, in **Fig. 3.6**, indicates the state of the external magnetic field, where, the upper and lower states indicate 'on' and 'off' conditions of the RF-AMF, respectively.

The initial rate of temperature rise ($\left.\frac{dT}{dt}\right|_{t=0}$) was determined under non-adiabatic limit from the temperature rise curves using linear regression analyses of the initial data (first 50 data points) and whole field approximation using phenomenological Box-Lucas equation. It was observed that the initial rate of temperature rise determined from linear regression analyses and Box-Lucas equation were similar to each other and the values determined from both techniques were linearly correlated (adjusted $R^2 = 0.99$). The slope and intercept of the linear regression analysis were found to be 1.07 ± 0.02 and 0.008 ± 0.001, respectively, indicating

good quantitative agreement between both techniques. Based on this finding, initial rates of temperature rise determined from linear regression analyses were only used for subsequent analyses.

Figure 3.7 shows the variation of initial rate of temperature rise, determined from linear regression analyses, as a function of sample concentration, where it can be seen that the initial rate of temperature rise increased with sample concentration and the values were larger for higher RF-AMF amplitudes.

3.2.2.2 Comparison of IRT and probe based temperature rise curves and convection correction

Figures 3.8a-b show the variation of ΔT, measured using IRT and conventional fiber optic temperature sensor, as a function of time during RF-AMF induced temperature rise under four different external field amplitudes for the samples W3 and W2, respectively. It can be seen that the temperature rise curves measured using IRT and conventional fiber optic temperature sensor were similar to each other. The temperature measured using IRT was initially higher up to a certain time and, thereafter, the IRT based curves crossed the fiber optic sensor based temperature curves. At larger time scales, ΔT_{max} values measured using IRT were slightly lower. Similar trends were observed for all the cases. The initial higher temperature followed by a crossover ultimately resulting in lower ΔT_{max} values were attributed to the internal and external convection phenomena. The crossover time (t_{cross}) and crossover temperature difference (ΔT_{cross}) were found to vary with sample concentration and RF-AMF amplitudes.

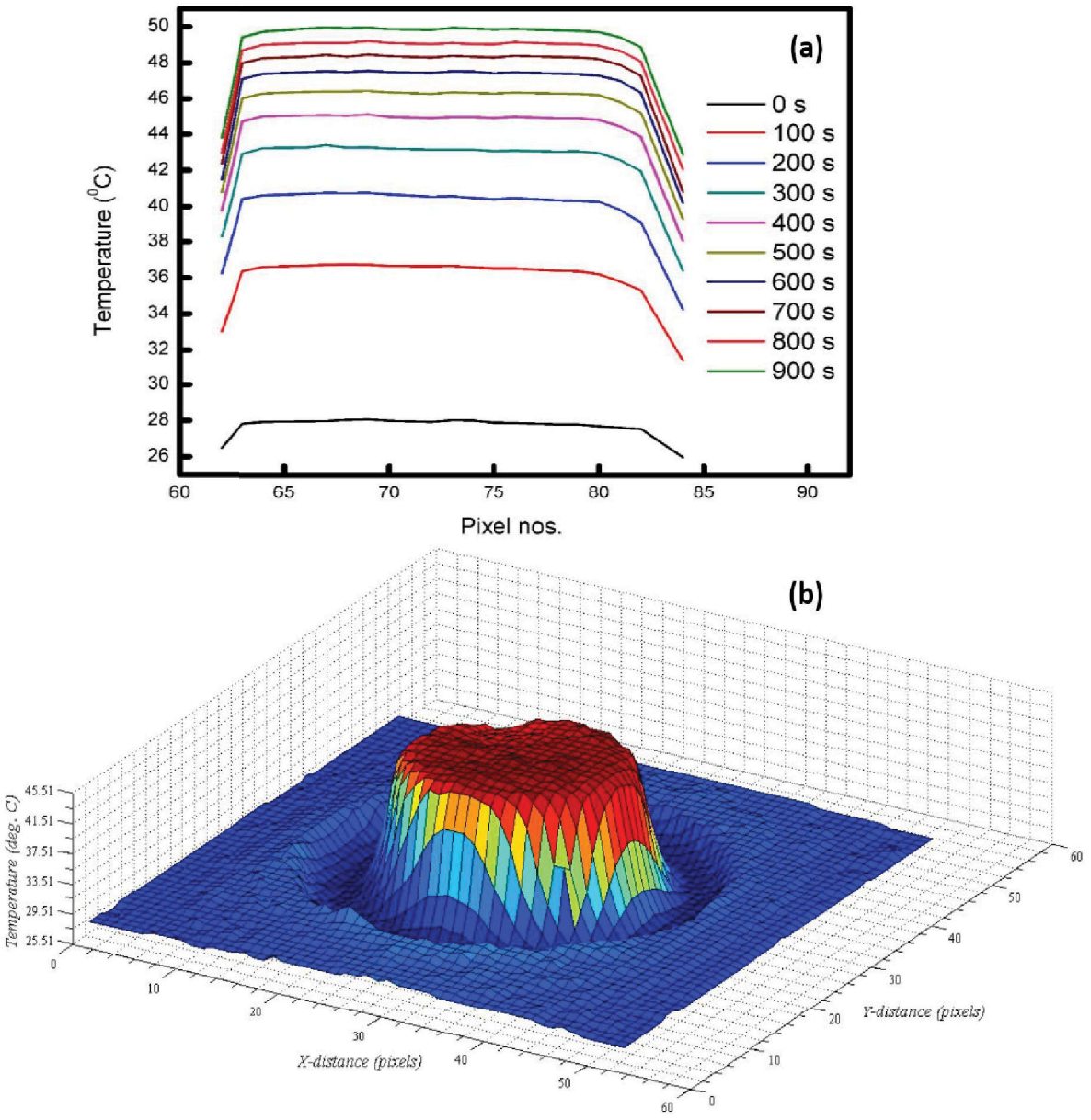


Figure 3.5: (a) Horizontal temperature profiles at various time intervals, during RF-AMF induced heating of the sample W2 (6 wt. %), under an external field amplitude of 63.0 kAm^{-1}. (b) 3-dimensional view of the surface temperature distribution of the sample W2 at t = 400 s, during RF-AMF induced heating under an external field amplitude of 63.0 kAm^{-1}.

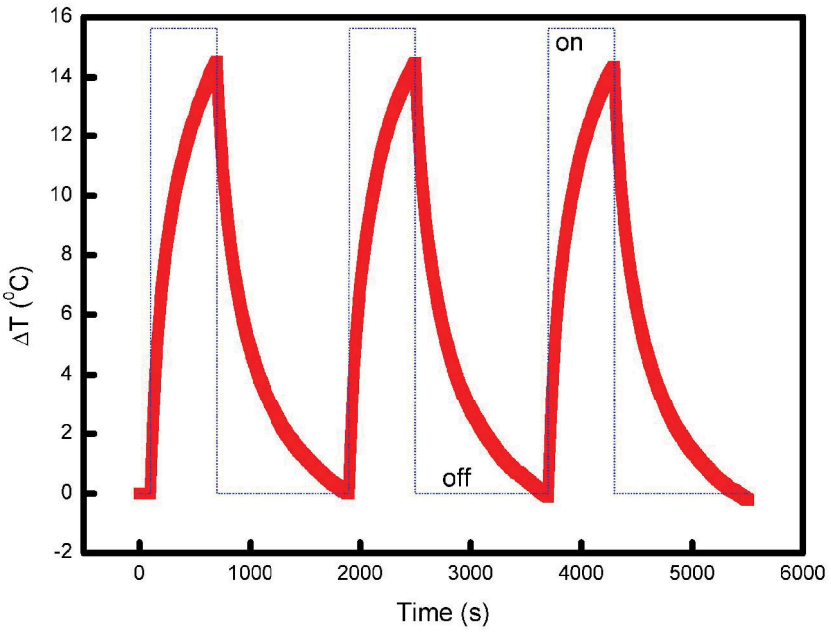


Figure 3.6: RF-AMF induced temperature rise followed by natural temperature decay for three consecutive cycles, for the sample W2 (6 wt. %), at an external field amplitude of 57.0 kAm^{-1}. The square wave indicates the state of the RF-AMF.

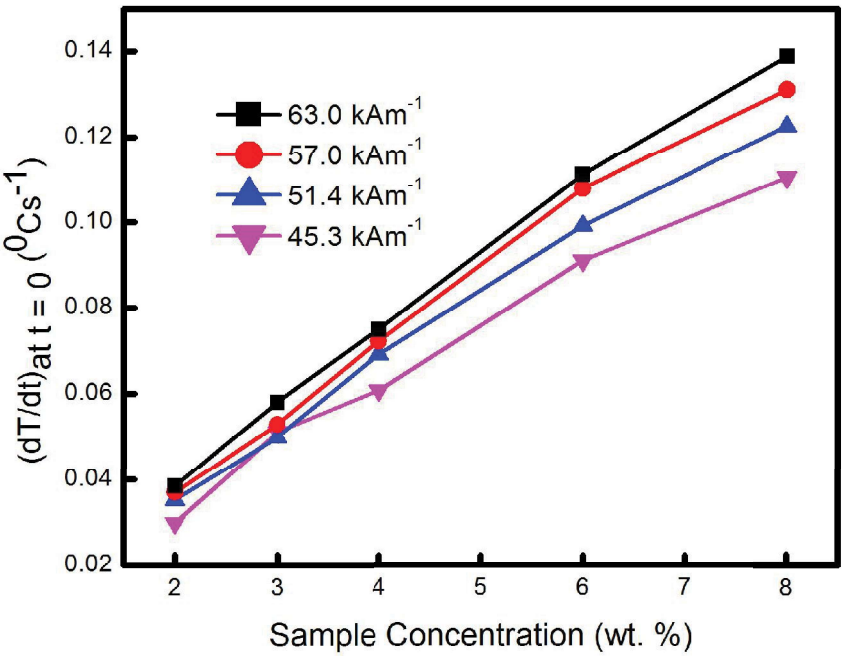


Figure 3.7: Variation of initial rate of temperature rise as a function of sample concentration for the water based magnetic nanofluids, during RF-AMF induced heating under four different external field amplitudes.

The temperature measurement performed using fiber optic temperature sensor reflects the internal fluid temperature of a particular location, whereas, IRT measures temperature over an area at the top surface of the magnetic nanofluids. During RF-AMF induced heating, the heat generated by the MNP is dissipated into the base fluid, causing a rise in the system temperature. This also results in rarefication of the base fluid, which subsequently moves upwards due to buoyancy forces [342, 396]. On the other hand, due to incompressibility of the fluid, comparatively cooler fluid, being heavier, travels downward due to gravity leading to a lower internal fluid temperature compared to the surface temperature. Hence, the top surface temperature rise measured using IRT was found to be higher, during initial time, as compared to the fiber optic temperature sensor. Such a scenario was earlier described by Huang et al. [342] using numerical simulations, where, they observed a RF-AMF induced maximum temperature rise just below the free surface of the fluid sample.

Beyond certain time, as temperature difference between the fluid and surrounding air increases, external convection loss sets in primarily from the top surface of the fluid which is exposed to the air. This caused the rate of temperature rise, measured using IRT, to decrease beyond certain time which resulted in the crossover of the IRT and fiber optic temperature sensor based curves. Beyond these crossover points the surface temperature rise measured using IRT was found to be lower compared to the rise in internal fluid temperature owing to the external convection losses. This ultimately resulted in lower ΔT_{max} values recorded by IRT as compared to the fiber optic temperature sensor, as shown in **Figs. 3.8a-b**.

Figure 3.8c shows the variation of ΔT_{cross} as a function of sample concentration for five different field amplitudes, where ΔT_{cross} indicates the temperature difference at the crossover point between IRT and fiber optic temperature sensor curves. It can be seen from **Fig. 3.8c** that ΔT_{cross} increased with sample concentration and the reason behind this observation is described below.

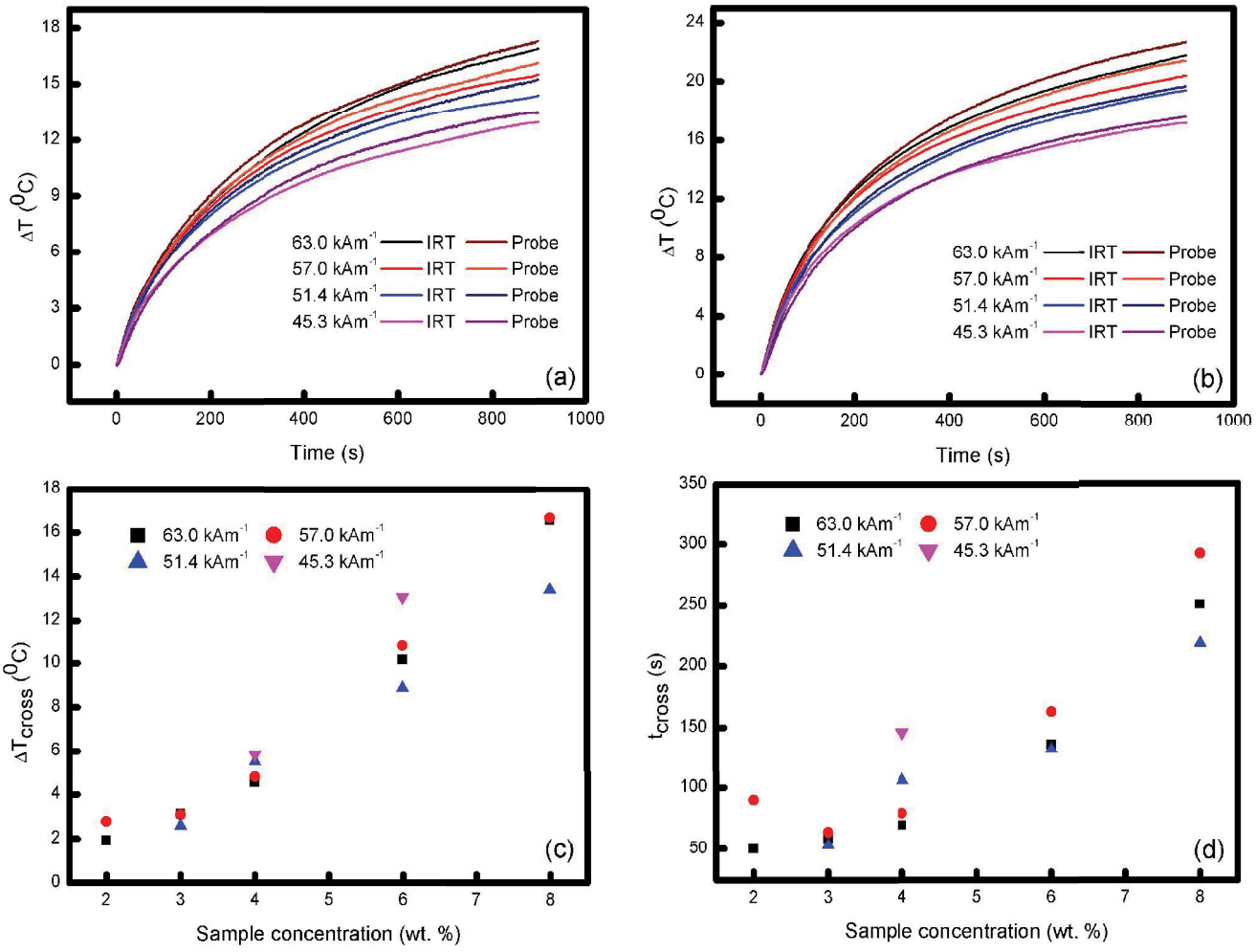


Figure 3.8: Variation of ΔT, measured using IRT and conventional fiber optic temperature sensor, as a function of time, during RF-AMF induced heating of the samples (a) W3 and (b) W2, under four different external field amplitudes. Variation of (c) crossover temperature difference (ΔT_{cross}) and (d) crossover time (t_{cross}) as a function of sample concentration.

In fluid convection, Prandtl number (P_r) is defined as the ratio of momentum diffusivity to thermal diffusivity ($P_r = \nu/\alpha_{diff}$, where ν is kinematic viscosity and α_{diff} is thermal diffusivity of the fluid) [396]. For water, P_r varies between 1-10 (typical ~ 7.56), which shows that $P_r >> 1$, indicating that momentum transfer is more favourable than heat transfer resulting in easier convection [396]. Hence, on exposure to an external RF-AMF, the heat generated inside the magnetic nanofluid is transferred to the top surface of the fluid primarily by convective circulation. For top facing natural (no forced air flow was present over the sample

surface) external convection scenario and $P_r > 0.5$ (satisfied in the present case), the Nusselt number ($N_{uL_{sh}}$) is given by: $N_{uL_{sh}} = 0.54(R_{aL_{sh}})^{0.25}$, where $R_{aL_{sh}}$ is the Rayleigh number and the subscript L_{sh} denotes the characteristic length scale of the system, which, for the present geometry, is given by $L_{sh}=D_{sh}/4=3.75\times10^{-3}$ m, where, D_{sh} is the diameter of the top surface of the sample holder (neglecting the thickness of the glass wall) [396]. $R_{aL_{sh}}$ is defined as $R_{aL_{sh}} = g_{ac}\beta_{le}(\Delta T)L_{sh}^3/\alpha_{diff}\nu$, where g_{ac} and β_{le} indicate acceleration due to gravity and coefficient of linear expansion, respectively, and ΔT is the temperature difference [396]. It has been reported that the viscosity of nanofluids increases with increasing sample concentration much beyond the predictions of Bachelor equation: $\eta_s/\eta_f = 1+2.5\psi_s+6.5\psi_s^2$, where, η_s and η_f indicate dynamic viscosity of nanofluid and carrier fluid, respectively, and ψ_s denotes sample concentration (volume fraction) [65]. Similarly, with increasing sample concentration, thermal conductivity of the nanofluid increases in accordance with the Maxwell's effective medium theory which is expressed as $k_s/k_f = \frac{k_p + 2k_f + 2\psi_s(k_p - k_f)}{k_p + 2k_f - \psi_s(k_p - k_f)}$, where k_s, k_f and k_p indicate nanofluid, carrier fluid and nanoparticle thermal conductivity, respectively [65]. Thermal diffusivity, α_{diff} is defined as the ratio of thermal conductivity to the product of density and specific heat, i.e., $\alpha_{diff} = k/\rho c$ [396]. Considering the product ρc to be almost constant, an increase in thermal conductivity k_s with sample concentration causes the thermal diffusivity to increase with sample concentration. Hence, with increasing sample concentration the product of α_{diff} and ν increases which results in a decreased $R_{aL_{sh}}$, ultimately leading to a reduced $N_{uL_{sh}}$ (as $N_{uL_{sh}} \propto R_{aL_{sh}}$) for higher sample concentration. Convective heat transfer coefficient (h_{conv}) is directly proportional to $N_{uL_{sh}}$ and can be expressed as $h_{conv} = k_a N_{uL_{sh}}/L_{sh}$, where k_a is the thermal conductivity of heat transfer fluid

(air in the present case) [396]. Hence, with increasing sample concentration, convective heat transfer coefficient decreases, which, in turn, increases the crossover temperature difference. This leads to an increase of ΔT_{cross} with sample concentration, as shown in **Fig. 3.8c**. Moreover, larger time is required for the magnetic fluids with higher concentration to achieve higher ΔT_{cross}. **Fig. 3.8d** shows the variation of t_{cross} (time required for the crossover to happen) as a function of sample concentration, where, t_{cross} was found to increase with sample concentration in agreement with the theoretical expectations.

The difference in the temperature reading between the IRT and fiber optic temperature curves ($\Delta T_{IRT\text{-}Probe}$), as a function of time, is shown in **Fig. 3.9a** for the sample W1 under four external field amplitudes, viz., 63.0, 57.0, 51.4 and 45.3 kAm^{-1}, where it can be seen that $\Delta T_{IRT\text{-}Probe}$ initially increased with time, attained a maximum and beyond that decreased with time. Similar trends were observed in the other samples under different external field amplitudes. The time corresponding to the maximum of $\Delta T_{IRT\text{-}Probe}$ was denoted as maximum error time ($t_{error\text{-}max}$) and **Fig. 3.9b** shows the variation of $t_{error\text{-}max}$ as a function of external field amplitude, where it can be seen that $t_{error\text{-}max}$ decreased with external field amplitude. This was attributed to the fact that higher external field amplitude caused the magnetic fluid temperature to increase faster leading to an earlier crossover between the IRT and fiber optic curves. **Figs. 3.9c-d** show the variation of $\Delta T_{IRT\text{-}Probe}$ as a function of ΔT_{IRT} for the sample W1 under an external field amplitude of 63.0 and 57.0 kAm^{-1}, respectively. The increasing trend of the $\Delta T_{IRT\text{-}Probe}$ curves was due to internal convection induced buoyancy effects, whereas, external convection losses caused $\Delta T_{IRT\text{-}Probe}$ to decrease for higher values of ΔT_{IRT}. An empirical data correction protocol was developed for incorporating the effects of internal and external convection phenomena. The increasing sections of the $\Delta T_{IRT\text{-}Probe}$ curves were fitted using a Box-Lucas equation of the form: $\Delta T_{IRT-\Pr obe} = m_{conv}(1 - e^{-n_{conv}\Delta T})$, where m_{conv}

and n_{conv} are numerical constants. For a small change in ΔT over a single stratification layer, $\Delta T_{IRT\text{-}Probe}$ is directly proportional to ΔT (using Taylor's expansion) which indicates the linear dependence of excess heat transfer across a single layer, on the temperature difference at both ends of the layer. For a series of the stratification layers, stacked over each other, the Box-Lucas equation was found to describe the scenario quite successfully. **Fig. 3.9e** shows the increasing section of the $\Delta T_{IRT\text{-}Probe}$ curve for the sample W1 under an external field amplitude of 57.0 kAm^{-1}, as a function of ΔT_{IRT}, along with the fitted Box-Lucas curve. The adjusted R^2 value of the regression analysis was found to be 0.99, which indicated good accuracy of the model. The values of m_{conv} and n_{conv} in this case were 1.07 (± 0.01) ^0C and 0.93 (± 0.02) $^0C^{-1}$, respectively.

Figure 3.9f shows the decreasing section of the $\Delta T_{IRT\text{-}Probe}$ curve for the sample W1 under an external field amplitude of 57.0 kAm^{-1} as a function of ΔT_{IRT}. The error involved in this case is purely due to external convection losses and hence, the heat loss was fitted with a linear function of ΔT_{IRT} with a negative slope, i.e., $\Delta T_{IRT\text{-}Probe} = -c_1 \times \Delta T_{IRT} + c_2$, where, c_1 and c_2 are numerical constants, which were determined using linear regression analyses. For better accuracy, the data was fitted with a single as well as dual slope linear regression analyses. **Table 3.2** shows the regression parameters in details. Based on the obtained calibration curves for the increasing and decreasing sections of the $\Delta T_{IRT\text{-}Probe}$ curves, data corrections were performed to check the efficacy of the above mentioned convection correction method.

Figures. 3.10a-b show the variation of ΔT as a function of time for the samples W1 and W2 under RF-AMF amplitudes of 57.0 and 63.0 kAm^{-1}, respectively. Here, the ΔT curves experimentally recorded using IRT and fiber optic temperature sensor along with the single and dual slope corrected curves are shown and perfect overlapping of the convection corrected fiber optic curves with the experimental IRT curves can be clearly seen. The dual slope corrected curves were found to be more accurate. **Fig. 3.10** clearly shows the efficacy

of the convection correction methodology for studying RF-AMF induced heating of magnetic fluids using IRT and validates the applicability of IRT based temperature measurement during MFH for water based ferrofluids.

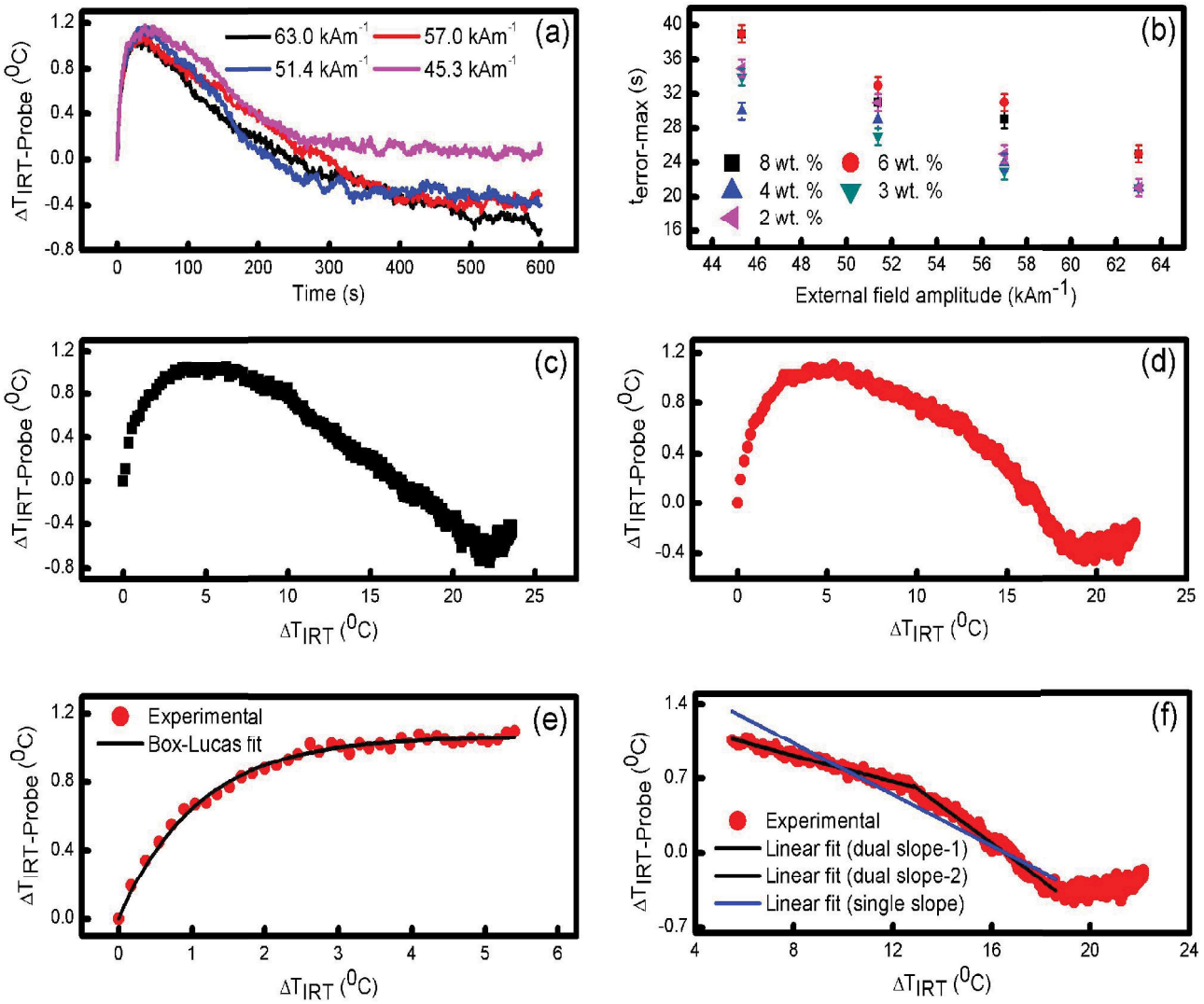


Figure 3.9: (a) Variation of $\Delta T_{IRT\text{-}Probe}$ as a function of time, during RF-AMF induced heating of the sample W1 under four different external field amplitudes. (b) Variation of the time corresponding to maximum error ($t_{error\text{-}max}$), as a function of RF-AMF amplitudes, for magnetic fluids of five different concentration. (c) Variation of $\Delta T_{IRT\text{-}Probe}$ as a function of ΔT_{IRT} during RF-AMF induced heating of the sample W1, under RF-AMF amplitudes of (c) 63.0 kAm^{-1} and (d) 57.0 kAm^{-1}. (e) Box-Lucas fitting of the increasing part of $\Delta T_{IRT\text{-}Probe}$ vs. ΔT_{IRT} curve for the sample W1, during RF-AMF induced heating under an external field amplitude of 57.0 kAm^{-1}. (f) Linear regression analyses of the decreasing part of $\Delta T_{IRT\text{-}Probe}$ vs. ΔT_{IRT} curve for the sample W1, during RF-AMF induced heating under an external field amplitude of 57.0 kAm^{-1}. Linear fits corresponding to single and dual slope correction procedures are shown in the figure.

Table 3.2: Parameters for linear regression analyses of the decreasing section of the $\Delta T_{IRT-Probe}$ vs. ΔT_{IRT} curve for the sample W1, during RF-AMF induced heating, under an external field amplitude of 57.0 kAm^{-1}.

Method	Slope (dimensionless)	Intercept ($^0C\ s^{-1}$)	Adjusted R^2
Single slope	-0.121 ± 0.001	1.99 ± 0.02	0.94
Dual slope	-0.061 ± 0.001	1.41 ± 0.01	0.96
	-0.171 ± 0.002	2.83 ± 0.03	0.98

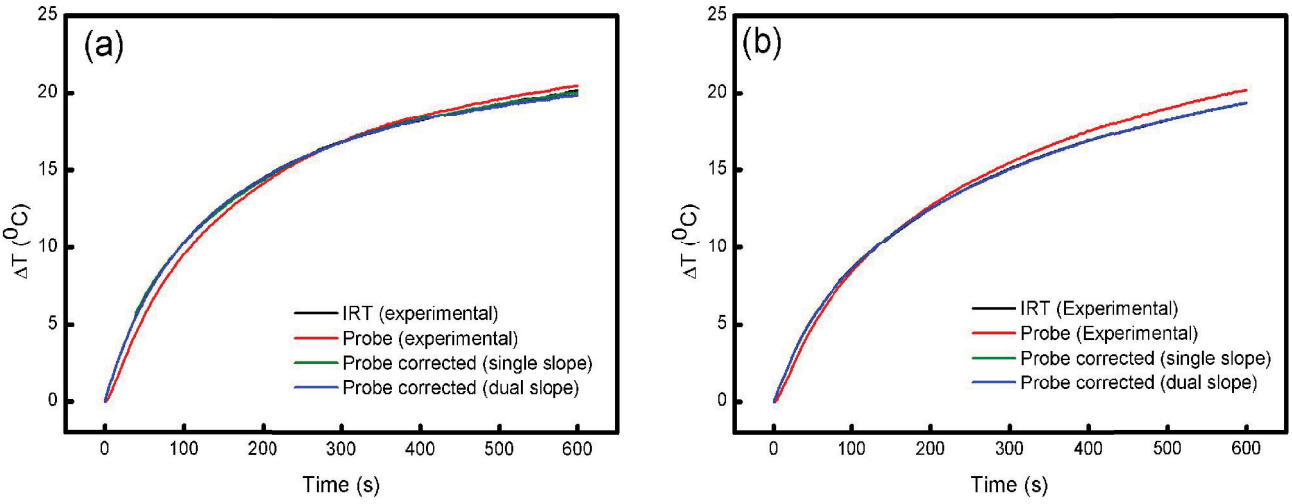


Figure 3.10: Empirical data correction protocol for ΔT vs. time curves, recorded using IRT and conventional fiber optic temperature sensor for the samples (a) W1 and (b) W2, during RF-AMF induced heating under external field amplitudes of 57.0 and 63.0 kAm^{-1}, respectively.

Specific absorption rate was determined from the initial rate of temperature rise using the equation: $SAR = \frac{\rho_{samp} c_{samp}}{m_{Fe}} \left.\frac{dT}{dt}\right|_{t=0}$ (Eq. 1.19 in chapter 1). **Table 3.3** shows the numerical values of SAR determined from fiber optic temperature sensor and IRT. The SAR values obtained from the IRT data, after incorporating convection correction, are also shown in **Table 3.3**, where it can be seen that the convection corrected SAR values are in very good agreement with those obtained from fiber optic temperature sensor (maximum error ~ ± 3.4

%), which shows the efficacy and applicability of IRT based technique for accurate determination of SAR during MFH studies. The highest SAR was found to be ~ 135.9 (± 4.6) W/g_{Fe} for the sample with 3 wt. % MNP concentration under an external field amplitude of 63.0 kAm^{-1} (f = 126 kHz). Vaishnava et al. [409] studied the RF-AMF induced heating of TMAOH coated Fe_3O_4 nanofluid under an RF-AMF amplitude of 20 kAm^{-1} and f = 125 kHz. Though the SAR value was not reported by them, they observed a ΔT_{max} of ~ 15.5 ^0C at t = 900 s which is much lower than the ΔT_{max} (at t = 900 s) obtained in the present study (highest ΔT_{max} ~ 23.6 ^0C for a field amplitude of 63.0 kAm^{-1} in the case of sample W1). The higher ΔT_{max} observed in the present study was attributed to the larger RF-AMF amplitudes used.

Table 3.3: Comparison of SAR obtained using IRT (SAR-IRT) and fiber optic temperature sensor (SAR-FO), along with the convection corrected SAR values (SAR-IRT-CC).

Sample code	Sample (wt. %)	RF-AMF amplitude (kAm^{-1})	SAR-IRT (W/g_{Fe})	SAR-FO (W/g_{Fe})	SAR-IRT-CC (W/g_{Fe})
W1	8	45.3	96.44 ± 3.5	84.80 ± 2.8	86.88 ± 3.5
		51.4	107.01 ± 3.7	95.29 ± 2.3	97.58 ± 3.7
		57.0	114.43 ± 2.8	104.23 ± 3.4	106.97 ± 2.8
		63.0	121.17 ± 2.7	111.15 ± 3.1	113.41 ± 2.7
W2	6	45.3	106.02 ± 2.8	96.59 ± 2.1	98.2 ± 2.8
		51.4	115.45 ± 2.4	108.99 ± 2.9	111.35 ± 2.4
		57.0	125.62 ± 3.7	117.29 ± 2.8	120.61 ± 3.7
		63.0	129.44 ± 4.0	123.87 ± 3.2	127.08 ± 4.0
W3	4	45.3	106.11 ± 3.4	98.10 ± 3.6	99.37 ± 3.4
		51.4	120.81 ± 3.9	113.51 ± 3.8	115.49 ± 3.9
		57.0	126.15 ± 3.1	122.00 ± 2.5	124.00 ± 3.1
		63.0	131.04 ± 3.7	127.95 ± 3.8	129.25 ± 3.7
W4	3	45.3	118.67 ± 4.2	101.42 ± 4.6	103.64 ± 4.2
		51.4	115.92 ± 5.4	121.51 ± 4.8	120.72 ± 5.4
		57.0	122.86 ± 5.1	122.30 ± 5.3	122.39 ± 5.1
		63.0	134.94 ± 4.6	136.94 ± 3.9	135.98 ± 4.6
W5	2	45.3	104.37 ± 6.8	95.08 ± 5.1	98.29 ± 6.8
		51.4	123.08 ± 6.2	112.16 ± 5.6	114.18 ± 6.2
		57.0	129.23 ± 6.5	128.28 ± 4.8	128.92 ± 6.5
		63.0	134.57 ± 6.8	136.00 ± 5.2	135.19 ± 6.8

3.2.2.3 Variation of specific absorption rate (SAR) with sample concentration and RF-AMF amplitude

Figure 3.11a shows the variation of convection corrected SAR as a function of sample concentration for the samples W1-W5. It can be seen from **Fig. 3.11a** that SAR decreased with sample concentration which was attributed to the increased dipolar interaction for higher sample concentration [198, 200, 279, 280, 410]. The dipolar interaction between two MNP (indicated by i and j, respectively) can be expressed as $E_{Dipolar}^{i,j} = \frac{\vec{\mu}_i.\vec{\mu}_j}{r_{i,j}^3} - \frac{3(\vec{\mu}_i.\vec{r}_{i,j})(\vec{\mu}_j.\vec{r}_{i,j})}{r_{i,j}^5}$, where, $\vec{\mu}_i$ and $\vec{\mu}_j$ are the magnetic moments of the ith and jth MNP, respectively, and $r_{i,j}$ and $E_{Dipolar}^{i,j}$ indicate interparticle distance and dipolar interaction energy, respectively [411]. It can be seen from the above expression that interparticle distance strongly influences the dipolar interaction energy and hence, with increasing sample concentration, as interparticle distance decreases, dipolar interaction is enhanced. Morup and Tronc [412] theoretically showed that Neel relaxation time (τ_N) decreases with increasing strength of the dipolar interaction and can be expressed as $\tau_N = \tau_0[\sigma_{AT} - \frac{\beta_{av}^2}{3}(1 - 0.75\sigma_{AT}^{-1})]$, where $\sigma_{AT} = KV_p/k_BT$ and $\beta_{av}^2 = \mu^2\left\langle \vec{B}_d^{\,2} \right\rangle /(k_BT)^2$. Here, $\left\langle \vec{B}_d^{\,2} \right\rangle$ indicates fluctuations of the dipolar field vector around a single particle. It can be clearly seen from the above expression that with increasing dipolar interaction strength, at higher sample concentration, Neel relaxation time decreases. The decrease in Neel relaxation time with increasing sample concentration was also reported by Urtizberea et al. [200] for maghemite based ferrofluids. Such lowering in Neel relaxation time results in a decreased effective relaxation time (τ) for the magnetic nanofluids as Brownian relaxation time (τ_B) is found to be relatively independent of dipolar interaction [413]. For the cases where the product of cyclic frequency (ω) and τ is significantly lower

than unity, i.e., $\omega\tau << 1$, SAR is directly proportional to $\omega\tau$ which leads to a reduced SAR with increasing sample concentration [52].

Under the influence of an external magnetic field, water based magnetic nanofluids are prone to agglomeration [414]. Such agglomeration results in an increased effective diameter (D_{eff}) which drastically enhances the dipolar interaction as dipole-dipole interaction between two MNP is directly proportional to D_{eff}^{6} [64]. Dynamic light scattering based studies indicated that the average hydrodynamic size in the highest concentration sample (W1 with 8 wt. %) was ~ 51 (± 6.3) nm which showed the presence of slight agglomeration in the water based TMAOH coated iron oxide nanofluids. Such agglomeration significantly reduces SAR at higher sample concentration. This is in agreement with the recent results obtained by Guibert et al. [202], where, it was shown that SAR decreased with increasing size of agglomerates.

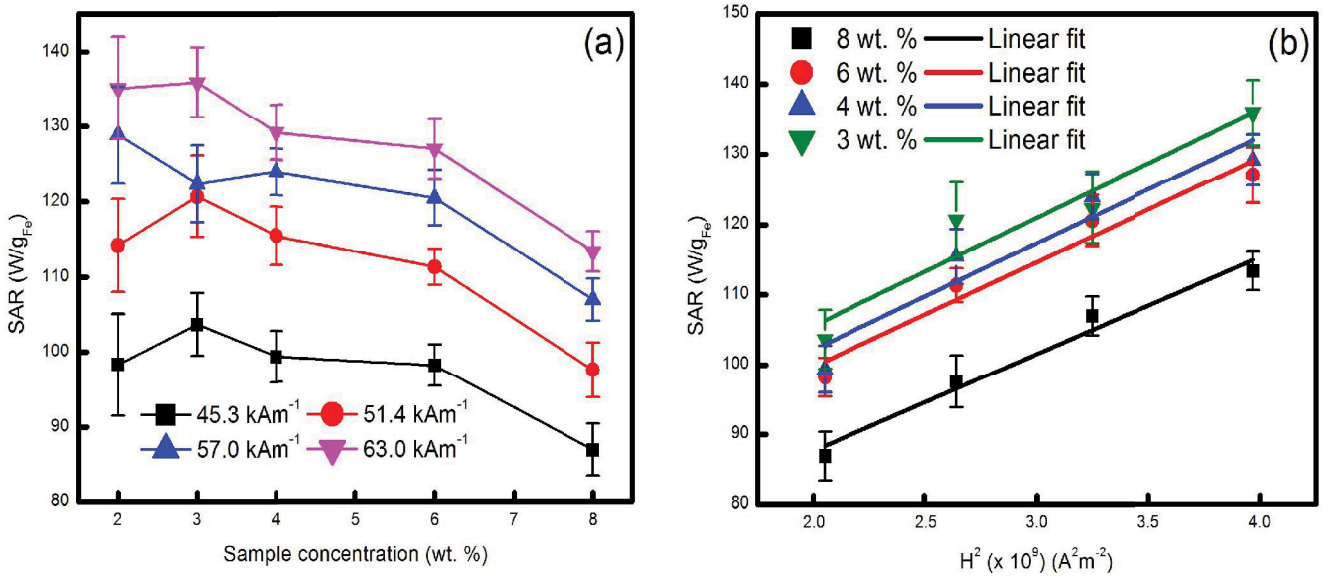


Figure 3.11: (a) Variation of convection corrected SAR as a function of sample concentration. SAR decreased with increasing sample concentration due to an enhancement of dipolar interaction. (b) Variation of convection corrected SAR as a function of square of the external field amplitudes for water based magnetic fluids of four different concentrations. SAR increased linearly with H^2 and the linear fits are shown by solid lines.

Figure 3.11b shows the variation of convection corrected SAR as a function of square of the external field amplitudes, where it can be seen that the SAR increased linearly (adjusted R^2 were ~ 0.96, 0.94, 0.88 and 0.88 for the samples W1-W4, respectively) with H^2 which is in accordance with the Rosensweig's model [51, 52] of RF-AMF induced heating under linear response regime. For a fixed sample concentration, as RF-AMF amplitude increases, electromagnetic energy density varies as ~ H^2 leading to a similar variation in SAR [282].

3.3 IRT based MFH studies on oil based ferrofluid containing oleic acid coated Fe_3O_4 MNP

For universal acceptance of IRT as a remote temperature measurement probe, the IRT based temperature measurement along with the convection correction protocol was performed in oil (kerosene) based magnetic fluids, which have widely different thermal diffusivity (thermal diffusivity of water and kerosene are ~ 1.43×10^{-7} and 7.9×10^{-8} m^2s^{-1}, respectively) and Prandtl number (Prandtl number for water and kerosene varies between 1-10 (typical 7.56) and 18.3-25.7, respectively). A higher Prandtl number for kerosene indicates larger momentum diffusivity and hence, faster convective circulation.

IRT based direct measurement of RF-AMF induced rise in sample temperature in the case of kerosene based magnetic fluid containing well dispersed oleic acid coated Fe_3O_4 MNP is reported here. The data analysis protocol for convection correction is tested for kerosene based magnetic nanofluids and the variation of SAR with external field amplitude is also probed. The oil based systems are well known for their stability as compared to the water based systems and hence, the variation of SAR as a function of sample concentration is also investigated for higher values of MNP loading, which also served as a motivation for using oil based system.

3.3.1 Experimental details and characterization studies

Oleic acid coated Fe_3O_4 MNP were synthesized using a chemical co-precipitation method as discussed in section 2.1.2 in chapter 2 and dispersed in kerosene. A master solution of 23 wt. % (hereafter indicated as K1) was prepared and later diluted to 16.5, 11 and 7.5 wt. % (hereafter indicated as K2, K3 and K4, respectively). The synthesized MNP were characterized using XRD, VSM, SAXS, DLS and FTIR spectroscopy in ATR mode using ZnSe crystal. XRD data indicated the presence of cubic spinel structure of Fe_3O_4 and the average crystallite size was obtained as ~ 8.0 (± 0.8) nm. VSM data indicated a saturation magnetization of ~ 42 emu/g. This value is significantly lower than the bulk saturation magnetization of 92 emu/g, but substantially higher than the values (like 34.39 emu/g for 6 nm and 22 emu/g for 9 nm Fe_3O_4 MNP coated with oleic acid) reported in other studies [345, 415]. The room temperature M-H curve did not show any hysteresis indicating superparamagnetic behaviour. The distance distribution function [P(r)] was calculated by performing Fourier transform of the scattering intensity obtained from SAXS and **Fig. 3.12a** shows the variation of P(r) as a function of MNP diameter. Using a log-normal distribution, the most probable size was obtained as 7 nm (σ_{ln} = 0.15) which was found in good agreement with the crystallite size measured using XRD. The **inset of Fig. 3.12a** shows the variation of ln(I(q)) as a function of ln(q), where, q indicates wave vector, and it was observed that for high q region (Porod's region), ln(I(q)) varied linearly with ln(q) with a slope of -3.9 ± 0.01. This indicated the spherical shape of the synthesized MNP (for spherical particles, $I(q) \sim q^{-4}$) [332]. **Fig. 3.12b** shows the hydrodynamic size distribution of the oleic acid coated MNP dispersed in kerosene obtained from DLS studies, where, a narrow unimodal size distribution was obtained. The data was fitted with a log-normal distribution (also shown in **Fig. 3.12b**) and the most probable size was found to be 10.4 nm (σ_{ln} = 0.2). The higher hydrodynamic size was attributed to the additional contributions from the surfactant and solvent layer

around the MNP. Here, the carboxylic acid group of oleic acid binds to the surface of the MNP and the aliphatic chains extend into the non-polar solvent [66]. **Fig. 3.12c** shows the FTIR spectra of the oleic acid coated MNP. The presence of a Fe-O characteristic absorption band at 583 cm^{-1} and a shoulder at 631 cm^{-1} can be clearly seen and were attributed to the symmetric stretching of Fe-O bonds of Fe_3O_4 [313, 315] The sharp absorption bands observed at 2923 and 2855 cm^{-1} were due to asymmetric and symmetric stretching of the $–CH_2-$ group of the oleic acid, respectively [313]. The strong absorption band located at 2362 cm^{-1} corresponded to the stretching vibrations of C=O from atmospheric CO_2 interference [315]. The absorption bands observed at 1607 and 1460 cm^{-1} were attributed to the asymmetric and symmetric stretching of the carboxylate (COO^-) functional group [313]. The absorption band observed at 1377 cm^{-1} was attributed to the $–CH_3$ umbrella mode of oleic acid [416]. The feeble absorption band at 1716 cm^{-1} was assigned to the stretching of carbonyl group of free oleic acid present in the sample [313, 416]. The FTIR data indicated that oleic acid was chemisorbed on the surface of Fe_3O_4 nanoparticles [417].

Hyperthermia experiments were carried out at a fixed frequency of 126 kHz and under five different magnetic field amplitudes, viz., 57.3, 51.4, 45.0, 36.7 and 26.0 kAm^{-1} using a high frequency induction heating system. The sample in a glass vial was kept at the centre of the heating coil supported by a custom made non-conducting fixture. Sample temperature measurements were performed using IRT and the temperature values were compared using a conventional fiber optic temperature sensor. Detailed experimental procedure is described in sections 2.4 and 2.5 (chapter 2). The final SAR values were reported as W/g_{Fe}, where, g_{Fe} indicate the mass of magnetic phase only [345]. The specific heat capacity and density of kerosene was considered as 2.01 $Jg^{-1}K^{-1}$ and 0.81 g/cc.

3.3.2 Results and discussions

3.3.2.1 IRT based temperature measurement during RF-AMF induced heating

Figures 3.13a-o show typical infrared images of the sample K1 (23 wt. %) at time t = 0, 10, 20, 30, 40, 50, 60, 70, 80, 90, 100, 110, 120, 130 and 140 s, respectively, during RF-AMF induced heating under an external field amplitude of 57.3 kAm^{-1}. The pseudo colour coded temperature scales are also shown along with the images. Though the room temperature was fixed at 28 (± 1) ^{0}C, the coil and the glass vial appeared at 23.45 ^{0}C (associated with a pseudo colour of black), which was due to difference in emissivity of the coil, glass and fluid sample. Hence, the true temperature for the samples (indicated by bright yellow with an associated temperature of 27.66 ^{0}C) was obtained after suitable emissivity (~ 0.92) corrections on the acquired infrared images.

It can be clearly seen from **Fig. 3.13** that the sample temperature increased with time due to RF-AMF induced heating. In the later images (i.e., **Figs. 3.13e-o**), the heating coil was not visible due to insufficient thermal contrast. It can be further seen from **Fig. 3.13** that the temperature of the custom made electrically non-conducting fixture, adjacent to the sample vial, also increased with time which was visually discernible. This was attributed to the heat loss from the sample vial to the fixture, a point often unnoticed with fiber optic temperature measurements, though important when it comes to clinical use of MFH. This result shows that the whole field temperature mapping using IRT is an excellent tool to measure the RF-AMF induced temperature rise and also for assessing thermal losses during experiment. Similar results were obtained for other samples and the observations were in good agreement with those obtained from fiber optic temperature sensor.

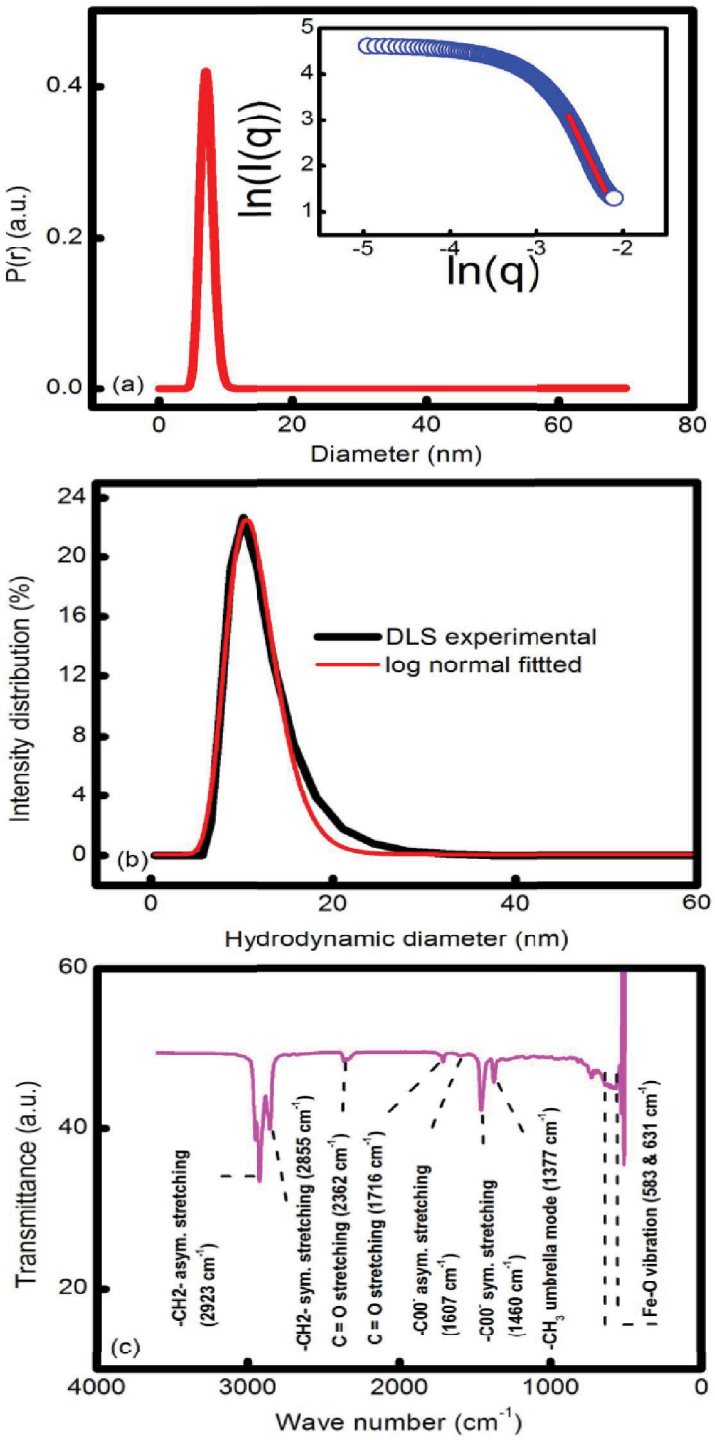


Figure 3.12: (a) Distance distribution function, P(r), obtained from SAXS, as a function of MNP diameter. (Inset) Variation of ln(I(q)) as a function of ln(q) for the synthesized MNP. The high q (Porod's region) data is fitted with a linear regression analysis (also shown in the figure). (b) Hydrodynamic size distribution of the MNP dispersed in kerosene. The data is fitted with a log-normal distribution (also shown in the figure). (c) FTIR spectra of the oleic acid coated MNP, where, the major absorption bands are indexed.

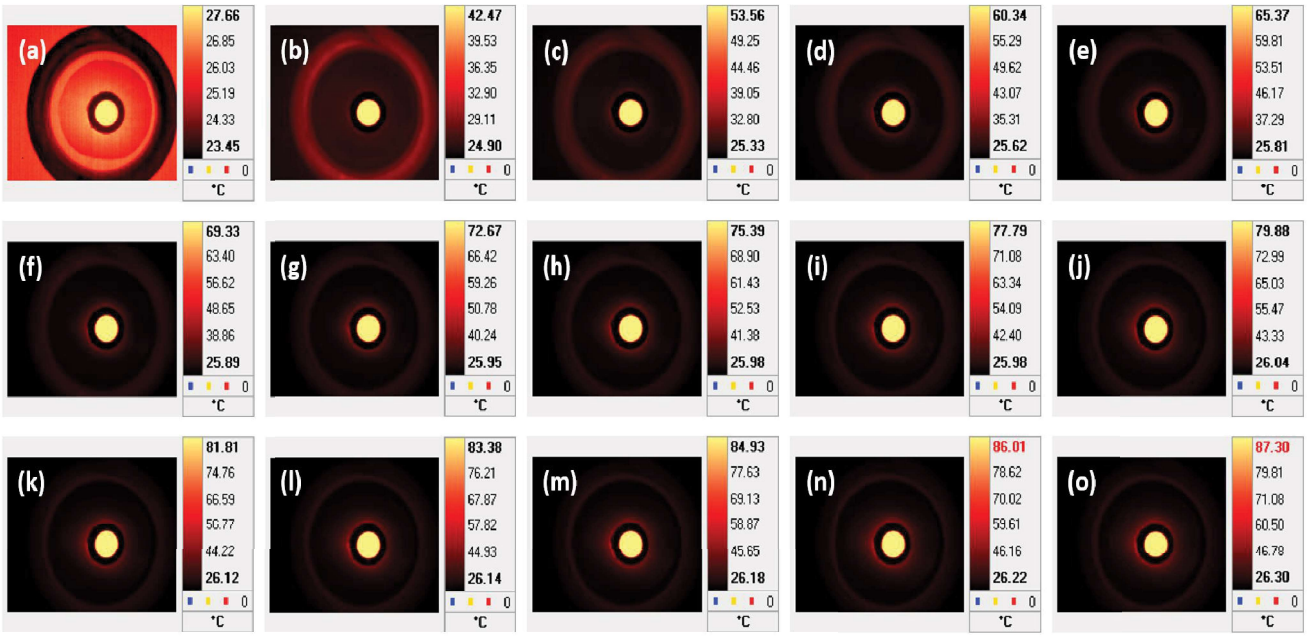


Figure 3.13: Typical infrared images of the sample K1 (23 wt. %) at time t = (a) 0, (b) 10, (c) 20, (d) 30, (e) 40, (f) 50, (g) 60, (h) 70, (i) 80, (j) 90, (k) 100, (l) 110, (m) 120, (n) 130 and (o) 140 s, respectively, during RF-AMF induced heating. The pseudo colour coded temperature scales are also shown along with the images. The RF-AMF amplitude was kept constant at 57.3 kAm^{-1}.

Spatial averaging over several pixels were performed to obtain the average temperature rise of the samples during RF-AMF induced heating which resulted in good accuracy of the IRT based non-contact temperature measurement technique. **Figs. 3.14a-d** show the variation of ΔT, measured using IRT, as a function of time during RF-AMF induced heating at five different external field amplitudes for the samples K1-K4, respectively. It can be clearly seen that the temperature increased with time during RF-AMF induced heating, which was found to be in agreement with our earlier observations (**Fig. 3.13**). The MNP get heated up due to Neel-Brownian relaxation and the temperature rise increased with increasing RF-AMF amplitude [16, 50, 51]. It was also observed that the rate of temperature rise was initially higher and decreased with time due to thermal losses to the surrounding. **Figs. 3.14e-f** show

the variations of ΔT_{max} (maximum temperature rise at the end of heating phase) as a function of RF-AMF amplitude and sample concentration, respectively. The horizontal lines in **Figs. 3.14e-f** indicate a temperature rise of 14 ^{0}C, which is the desired ΔT_{max} for hyperthermia applications. Apart from the sample K4, at H = 36.7 and 26.0 kAm^{-1}, the ΔT_{max} values for all other samples were found to be higher than the hyperthermia limit. **Fig. 3.14e-f** show that for a fixed sample concentration, ΔT_{max} continuously increased with RF-AMF amplitude and for a fixed RF-AMF amplitude, ΔT_{max} was higher for larger sample concentration.

IRT is a whole field temperature mapping technique and **Fig. 3.15a** shows the horizontal line scans across the top surface of the sample K1 at time t = 0-150 s, in steps of 10 s, during RF-AMF induced heating under a field amplitude of 57.3 kAm^{-1}. It can be clearly seen from **Fig. 3.15a** that sample temperature increased with time. The observed flat surface temperature distribution during RF-AMF induced heating indicated uniform sample temperature increase without any temperature hot spot. **Fig. 3.15b** shows the 3-dimensional surface plot at time t = 30 s during RF-AMF induced heating of sample K1 under a field amplitude of 57.3 kAm^{-1}, which shows the uniformity of the fluid surface temperature, ensuring homogenous and isotropic temperature rise in the oil based ferrofluids during RF-AMF induced heating. Single point temperature measurement using fiber optic temperature sensor does not provide sufficient information on the uniformity in the temperature profile of the magnetic fluids and hence, IRT based surface temperature mapping was found to have several advantages.

Figure 3.16a shows the IRT based temperature variation as a function of time for the sample K1 during RF-AMF induced heating under an external field amplitude of 57.3 kAm^{-1} followed by natural cooling for three consecutive cycles. It can be seen from **Fig. 3.16a** that the sample temperature increased on exposure to RF-AMF and started decreasing when the field was turned off. The reversible temperature rise and decay for all three cycles indicated the excellent stability and repeatable thermal response of the magnetic fluids.

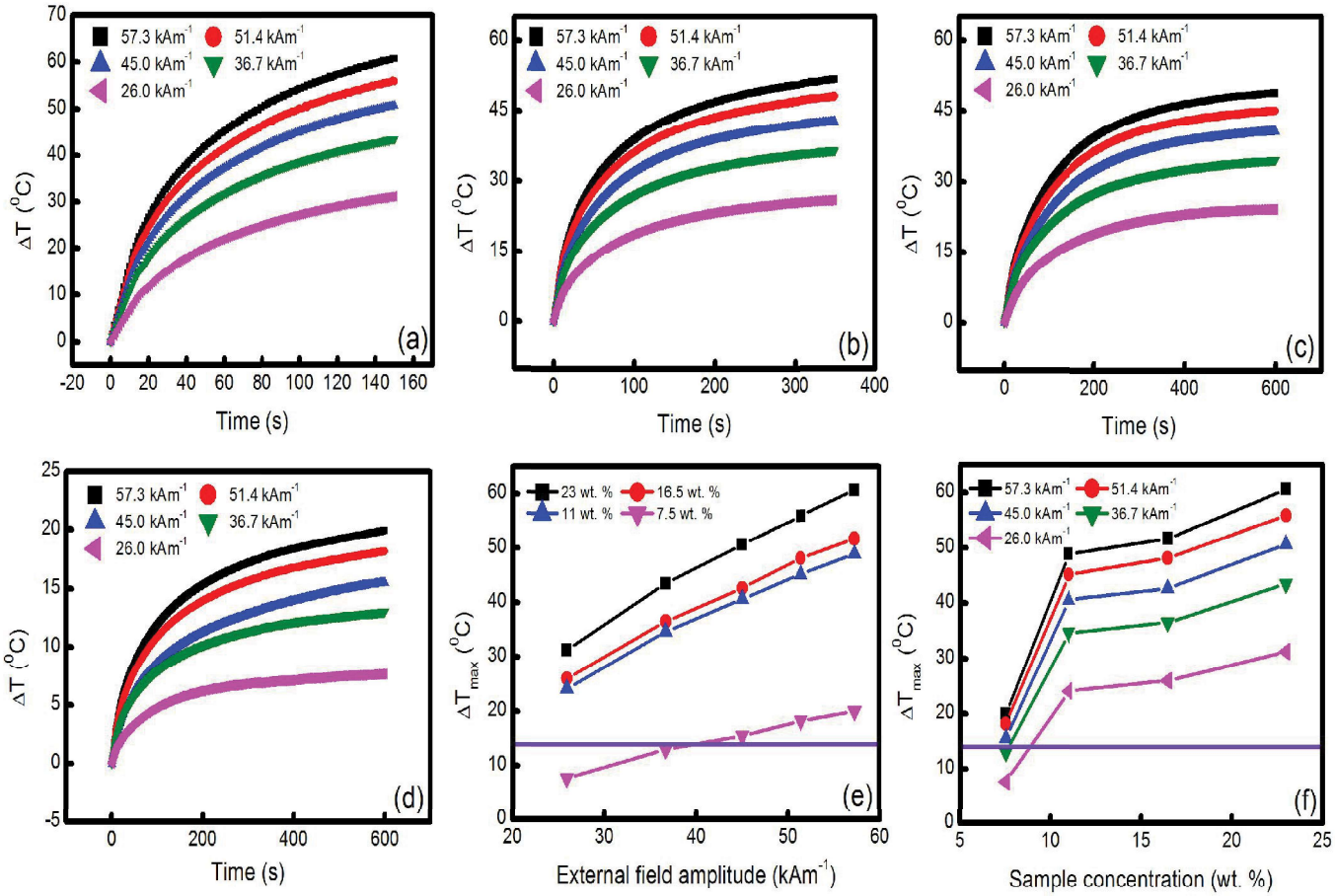


Figure 3.14: IRT based Temperature increase (ΔT) as a function of time, during RF-AMF induced heating under various RF-AMF amplitudes for four different sample concentrations, viz., (a) 23, (b) 16.5, (c) 11 and (d) 7.5 wt. %. Variation of ΔT_{max} as a function of (e) external field amplitude and (f) sample concentration, where, the horizontal lines indicate the hyperthermia limit ($\Delta T = 14\ ^0C$).

Figure 3.16b shows the RF-AMF induced temperature rise and natural temperature decay for the three consecutive heating cycles in the case of sample K1 (for H = 57.3 kAm^{-1}) under cyclic boundary conditions, where the three curves were found to overlap each other perfectly and the area under the curves were found to be the same. Similar results were obtained for other samples. This again shows the perfectly reversible thermal behaviour of the oil based magnetic nanofluids, used in the present study, without significant thermal hysteresis.

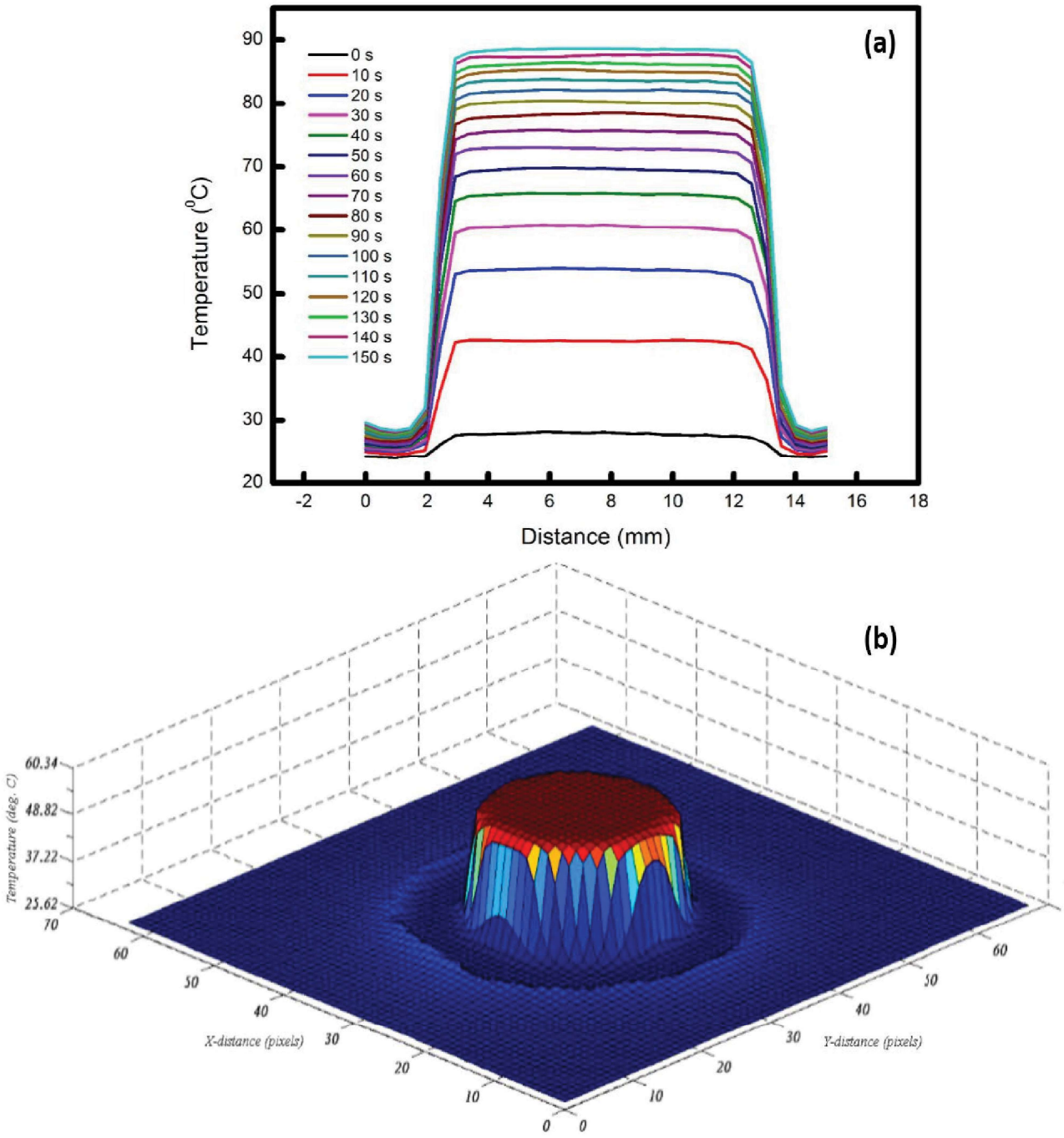


Figure 3.15: (a) Horizontal line scans across the top surface of the sample K1 at time t = 0-150 s, in steps of 10 s, during RF-AMF induced heating under an external field amplitude of 57.3 kAm^{-1}. (b) 3-dimensional surface plot at time t = 30 s, during RF-AMF induced heating of sample K1 under an external field amplitude of 57.3 kAm^{-1}.

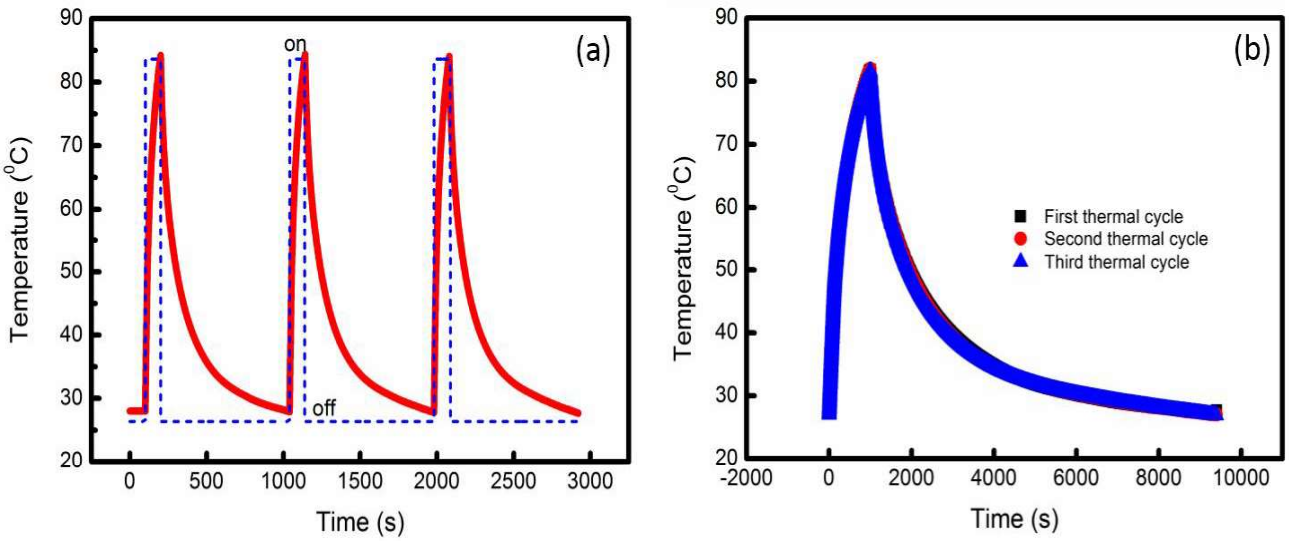


Figure 3.16: (a) Temperature (measured using IRT) variation as a function of time for the sample K1 (23 wt. %), during RF-AMF induced heating under an external field amplitude of 57.3 kAm^{-1} followed by natural cooling for three consecutive cycles. The square wave indicates the state of the external RF-AMF, where, the upper and lower states represent 'on' and 'off' conditions, respectively. (b) RF-AMF induced temperature rise and natural temperature decay for the three consecutive heating cycles in the case of sample K1 (for H = 57.3 kAm^{-1}), under cyclic boundary conditions.

Figure 3.17 shows the variation of initial rate of temperature rise ($\left.\frac{dT}{dt}\right|_{t=0}$) as a function of sample concentration for five different external field amplitudes. Here, the initial rates were determined by linear regression analyses and Box-Lucas methods using the temperature data obtained from IRT based measurements. It was observed that the initial rate determined using linear regression analyses and Box-Lucas methods were linearly correlated. It can be seen from **Fig. 3.17** that the initial rate of temperature rise increased with sample concentration for all fields due to an increase in effective number of heat sources per unit volume with increasing sample concentration. SAR values were determined from the initial rate of temperature rise using Eq. 1.19 (in chapter 1).

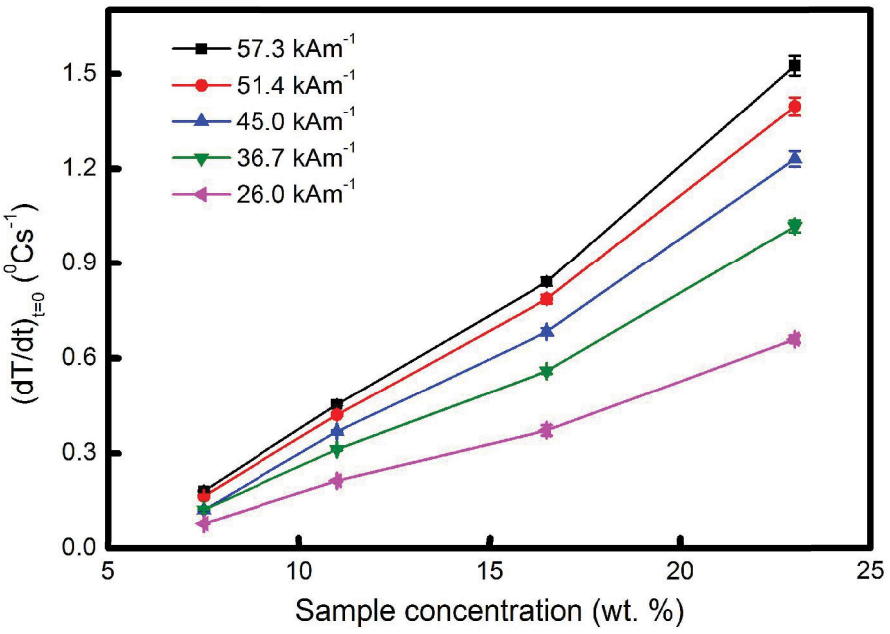


Figure 3.17 Variation of initial rate of temperature rise ($\left(\frac{dT}{dt}\right|_{t=0}$) as a function of sample concentration, for five different external field amplitudes, in the case of oil based ferrofluid containing oleic acid coated Fe_3O_4 MNP.

3.3.2.2 Comparison of IRT and probe based temperature rise curves and convection correction

Figures 3.18a-b show the variation of ΔT, measured using IRT and fiber optic temperature sensor, as a function of time for samples K2 (16.5 wt. %) and K3 (11 wt. %), respectively, under five different field amplitudes. Three major observations were made from the combined graphs, i) temperature rise curves measured using IRT and fiber optic temperature sensor were qualitatively similar but not exactly coinciding; ii) the response time of IRT based temperature measurement was comparably higher (initial low slope regions in the temperature rise curves, obtained with fiber optic temperature sensor, were absent in the case of IRT) and iii) the temperature measured using IRT was initially higher up to a certain time and beyond that the IRT based curves crossed the fiber optic curves and at higher time intervals the ΔT_{max} obtained from IRT was slightly lower than that obtained from fiber optic

temperature sensor. Similar trends were observed in all the cases. But the crossover time (t_{cross}) and crossover temperature difference (ΔT_{cross}) were found to vary with sample concentration and field amplitudes as shown in **Figs. 3.18c-d**. The faster response time of IRT based temperature measurement was attributed to the real time temperature measurement using IRT. On the other hand, the various regimes of the thermal profile, viz., initial higher temperature, crossover at certain ΔT_{cross} and lower ΔT_{max} compared to fiber optic temperature sensor were due to the internal and external convection mechanisms as discussed earlier (section 3.2.2).

The initial higher temperature observed using IRT was attributed to the internal convection aided upward movement of the heated and rarefied nanofluid due to buoyancy force. On the other hand, the crossover between the IRT and fiber optic temperature sensor based temperature rise curves and lower ΔT_{max} observed by IRT, at larger time, were due to external convection losses from the top surface. **Fig. 3.18c** shows the variation of ΔT_{cross} as a function of sample concentration where it can be seen that ΔT_{cross} increased with sample concentration which was attributed to the lower values of convective heat transfer coefficient of the magnetic nanofluids with higher sample concentration, as discussed earlier for the water based magnetic fluids. This led to a higher crossover time (t_{cross}) for samples with higher MNP loading as shown in **Fig. 3.18d**. Unlike the water based ferrofluids, in **Fig. 3.18d** the variation of $t_{cross}/t_{heating}$ was plotted as the heating time varied with sample concentration (i.e., 150, 350, 600 and 600 s for the samples K1, K2, K3 and K4, respectively). **Fig. 3.18d** clearly showed that the ratio of $t_{cross}/t_{heating}$ increased with sample concentration in agreement with the theoretical expectations. It must be noted in this regard, that ΔT_{cross} values were significantly higher (~ 10- 50 ^{0}C) in the case of kerosene based magnetic fluids as compared to the water based fluids (ΔT_{cross} ~ 2-10 ^{0}C, as can be seen from **Fig. 3.8**). This was due to the higher Prandtl number of kerosene which indicated larger momentum diffusivity, i.e.,

momentum transfer is favoured in kerosene as compared to heat transfer resulting in a comparatively higher temperature difference for the crossover to occur.

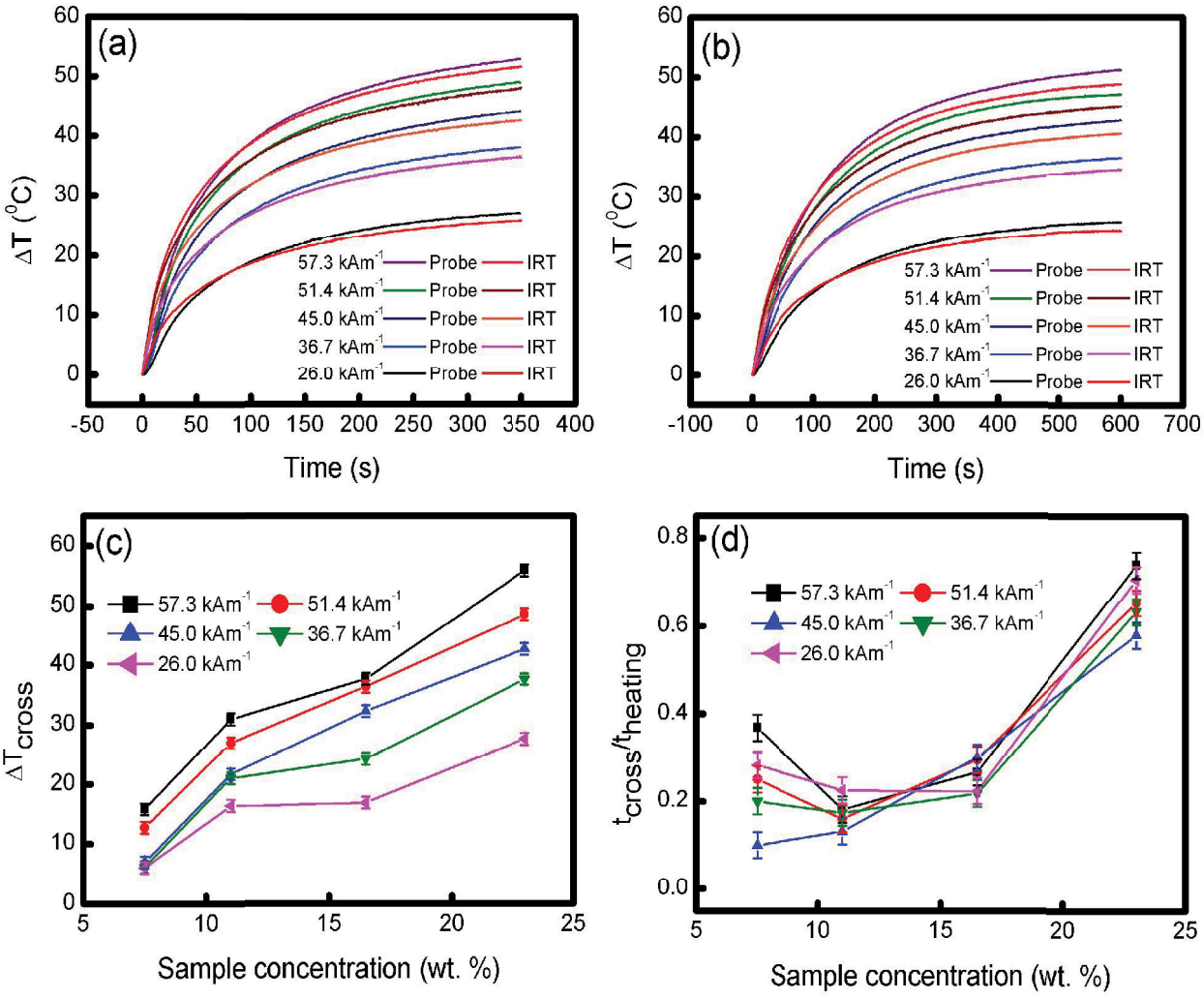


Figure 3.18: Variation of ΔT, measured using IRT and fiber optic temperature sensor, as a function of time, during RF-AMF induced heating under various external field amplitudes for two samples, viz., (a) K2 (16.5 wt. %) and (b) K3 (11 wt. %). (c) Variation of crossover temperature difference (ΔT_{cross}) as a function of sample concentration, for five different external field amplitudes. (d) Variation of $t_{cross}/t_{heating}$ as a function of sample concentration, for five different external field amplitudes, where, t_{cross} and $t_{heating}$ indicate crossover time and heating time (period for which, RF-AMF is switched on), respectively.

The empirical data analysis protocol, developed for incorporating the convection correction, was applied on the acquired data and a typical example of the accuracy of the empirical dual slope data correction procedure is shown in **Fig. 3.19** for the sample K1 (23 wt. %), under an applied field amplitude of 57.3 kAm^{-1}. It can be clearly seen from **Fig. 3.19** that the dual slope corrected probe data and IRT based data were in good quantitative agreement. As the initial temperature rise was found to be higher for IRT based measurements, SAR values estimated from IRT based temperature rise curves were also found to be higher as compared to the corresponding values obtained from fiber optic temperature sensor based measurements. **Table 3.4** shows a comparison between the SAR values obtained by both the techniques where it can be seen that the SAR values obtained using IRT measurements were indeed higher. This was attributed to the additional heat transport to the top surface due to internal convection. Nevertheless, it was also seen that the convection corrected IRT based SAR values (also shown in **Table 3.4**) were in very good agreement with the fiber optic temperature sensor based values (maximum error was within ± 5 %). This shows the efficacy and accuracy of IRT based temperature measurement during RF-AMF induced heating of magnetic nanofluids. The maximum SAR obtained in the present case was 95.9 (± 3.4) W/g_{Fe} for a sample concentration and field amplitude of 23 wt. % and 57.3 kAm^{-1}, respectively. The convection corrected SAR for this case was ~ 75.2 (± 3.4) W/g_{Fe}.

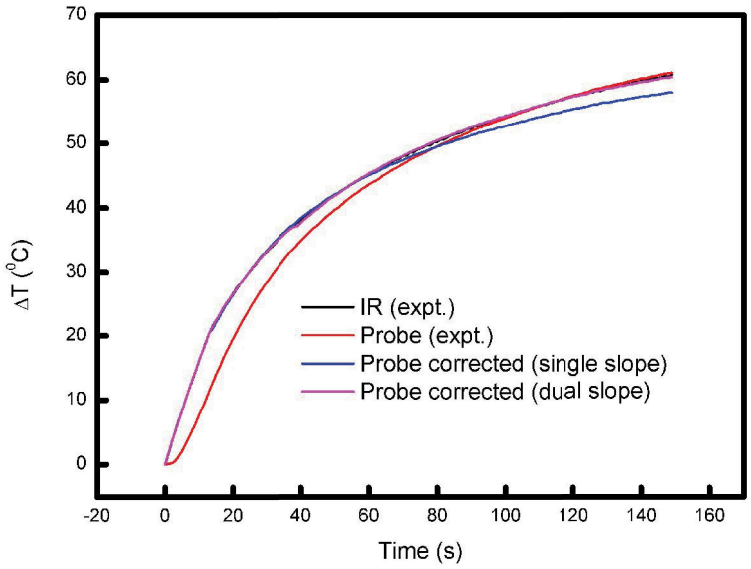


Figure 3.19: ΔT vs. time curves, recorded using IRT and conventional fiber optic temperature sensor for the sample K1 (23 wt. %), during RF-AMF induced heating under an external field amplitude of 57.3 kAm^{-1}. The convection corrected ΔT data are also shown in the figure and dual slope correction procedure is found to be more accurate.

Table 3.4: Comparison of SAR obtained using IRT (SAR-IRT) and fiber optic temperature sensor (SAR-FO), along with convection corrected SAR values (SAR-IRT-CC) for the samples K1-K4.

Sample code	wt. %	RF-AMF amplitude (kAm^{-1})	SAR–FO (W/g_{Fe})	SAR-IRT (W/g_{Fe})	SAR-IRT-CC (W/g_{Fe})
K1	23.0	57.3	75.1 ± 3.1	95.9 ± 3.4	75.2 ± 3.4
		51.4	68.7 ± 1.9	87.8 ± 1.7	68.9 ± 1.7
		45.0	60.1 ± 2.9	77.3 ± 3.4	59.8 ± 3.4
		36.7	50.3 ± 2.6	63.9 ± 3.0	50.1 ± 3.0
		26.0	32.8 ± 2.8	41.5 ± 3.0	32.7 ± 3.0
K2	16.5	57.3	63.2 ± 2.4	70.5 ± 2.6	63.0 ± 2.6
		51.4	58.3 ± 2.4	65.9 ± 2.0	58.5 ± 2.0
		45.0	50.0 ± 2.8	57.3 ± 2.6	50.4 ± 2.6
		36.7	42.4 ± 1.9	46.9 ± 2.2	42.6 ± 2.2
		26.0	27.9 ± 2.8	31.2 ± 3.2	27.5 ± 3.2
K3	11.0	57.3	53.7 ± 2.6	57.1 ± 2.4	53.2 ± 2.4
		51.4	50.5 ± 2.6	52.9 ± 2.6	50.4 ± 2.6
		45.0	45.4 ± 2.6	46.3 ± 3.0	45.8 ± 3.0
		36.7	36.6 ± 2.1	39.2 ± 2.6	36.4 ± 2.6
		26.0	24.2 ± 2.8	26.7 ± 2.6	24.5 ± 2.6
K4	7.5	57.3	25.4 ± 2.5	30.3 ± 2.0	25.8 ± 2.0
		51.4	24.3 ± 2.6	27.6 ± 2.1	24.1 ± 2.1
		45.0	21.5 ± 3.0	20.3 ± 2.5	20.8 ± 2.5
		36.7	16.1 ± 2.8	20.5 ± 2.5	16.4 ± 2.5
		26.0	11.1 ± 3.4	13.1 ± 3.0	11.7 ± 3.0

3.3.2.3 Variation of SAR with sample concentration and RF-AMF amplitude

Figure 3.20a shows the variation of SAR as a function of sample concentration for five different external field amplitudes. Here, SAR values were found to increase with sample concentration for all field amplitudes. The SAR values were expressed as mean ± SD, where SD is the standard deviation for three consecutive measurements. The increase in SAR for the samples K4-K1 was attributed to an increase in effective number of heat sources per unit volume with increasing sample concentration. The kerosene based oleic acid coated iron oxide nanofluid was sterically stabilized, where the aliphatic chains of oleic acid extended into the non-polar solvent, and hence, the aggregation was insignificant. This was also evident from the DLS studies, where, a narrow unimodal size distribution was obtained for all the samples. It has been reported by Guibert et al. [202] that the SAR values in samples with loosely formed or very small aggregates were comparable to that of individual and well dispersed nanoparticles, whereas, closely packed or large aggregates caused a significant reduction in SAR values due to enhanced dipolar interaction. Due to the absence of agglomeration, the dipolar interaction was not enhanced at higher concentration in kerosene based samples and the individual particle model remained valid leading to an increase in SAR with increasing sample concentration [52, 202].

The relaxation mechanism of the oleic acid coated MNP is primarily Neel dominated and considering the values of crystallite size, hydrodynamic size and viscosity of kerosene as 8 nm, 10 nm and 16.4×10^{-4} Pa s, respectively; Neel, Brownian and effective relaxation times were found to be ~ 1.9×10^{-10}, 6.2×10^{-7} and 1.89×10^{-10} s, respectively. The product of cyclic frequency and effective relaxation time was found to be ~1.5×10^{-4}, i.e., $\omega\tau<<1$. According to Rosensweig's model [51], dissipated power, P, is directly proportional to $f(\omega\tau)$, where $f(\omega\tau) = \omega\tau(1+\omega^2\tau^2)^{-1}$ and for the cases where $\omega\tau<<1$, P is directly proportional to $\omega\tau$ [51, 52]. Using Neel and Vogel-Fulcher models, Castillo and Rinaldi [418] have reported that for oleic acid

coated iron oxide nanoparticles, the effective anisotropy energy density increases with increasing sample concentration. With increasing anisotropy energy density, the Neel relaxation time increases causing the effective relaxation time (τ) to increase, which led to a higher heating power resulting in an increase in SAR with increasing sample concentration for the oil based ferrofluids.

This is in contrast to the findings obtained in the case of water based magnetic nanofluid containing TMAOH coated Fe_3O_4 MNP (**Fig. 3.11a**), where a reduction in SAR was observed for higher sample concentration due to an enhancement in dipolar interaction. In the case of water based ferrofluids slight agglomeration enhanced the dipolar interaction which reduced the anisotropy energy density and effective relaxation time with increasing sample concentration, resulting in a substantial decrease in SAR.

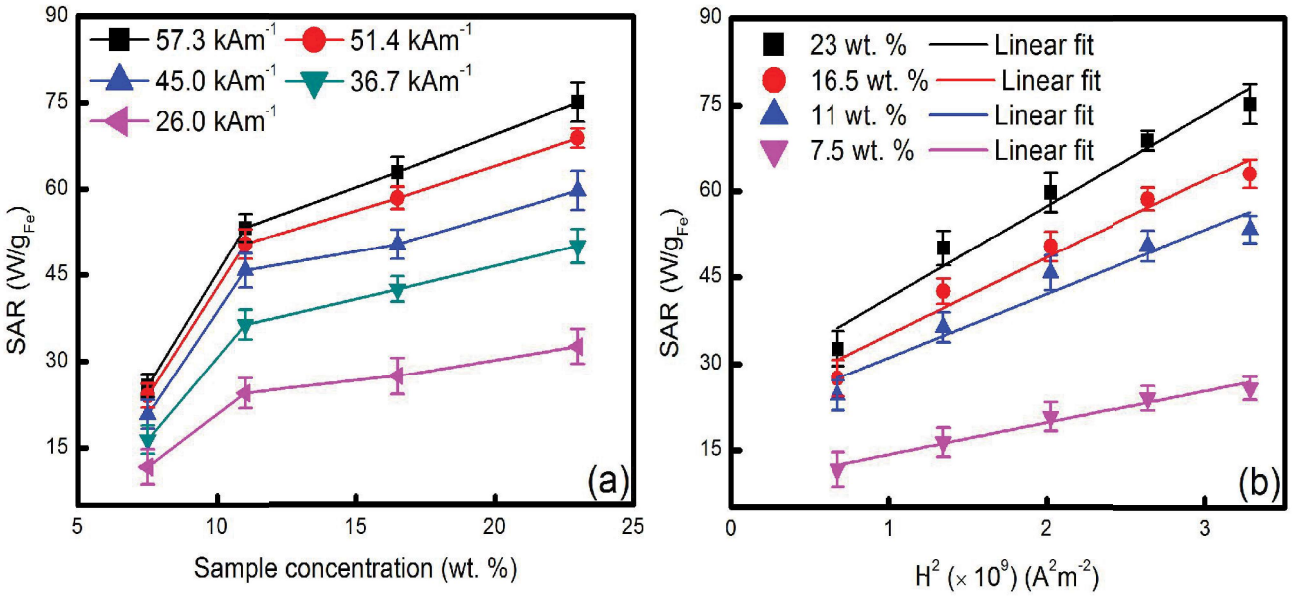


Figure 3.20: (a) Variation of convection corrected SAR as a function of sample concentration, for the samples K1-K4, under five different external field amplitudes. SAR increased with sample concentration due to an enhancement of effective number of heat sources per unit volume. (b) Variation of SAR as a function of square of the external field amplitudes. The linear fits are shown as solid lines.

Figure 3.20b shows the variation of convection corrected SAR as a function of square of the external field amplitudes, where it can be seen that SAR increased linearly (adjusted R^2 were found to be 0.96, 0.95, 0.92 and 0.97 and for the samples K1-K4, respectively) with H^2, in accordance with the Rosensweig's model under linear response regime [51].

3.4 Conclusions

Infrared thermography (IRT) was successfully applied to study the RF-AMF induced heating in water and kerosene based magnetic nanofluids containing TMAOH and oleic acid coated Fe_3O_4 MNP, respectively. It was further observed that the RF-AMF induced temperature rise curves measured using fiber optic temperature sensor and IRT were remarkably similar. Nevertheless, IRT data indicated a higher initial rate of temperature rise and a lower maximum temperature at the end of the heating period, which were attributed to the internal and external convection phenomena, respectively. The deviation between the temperature data obtained from IRT and fiber optic temperature sensor was found to initially increase with temperature difference, but the trend was reversed after attaining a maximum. The increasing and decreasing parts of the temperature difference curves were fitted with Box-Lucas and linear equations, respectively, and based on these calibration curves, an empirical data analysis procedure was developed for incorporating the convection phenomena. The convection corrected SAR values obtained from IRT were found to be in good agreement (maximum errors were limited within ± 3.4 % and ± 5 % for the water and kerosene based magnetic fluid, respectively) with those obtained from fiber optic temperature sensor. Additionally, IRT based experiments enabled surface temperature mapping which showed a uniform and homogenous temperature rise in the magnetic fluids during RF-AMF induced heating. This study clearly showed the efficacy and accuracy of IRT based temperature measurement during RF-AMF induced heating of magnetic nanofluid which offers several

advantages over conventional fiber optic temperature sensor based point measurements, viz., non-contact and real time temperature measurement, sample contamination free measurement and visualization of the entire surface temperature distribution. The developed convection correction protocol was successfully applied for water and oil based magnetic fluids, with significantly varying thermal diffusivity and Prandtl number, indicating the universal adaptability of IRT as an alternate temperature measurement methodology during magnetic fluid hyperthermia.

In the case of water based magnetic fluids, the highest SAR was obtained as ~ 135.9 (± 4.6) W/g_{Fe} for a sample concentration of 3 wt. % under an external field amplitude of 63.0 kAm^{-1} (126 kHz) and SAR was found to decrease with increasing sample concentration due to an enhancement in dipolar interaction, possibly due to slight aggregation. On the other hand, for oil based ferrofluids, in the absence of agglomeration, enhancement of dipolar interaction was insignificant and SAR was found to increase with sample concentration due to an increase in the effective number of heat sources per unit volume. The highest SAR obtained in the case of kerosene based ferrofluid was ~ 75.2 (± 3.4) W/g_{Fe} for a sample concentration of 23 wt. % under an external field amplitude of 57.3 kAm^{-1}.

Chapter 4

Studies on magnetic fluid hyperthermia in water based magnetic nanofluids containing phosphate coated magnetic nanoparticles

Chapter 4 Studies on magnetic fluid hyperthermia in water based magnetic nanofluids containing phosphate coated magnetic nanoparticles

4.1 Introduction

In hyperthermia therapeutic procedure, biological tissues are heated above physiological temperature range using various stimuli such as phased array microwave heating, radio frequency heating, laser heating and whole body water bath heating [419, 420]. MFH is one such therapeutic procedure, where the cancerous tissues are heated above their normal physiological temperature range, leading to the death of cancerous cells using heat dissipation from the MNP which are exposed to a RF-AMF [51, 189]. The cancerous tissues, in general show lower thermal resistance, in comparison to normal tissues, due to poor development of blood vessels and lack of oxygen, which enables destruction of cancerous cells by localized heating using MFH [191, 421]. Considering the immense clinical benefits, it is important to enhance the heating efficiency of the magnetic nanoparticles which will minimize the ferrofluid dose and related toxicity effects [216, 422], thereby, enabling MFH to be readily adaptable for cancer treatments. Many of the reported results are on materials that are not bio-compatible and MNP concentrations which are much above the desired concentration limits [423]. To adopt the MFH as a routine tumor therapy, systematic studies on stable nanofluids, preferably biocompatible, are a prerequisite.

Bare MNP are prone to oxidation and agglomeration induced instabilities due to their excess reactivity, which is attributed to unsaturated surface bonds [424]. Hence, surface capping of MNP using suitable organic or inorganic molecules is exploited as one of the promising strategies to improve thermal stability of MNP and to prevent oxidation and agglomeration [315]. It has been reported that phosphonated molecules do not induce spin canting in MNP [425, 426] and hence phosphate coated Fe_3O_4 and $CoFe_2O_4$ MNP were chosen in the present

study to investigate the RF-AMF induced heating efficiency, where the variation of SAR with external field amplitude and sample concentration was probed.

4.2 MFH in water based ferrofluid containing phosphate coated Fe_3O_4 MNP

In general, presence of a thin coating of phosphate on the MNP surface does not reduce the saturation magnetization significantly and provides good stability by acting as a protective layer against oxidation [315]. Further, inorganic phosphate is present in all forms of life and phosphate is essential for structures of DNA, RNA, cell membrane in the form of phospholipids, bones and teeth, which makes the phosphate coated MNP bio-compatible. In the present study, RF-AMF induced hyperthermia in a water based stable ferrofluid containing phosphate coated superparamagnetic Fe_3O_4 MNP, synthesized by co-precipitation method, was studied and the effect of sample concentration on heating efficiency was probed. The presence of an optimum sample concentration for maximum SAR and decrease in SAR at higher sample concentration due to enhancement of dipolar interaction were explained on the basis of Hasse-Nowak [280] and Mroup-Tronc [412] models, respectively.

4.2.1 Experimental details and characterization studies

The phosphate coated Fe_3O_4 MNP were synthesized using a chemical co-precipitation technique as discussed in section 2.1.2 in chapter 2 and dispersed in water. The synthesized MNP were characterized using XRD, VSM, DLS, transmission electron microscopy (TEM), TGA and FTIR spectroscopy. TEM was carried out to study the morphology and size of particles using JEOL 2011 TEM instrument under an accelerating voltage of 200 kV. A drop of the phosphate coted Fe_3O_4 MNP dispersed in isopropyl alcohol was placed on a carbon coated copper grid (0.3 cm diameter with a mesh size of 200 holes/cm) and dried overnight at

room temperature for TEM studies. The TEM images were analysed using Image Pro Plus software.

A master solution of 6 wt. % (hereafter indicated as A6) was prepared which was later diluted to 2.5, 2.0, 1.5, 1.0 and 0.5 wt. % (hereafter indicated as A1, A2, A3, A4 and A5, respectively). The hyperthermia measurements were carried out at a fixed frequency of 126 kHz and under five different external field amplitudes, viz., 57.3, 51.4, 45.0, 36.7 and 26.0 kAm^{-1}. Detailed description of the experimental set-up is given in chapter 2 (sections 2.4 and 2.5). The final SAR values were reported as W/g_{MNP}, where g_{MNP} indicates weight of the MNP per cc of the sample. The specific heat capacity and density of the base fluid (water) were considered as 4.18 $Jg^{-1}\,{}^{0}C^{-1}$ and 1 g/cc, respectively.

The XRD pattern of phosphate coated MNP is shown in **Fig. 4.1a**, where clear peaks corresponding to Bragg diffraction from (220), (311), (400), (422), (511) and (440) planes of Fe_3O_4 (JCPDS file no. 19-0629) were observed. The average crystallite size obtained from the highest intensity peak (corresponding to (311) plane), using Scherrer's equation, was found to be ~ 7.8 (± 0.8) nm. **Fig. 4.1b** shows the room temperature M-H curve for the phosphate coated MNP and it was observed that the saturation magnetization was ~ 52 emu/g, whereas, the saturation magnetization of the uncoated MNP was 63.6 emu/g (not shown). The reduction in saturation magnetization (~11.6 emu/g) was due to the presence of non-magnetic phosphate coating. The M-H curve did not show remanence at room temperature indicating superparamagnetic response of the synthesized MNP. **Fig. 4.1c** shows the hydrodynamic size distribution of the phosphate coated Fe_3O_4 MNP dispersed in water. The average hydrodynamic diameter was ~ 32 (± 3) nm which was ~ 4 times higher than the size determined from XRD studies. This was attributed to the agglomeration of more than one MNP in water medium and adsorption of water layer over the MNP due to higher affinity of phosphate molecules towards water molecule via hydrogen bonding [315, 427]. The zeta

potential of the water dispersed MNP was found to be in the range of -32.1 to -33.9 mV which indicated good stability of the phosphate coated MNP in water medium. **Fig. 4.1d** shows a typical TEM image of the phosphate coated MNP, which showed nearly spherical morphology of the MNP. The size distribution along with the average size (~ 14 nm) is shown in the **inset of Fig. 4.1d**. **Fig. 4.1e** shows the weight loss as a function of temperature in the range of 30-1000 ^{0}C, where, the weight loss was ~ 6 %. Fig. **4.1f** show the FTIR spectra of the phosphate coated MNP, where, the presence of a strong Fe-O characteristic band at ~584 cm^{-1} and a shoulder at 630 cm^{-1} (attributed to the symmetric stretching of Fe-O bond of magnetite [315, 428]) can be clearly seen. The bands at 2350 cm^{-1} and 1404 cm^{-1} were attributed to the stretching vibrations of C=O and C-O bonds, respectively. The former was present due to the interference of atmospheric CO_2, whereas, the later was due to the formation of carbonates by reaction of atmospheric CO_2 with the hydrated alkaline surfaces [315, 429]. The broad band at 3000-3400 cm^{-1} and the sharp band at 1640 cm^{-1} were present due the stretching and bending modes of hydroxyl groups from the adsorbed water molecules [315]. P-O-Fe stretching presented a broad absorption band around 900-1200 cm^{-1} which confirmed the presence of phosphate coating on the surface of the MNP [315].

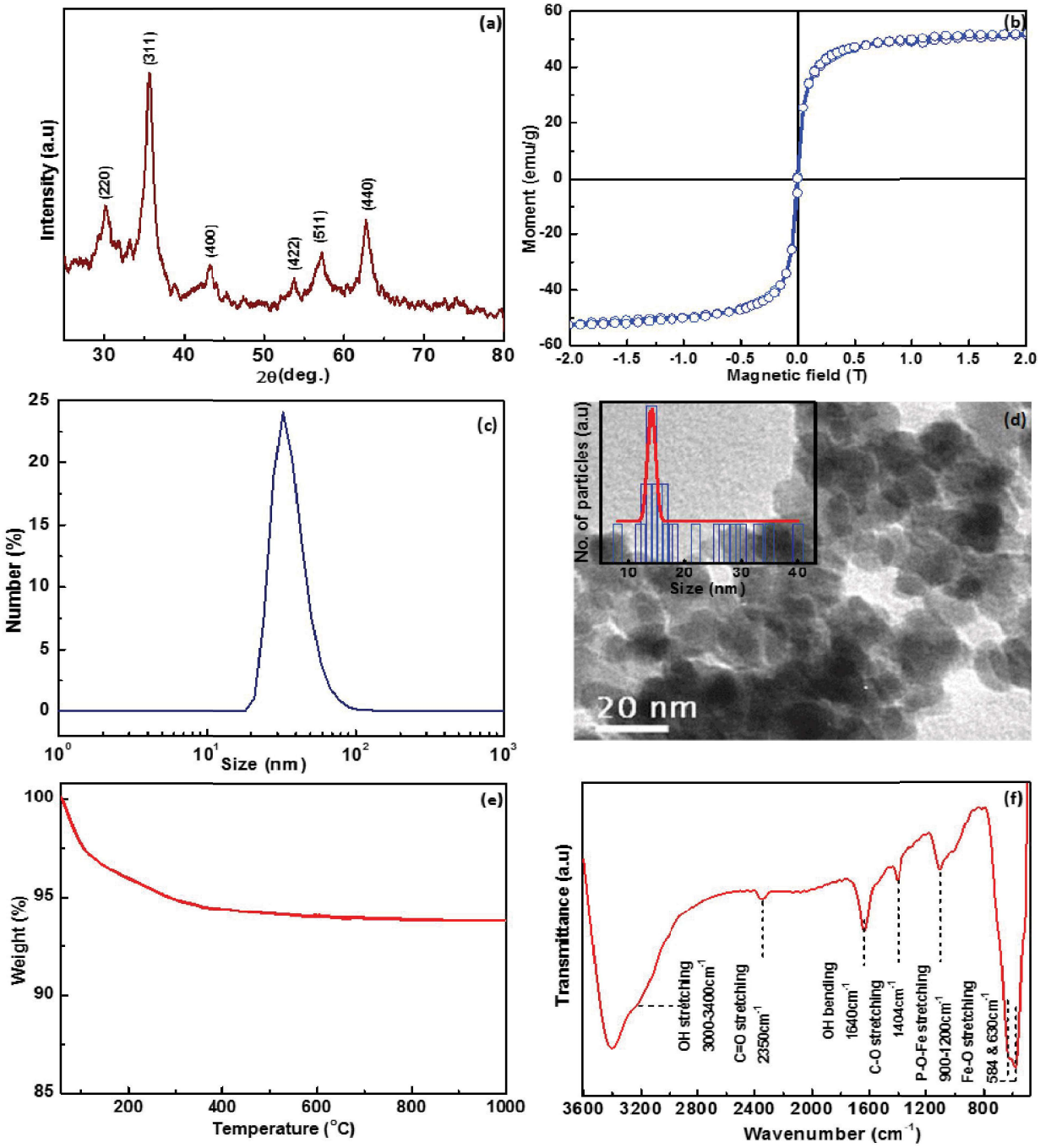


Figure 4.1: (a) Powder XRD pattern of the phosphate coated Fe_3O_4 MNP. The average crystallite size (~ 7.8 nm) is calculated from the strongest diffraction peak corresponding to the (311) plane. (b) Room temperature M-H curve for the phosphate coated Fe_3O_4 MNP. The saturation magnetization is ~ 52 emu/g. (c) Hydrodynamic size distribution of the phosphate coated MNP dispersed in water. (d) TEM image of the synthesized phosphate coated MNP. (Inset) Number distribution obtained from the TEM image. (e) Weight loss, as a function of temperature, for the phosphate coated MNP. (f) FTIR spectra of the phosphate coated MNP, where, the major absorption bands are indexed.

4.2.2 Results and discussions

4.2.2.1 RF-AMF induced heating

Figures 4.2a-f show the temperature increase ($\Delta T = T - T_i$, where, T_i is the initial sample temperature) as a function of time for the phosphate coated Fe_3O_4 MNP based magnetic nanofluids at six different concentrations, viz., 0.5, 1.0, 1.5, 2.0, 2.5 and 6.0 wt. %, respectively, during RF-AMF induced heating under five different external field amplitudes, viz., 57.3, 51.4, 45.0, 36.7 and 26.0 kAm^{-1}. It can be seen that, in all the cases, sample temperature increased with time and the rates of temperature rise and the ΔT_{max} (at t=1200) values varied with the external field amplitude and sample concentration. In the presence of a RF-AMF, the MNP gets heated up due to Neel and Brownian relaxation [16, 50, 51]. For a fixed concentration, temperature rise was higher for larger field amplitudes, whereas, concentration dependent changes on temperature rise were not straight forward. For e.g., in the case of H = 57.3 kAm^{-1}, ΔT_{max} increased from 6.36 (± 0.03) to 18.45 (± 0.03) ^0C with an increase in sample concentration from 0.5 to 2.0 wt. % (**Figs. 4.2a-d**), whereas, for sample concentration of 6 wt. %, ΔT_{max} was found to decrease to 13.74 (± 0.03) ^0C (as can be seen from **Fig. 4.2f**).

Figure 4.3a shows the variation of ΔT_{max} as a function of RF-AMF amplitude for all six sample concentrations, where, ΔT_{max} was found to increase with the field amplitude. The dotted horizontal line shown in **Fig. 4.3a** corresponded to a ΔT_{max} of 14 ^0C which indicated the relevant temperature range for hyperthermia limit (~ 42 ^0C). It was observed from **Fig. 4.3a** that for lower sample concentration, i.e., 0.5 and 1.0 wt. %, the ΔT_{max} values were much less than the hyperthermia limit for the experimental magnetic field values. On the other hand, for magnetic field amplitudes beyond 45.0 kAm^{-1}, the samples with 1.5, 2.0 and 2.5 wt. % concentrations were found to be beneficial for MFH applications. Surprisingly, for the sample A6 (6 wt. % MNP concentration), ΔT_{max} was lower, which was further studied in

detail by observing the variation of ΔT_{max} with sample concentration under different external field amplitudes.

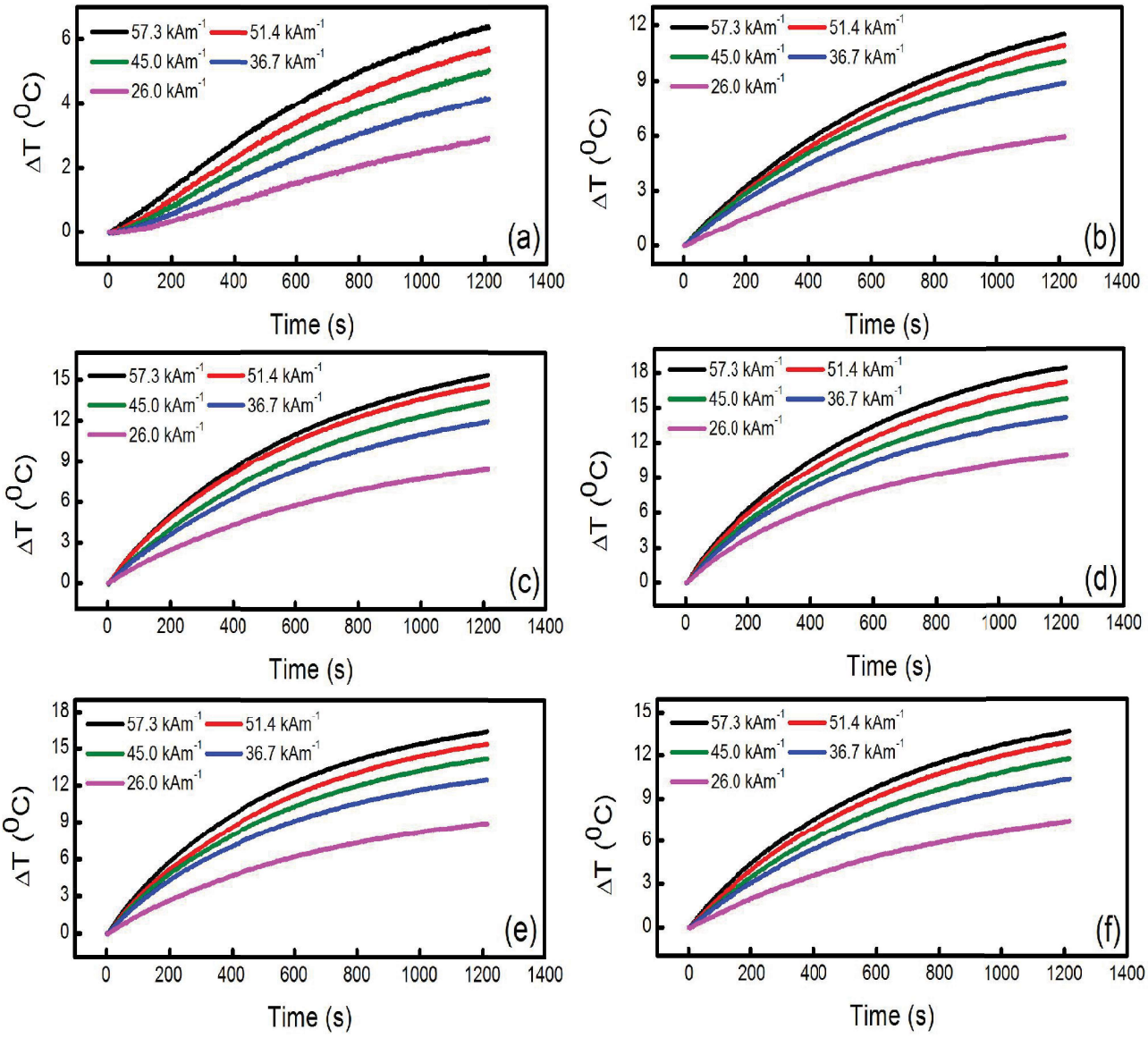


Figure 4.2: Temperature increase (ΔT) as a function of time for phosphate coated Fe_3O_4 MNP based ferrofluids at various external field amplitudes for six different sample concentrations, viz., (a) 0.5 (b) 1.0, (c) 1.5, (d) 2.0, (e) 2.5 and (f) 6.0 wt. %.

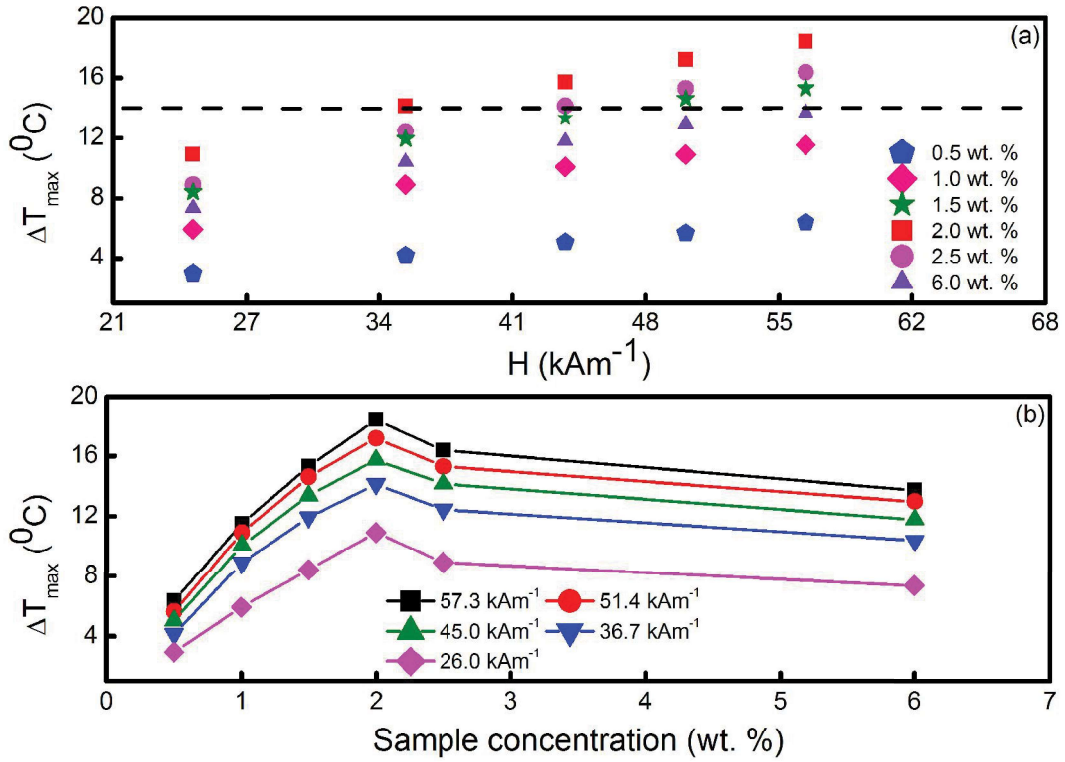


Figure 4.3: (a) Variation of ΔT_{max} as a function of external field amplitude, for six different sample concentrations, in the case of water based ferrofluid containing phosphate coated Fe_3O_4 MNP. The horizontal dotted line indicates a ΔT of 14 ^{0}C (hyperthermia limit). (b) Variation of ΔT_{max} as a function of sample concentration for five different external field amplitudes.

The effect of sample concentration on ΔT_{max} is shown in **Fig. 4.3b** for five different external field amplitudes, where it can be seen that ΔT_{max} initially increased with sample concentration, attained a maximum and beyond that started decreasing which was found to be in agreement with our earlier observations made from **Fig. 4.2f**. It was further observed from **Fig. 4.3b** that ΔT_{max} values were highest around an optimum sample concentration of 2 wt. % for all the cases. Such concentration dependent peculiar behaviour of the water based ferrofluid was attributed to the enhancement of dipolar interaction at higher concentrations, which is discussed in the next section.

4.2.2.2 Effects of sample concentration on RF-AMF induced heating efficiency

Three different numerical techniques, namely Box-Lucas, exponential rise and linear regression analyses of the initial data were used for determining the initial rates of temperature rise under non-adiabatic approximation. These three data analysis protocols were earlier discussed in detail (section 2.5 in chapter 2). The adjusted R^2, indicating goodness of fit, were found to be very high (> 0.99) for all three techniques and the average value of initial rates of temperature rise, determined from these three techniques, were further used for quantification of SAR. **Table 4.1** shows the rates of temperature rise determined from the three methods along with the average values for the sample A3 under five different external field amplitudes. SAR values were quantified using the equation: $SAR = \frac{c_{samp}\rho_{samp}}{m_{Fe}} \left.\frac{dT}{dt}\right|_{t=0}$ (eq. 1.19 in chapter 1) and the SAR values are also listed in **Table 4.1.**

Table 4.1: Comparison of initial rates of temperature rise and SAR values calculated using three different data analysis techniques (Box-Lucas fit, exponential fit and linear regression analysis) for the sample A3, under five different external field amplitudes.

Sample	Magnetic field (kAm^{-1})	dT/dt ($^0C\ s^{-1}$)				SAR (W/g_{MNP})
		Box-Lucas fit	Exponential fit	Linear fit	Average	
A3 (1.5 wt. %)	57.3	0.0289	0.0282	0.0294	0.0288 ± 0.0008	11.1 ± 0.6
	51.4	0.0277	0.0267	0.0284	0.0276 ± 0.0009	10.6 ± 0.6
	45.0	0.0229	0.0229	0.0235	0.0231 ± 0.0003	8.9 ± 0.7
	36.7	0.0204	0.0201	0.0209	0.0205 ± 0.0004	7.9 ± 0.4
	26.0	0.0138	0.0136	0.0138	0.0137 ± 0.0001	5.3 ± 0.4

Figure 4.4 shows the variation of SAR as a function of square of the external field amplitudes for six different sample concentrations, viz., 0.5, 1.0, 1.5, 2.0, 2.5 and 6.0 wt. % and it can be seen that for all the cases, SAR varied linearly with H^2, which was found to be in good agreement with the Rosensweig model of field induced heating in magnetic fluids

under the linear response regime, i.e., $H_{max}<H_{sat}$, where, H_{max} and H_{sat} are the maximum applied magnetic field and saturation magnetic field for the MNP, respectively [51, 282]. The adjusted R^2 values for the linear regression analyses were ~ 0.96, 0.83, 0.93, 0.97, 0.89 and 0.88 for the samples A1-A6, respectively. For a fixed concentration, as magnetic field amplitude increases, electromagnetic energy density varies as ~ H^2 leading to higher SAR values [282].

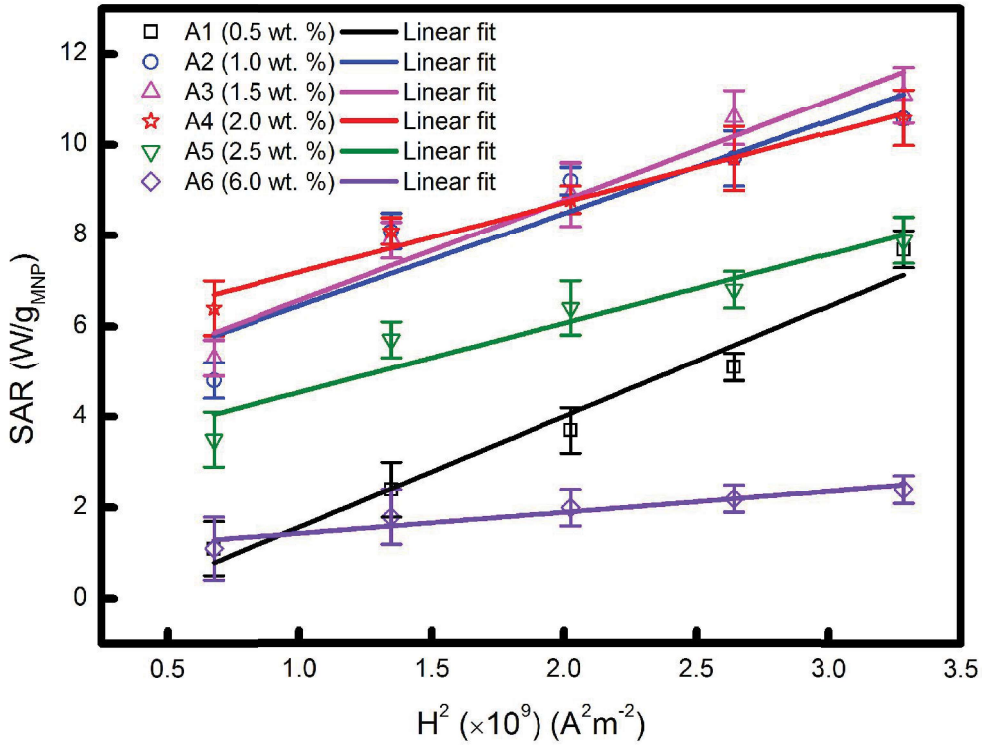


Figure 4.4: Variation of SAR as a function of square of the external field amplitude (H^2), for six different sample concentrations, viz., 0.5, 1.0, 1.5, 2.0, 2.5 and 6.0 wt. %. It can be seen that SAR varies linearly with H^2 and the linear regression curves are also shown in the figure.

Figure 4.5a shows the variation of SAR as a function of sample concentration and it can be seen that SAR initially increased and attained a maximum value and then gradually decreased. This was found to be in agreement with our earlier results, where, ΔT_{max} also showed a distinct maximum at a certain concentration (**Fig. 4.3b**). The **inset of Fig. 4.5a**

shows the temperature increase as a function of time for six different concentrations of the water based magnetic nanofluid at a fixed external field amplitude of 57.3 kAm^{-1}, where a similar trend in the temperature rise curves can be observed with increasing sample concentration. It was further observed from **Fig. 4.5a** that the optimum sample concentration for the highest SAR was ~1.5 wt. %. **Table 4.2** shows the optimum sample concentration, ΔT_{max} and SAR values for five different external field amplitudes. The maximum SAR, obtained in the present study, was ~ 11.1 (±0.6) W/g_{MNP} for the sample A3 (1.5 wt. %) at an external field amplitude of 57.3 kAm^{-1}. The corresponding ΔT_{max} was ~ 15.35 (± 0.03) ^0C. The ΔT_{max} for the sample A4 (2 wt. %) at a field amplitude of 36.7 kAm^{-1} was found to be ~ 14.16 (± 0.03) ^0C, which indicated the suitability of this sample for MFH applications.

Table 4.2: Optimum sample concentration and maximum SAR and ΔT_{max} for the water based ferrofluids, containing phosphate coated Fe_3O_4 MNP, under five different RF-AMF amplitudes.

RF-AMF amplitude (kAm^{-1})	**Optimum concentration (wt. %)**	**Maximum SAR (W/g_{Fe})**	**ΔT_{max} (^0C) (±0.03 ^0C)**
57.3	1.5	11.1 ± 0.6	15.35
51.4	1.5	10.6 ± 0.6	14.65
45.0	1.0	9.2 ± 0.3	10.05
36.7	1.0-2.0	8.1 ± 0.4	8.88-14.16
26.0	2.0	6.4 ± 0.6	10.93

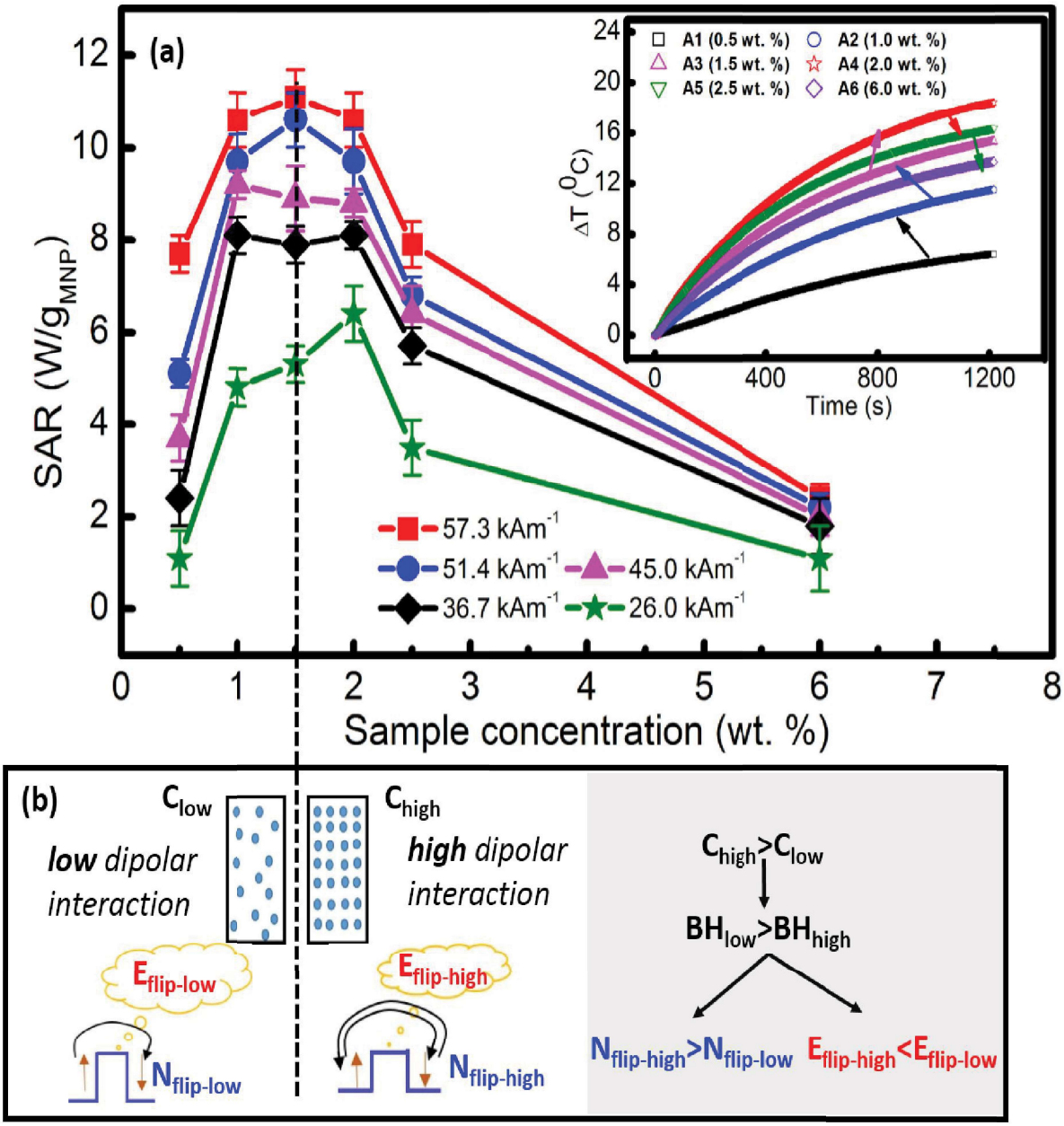


Figure 4.5: (a) Variation of SAR as a function of sample concentration, for five different external field amplitudes. (Inset) The variation of ΔT as a function of time, for six different sample concentrations, at a fixed RF-AMF amplitude of 57.3 kAm^{-1}. The arrows are shown to aid in following the non-monotonic behaviour of the temperature rise with increasing sample concentration. (b) Schematic diagram, showing the lowering of anisotropy energy barrier due to enhancement of dipolar interaction at higher sample concentration. The vertical line separates the increasing and decreasing trend of the SAR values. The subscripts 'low' and 'high' indicate low and high concentration, respectively. C, BH, N_{flip} and E_{flip} indicate sample concentration, anisotropy barrier height, nos. of flip per unit time and energy release per flip, respectively.

The observed non-monotonic variation of SAR with concentration, as shown in **Fig. 4.5a**, was attributed to the enhancement of dipolar interaction. Under the influence of a RF-AMF, each MNP generates heat due to relaxation mechanisms and with increasing concentration the number of heat sources increases, which could have resulted in a monotonic increase of SAR with concentration (as seen in the case of oil based ferrofluid containing oleic acid coated Fe_3O_4 MNP: **Fig. 3.20a** in chapter 3). However, with increasing sample concentration, dipolar interaction also increases, where the independent particle model becomes invalid. Several experimental and theoretical studies have reported the detrimental effect of dipolar interaction with increasing sample concentration on SAR in magnetic fluids [52, 198, 200, 279, 280, 410, 411, 430]. With increasing sample concentration, interparticle distance decreases resulting in an enhancement of dipolar interaction which strongly influences the Neel relaxation mechanism by lowering the anisotropy energy barrier [198, 431]. On the other hand, Brownian relaxation remains comparatively independent of sample concentration as the interparticle forces are hydrodynamic in nature [413].

The total energy (E_t) of a MNP under the simultaneous influences of RF-AMF and dipolar interaction can be expressed as the sum total of Zeeman energy (E_Z), anisotropy energy (E_A) and dipolar energy ($E_{Dipolar}$): $E_t=E_Z+E_A+E_{Dipolar}$ [411]. The Zeeman energy represents the energy stored under the influence of the external time varying magnetic field (RF-AMF) and is expressed as: $E_Z = -\vec{\mu}.\vec{H}(t)$, where, $\vec{\mu}$ and $\vec{H}(t)$ are the moment of the MNP and time varying external magnetic field, respectively. The anisotropy energy is directly dependent on the effective anisotropy energy density and volume of the MNP and is expressed as $E_A = KV_p(\vec{\mu}.\hat{n}/|\vec{\mu}|^2)$, where, $\hat{n}$ is the unit vector along the magnetic easy axis for the MNP [411]. Lastly, the dipolar interaction energy between two MNP (i and j) is expressed as $E^{i,j}_{Dipolar} = \vec{\mu}_i.\vec{\mu}_j / r^3_{i,j} - 3(\vec{\mu}_i.\vec{r}_{i,j})(\vec{\mu}_j.\vec{r}_{i,j})/r^5_{i,j}$, where, $\vec{\mu}_i$ and $\vec{\mu}_j$ are the magnetic moments of

the i^{th} and j^{th} MNP, respectively, and $r_{i,j}$ is the interparticle distance. It can be seen from this expression that the dipolar interaction is strongly dependent on interparticle distance and hence, with increasing sample concentration, variation in dipolar interaction drastically changes the RF-AMF induced heating of MNP dispersions.

During Neel relaxation, the magnetic moments of the individual MNP flips direction across the anisotropy energy barrier. The dissipated power (P_{dis}) for this process is directly proportional to the product of number of flips per unit time (N_{flip}) and energy released per flip (E_{flip}), i.e., $P_{dis} \propto N_{flip}.E_{flip}$ [410]. For lower sample concentration, the dipolar interaction is less significant and hence, the anisotropy energy barrier is higher leading to a large value of energy release per flip. On the other hand, the probability of such flipping is lower for large energy barrier resulting in a comparatively lower number of flips per unit time. With increase in sample concentration, the anisotropy energy barrier decreases due to dipolar interaction resulting in a higher number of flips per unit time albeit with lower energy release per flip [412]. The scenario is schematically shown in **Fig. 4.5b**, where it can be seen that for higher (C_{high}) sample concentration (beyond optimum concentration), anisotropy barrier height decreased and hence, number of flips per unit time was comparatively more than that of the low concentration (indicated as C_{low}) cases, i.e., $N_{flip\text{-}high} > N_{flip\text{-}low}$, where the subscripts 'low' and 'high' indicates low and high concentration, respectively. On the other hand, due to reduced height of the anisotropy barrier, caused by dipolar interaction, energy release per flip was lower in the high concentration cases, i.e., $E_{flip\text{-}high} < E_{flip\text{-}low}$. Hence, with increasing sample concentration E_{flip} decreased, whereas, N_{flip} increased. This caused the SAR to peak at a certain optimum concentration, where the product $N_{flip}.E_{flip}$ was maximum for a given magnetic field. This explained the non-monotonic variation of SAR with sample concentration as shown in **Fig. 4.5a**.

As the number of flips per unit time (N_{flip}) increased with sample concentration due to reduced anisotropy barrier height, the Neel relaxation time (τ_N) decreased with increasing sample concentration [412, 413]. Considering the fluctuations of the dipolar field ($\vec{B}_d$) vector around a single MNP, the following equation for Neel relaxation under dipolar interaction was proposed by Morup and Tronc [412].

$$\tau_N = \tau_0[\sigma_{AT} - \frac{\beta_{av}^2}{3}(1 - 0.75\sigma_{AT}^{-1})] \quad (4.1)$$

Here, σ_{AT} (=KV_p/k_BT) is the ratio of anisotropy energy to thermal energy and $\beta_{av}^2 = \mu^2\left\langle \vec{B}_d^{\,2} \right\rangle /(k_BT)^2$, which is a numerical parameter related to the strength of dipolar interaction, respectively. It is evident from Eq. 4.1 that with increasing strength of the dipolar interaction, Neel relaxation time decreases. Urtizberea et al. [200] observed a lowering of Neel relaxation time with increasing sample concentration for maghemite based ferrofluid which was found to be in good agreement with the present results. In the present study, the product of cyclic frequency and effective relaxation time was ~ 0.02, i.e., $\omega\tau<<1$. It can be seen from Eq. 1.16 (in chapter 1) that dissipated power, P is directly proportional to $f(\omega\tau)$, where $f(\omega\tau)= \omega\tau(1+ \omega^2\tau^2)^{-1}$ [51, 52]. Therefore, the maximum heating occurs at $\omega\tau = 1$ and for $\omega\tau<<1$ (as in the present case), $f(\omega\tau) \sim \omega\tau$, i.e., P is directly proportional to the effective relaxation time [52]. This resulted in the decrease of SAR with reducing relaxation time, beyond certain optimum sample concentration due to enhanced dipolar interaction.

Apart from lowering of anisotropy barrier height and Neel relaxation, enhancement of dipolar interaction with increasing sample concentration also resulted in lowering of ensemble averaged equilibrium susceptibility (χ_0) of the MNP which caused the dissipated power to reduce for higher sample concentration as P is directly proportional to χ_0 ($P \sim \chi_0$ from Eq.

1.16 in chapter 1). Jonsson et al. [432] had theoretically shown that χ_0 decreases with increasing sample concentration and proposed the following equation.

$$\chi_0 = \frac{\mu_0 \mu^2}{3k_B T}\left(1 - \frac{\xi_d^2 R_{geo}^2}{18}\right) \tag{4.2}$$

Here, $\xi_d = \mu_0 \mu^2 C / 4\pi V_p k_B T$, C is the sample concentration and R_{geo} is a numerical constant whose value is 16.8 for typical cubic MNP [200]. With increasing sample concentration, ξ_d increased, causing χ_0 to decrease, thereby, reducing SAR for higher sample concentration as observed in the present study.

The SAR for a magnetic fluid under the application of a RF-AMF can be represented as SAR ~ A.f, where, A is the area under the hysteresis curve (high frequency hysteresis loop) and f is the frequency of the applied magnetic field [280, 410]. With increasing dipolar interaction, the area under the hysteresis curve decreased due to transitions from major to minor loops [198] for low field conditions ($H_{max}<H_{sat}$, where H_{max} and H_{sat} indicate maximum applied magnetic field amplitude and saturation magnetic field amplitude for the MNP, respectively), causing the SAR to decrease significantly for higher sample concentration. Using molecular dynamics simulation based on Landau-Lifschitz-Gilbert equation of motion and Langevin dynamics, Haase and Nowak [280] theoretically showed that the area under the hysteresis curve varies non-monotonically with sample concentration. Typical result of their theoretical calculations is shown in **Fig. 4.6** [280] for simple cubic ordering of MNP with saturation magnetization of 800 kAm^{-1} and anisotropy energy density of 10 kJ/m^3 at temperature T = 300 K. It can be seen from **Fig. 4.6** that the hysteresis area initially increased with concentration, attained a maximum at an optimum concentration and decreased thereafter with increasing concentration. This essentially indicated the presence of an optimum sample concentration for highest SAR, as found in the present study.

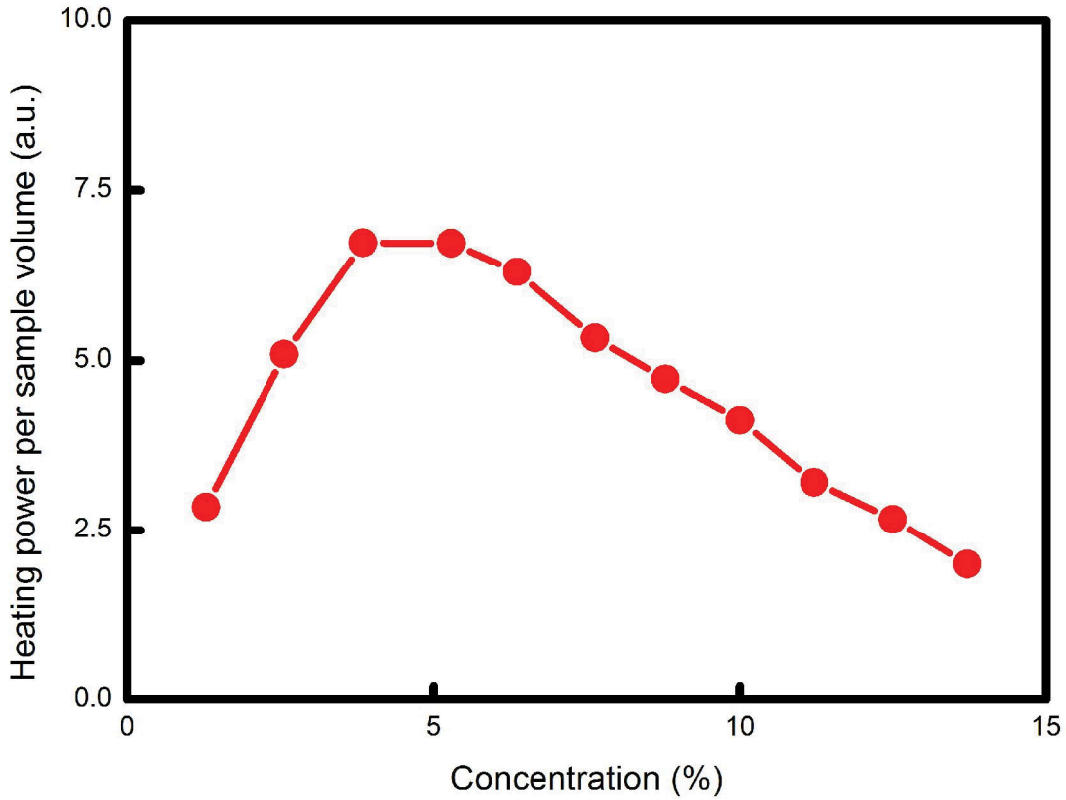


Figure 4.6: Theoretical variation of heating power per sample volume as a function of sample concentration. Redrawn from (with permission) Haase and Nowak [280].

Water based ferrofluids are prone to agglomeration and it becomes prominent under the influence of an applied magnetic field [414, 433]. Such agglomeration leads to an increase in the effective particle diameter (D_{eff}) which eventually leads to a drastic enhancement of dipolar interaction as dipole-dipole interaction between two MNP is proportional to D_{eff}^{6} [64]. It must be noted in this regard, that the average hydrodynamic size of the phosphate coated MNP, dispersed in water, was ~ 32 nm, which was ~ 4 times higher than the average crystallite size (~ 7.8 nm). This indicated agglomerates with more than one MNP. The higher affinity of phosphate molecules towards water molecule via hydrogen bonding would have also contributed to the agglomeration [427]. Hence, agglomeration was found to be a major cause for the observed reduction in the SAR values beyond a certain concentration, in

agreement with the recent findings of Guibert et al. [202] on significant decrease in SAR in large and dense aggregates of MNP in a dispersion medium. The observed decrease in the heating efficiencies at higher sample concentration can also be due to the deviations from log-normal distribution of the magnetic dipole moment, twinning defects or inhomogeneous oxide phases [434].

4.3 MFH in water based ferrofluid containing phosphate coated $CoFe_2O_4$ MNP

MNP with sizes around ferromagnetic-superparamagnetic limits exhibit enhanced heating due to substantial hysteresis losses in addition to the relaxation losses [52]. Hence, for successful hysteresis loss mediated heating, a reasonably high values of magnetization and coercivity are desired [435]. It must be noted in this regard that a very high value of coercivity is not beneficial for practical *in vivo* applications of MFH due to cluster formation induced by remnant magnetization in the absence of an external magnetic field. It is evident that magnetocrystalline and shape anisotropy factors play a crucial role in RF-AMF induced heating efficiency of such MNP with sizes around ferromagnetic-superparamagnetic limit.

In the present study, RF-AMF induced heating efficiency of a water based magnetic nanofluid containing phosphate coated $CoFe_2O_4$ MNP was investigated, where the effects of sample concentration on heating efficiency was probed.

4.3.1 Experimental details and characterization studies

Phosphate coated $CoFe_2O_4$ MNP were synthesized using a co-precipitation method described in chapter 2 (section 2.1.2). A master solution of 5 wt. % concentration (hereafter indicated as C5) was prepared and later diluted to 4, 3, 2 and 1 wt. % (hereafter indicated as C4, C3, C2 and C1, respectively). The synthesized MNP were characterized using XRD, SAXS and VSM. Powder XRD pattern of the cobalt ferrite MNP showed Bragg reflection peaks

corresponding to the cubic spinel structure and using Scherrer's formula, the average crystallite size was found to be ~ 12 (± 1) nm. The scattering intensity obtained from SAXS was fitted with a spherical model and the distance distribution function was obtained by performing Fourier transform of the intensity profile. **Fig. 4.7a** shows the variation of distance distribution function (P(r)) as a function of MNP diameter. Using a log-normal size distribution function the most probable diameter was obtained as ~ 18 nm (σ_{ln} ~ 0.4) which was found to be higher than the average crystallite size. **Fig. 4.7b** shows the variation of ln(I(q)) as a function of ln(q), where, I(q) indicates scattering intensity profile as a function of wave vector, q. It was observed from **Fig. 4.7b** that for high q region (Porod' region), ln(I(q)) varied linearly with ln(q) with a slope of -3.25 ± 0.01, which indicated the spherical shape of the synthesized MNP (for ideal spherical particles, $I(q) \sim q^{-4}$) [332].

Figure 4.8 shows the room temperature magnetization curve of the $CoFe_2O_4$ MNP, where it can be seen that the MNP exhibited ferromagnetic nature. The saturation magnetization was obtained as 31.66 emu/g (without correction to dead layer). The saturation magnetization was lower than the bulk value of 86.61 emu/g [53], which was attributed to the presence of a thick phosphate coating on the MNP surface. **The first inset (I1) of Fig. 4.8** shows the magnified section of the room temperature M-H curve from H = 0 to ± 0.22 T, where the presence of the hysteresis loop can be clearly seen. The remnant magnetization and coercive field were ~ 3.82 emu/g and 146 G, respectively. These values were lower than the remnant magnetization and coercivity values (14 emu/g and 240 G, respectively) reported by Veverka et al. [435] for ~ 18 nm uncoated $CoFe_2O_4$ MNP annealed at 400 ^{0}C for 3 hours in air atmosphere. The low values of the remnant magnetization and coercivity, obtained in the present study, indicated the suitability of the phosphate coated $CoFe_2O_4$ MNP for practical MFH applications. **The second inset (I2) of Fig. 4.8** shows the low temperature (~ 5 K) M-H curve for the phosphate

coated $CoFe_2O_4$ MNP. In this case, the values of the saturation magnetization, remnant magnetization and coercive field were ~ 44.66 emu/g, 32.22 emu/g and 8302 G, respectively. The higher values were attributed to the lower thermal energy at 5 K.

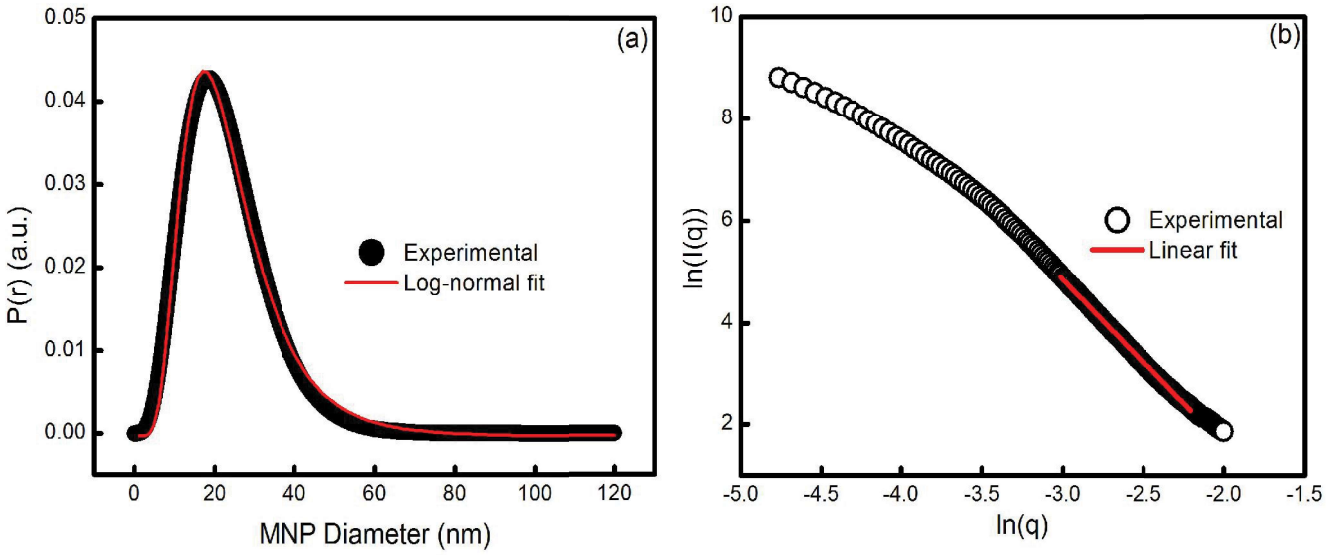


Figure 4.7: (a) Distance distribution function (P(r)), obtained from SAXS, as a function of MNP diameter for the phosphate coated $CoFe_2O_4$ MNP. The data is fitted with a log-normal distribution (also shown in the figure). (b) Variation of ln(I(q)), as a function of ln(q), for the phosphate coated $CoFe_2O_4$ MNP. The high q region is fitted with a straight line (also shown in the figure).

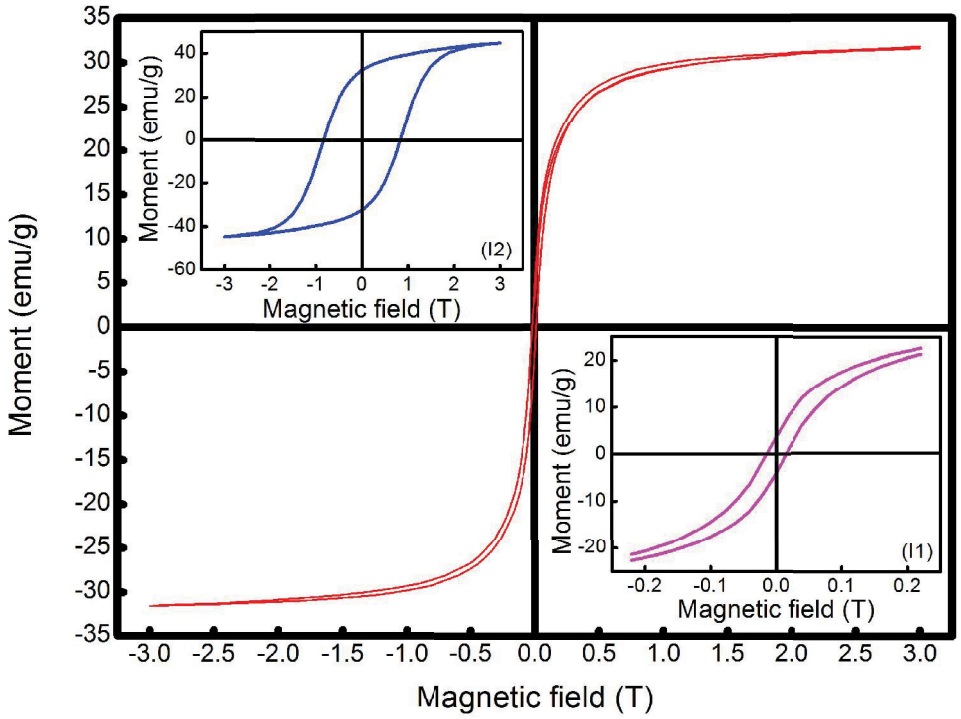


Figure 4.8: Room temperature magnetization curve of the $CoFe_2O_4$ MNP. (Inset 1) Magnified region of the room temperature M-H curve, from H = 0 to ± 0.22T, where, the hysteresis loop is clearly discernible. (Inset 2) Low temperature (~ 5 K) M-H curve of the $CoFe_2O_4$ MNP, where, a wide hysteresis loop is clearly seen.

The anisotropy energy density was calculated from the room temperature hysteresis (M-H) loop using an equation of the form: $K = (H_c \times M_s)/0.98$, where, H_c is the coercive field in Oe, M_s is the saturation magnetization in G and 0.98 is a numerical constant [436]. The anisotropy energy density was estimated as 2.9×10^5 erg/cc (or ~ 290 kJ/m^3) which was found to be in good agreement with the value of 274 kJ/m^3 reported by Andreu et al. [53] and approximately one order higher than the anisotropy energy density of Fe_3O_4 MNP of similar sizes [18]. For superparamagnetic MNP, the thermal energy is higher than the anisotropy barrier (~ KV_p) which causes spontaneous spin flipping at room temperature. On the other hand, with increasing anisotropy energy density and MNP volume (V_p), thermal energy is not sufficient enough to overcome the barrier height leading to blocked state, which exhibit

ferromagnetic behaviour. It has been reported that for $CoFe_2O_4$ MNP, the ferromagnetic to superparamagnetic transition occurs for MNP sizes below ~ 10 nm and hence, in the present study, the phosphate coated $CoFe_2O_4$ MNP with most probable size of ~ 18 nm exhibited ferromagnetic behaviour [53, 54]. Temperature dependent magnetization studies (ZFC/FC: zero field cooled/field cooled) also revealed that the blocking temperature was beyond room temperature (300 K) which was in agreement with ferromagnetic nature of $CoFe_2O_4$.

MFH experiments were carried out at a fixed frequency of 126 kHz and under four different external field amplitudes of 51.4, 45.0, 36.7 and 26.0 kAm^{-1}. Agar based samples were prepared by following a procedure described in section 2.1.4 (in chapter 2) and the sample with 2 wt. % MNP concentration (C2) was used for preparing the agar based samples. Two samples with different agar concentrations, viz., 1 and 2 wt. %, hereafter indicated as C2A1 and C2A2, respectively, were prepared. RF-AMF induced rise in sample temperature was measured using fiber optic temperature sensor and infrared thermography (IRT). Detailed description of the experimental set-up and procedure can be found in chapter 2 (sections 2.4 and 2.5). The final SAR values were reported as W/g_{MNP}, where, g_{MNP} indicates weight of the MNP per cc of the sample [435]. The specific heat capacity and density of the base fluid (water) were considered as 4.18 $Jg^{-1}\,{}^0C^{-1}$ and 1 g/cc, respectively.

4.3.2 Results and discussions

4.3.2.1 RF-AMF induced heating

Figures 4.9a-d show the typical infrared images at t = 0, 100, 200 and 300 s, respectively, during RF-AMF induced heating of the sample C2 under an external field amplitude of 51.4 kAm^{-1}. The pseudo colour coded temperature scales are also shown along with the infrared images, where the fluid sample is clearly discernible. The emissivity was optimized to reflect

the true temperature of the fluid sample. It is evident from **Figs. 4.9a-d** that sample temperature increased with time and spatial averaging over several locations were performed to obtain the average temperature rise as a function of time. The temperature rise curves obtained from IRT were corrected for internal and external convection phenomena, as discussed in chapter 3, and the convection corrected temperature values were used for further analyses.

Figures 4.10a-e show the temperature rise ($\Delta T = T-T_i$, where, T_i = initial temperature = 28 ^{0}C) as a function of time during RF-AMF induced heating of the magnetic nanofluids with 1, 2, 3, 4 and 5 wt. % concentration and under four different external field amplitudes, viz., 51.4, 45.0, 36.7 and 26.0 kAm^{-1}, respectively. It can be clearly seen from **Fig. 4.10** that sample temperature continued to increase with time during RF-AMF induced heating. For a fixed sample concentration, rate of temperature rise and maximum temperature rise at the end of heating phase (ΔT_{max}) increased with external field amplitudes. On the other hand, for a fixed external field amplitude, ΔT_{max} continued to increase with sample concentration. For H = 51.4 kAm^{-1}, ΔT_{max} values were 11.1 (± 0.2), 27.2 (± 0.5), 36.5 (± 0.3), 43.5 (± 0.4) and 49.9 (± 0.3) ^{0}C for the samples C1-C5, respectively. This shows that apart from the sample C1 with 1 wt. % MNP concentration, ΔT_{max} values were beyond the hyperthermia limit for other samples indicating their suitability for MFH based cancer treatment.

Figure 4.10f shows the temperature rise as a function of time for the sample C5 (highest MNP loading of 5 wt. %), during RF-AMF induced heating under an external field amplitude of 51.4 kAm^{-1} followed by natural cooling for three consecutive cycles. The reversible temperature rise and decay for three consecutive cycles indicated very good thermal stability and reversible thermal response of the water based magnetic nanofluid containing phosphate coated $CoFe_2O_4$ MNP, which is essential for practical applications. The square wave

indicated the state of the RF-AMF, where, the higher and lower states indicated 'on' and 'off' stages, respectively. Similar results were obtained for other samples.

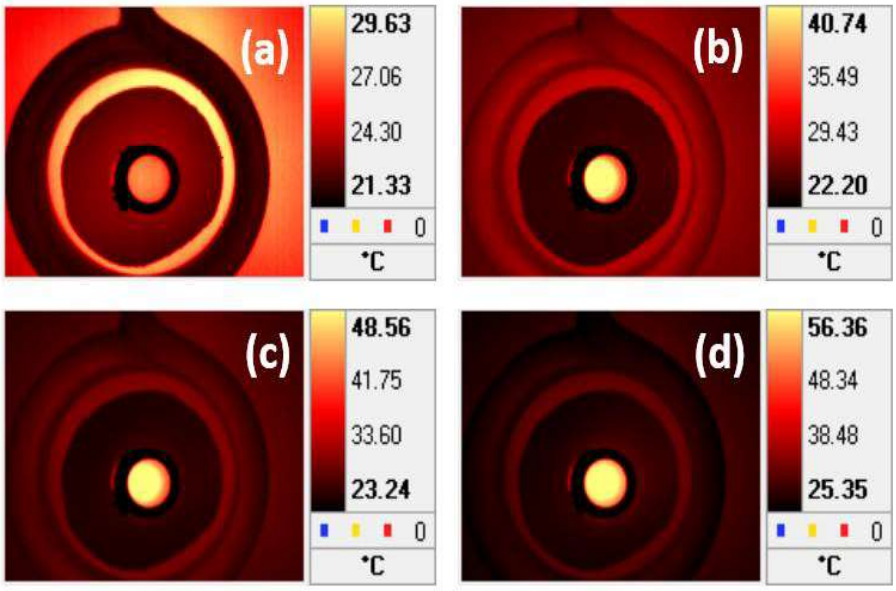


Figure 4.9: Typical infrared images of the sample C2 at time t = (a) 0, (b) 100, (c) 200 and (d) 300 s, during RF-AMF induced heating under an external field amplitude of 51.4 kAm^{-1}. The pseudo colour coded temperature scales are shown along with the images. The emissivity was optimized to reflect the true temperature of the fluid sample.

Figure 4.11a shows the variation of ΔT_{max} as a function of square of the external field amplitudes for the samples C1-C5. It can be seen from **Fig. 4.10a** that ΔT_{max} increased linearly with H^2 and the linear regression analyses are also shown in the figure. The adjusted R^2 values were ~ 0.96, 0.98, 0.98, 0.99 and 0.99 for the samples C1-C5, respectively, indicating good accuracy of the linear fits. Adiabatic reconstruction of the temperature rise curves were performed using the data analysis protocol described in section 2.6.6 (in chapter 2) and initial rates of temperature rise were determined using linear regression analyses of the initial data (0-30 s) of the adiabatically reconstructed temperature rise curves. It was observed

that the adiabatically reconstructed initial rates of temperature rise were, on average, ~ 18 % higher than the experimentally measured initial rates which indicated the thermal losses due to the non-adiabatic nature of the experimental set-up.

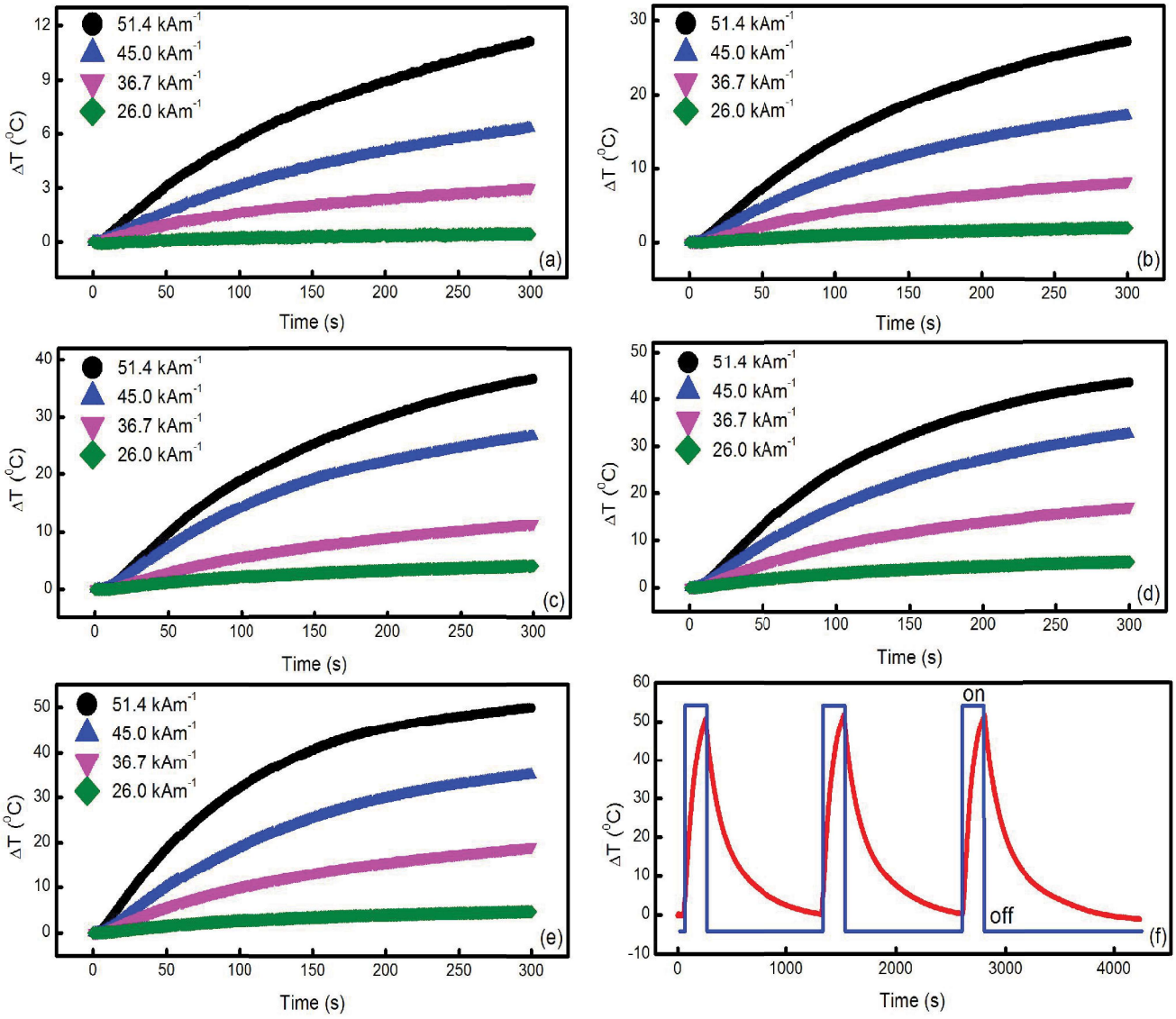


Figure 4.10: Variation of temperature rise (ΔT), as a function of time, for the phosphate coated $CoFe_2O_4$ nanofluids of five different concentrations, viz., (a) 1, (b) 2, (c) 3, (d) 4 and (e) 5 wt. %, during RF-AMF induced heating under four different external field amplitudes, viz., 51.4, 45.0, 36.7 and 26.0 kAm^{-1}. (f) RF-AMF induced temperature rise followed by natural temperature decay for three consecutive cycles, for the sample C5 (5 wt. % MNP concentration), under an external field amplitude of 51.4 kAm^{-1}. The square wave indicated the state of RF-AMF.

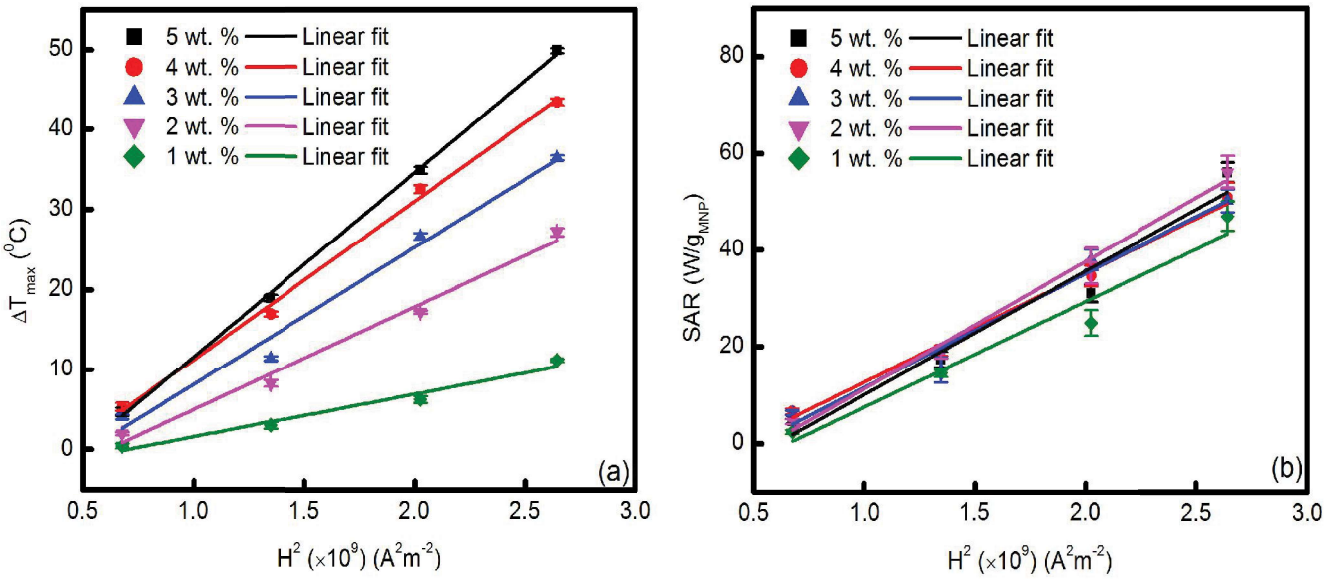


Figure 4.11: (a) Variation of ΔT_{max} as a function of H^2 for the samples C1-C5. ΔT_{max} increased linearly with H^2 and the linear regression analyses are also shown in the figure. (b) Variation of SAR as a function of H^2 for the samples C1-C5. SAR increased linearly with H^2 and the linear regression analyses are also shown in the figure.

Figure 4.11b shows the variation of SAR as a function of H^2 for the samples C1-C5 and it can be seen that SAR increased linearly with H^2 (linear regression analyses are also shown in the figure) which was found to be in agreement with Rosensweig's model of field induced heating ($P \sim H^2$, Eq. 1.16 in chapter 1) [51]. The adjusted R^2 values were 0.94, 0.99, 0.96, 0.99 and 0.94 for the samples C1-C5, respectively. This was found to be in contradiction with other studies, where it has been reported that, for $CoFe_2O_4$ MNP, SAR varied linearly with $H^{2.8}$ [53, 437]. A linear variation of SAR with H^2, in turn indicated a linear variation of ΔT_{max} with H^2 as observed in **Fig. 4.11a**. RF-AMF induced heating under an external field amplitude of 57.3 kAm^{-1}, resulted in a maximum SAR of ~ 79.7 ± 3.1 W/g_{MNP} and maximum ΔT_{max} of ~ 55.9 ± 0.3 ^0C for magnetic nanofluids with 2 and 5 wt. % MNP concentration, respectively. **Table 4.3** shows the values of ΔT_{max} and SAR for the samples C1-C5 during

RF-AMF induced heating under four different external field amplitudes, viz., 51.4, 45.0, 36.7 and 26.0 kAm^{-1}.

Table 4.3: ΔT_{max} (maximum temperature rise at the end of heating phase) and specific absorption rate (SAR) for the samples C1-C5, during RF-AMF induced heating, under four different external field amplitudes, viz., 51.4, 45.0, 36.7 and 26.0 kAm^{-1}.

Sample	RF-AMF amplitude (kAm^{-1})	ΔT_{max} (^0C)	SAR (W/g_{MNP})
C1	51.4	11.1 ± 0.2	47.0 ± 3.1
	45.0	6.3 ± 0.4	24.9 ± 2.7
	36.7	3.0 ± 0.4	14.6 ± 0.8
	26.0	0.4 ± 0.3	2.4 ± 0.4
C2	51.4	27.2 ± 0.5	56.2 ± 3.4
	45.0	17.2 ± 0.2	36.7 ± 3.7
	36.7	8.2 ± 0.4	18.6 ± 1.1
	26.0	2.0 ± 0.2	4.6 ± 0.5
C3	51.4	36.5 ± 0.3	50.2 ± 2.4
	45.0	26.7 ± 0.4	38.0 ± 2.1
	36.7	11.4 ± 0.3	15.2 ± 2.5
	26.0	4.1 ± 0.3	6.3 ± 0.5
C4	51.4	43.5 ± 0.4	50.8 ± 3.1
	45.0	32.6 ± 0.5	34.6 ± 2.2
	36.7	17.0 ± 0.3	19.2 ± 1.1
	26.0	5.3 ± 0.5	6.6 ± 0.6
C5	51.4	49.9 ± 0.3	56.1 ± 2.1
	45.0	34.9 ± 0.4	31.0 ± 1.8
	36.7	19.0 ± 0.4	17.4 ± 1.6
	26.0	4.7 ± 0.5	4.6 ± 0.5

It can be seen from **Table 4.3** that for an external field amplitude of 51.4 kAm^{-1}, the highest SAR (~ 56.2 ± 3.4 W/g_{MNP}) was obtained for the sample C2 (2 wt. %). The SAR values obtained in the present study were significantly higher than that reported by Andreu et al. [53], where, the highest SAR of ~ 1.2 W/g was obtained for 7.4 nm $CoFe_2O_4$ MNP dispersed in diethylene glycol under an external field amplitude of 3 kAm^{-1} and excitation frequency of 111 kHz. Surendra et al. [438] reported a very high SAR value of 2131 W/g (H = 18.31 kAm^{-1}) for oleic acid coated $CoFe_2O_4$ (size ~ 12 nm) dispersed in hexane which was attributed to the high saturation magnetization and reduced spin randomization of the oleic acid coated

$CoFe_2O_4$ MNP. Nevertheless, the SAR and ΔT_{max} values obtained in the present study were sufficiently high for practical applications in MFH based cancer treatment.

4.3.2.2 Effects of sample concentration and medium viscosity on RF-AMF induced heating efficiency

Figure 4.12a shows the variation of SAR as a function of sample concentration for the samples C1-C5 during RF-AMF induced heating under four different external field amplitudes, viz., 51.4, 45.0, 36.7 and 26.0 kAm^{-1}. Though slight decrease in SAR was observed for higher sample concentration, it can be seen from **Fig. 4.12a** that SAR did not vary significantly with sample concentration. This was found to be in contrast with water based ferrofluid containing phosphate coated Fe_3O_4 MNP, where a distinct maximum in SAR was observed and for higher sample concentration, SAR decreased (**Fig. 4.5a**) due to the enhancement of dipolar interaction. Enhancement of dipolar interaction also resulted in decreased SAR for higher sample concentration in the case of water based ferrofluid containing TMAOH coated Fe_3O_4 MNP (**Fig. 3.11a** in chapter 3).

In the cases of TMAOH or phosphate coated Fe_3O_4 MNP, Neel-Brownian relaxation assisted heating dominated due to the superparamagnetic nature of the MNP and with increasing sample concentration, Neel relaxation time decreased (Eq. 4.1) which resulted in a lower SAR [200, 412]. Additionally, enhancement of dipolar interaction caused the ensemble averaged equilibrium susceptibility to decrease (Eq. 4.2), which also contributed to the lowering of SAR with increasing sample concentration [432]. On the other hand, for phosphate coated $CoFe_2O_4$ MNP, with sizes above superparamagnetic/ferromagnetic limit, the heating mechanism is significantly dominated by hysteresis losses, where sample concentration has less pronounced role on RF-AMF induced heating, especially when anisotropy energy density is high [53, 439]. Using numerical minimization of the

thermodynamical action for the transition between two metastable states (across the anisotropy energy barrier), Berkov et al. [439, 440] showed that in MNP with high or moderate anisotropy energy densities, the anisotropy energy barrier distribution does not shift to lower energy values with increasing sample concentration, i.e., the effects of enhancement of dipolar interaction on MNP with higher anisotropy energy density (the K value of $CoFe_2O_4$ is ~ 1 order higher than that of Fe_3O_4 of similar sizes) are less prominent [53]. This phenomenon was explained on the basis of Berkov and Gorn (BG) model [439], where a numerical simulation of AC susceptibility (imaginary component) as a function of sample concentration, excitation frequency, damping parameter and anisotropy energy density of the MNP is done. According to the BG model, MNP systems can be divided into two categories, viz., low anisotropy systems ($\beta_{BG}<1$) and moderate to high anisotropy systems ($\beta_{BG}>1$), where, β_{BG} is a dimensionless parameter defined as $\beta_{BG} = 20K/M_s^2$, where, K is the anisotropy energy density in J/m^3 and M_s is the saturation magnetization in kAm^{-1} [53, 439]. For the $CoFe_2O_4$ MNP, used in the present study, K ~ 290 kJ/m^3 and M_s ~ 155.36 kAm^{-1}, and hence, β_{BG} ~ 240>>1 indicating very high anisotropy of the system. For such conditions, the BG model predicts that the anisotropy energy barriers are dependent on the individual MNP and the effects of inter-particle interactions are less significant and cause a decrease in barrier height (and SAR) at substantially higher sample concentrations only (beyond volume fraction of ~ 0.08) [53, 439]. In the present study, highest volume fraction was ~ 0.01 and hence, SAR did not vary significantly with sample concentration as shown in **Fig. 4.12a**. On the other hand, for Fe_3O_4 MNP (size ~ 7.8 nm) with saturation magnetization of 268.84 kAm^{-1} and anisotropy energy density of 367 kJ/m^3, the value of β_{BG} is ~ 102 that is substantially lower than that of $CoFe_2O_4$ which indicated that the effects of sample concentration on RF-AMF induced heating efficiency is much more pronounced for Fe_3O_4 based ferrofluids (see **Figs. 4.5a and 3.11a**).

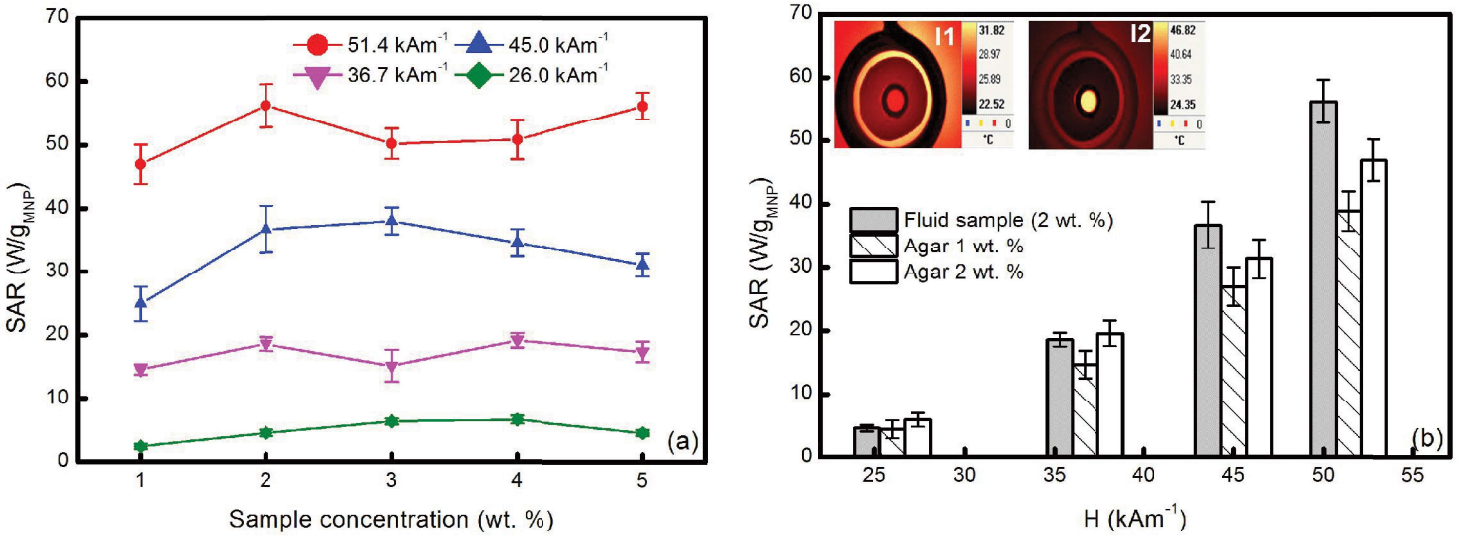


Figure 4.12: (a) Variation of SAR as a function of sample concentration, for the samples C1-C5, during RF-AMF induced heating under four different external field amplitudes, viz., 51.4, 45.0, 36.7 and 26.0 kAm^{-1}. (b) Bar chart, showing the SAR values of the sample C2 and agar immobilized samples C2A1 and C2A2 containing 1 and 2 wt. % agar concentrations, respectively. Typical infrared images of the agar immobilized sample C2A2, at time t = 0 (Inset: I1) and 200 s (Inset: I2), respectively, during RF-AMF induced heating under an external field amplitude of 51.4 kAm^{-1}.

Moreover, enhancement of dipolar interaction caused a lowering of Neel relaxation time and ensemble averaged equilibrium susceptibility (χ_0 that is proportional to initial susceptibility, χ_i for low field conditions [51]) which resulted in a faster decay of SAR in systems, where heating mechanism is Neel-Brownian relaxation dominated (like phosphate or TMAOH coated superparamagnetic Fe_3O_4 MNP), whereas, for systems with hysteresis loss mediated heating, enhancement of dipolar interaction results in lowering of the initial static susceptibility (neglecting the effects on Neel relaxation time), leading to a less pronounced variation of SAR with increasing sample concentration.

RF-AMF induced heating experiments were performed on the agar based samples C2A1 and C2A2, with 1 and 2 wt. % agar concentrations, respectively and **Fig. 4.12b** shows a bar chart comparing the SAR values of the fluid (C2 with 2 wt. % MNP loading) and agar based

samples. The **insets of Fig. 4.12b (I1 and I2)** show the typical infrared images of the sample C2A2 at time t = 0 and 200 s, respectively, during RF-AMF induced heating under an external field amplitude of 51.4 kAm^{-1}. It can be seen from the **insets of Fig. 4.12b** that sample temperature increased with time and spatially averaged sample temperature, after incorporating convection correction and adiabatic reconstruction protocol, was used for determining the rates of temperature rise which were then used for SAR determination for the samples C2A1 and C2A2 using Eq. 1.19 (in chapter 1). It can be seen from **Fig. 4.12b** that the SAR of the agar based samples were lower than the fluid based sample which was attributed to the abrogation of Brownian relaxation on gel formation. It was further observed that SAR reduced by 20-30 % due to abrogation of Brownian relaxation which was lower than the reported values of 40-50 % [51, 256, 441] in the cases of superparamagnetic Fe_3O_4 MNP, where the heating mechanism is Neel-Brownian relaxation dominated.

It can be further seen from **Fig. 4.12b** that the SAR did not decrease with increase in agar concentration which was also attributed to the ferromagnetic nature of the $CoFe_2O_4$ MNP. With increasing agar concentration, sample viscosity increased leading to possible agglomeration of $CoFe_2O_4$ MNP which drastically modified the heating efficiency [439]. According to BG model [439], slight agglomeration of the phosphate coated $CoFe_2O_4$ MNP in highly viscous agar gel resulted in correlations between the anisotropy axes directions of the neighbouring MNP leading to an increase in anisotropy barrier height which ultimately increased the effective coercivity (H_c is directly proportional to K [436]) of the agar based samples. An increase in the effective coercivity resulted in higher SAR due to larger hysteresis losses for the agar based sample with higher agar concentration as observed in **Fig. 4.12b**. Hence, for systems with high anisotropy energy density, increasing agar concentration did not decrease the global SAR significantly, which is beneficial for practical applications of MFH in tissue like environment.

4.4 Conclusions

RF-AMF induced heating in water based ferrofluids containing phosphate coated superparamagnetic Fe_3O_4 and ferromagnetic $CoFe_2O_4$ MNP were studied. The SAR values were measured at a fixed frequency of 126 kHz and under different external field amplitudes. In the case of phosphate coated Fe_3O_4 MNP, for a fixed sample concentration, the maximum temperature rise (ΔT_{max}) was found to increase with external field amplitude. The SAR values were determined from the initial rates of temperature rise and it was observed that SAR varied linearly with square of the external field amplitude, in accordance with Rosensweig's model. It was further observed that, for the phosphate coated Fe_3O_4 MNP based ferrofluids, SAR increased initially with sample concentration, attained a maximum at an optimum concentration and decreased thereafter with increasing sample concentration. The decrease in SAR beyond the optimum sample concentration was attributed to the enhancement of dipolar interaction and particle agglomeration. With increasing sample concentration, interparticle distance decreased resulting in an enhancement of dipolar interaction, which caused the anisotropy energy barrier to decrease. For a lower anisotropy barrier height, number of spin flips increased albeit with a lower energy release per flip and SAR was optimum for the condition when the product of number of flips per unit time and energy release per flip was maximum. For higher sample concentration, enhancement of dipolar interaction resulted in reduced Neel relaxation time and ensemble averaged equilibrium susceptibility, both of which contributed to the lowering of SAR. The highest SAR for the phosphate coated Fe_3O_4 MNP was ~ 11.1 ± 0.6 W/g_{MNP} for a sample concentration of 1.5 wt. %, under an external field amplitude of 57.3 kAm^{-1}.

On the other hand, in ferromagnetic phosphate coated $CoFe_2O_4$ MNP (saturation magnetization, remnant magnetization, coercive field and anisotropy energy density were ~ 31.66 emu/g, 3.82 emu/g and 146 G, 290 kJ/m^3, respectively) based ferrofluids, SAR and

ΔT_{max} increased linearly with H^2 and the maximum value of SAR obtained was ~ 56.2 ± 3.4 W/g_{MNP} for a sample concentration of 2 wt. % (at an external field amplitude of 51.4 kAm^{-1}). It was observed that SAR did not vary with sample concentration due to significant contribution from hysteresis losses to the global SAR, in agreement with Berkov and Gorn model. To assess the Brownian contribution to global SAR, experiments were performed on agar immobilized samples, where, the Brownian relaxation was found to contribute up to ~ 20-30 % to the global SAR, which was significantly lower than the reported values of 40-50 % in the cases of superparamagnetic MNP. The SAR was found to be higher for agar sample with 2 wt. % agar concentration which was attributed to the increase in anisotropy barrier height, effective coercivity and hysteresis losses.

Phosphate coating makes the MNP biocompatible, improve dispersity and stability of the MNP in aqueous phase at biologically relevant pH, which is beneficial for practical applications. The experimental findings clearly show the efficacy of water based magnetic nanofluids containing phosphate coated superparamagnetic Fe_3O_4 and ferromagnetic $CoFe_2O_4$ MNP for magnetic fluid hyperthermia applications. The results offer possibility to fine tune sample concentration for improving the RF-AMF induced heating efficiency.

Chapter 5

Magnetic hyperthermia in magnetic nanoemulsions: Effects of polydispersity, particle concentration, medium viscosity and orientational ordering

Chapter 5 Magnetic hyperthermia in magnetic nanoemulsions: Effects of polydispersity, particle concentration, medium viscosity and orientational ordering

5.1 Introduction

In conventional MFH based cancer treatment, a fluid containing MNP is injected into a tissue containing cancerous cells and, thereafter, exposed to a RF-AMF, which causes an increase in the fluid temperature beyond 42 ^{0}C that leads to cellular degradation. In 2011, Kumar and Mohammad [217] broadened the definition of MFH to include magnetically modulated drug delivery which stimulated several exciting opportunities of using larger sized magnetic nano-carriers (size ~ 100-200 nm), like nano-composites or nano-emulsions, for multimodal therapy, where the nano-carriers are loaded with anti-cancer drugs (like doxorubicin, daunorubicin, paclitaxel, etc.) [128, 164] or photodynamic agents (chloroaluminum phthalocyanine or Zn(II)-phthalocyanine) [168-170] for combining hyperthermia with drug delivery or photodynamic therapies, respectively. Such larger sized nano-carriers loaded with anti-cancer drugs are beneficial for enhanced permeation and retention (EPR) in the leaky vasculature surrounding the cancerous cells and for reduced uptake by macrophages or filtration by spleen, liver and human complement system [256, 261, 262]. Several studies [128, 164, 166, 168-170, 263-265] show that such larger sized nano-carriers are essential for achieving synergistic multimodal therapy with higher treatment efficiency. Recent studies also indicate that a high temperature rise is not a prerequisite for MFH induced drug delivery, thereby, opening up the possibilities of using nano-carriers with even lower MNP loading as multi-modal MFH agents [268].

Magnetic nanoemulsions are ideal model candidates for larger sized nano-carriers due to their structural and dimensional similarities with encapsulated ultra-magnetic liposomes (UML) [256, 264]. Though the RF-AMF induced heating in MNP based nanofluid is well studied,

several challenges still exist in the basic understanding of the heating mechanism in magnetic nanoemulsions and magnetic clusters. Due to larger size of the emulsion droplets, Brownian relaxation is the dominant heating mechanism, whereas, in the case of smaller sized MNP, both Neel and Brownian contributions are present. The size and polydispersity of the droplets play a crucial role in heat generation through Brownian relaxation. The effect of demagnetizing field and inter-particle interaction also needs to be understood for the effective utilization of MFH towards cancer treatment. Finally, the role of interfacial thermal resistance and medium viscosity on the heat transfer from the droplets to the dispersion medium needs to be understood clearly. Despite the fact that the role of polydispersity [51, 442], demagnetizing field [378, 443] and dipole-dipole interactions [280, 410] on heating efficiency is studied theoretically (analytically or numerically), more experimental data are essential to understand the efficiency of multimodal therapy for practical applications.

In the present study, RF-AMF induced heating in model oil-in-water magnetic nanoemulsions is systematically investigated and the effects of polydispersity, MNP concentration, medium viscosity and external DC magnetic field induced orientational ordering on heating efficiency are probed.

5.2 Effects of polydispersity, particle concentration and medium viscosity on RF-AMF induced heating efficiency

In magnetic nanoemulsion, both the MNP (10 nm) and the droplets (20 times bigger at ~ 200 nm) act as heat generators. The magnetically triggered heating efficiency with and without Brownian relaxation mechanism (studied by immobilizing the emulsion droplets in a tissue mimicking agar gel) was compared and the effect of demagnetizing field was also investigated. The experimental findings were compared with theoretical results obtained

under linear response regime. The morphological consistency of the emulsion droplets immobilized in agar gel was also studied using atomic force microscopy (AFM).

5.2.1 Experimental details and characterization studies

Oleic acid coated single domain superparamagnetic Fe_3O_4 MNP, dispersed in hexane (hereafter indicated as O1), were synthesized by a chemical co-precipitation technique described in section 2.1.2 in chapter 2. Magnetically polarizable oil-in-water emulsions were prepared using a classical inversion method, as described in section 2.1.3 in chapter 2. The water dispersed oil droplets were electrostatically stabilized using an anionic surfactant: sodium dodecyl sulphate (SDS). Three different magnetic nanoemulsions (hereafter indicated as E1, E2 and E3) of nearly identical droplet size but different polydispersity were prepared. The concentration of MNP was kept constant for E1 and E2, whereas, for E3, MNP loading was lower. The abrogation of Brownian relaxation of the emulsion droplets was achieved by immobilizing the droplets in a 4 wt. % concentration agar gel (hereafter indicated as EA1), following a procedure described in section 2.1.4 chapter 2.

The synthesized MNP were characterized using XRD, SAXS, DLS, FTIR spectroscopy and VSM. XRD pattern indicated the cubic spinel structure of Fe_3O_4 MNP and the average crystallite size was obtained as 8 (± 0.8) nm, whereas, the most probable diameter from SAXS was obtained as 6.9 nm (σ_{ln} = 0.14). SAXS data also indicated the spherical shape of the synthesized MNP [258]. DLS studies showed a narrow unimodal distribution of the hydrodynamic diameter of the MNP dispersed in hexane with the most probable size of 10.6 nm (σ_{ln} = 0.25) [258]. Detailed analysis of the FTIR spectra indicated that oleic acid was chemisorbed on the surface of Fe_3O_4 MNP [258, 417]. The saturation magnetization was found to be ~ 42 emu/g (without correction to dead layer) and room temperature M-H curve (**inset of Fig. 5.1** shows a section of the M-H curve) showed no remanence confirming

superparamagnetic (SPM) behaviour of the synthesized MNP [258]. **Fig. 5.1** shows the temperature dependent magnetization (ZFC and FC) of the oleic acid coated Fe_3O_4 MNP in the temperature range of 4-300 K and it can be seen from the figure that the field cooled (FC) magnetization continued to increase with decreasing temperature, whereas, for the ZFC curve, the magnetization showed a maximum at ~ 189 K. The ZFC and FC curves were found to be clearly bifurcated below ~ 192.4 K but coincident at higher temperature (200-300 K). From **Fig. 5.1**, the average blocking temperature (T_B) was estimated as ~ 191 K. Incorporating the value of T_B, effective uniaxial anisotropy energy density ($K = 25k_BT_B/V_p$) [18] was estimated as 36.7 $\times 10^5$ erg/cm^3, which was found to be in good agreement with the anisotropy energy density of 35.6 $\times$ 10^5 erg/cm^3 reported by Goya et al. [444] for superparamagnetic Fe_3O_4 MNP. The anisotropy energy density was also estimated from the M-H curve using Brown's law of approach to magnetic saturation [445] following the equation: $M(H) = M_s (1-\alpha_B/H^2)$, where, α_B is a numerical parameter and effective uniaxial anisotropy energy density is estimated from the equation, $K = \mu_0 M_s(15\alpha_B/4)^{0.5}$ [446] and using this method, K was estimated as ~ 32.7 $\times$ 10^5 erg cm^{-3} which was found to be in good agreement with the value obtained from temperature variation of magnetization (ZFC-FC).

Figure 5.2a shows the hydrodynamic size distribution of the emulsion droplets dispersed in water, obtained using DLS studies, where unimodal distributions were obtained. The average hydrodynamic diameters of the samples E1, E2 and E3 were 192, 180 and 164 nm, respectively. The size polydispersity indices, obtained from the correlation functions using the cumulant method, were 0.01, 0.17 and 0.06 for the samples E1, E2 and E3, respectively. The most probable sizes (using log-normal distributions) were obtained as 200 nm (σ_{ln} = 0.2), 160.6 nm (σ_{ln} = 0.4) and 181.6 nm (σ_{ln} = 0.3) for the samples E1, E2 and E3, respectively. **Fig. 5.2b** shows the variation of zeta potential, at neutral pH, for the emulsion samples. The

average zeta potentials were found to be -52, -55 and -57 mV for the samples E1, E2 and E3, respectively, indicating superior stability of the droplets in water phase. Thermogravimetric analysis (TGA) were carried out to quantify the weight % of MNP in the emulsion samples and it was observed that the concentration of MNP in the samples E1, E2 and E3 were 4.7, 4.6 and 1.7 wt. %, respectively (experimental weight loss data are shown in **Fig. 5.2c**), which were later used for SAR calculation. This clearly showed that the samples E1 and E2 were of similar sizes and MNP loading but with different polydispersity, whereas, the MNP loading was substantially lower for the sample E3. **Table 5.1** shows the details of the samples E1, E2 and E3.

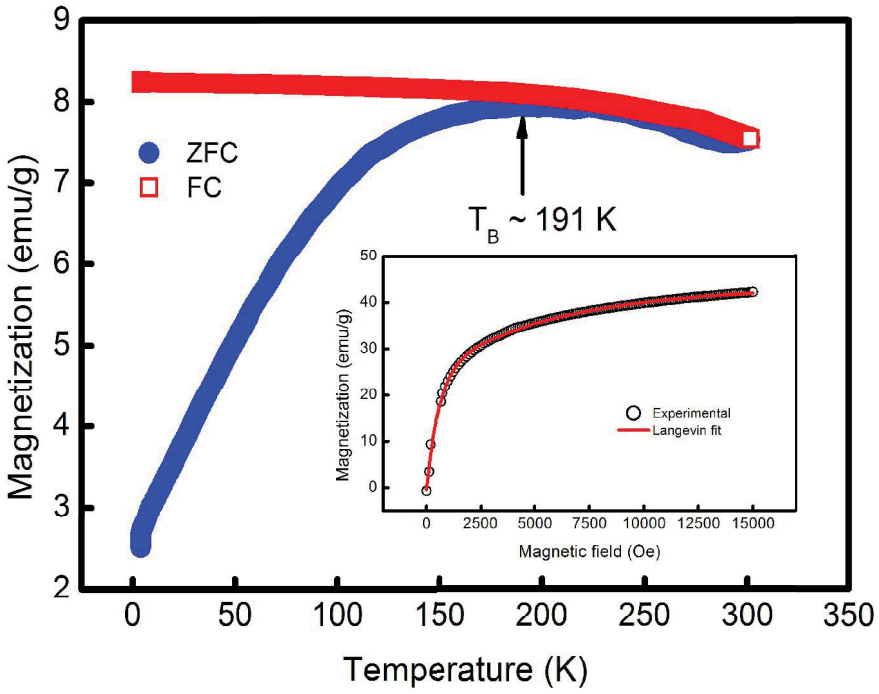


Figure 5.1: Temperature dependent magnetization (ZFC: zero field cooled and FC: field cooled) for the oleic acid coated Fe_3O_4 MNP, in the temperature range of 4-300 K. The blocking temperature (T_B) is obtained as ~ 191 K. (Inset) Magnetization as a function of applied magnetic field for the oleic acid coated Fe_3O_4 MNP at room temperature. The saturation magnetization is obtained as ~ 42 emu/g.

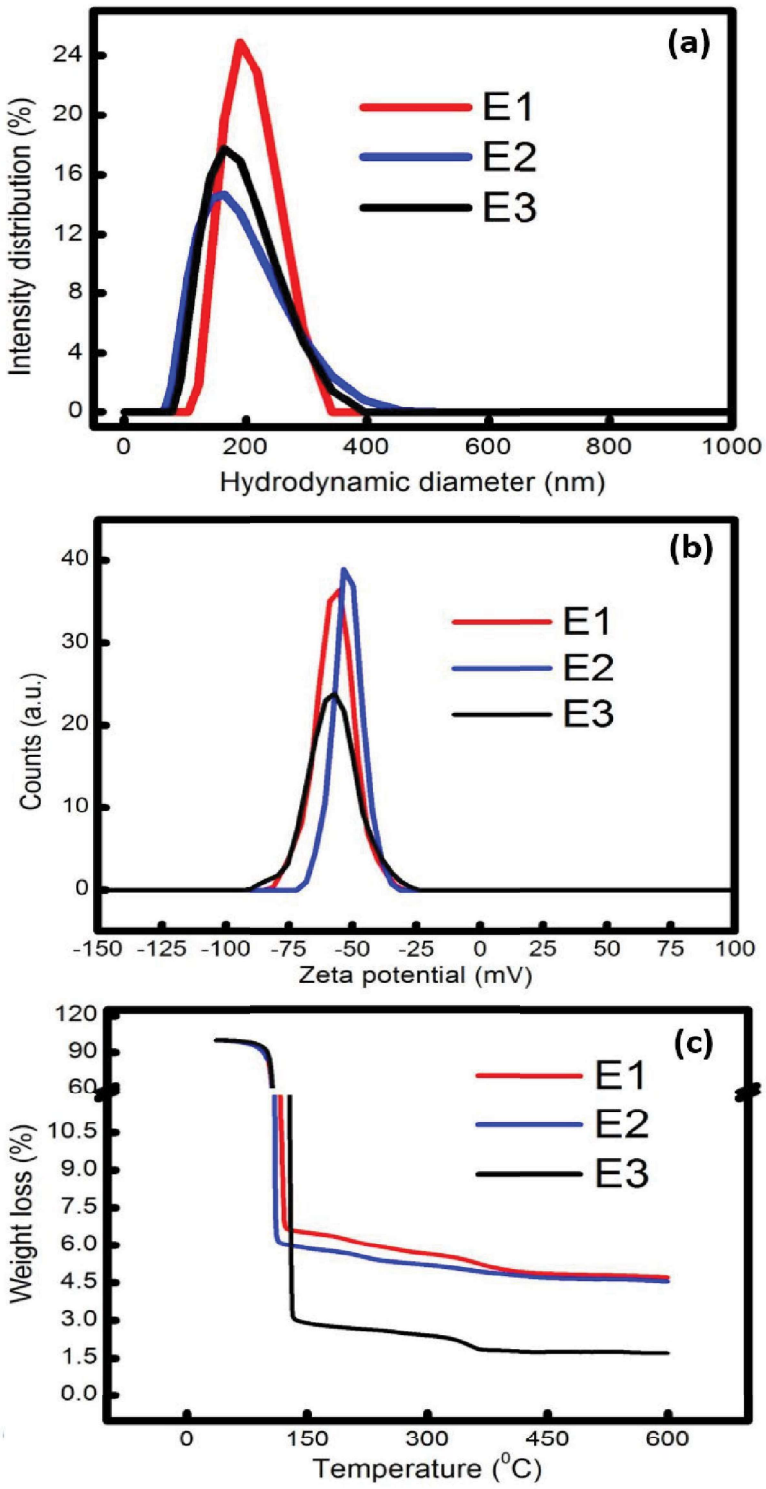


Figure 5.2: (a) Hydrodynamic size distributions of the emulsion samples E1, E2 and E3. (b) Zeta potential distributions for the emulsion samples. (c) Weight loss data for the emulsion samples, determined from thermogravimetric analysis (TGA). The MNP concentration for the samples E1, E2 and E3 are 4.7, 4.6 and 1.7 wt. %, respectively.

Table 5.1: Details of the samples E1, E2 and E3.

Sample	MNP loading (wt. %)	Average hydrodynamic diameter from DLS (nm)	Poly dispersity index (PDI) using cumulant method	Most probable diameter from log-normal distribution	σ_{ln}	Zeta potential (mV)
E1	4.7	192	0.01	200	0.2	-52
E2	4.6	180	0.17	161	0.4	-55
E3	1.7	164	0.06	182	0.3	-57

The morphology of the emulsion droplets (sample E1), immobilized in an agar gel, was studied using atomic force microscopy (AFM). A small amount of the agar solution containing the magnetic nanoemulsion was drop casted on a freshly prepared mica substrate and AFM imaging was carried out under semi-contact mode. The detailed experimental and image analysis procedures and tip shape de-convolution protocol are described in section 2.2.7 in chapter 2. **Fig. 5.3a** shows the AFM topography image of the agar immobilized magnetic nanoemulsion (sample EA1) on a mica substrate. The spherical emulsion droplets can be clearly seen from the image. **Fig. 5.3b** shows the magnified view of a 3 μm × 3 μm section (as indicated in **Fig. 5.3a**), which was used for dimensional analyses of the emulsion droplets. **Fig. 5.3c** shows the intensity profiles across three different emulsion droplets (marked in **Fig. 5.3b**) and it can be seen that the average droplet diameter was ~ 200 nm, which was in very good agreement with the most probable hydrodynamic diameter (~ 200 nm) obtained from DLS studies. The AFM topography images (**Figs. 5.3a-b**) also confirmed the structural integrity and spherical morphology of the emulsion droplets immobilized in a tissue mimicking agar gel, which is beneficial for multimodal hyperthermia applications.

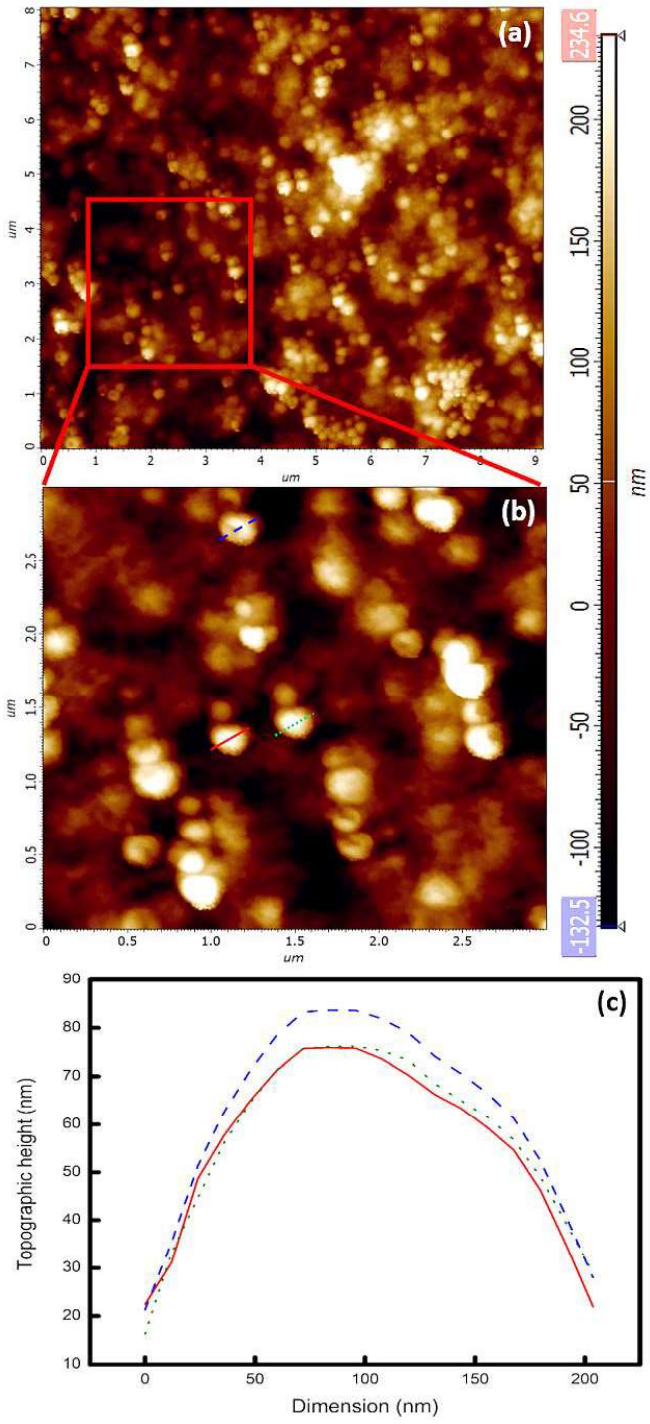


Figure 5.3: (a) AFM topography image of the agar immobilized magnetic nano-emulsion sample (EA1) on a mica substrate, where the emulsion droplets can be clearly seen. The topography height scale and lateral dimensions are shown along with the image. (b) Magnified view of a 3 μm × 3 μm area (indicated by the red square in Fig. 5.3a). Dimensional analyses are performed and the intensity profiles as a function of size are shown in (c). The average droplet diameter is found to be ~ 200 nm.

5.2.2 Results and discussions

5.2.2.1 RF-AMF induced heating of octane based ferrofluid

Figure 5.4a shows the variation of ΔT (= $T-T_i$, where T_i is the initial temperature) as a function of time during RF-AMF induced heating of the sample O1 under a fixed frequency of 126 kHz and five different external field amplitudes, viz., 57.3, 51.4, 45.0, 36.7 and 26.0 kAm^{-1}. The temperature rise of the base fluid as a function of time (under the highest field amplitude of 57.3 kAm^{-1}) is also shown in **Fig. 5.4a**. It can be seen that the temperature rise for the base fluid was insignificant and it was subtracted from RF-AMF induced temperature rise of the sample under various external field amplitudes. **Fig. 5.4a** shows that ΔT initially increased linearly with time and at larger time scales, ΔT showed a saturation which was attributed to the heat loss to the surrounding due to non-adiabatic experimental conditions. It can be further seen that the rate of temperature rise and maximum temperature rise at the end of heating phase (ΔT_{max}) increased with RF-AMF amplitudes. During thermal cycling, it was observed that the sample temperature increased on application of the RF-AMF and started decreasing immediately after the field was turned off, which indicated excellent stability and repeatable thermal response of the magnetic fluid. The initial rates of temperature rise were calculated from the temperature rise curves, after suitable adiabatic reconstruction, as discussed in section 2.6.6 in chapter 2. It was also observed that the initial rates obtained from the adiabatically reconstructed graphs were, on average, ~ 20 % higher than the initial rates determined from the experimentally measured temperature rise curves, which indicated the presence of non-adiabatic thermal losses. Initial rates of temperature rise, determined from the adiabatically reconstructed temperature rise curves, were further used for quantification of SAR and the SAR values were reported as mean ± standard deviation (SD) of three consecutive experiments.

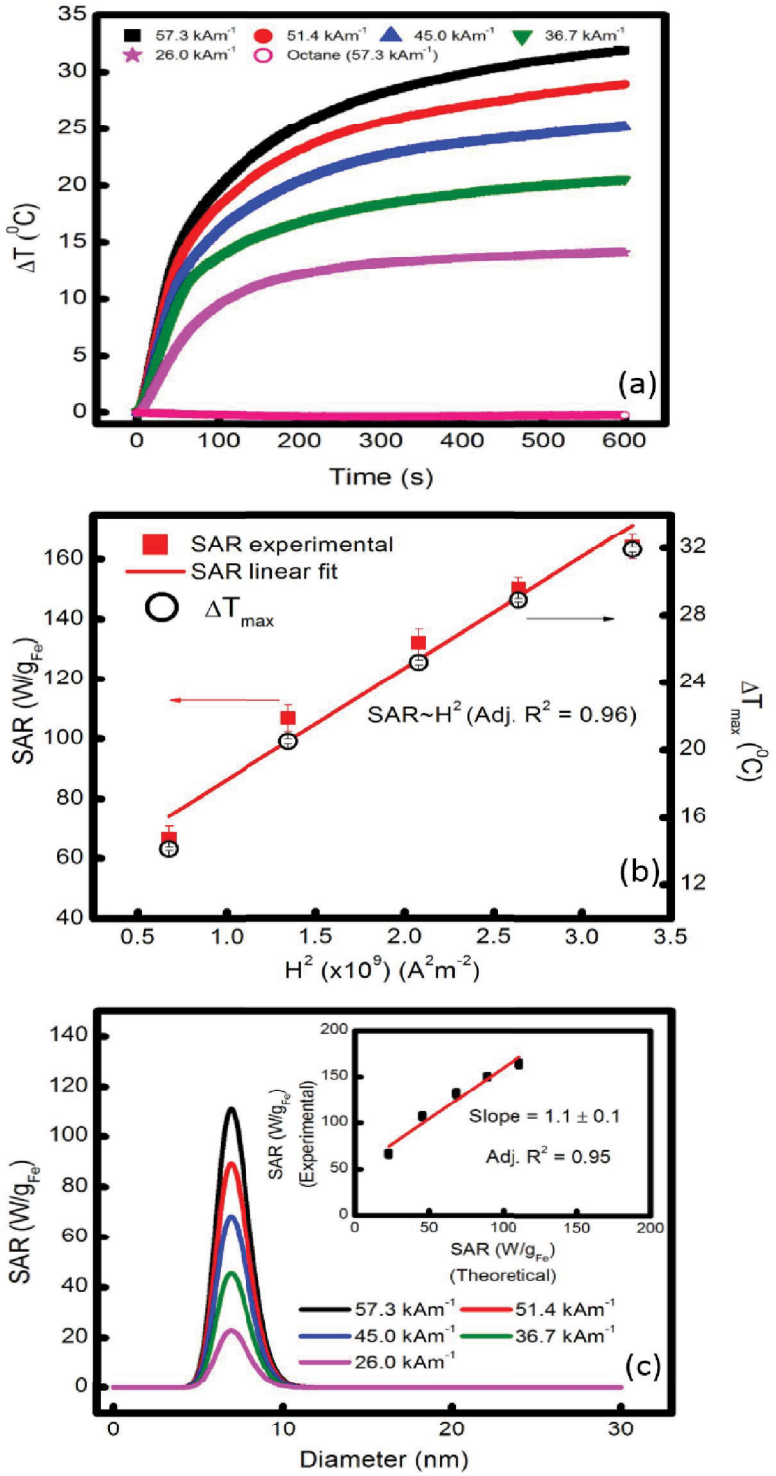


Figure 5.4: (a) ΔT as a function of time, for the sample O1, at a fixed frequency of 126 kHz and under five different external field amplitudes, viz., 57.3, 51.4, 45.0, 36.7 and 26.0 kAm^{-1}. The temperature rise as a function of time for the dispersion medium alone is also shown. (b) Linear variation (adjusted $R^2 = 0.96$) of SAR and ΔT_{max} as a function of H^2, for the sample O1. (c) Theoretically calculated SAR values, at 300 K, under five different external field amplitudes. (Inset) The variation of experimentally determined SAR values as a function of the theoretically calculated SAR values.

Figure 5.4b shows the variation of SAR and ΔT_{max} as a function of H^2 for the sample O1. It can be seen from the figure that SAR varied linearly with H^2, in accordance with the Rosensweig's model under linear response regime [51]. As P ~ H^2 and dT(t)/dt ~ P (Eq. 2.19 in chapter2), it is evident that $\Delta T_{max} = \int_{t-on}^{t-off} (SAR / c_{samp}) dt$, indicating a linear variation of ΔT_{max} with H^2, as shown in **Fig. 5.4b** for the sample O1. Here, t-on and t-off indicate the time when the RF-AMF was switched on and off, respectively, and c_{samp} indicate specific heat capacity of the sample. The highest ΔT_{max} obtained for the sample O1, under an external field amplitude of 57.3 kAm^{-1}, was ~ 31.9 (± 0.2) ^{0}C for a heating time of 600 s.

Figure 5.4c shows the theoretically calculated SAR values as a function of particle size for the sample O1 under five different external field amplitudes. The theoretical calculations were based on Eqs. 1.16 and 1.18 (in chapter 1), where the various expressions of τ_N, τ_B and χ_i were used (detailed description is provided in section 1.7.5 of chapter 1). The values of viscosity, coating thickness, τ_0, anisotropy constant, most probable diameter and σ_{ln} were considered as 0.00051 Pa.s, 2 nm, 10^{-9} s, 25 kJ/m^3, 6.9 nm and 0.14, respectively, for performing the theoretical calculations. It can be seen that SAR was highest at ~ 7 nm, which was found to be in good agreement with the most probable size of the synthesized MNP (~ 6.9 nm). The highest SAR (at H = 57.3 kAm^{-1}) obtained from theoretical calculation was ~ 110.9 W/g_{Fe}. On the other hand, the highest SAR obtained from experimental measurements was 164.4 (±4.3) W/g_{Fe} and the theoretical SAR values were found to be significantly lower than the experimental SAR values. This discrepancy between the experimental and theoretical values can be attributed to a number of reasons, viz., distribution in anisotropy constant, variation in attempt frequent (strongly depends on linear damping coefficient), sensitivity of shape anisotropy of the MNP, dipolar interactions, variation in hydrodynamic size, non-constant magnetic field distribution inside the sample volume, increased magnetic

flux density due to the presence of MNP in the path of the magnetic field lines, etc. [374, 387, 447, 448]. Moreover, the theoretical calculations were based on only Neel-Brownian relaxation mechanism, whereas, in reality, at extremely high frequency of the external magnetic field (126 kHz in the present case), hysteresis loss also plays a significant role in RF-AMF induced heating. Presence of such high frequency (~ 100 kHz) hysteresis loops for SPM MNP has been theoretically predicted and experimentally measured [380, 449]. Such a scenario was also reported by Liu et al. [256], where, theoretically calculated SAR values were ~ 43 % of the experimentally measured values, whereas, in the present case, theoretical values were found to be ~ 67.5 % of the experimental values. Nevertheless, the experimental and theoretical SAR values were found to be linearly correlated, as shown in the **inset of Fig. 5.4c**. The slope of the linear regression analysis was found to be 1.1 ±0.1 with an adjusted R^2 = 0.95, indicating a good linear correlation between the theoretical and experimental values.

5.2.2.2 RF-AMF induced heating of magnetic nanoemulsion

The SPM MNP located inside the oil droplets (size ~ 200 nm) undergo Neel-Brownian relaxation, thereby, increasing the local temperature of the oil droplets. But the confinement of the MNP inside the oil droplets leads to a reduced interparticle distance resulting in an enhancement of dipolar interaction which drastically modifies the RF-AMF induced heating by strongly affecting Neel relaxation time and ensemble averaged equilibrium susceptibility [200, 280, 412, 450]. Moreover, the MNP loaded inside the emulsion droplets experience a magnetic field that is significantly lower than the externally applied field due to the de-magnetization effect of the emulsion droplets, which further reduces the effective RF-AMF induced heating of the MNP loaded inside the oil droplets [443].

Heat transfer from the MNP to the oil droplets, which causes a rise in the local droplet temperature, primarily occurs via diffusion and convection mechanisms. In the present

analyses, the effect of convection was neglected (convection based calculation yielded ~ 40 % lower temperature rise in the case of micro-droplets loaded with MNP with droplet volume (V_{drop}) ~33 nL and droplet radius (r_{drop}) ~ 200 μm [451], as compared to nanoemulsions with r_{drop} ~ 100 nm and V_{drop} ~ 4.2×10^{-9} nL in the present study). Diffusion limited temperature rise (ΔT_{drop}) of the droplets can be expressed as $\Delta T_{drop} \sim SAR_{MNP} \times \frac{4\pi r_{drop}^2}{k_{oil}} \times C_{MNP}^{drop}$, where SAR_{MNP}, k_{oil} and C_{MNP}^{drop} indicate SAR of the MNP (dispersed in the oil medium), thermal conductivity of the oil medium and concentration of the MNP inside the droplet, respectively [451]. The heated droplets act as individual heat sources and, in turn, results in an increase in global sample temperature. Recent studies on sub-nanometer temperature probing indicated that temperature difference between the MNP surface and its surrounding decreased abruptly and became significantly lower over length scales of a few nm [452, 453]. Riedinger et al. [454] observed a decrease of ΔT from ~ 44 ^{0}C to 10 ^{0}C, when the distance between MNP surface and thermally labile azo (2, 2′-azobis [N-(2-carboxyethyl)-2-methylpropionamidine]) bonds were increased using polyethylene glycol (PEG) spacers of increasing molecular weight (from 500 to 8000 Da). This shows that for magnetic nanoemulsions, heat transfer from oil droplets alone cannot be responsible for significant global temperature rise at macroscopic length scales, which is experimentally measured in the present study. This indirectly indicates towards the presence of a second heat generation mechanism in magnetic nanoemulsion mediated through whole-scale Brownian relaxation of the oil droplets. Trisnanto and Kitamoto [455] showed the field dependence of Brownian relaxation dynamics, where at field amplitudes lower than the dipolar interaction energy, whole-scale Brownian relaxation of the cluster (multiple magnetic moments inside a hydrodynamic volume) was observed, whereas, for field amplitudes greater than dipolar interaction energy, stronger Brownian relaxation of the individual particles was observed, indicating the

possibility of RF-AMF induced heating at two different length scales, i.e., intra cluster and cluster as a whole. Due to the presence of MNP inside the droplet volume, the oil droplets attain a non-zero induced magnetic moment, m_{drop} (droplet moment) and a net emulsion magnetization, $M_e = n_{drop}m_{drop}$, where n_{drop} is the droplet concentration. Under the application of an external field, the droplet magnetic moment is a function of the applied field amplitude (H_{app}) and can be expressed by the following equation [443].

$$m_{drop} = \chi_{fluid} V_{drop} H_{drop} = \frac{\chi_{fluid} V_{drop} H_{app}}{1 + 4\pi\chi_{fluid} n_{de-mag}} \tag{5.1}$$

Here, χ_{fluid}, V_{drop}, H_{drop} and $n_{de\text{-}mag}$ indicate susceptibility of the magnetic fluid, droplet volume, magnetic field inside the droplet and demagnetization factor (=1/3 for spherical droplets), respectively. Hence, under Rosensweig's model [51], the power dissipation per unit volume, in the case of magnetic nanoemulsion droplets exposed to a RF-AMF, is given by the following expression.

$$P_{drop} = \frac{1}{2}\omega\mu_0\chi_{fluid}^{//}H^2 = \frac{1}{2}\omega\mu_0\chi_0^{fluid}H^2 \frac{\omega\tau_B}{1 + \omega^2\tau_B^2} \tag{5.2}$$

This expression is identical to Eq. 1.16 (in chapter 1), the only differences being in the relaxation time approximation and fluid susceptibility. For the emulsion droplets of size ~ 200 nm, Neel relaxation time is exponentially high and the effective relaxation time is primarily Brownian dominated and hence, τ_B is used in Eq. 5.2.

Brownian relaxation in such larger sized nano structures like poly(N-isopropylacrylamide) (PNIPAM) coated iron oxide nanoparticle (size ~ 300 nm) [456], magnetic polymer colloids (size ~ 225 nm) consisting of cobalt ferrite MNP embedded in poly(methyl methacrylate) matrix [163] and MNP loaded polymer nano spheres (size ~ 105 nm) [256] have been experimentally confirmed using dynamic susceptibility measurements.

The RF-AMF induced temperature rise of the magnetic nanoemulsions were experimentally studied under different external field amplitudes. **Figs. 5.5a-c** show the variation of ΔT as a function of time during RF-AMF induced heating of the samples E1, E2 and E3, respectively, under four different external field amplitudes, viz., 63.0, 57.0, 51.4 and 45.3 kAm^{-1}. For the sample E3, heating was limited up to 600 s to avoid convection induced heat losses at higher time scales as the rate of temperature rise was much lower as compared to the sample E1 and E2. It can be seen from **Figs. 5.5a-c** that ΔT increased continuously with time and the rate of temperature rise and ΔT_{max} (at the end of heating phase) increased with external field amplitude. Adiabatic reconstruction of the experimentally measured ΔT curves were performed and the linear loss coefficient and ΔT_{LL} values were determined for the samples E1, E2 and E3 during natural cooling after RF-AMF induced heating. The average values of linear loss coefficient for the samples E1, E2 and E3 were found to be 0.00395, 0.00390 and 0.00381 s^{-1}, respectively. The initial rates of temperature rise were determined from the adiabatically reconstructed ΔT curves and SAR values were quantified using the initial rates. **Fig. 5.5d** shows the variation of SAR as a function of H^2 for the samples E1, E2 and E3 and ΔT_{max} as a function of H^2 for the samples E1 and E2. It can be seen from **Fig. 5.5d** that SAR and ΔT_{max} increased linearly with H^2, in accordance with the theoretical expectations ($P \sim H^2$) [51]. It can be further seen that ΔT_{max} varied between 18.03 ± 0.18 to 13.03 ± 0.15 ^0C for the sample E1, when the external field amplitude was decreased from 63.0 to 45.3 kAm^{-1}, which makes the sample E1 suitable for MFH applications. The highest SAR, obtained in the present study, was ~ 111.8 ± 3.4 W/g_{Fe} for the sample E1, under an external field amplitude of 63.0 kAm^{-1}. On the other hand, it was observed from **Fig. 5.5d** that SAR and ΔT_{max} were significantly lower for the sample E2 under similar experimental conditions. For the sample E2, ΔT_{max} varied between 9.11 ± 0.11 to 5.28 ± 0.15 ^0C, when the external field amplitude was decreased from 63.0 to 45.3 kAm^{-1}. The highest SAR, recorded for the sample E2, was

found to be ~ 34.8 ± 2.1 W/g_{Fe}, which was ~ 69 % lower than the highest SAR recorded for the sample E1. For the sample E3 (1.7 wt. % MNP concentration), SAR varied between 30.3 ± 2.4 to 8.5 ± 2.4 W/g_{Fe}, when the external field amplitude was decreased from 63.0 to 45.3 kAm^{-1}.

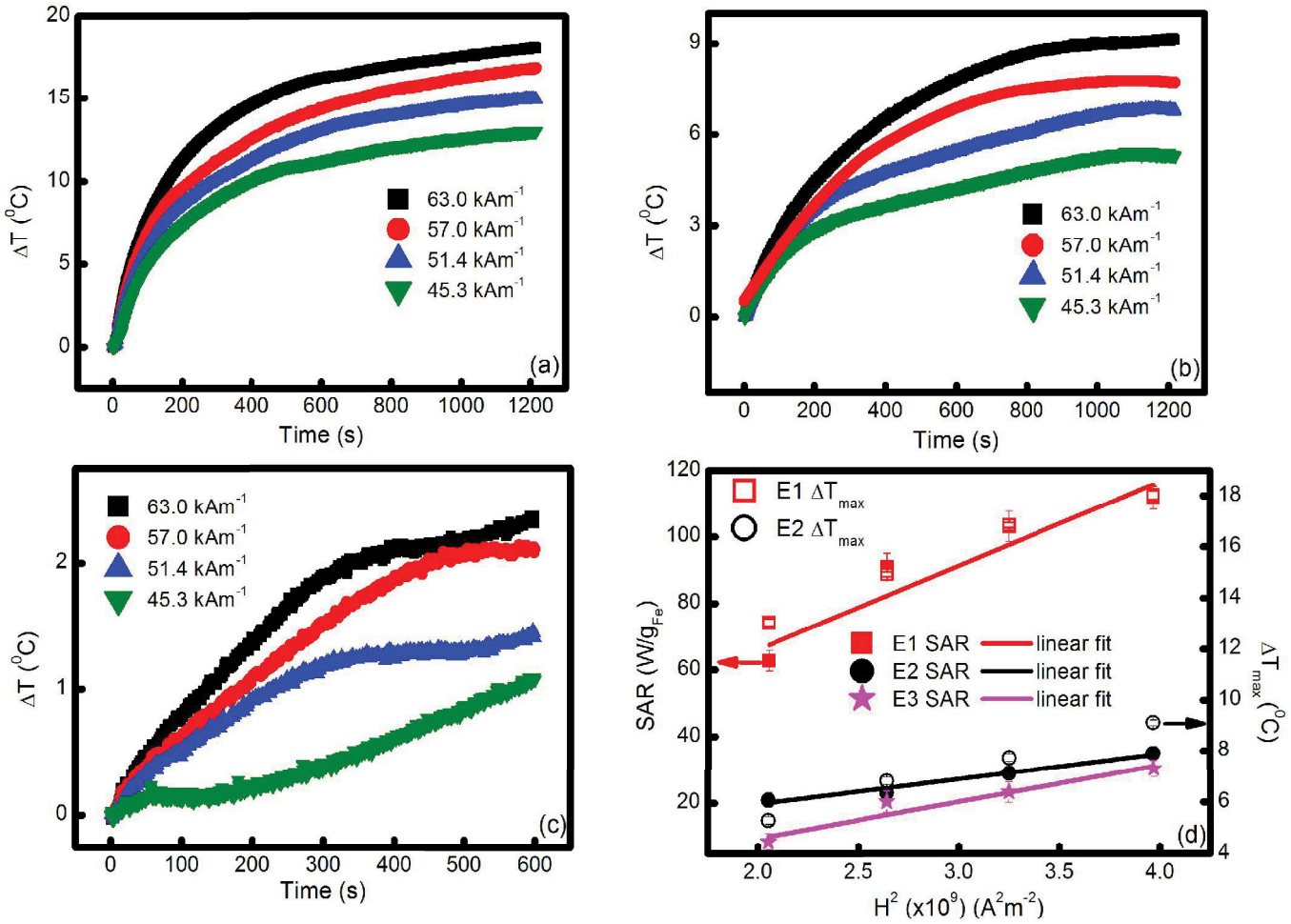


Figure 5.5: ΔT as a function of time, for the samples (a) E1, (b) E2 and (c) E3, during RF-AMF induced heating under four different external field amplitudes, viz., 63.0, 57.0, 51.4 and 45.3 kAm^{-1}. (d) Linear Variation of SAR (adjusted R^2 = 0.9, 0.97 and 0.93 for the samples E1, E2 and E3, respectively), as a function of H^2, for the emulsion samples. Linear variation of ΔT_{max}, as a function of H^2, for the samples E1 and E2.

5.2.2.3 Effects of polydispersity and MNP concentration on heating efficiency

The lower SAR obtained for the sample E3 was attributed to the comparatively lower MNP concentration (1.7 wt. % for E3 as compared to 4.7 and 4.6 wt. % for E1 and E2, respectively). But the same was not true for the samples E1 and E2 as the MNP concentrations were similar in these two samples. To understand the drastic variation of SAR in two very similar system under same experimental conditions, theoretical calculations on SAR variation with droplet size, using Eq. 5.2 and assuming log-normal size distributions, were performed and the obtained results are shown in **Fig. 5.6** for H = 63.0 kAm^{-1}. In these calculations the values of viscosity, τ_0, temperature and anisotropy constants were considered as 0.00089 Pa.s, 10^{-9} s, 300 K and 25 kJ/m^3, respectively. It can be seen from **Fig. 5.6** that SAR of the sample E1 (with most probable radius of 100 nm and σ_{ln} = 0.2, which were experimentally determined from the log-normal fitting of the DLS data) was significantly higher than that for the sample E2 (with most probable radius of 80.3 nm and σ_{ln} = 0.4). The **inset of Fig. 5.6** shows the theoretically calculated SAR values for the samples E1 and E2 for external field amplitudes of 57.0, 51.4 and 45.3 kAm^{-1}, respectively, where similar trends were observed. This variation can be either due to variation in the most probable size or due to the variation in size polydispersity. To ascertain the relative contributions of both the factors, theoretical calculations were also performed on the hypothetical E1 and E2 samples with same most probable sizes but different polydispersity and the results are also shown in the **Fig. 5.6**. It is evident from **Fig. 5.6** that, when the polydispersity of the sample E1 was increased from 0.2 to 0.4, SAR drastically reduced from 90.07 to 47.82 W/g_{Fe}. Similarly, when the polydispersity of the sample E2 was reduced from 0.4 to 0.2, the SAR was found to increase from 56.06 to 105.56 W/g_{Fe}. Such theoretical comparisons clearly indicated that though droplet size played a vital role in the final SAR values of the sample, the effect of size

polydispersity was much more significant and with increase in size polydispersity, SAR decreased drastically. Hence, the sample E2 exhibited a lower SAR due to its higher size polydispersity (polydispersity values evaluated from the DLS data using cumulant method were found to be 0.011 and 0.17 for the samples E1 and E2, respectively). It was observed that the theoretically calculated SAR decreased from 90.07 to 56.06 W/g_{Fe} (a decrease of ~ 37.8 %), for the samples E1 and E2, when σ_{ln} was varied from 0.2 to 0.4. The detrimental effect of size polydispersity on SAR was also numerically studied by Rosensweig [51] for MNP based nanofluids, where it was reported that the heating rate decreased by ~ 37.5 % when σ_{ln} was doubled, which is found to be in good agreement with the ~ 37.8 % reduction in heating efficiency obtained in the present study.

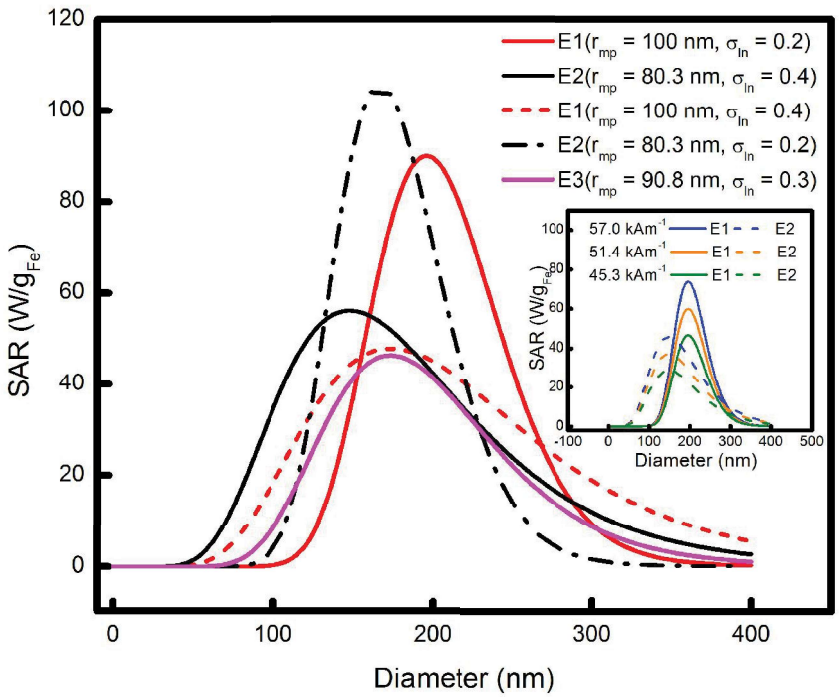


Figure 5.6: Effect of size polydispersity on SAR. Theoretically calculated SAR for the emulsion samples E1, E2 and E3 with the most probable radii (r_{mp}) of 100, 80.3 and 90.8 nm, respectively, under an external field amplitude of 63.0 kAm^{-1}. The σ_{ln} values are 0.2, 0.4 and 0.3 for the samples E1, E2 and E3, respectively. The SAR variation of the hypothetical samples E1 (r_{mp} = 100 nm and σ_{ln} = 0.4) and E2 (r_{mp} = 100 nm and σ_{ln} = 0.4) are also shown. (Inset) Theoretically calculated SAR values for the samples E1 and E2 for external field amplitudes of 57.0, 51.4 and 45.3 kAm^{-1}, respectively.

Though size polydispersity is generally found to drastically reduce SAR of MNP based nanofluids [51, 457, 458], an opposite effect was reported by Menendez et al. [442] from theoretical modelling using major hysteresis loops. On the other hand, in the present case, the maximum value of the external field amplitude (H_{max}) was not sufficient for major loop cycling, i.e., $H_{max} << H_A$, where, H_A indicates anisotropy field amplitude and $H_A = 2K/\mu_0 M_S$). The anisotropy field amplitude for F_3O_4 has been experimentally found to be ~ 2×10^3 Oe (~ 160 kAm^{-1}) [293], whereas, H_{max} in the present study, was limited up to 63.0 kAm^{-1}, which confirmed that the major loop condition was not valid in the present study. This indicated a negative effective of size polydispersity on SAR, as experimentally measured in the present study.

It is obvious that in polydisperse suspensions, multiple relaxation times occur and hence, the relaxation dynamics vary significantly from the monodisperse systems. Trisnanto and Kitamoto [455] found that the Brownian relaxation time varied with size polydispersity. The amplitude of the RF-AMF governs the particle rotation angle and is strongly affected by dipolar interactions in aggregated systems. To further illustrate the drastic effect of polydispersity on heating efficiency of magnetic nanoemulsions, SAR values of the sample E2 (4.6 wt. % MNP concentration) was compared with those obtained for the sample E3 (1.7 wt. % MNP concentration) with most probable size of ~ 181.6 nm ($\sigma_{ln} = 0.3$). It was observed that the SAR values obtained for E3 were comparable to those obtained for E2 (see **Fig. 5.5d** for comparison), which clearly showed the drastic effect of polydispersity that reduces SAR significantly. The theoretical SAR for the sample E3 (shown in **Fig. 5.6**) was also found to be comparable to that obtained for the sample E2. This clearly indicated that higher MNP loading in emulsion droplets may not significantly enhance the SAR in highly polydisperse samples.

Size polydispersity can lead to non-homogeneous local heating (inside a target cell, or local environment surrounding a tumor), thereby, restricting the practical application of a ferrofluid or magnetic nanoemulsion for MFH, as it may lead to localized fluctuations in heating rendering the treatment protocol unpredictable [442]. Hence, a control over size polydispersity and proper understanding of its implications are essential for fruitful applications of MFH for cancer treatment, especially for larger sized magnetic nano-carriers (like magnetic nanoemulsion), which are designed for multimodal therapy or synergistic use of targeted drug delivery (aided by RF-AMF induced heating) and MFH.

5.2.2.4 Effects of medium viscosity on heating efficiency

To study the contribution of Brownian relaxation of the droplets on global SAR of the emulsion samples, RF-AMF induced heating studies on agar based samples were carried out, where the emulsion droplets were immobilized in an agar gel (4 wt. %) to eliminate the contributions from Brownian relaxation. Agar consist of a neutral gel forming agarose polymer and agaropectin, which is a charged polymer containing sulphate ions. Hence, RF-AMF induced heating of agar matrix (without MNP loading) was initially measured and **Fig. 5.7a** shows the variation of ΔT as a function of time for the agar matrix alone. It can be seen that the temperature increased up to ~ 0.53 ± 0.08 ^{0}C after 700 s and the initial temperature rise was insignificant and hence, contribution from agar matrix to RF-AMF induced heating of MNP loaded agar samples was neglected. As the agar based samples mimic tissues, temperature measurements during RF-AMF induced heating was carried out using IRT to obtain an average temperature over a comparatively larger area. Notwithstanding this, IRT based temperature measurements indicated surface temperature rise only, which was compared with the temperature data recorded using fiber optic temperature sensor and a data correction protocol was implemented for reconstructing the sample temperature from IRT

based data. **Fig. 5.7a** also shows the ΔT as a function of time, measured using IRT and probe, for an agar based sample loaded with 0.5 wt. % MNP, under an external field amplitude of 26.0 kAm^{-1}. The convection corrected IRT data is also shown in **Fig. 5.7a**, where, it can be seen that the corrected IRT based and probe based curves were coinciding. The same data analyses protocol was applied on all IRT based data before further analyses.

Figure 5.7b shows the variation of ΔT as a function of time for the sample EA1 under four different external field amplitudes, viz., 63.0, 57.0, 51.4 and 45.3 kAm^{-1}. It can be seen that ΔT continuously increased with time and the rate of temperature rise and ΔT_{max} increased with external field amplitudes. The experimentally measured temperature rise curves were adiabatically reconstructed [297] and the initial rates of temperature rise were determined using linear regression analyses of the adiabatically reconstructed curves, which were then used for SAR calculation. The specific heat of agar based samples was considered as 4.18 $Jg^{-1}K^{-1}$ [459].

Figure 5.7c shows the variation of SAR and ΔT_{max} as a function of H^2, where, it can be seen that SAR increased linearly with H^2, in accordance with the Rosensweig's model [51]. It was further observed that ΔT_{max} varied between 8.08 ± 0.1 to 4.8 ± 0.2 ^0C, when the external field amplitude decreased from 63.0 to 45.3 kAm^{-1}. It was also observed that the ΔT_{max} values were significantly lower compared to the fluid based emulsion sample (E1) (see **Fig. 5.5d** for comparison). Nevertheless, such values of temperature rise are sufficient for multimodal treatment modalities involving MFH and thermally activated drug release [268]. Recent studies clearly show that a global temperature rise of ~ 10 ^0C can cause a local temperature rise of ~ 44 ^0C (measured within the local nano-environment surrounding the MNP) which is sufficient for thermal ablation [454], rendering magnetic nanoemulsions as potential candidates for multimodal hyperthermia applications.

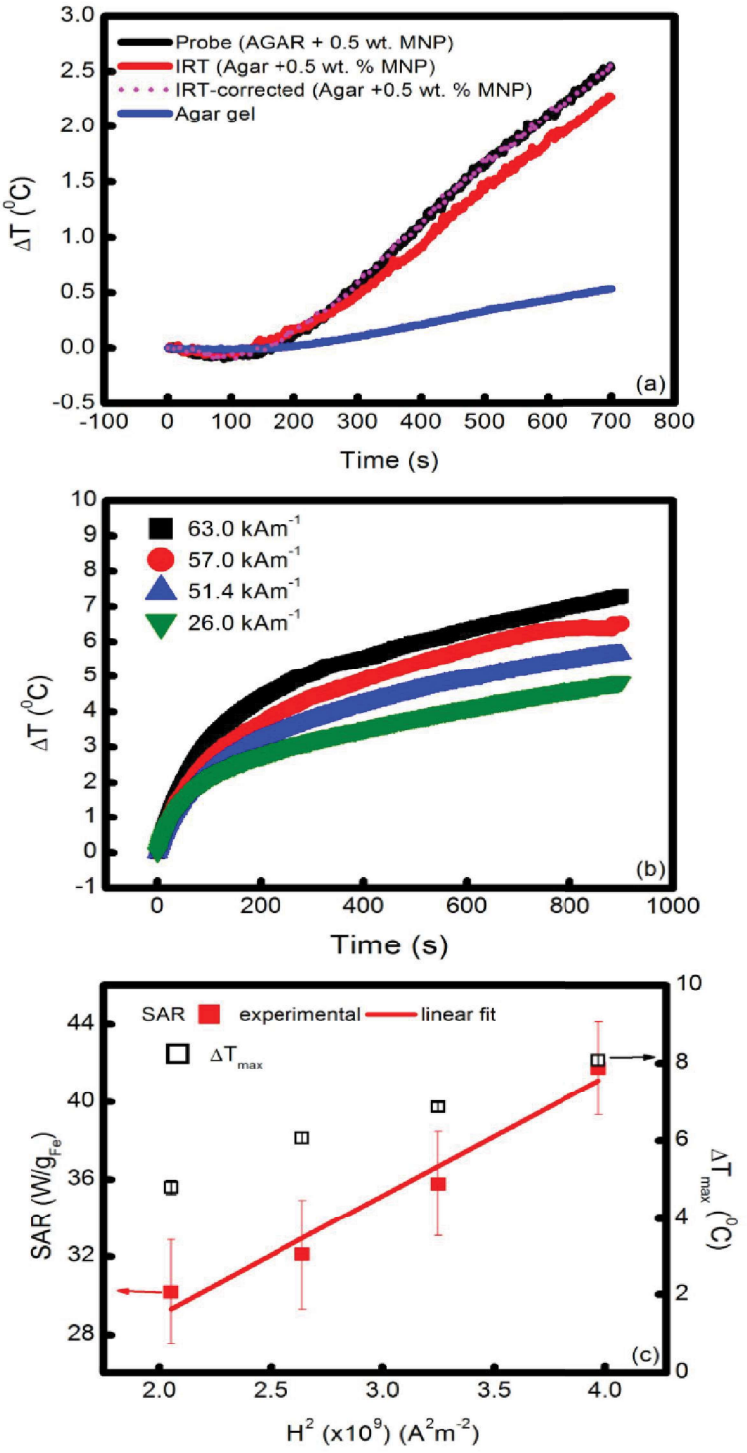


Figure 5.7: (a) ΔT as a function of time, for the agar matrix alone (without any MNP loading), where, it can be seen that temperature rise is insignificant. Additionally, ΔT as a function of time, measured using fiber optic temperature sensor and IRT, for the agar based sample loaded with 0.5 wt. % MNP, under an external field amplitude of 26.0 kAm^{-1}, is shown. The convection corrected IRT based temperature rise profile is also shown in the figure. (b) ΔT as a function of time, for the agar based sample EA1, under four different external field amplitudes, viz., 63.0, 57.0, 51.4 and 45.3 kAm^{-1}. (d) Linear variation of SAR and ΔT_{max} as a function of H^2 for the sample EA1.

The maximum SAR, obtained for the sample EA1, was found to be ~ 41.73 ± 2.4 W/g_{Fe} under an external field amplitude of 63.0 kAm^{-1}, which was significantly lower than the value obtained for E1 (~ 111.78 ± 3.4 W/g_{Fe}) under similar experimental conditions. **Fig. 5.8a** shows a bar chart of the SAR values for the samples E1 and EA1 as a function of the external field amplitude. The lower SAR values obtained for the agar based sample EA1 were attributed to the absence of Brownian relaxation of the droplets due to immobilization in agar gel. Due to an increase in surrounding viscosity of agar based samples, τ_B (~ η) increased, resulting in an insignificant contribution from the Brownian relaxation of the emulsion droplets to the total SAR. The SAR ratio (SAR-EA1/SAR-E1) was computed for four different external field amplitudes and it was observed that SAR ratio (also shown in **Fig. 5.8a**) varied from 0.37 ± 0.03 to 0.48 ± 0.07, when the external field amplitude was decreased from 63.0 to 45.3 kAm^{-1}. This clearly showed that Brownian relaxation of the oil droplets contributed ~ 40-50 % of the total SAR in the case of emulsion samples. This was found in very good agreement with the earlier reported value of ~ 53 % contribution from Brownian relaxation to the total SAR [256, 441].

Due to abrogation of Brownian relaxation of the emulsion droplets, the SAR of the sample EA1 is primarily due to the RF-AMF induced heating of the MNP loaded in the oil medium. **Fig. 5.8b** shows the SAR ratio (SAR-EA1/SAR-O1) between the samples EA1 and O1 as a function of external field amplitude. The SAR ratio varied from ~ 0.21 to 0.24, when the external field amplitude was decreased from 63.0 to 45.3 kAm^{-1}. The magnetic field experienced by the MNP loaded inside the droplets (H_{drop}) is significantly lower than the applied external magnetic field (H_{app}) due to the demagnetization effect of the encapsulated MNP and following Eq. 5.1, H_{drop} is represented by the following equation [443].

$$H_{drop} = \frac{H_{app}}{1 + 4\pi\chi_{fluid} n_{de-mag}} \quad (5.3)$$

Considering, $n_{de\text{-}mag}$ and χ_{fluid} as 1/3 [443] and 0.3 [460], respectively, it can be shown that $(H_{drop}/H_{app})^2 \sim 0.19$, which was found to be in good agreement with the experimentally obtained SAR ratio. This clearly indicated that the residual SAR (after abrogation of Brownian relaxation) measured in the agar based sample is due to the heat transfer from the oil droplets which were, in turn, heated by the Neel-Brownian relaxation of the MNP loaded inside the droplets, albeit under lower external field amplitudes due to the effect of de-magnetization. Gudoshnikov et al. [378] also reported the detrimental effect of cluster demagnetizing field on RF-AMF induced heating efficiency and showed that the effect is more drastic for clusters with aspect ratio of ~ 1, i.e., for spherical or nearly spherical assemblies which is the case in the present study.

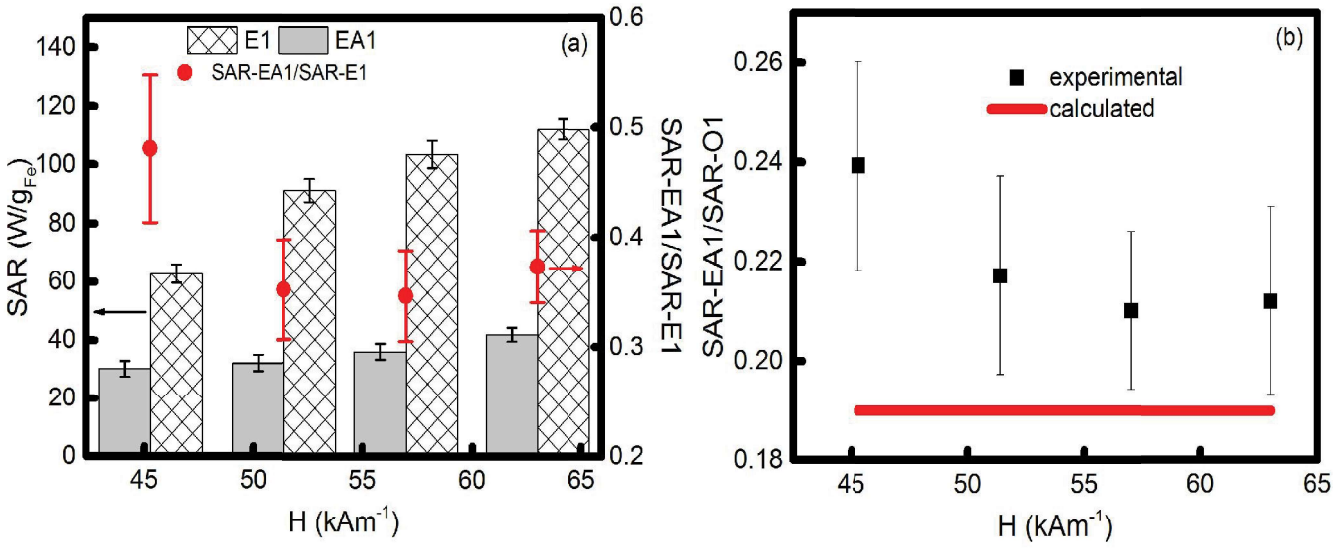


Figure 5.8: (a) Bar chart, showing the SAR values for the samples E1 and EA1 as a function of external field amplitude. SAR ratio (SAR-EA1/SAR-E1) between the samples EA1 and E1 is also shown. (b) SAR ratio (SAR-EA1/SAR-O1) of the agar based sample, EA1 and MNP based nanofluid, O1 as a function of external field amplitude.

This study clearly showed that magnetic nanoemulsions are potential candidates for multimodal hyperthermia applications as they retained their spherical morphology even after immobilization in a tissue mimicking agar matrix. Further, the experimental findings indicated that size polydispersity and medium viscosity played a very significant role on magnetically triggered heating efficiency. The effect of external DC magnetic field induced orientational ordering on heating efficiency is discussed in the subsequent section.

5.3 Effects of orientational ordering on heating efficiency of magnetic nanoemulsions immobilized in an agar gel

Presence of an external DC magnetic field (H_{DC}) during gel formation, leads to orientational ordering of the agar immobilized emulsion droplets resulting in linear chain-like structures along the direction of the external DC magnetic field. Studies reveal that external H_{DC} induced texturing leads to significant variation in RF-AMF induced heat generation, depending on the angle (ϕ) between the texturing direction and RF-AMF [461, 462]. Muller et al. [463] reported ~ 20-100 % increase in SAR values when the angle between the texturing field and RF-AMF was varied from 90^0 (perpendicular orientation) to 0^0 (parallel orientation). Serantes et al. [286] also reported a higher SAR for the parallel orientation ($\phi = 0^0$) of the chains (magnetite MNP of size ~ 44 nm and texturing field of ~ 0.12 T) as compared to perpendicular orientation ($\phi = 90^0$). Simeonidis et al. [464] reported an opposite trend for ellipsoidal MNP, where, the shape anisotropy was dominant. Higher heating efficiency was also reported for chains of bacterial magnetosomes compared to suspensions of individual magnetosomes [465]. These studies clearly show an improvement in heating efficiency for textured magnetic structures.

Here, the effect of orientational ordering on heating efficiency of the immobilized magnetic nanoemulsion droplets is studied, which is of immense importance from fundamental as well

as application points of view due to the relaxation dynamics of magnetic nanoemulsion at two different length scales and potential application of these larger sized nano-carriers for multimodal therapy.

5.3.1 Experimental details and characterization studies

Oil-in-water magnetic nanoemulsion with oleic acid coated superparamagnetic Fe_3O_4 MNP in the oil medium was used in the present study and the weight loss curve, obtained from TGA, indicated a MNP concentration of ~ 5 wt. % in the emulsion sample (hereafter indicated as E). The agar (1.2 wt. %) based samples were prepared using a procedure described by Serantes et al. [286] and for studying the effects of external DC magnetic field (~ 1485 ± 21 G) induced orientational ordering on heating efficiency, three different agar based samples were prepared (hereafter indicated as EA_{para}, EA_{per} and EA, respectively) using an experimental protocol described in section 2.1.4 in chapter 2. For the samples, EA_{para} and EA_{per}, the direction of RF-AMF (during heating phase) was parallel and perpendicular to the direction of orientational ordering, respectively. On the other hand, no orientational ordering was present in the sample EA as the external DC magnetic field was not applied during gel formation in this case.

The morphology of the emulsion droplets and external DC magnetic field (H_{DC}) induced orientational ordering was studied using atomic force microscopy (AFM). The emulsion droplets were serially diluted (20 μL of sample E in 980 μL of Milli-Q water) and drop casted on freshly cleaved mica substrates which was then allowed to dry at ambient temperature under air atmosphere. Samples were also prepared under the influence of H_{DC}, where, the mica substrate was placed in the vicinity of a permanent bar magnet (field strength ~ 650 ± 20 G) followed by drop casting and air-drying. Agar based samples were also prepared following a similar procedure, where the gel formation occurred in-situ on the mica

substrates during natural drying under air environment with or without the presence of H_{DC}. AFM topography imaging was carried out in semi-contact mode using a conventional silicon tip with bending radius and resonant frequency of ~ 10 nm and ~ 209.7 kHz, respectively. The magnetic moment of the emulsion droplets was studied using magnetic force microscopy (MFM) using a CoCr coated tip with bending radius and resonance frequency of ~ 40 nm and ~ 67.4 kHz, respectively, under semi-contact topography guided lift mode with a typical lift distance (z) of ~ 500 nm. Tip shape de-convolution (detailed procedure described in section 2.2.7 in chapter 2) was performed before quantitative analyses of the topography and phase images. The MFM data was analysed using classical point dipole approximation [338, 339].

5.3.2 Results and discussions

5.3.2.1 Atomic force microscopy based studies on orientational ordering

Under the influence of an external DC magnetic field (H_{DC}), the magnetic nanoemulsion droplets are oriented along the direction of the external field and the interaction strength between two droplets can be expressed as $\Lambda = \frac{\pi \mu_0 d_{droplet}^3 \chi^2 H^2}{72 k_B T}$, where, Λ, $d_{droplet}$ and χ indicate magnetic coupling constant, droplet diameter and effective susceptibility, respectively [159, 160]. As described in section 1.7.6 in chapter 1, for $\Lambda >> 1$, the magnetic nanoemulsion droplets undergo disorder-order transition and form linear chain-like structures due to head-on aggregation along the direction of H_{DC}, which was probed using AFM in the present study.

Figure 5.9a shows the AFM topography image (90 μm × 90 μm) of the nanoemulsion droplets under the influence of H_{DC}, where formation of linear chain-like structures along the direction of H_{DC} (shown by arrow in **Fig. 5.9a**) was clearly observed. It can be also seen from **Fig. 5.9a** that in few cases, zippering of the linear chain-like structures occurred due to lateral

interactions of the chains with mean-square of the lateral field due to chain fluctuations [114]. **Fig. 5.9b** shows a magnified view (10 μm × 10 μm) of a section of **Fig. 5.9a** (as indicated by the rectangle), where the individual droplets were clearly discernible. It is evident from **Fig. 5.9b** that under the influence of H_{DC}, droplets undergo disorder-order transition and form linear chains due to head-on aggregation along the direction of H_{DC} and the average chain length was found to be 60-90 μm. It can be clearly seen from **Fig. 5.9b** that the spherical morphology of the droplets remained intact even after orientational ordering and average topographic height of the droplets were found to be ~220 (± 17) nm which was in good agreement with the most probable size (~ 200 nm) of the emulsion droplets measured using DLS. **Fig. 5.9c** shows the 3D topography of **Fig. 5.9b**, where, the presence of individual droplets along the chain is clearly seen.

To study the residual magnetization of the emulsion droplets after H_{DC} induced linear chain formation, magnetic force microscopy (MFM) studies were carried out under topography guided lift (z ~ 500 nm) mode and **Fig. 5.9d** shows the magnified (1.5 μm × 1.5 μm) MFM topography image of a section of the linear chain-like structure shown in **Fig. 5.9b** (indicated by the rectangle). The emulsion droplets were clearly discernible from the MFM image and **Fig. 5.9e** shows a 3D surface plot of the MFM topography image. **Fig. 5.9f** shows the MFM phase image at a lift distance of 500 nm from the surface. The MFM phase image clearly showed the presence of the emulsion droplets and the average phase difference ($\Delta\beta_{mag}$) was found to be ~ 0.2^0 indicating very feeble tip-droplet magnetic interactions. At resonance frequency, the MFM phase difference is directly proportional to the gradient of magnetic force along Z-direction ($\partial F_z/\partial z$) and is expressed by $\Delta\beta_{mag} = -\frac{Q}{k_{spring}}\frac{\partial F_z}{\partial z}$ (Eq. 2.3 in chapter 2) [338], where, Q is the quality factor of the MFM cantilever (~ 500) and k_{spring} is the spring constant. Under classical point-dipole approximation, the magnetic force gradient along Z-

direction can be expressed as $\frac{\partial F_z}{\partial z} = \frac{24 m_{tip} m_{drop}}{z^5}$, where, m_{tip}, m_{drop} and z indicate magnetic moment of the MFM tip (~ 6×10^{-15} Am^2), magnetic moment of the emulsion droplet and lift distance (~ 500 nm), respectively [339]. Using the above expressions, the residual volume magnetization of the emulsion droplets (in the absence of an external field) was estimated as 1.1×10^{-6} emu/cc, indicating the superparamagnetic (SPM) nature of the droplets. Such SPM droplets are ideal candidates for multimodal hyperthermia therapy as they do not form clusters in tissue environment in the absence of an external magnetic field, thereby, avoiding *in vivo* blockage and ensuring easy removal [295].

Figure 5.10a shows the AFM topography image (10 μm × 10 μm) of the emulsion droplets immobilized in an agar matrix without an external magnetic field. It can be clearly seen from **Fig. 5.10a** that in the absence of a texturing field, the droplets were randomly oriented and no orientational ordering could be seen. **Fig. 5.10b** shows a magnified view (2.5 μm × 2.5 μm) of a section of **Fig. 5.10a** (indicated by the rectangle), where the structural integrity and spherical morphology of the emulsion droplets were found to be intact indicating its suitability for safe loading of anti-cancer drugs or photodynamic agents inside the droplets along with the MNP for multimodal hyperthermia therapy. **Fig. 5.10c** shows the 3D surface topography of **Fig. 5.10b**. It must be noted in this regard that the increased unsharpness of the topography images in these cases, as compared to the water based samples, was due to higher surface roughness and non-uniformity of the agar based samples.

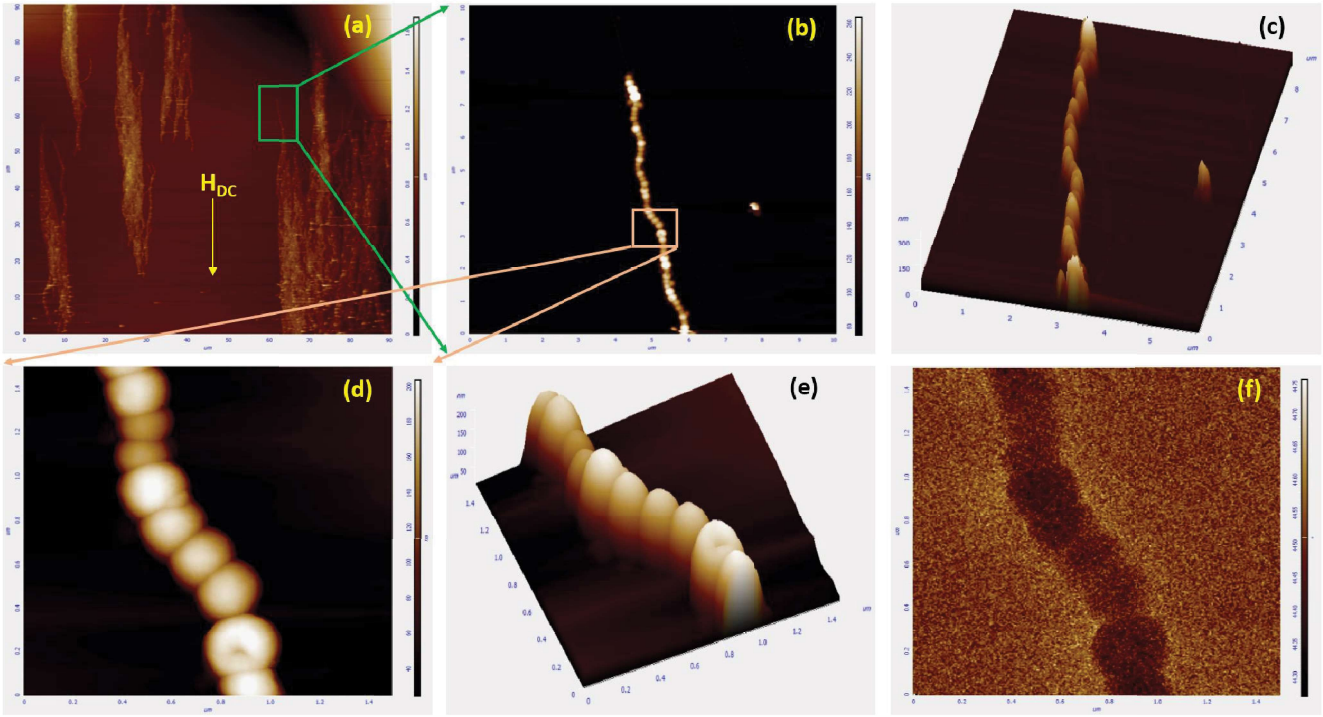


Figure 5.9: (a) AFM topography image (90 µm × 90 µm) of the dried nanoemulsion droplets, drop casted on a freshly cleaved mica surface, under the influence of H_{DC} (direction of H_{DC} shown by an arrow). (b) A magnified view (10 µm × 10 µm) of a section (indicated by the green rectangle) of Fig. 5.9a. (c) 3D surface topography of Fig. 5.9b. (d) Magnified (1.5 µm × 1.5 µm) MFM topography view of a section (indicated by the orange rectangle) of the linear chain-like structure shown in Fig. 5.9b. (e) 3D surface topography of Fig. 5.9d. (f) MFM phase image (lift distance ~ 500 nm) of Fig. 5.9d.

Figure 5.10d shows the formation of linear chain-like structures, under the influence of an external DC magnetic field, in the case of agar immobilized emulsion droplets. The linear chains appeared thicker in this case, as compared to the water based samples, which was attributed to increased zippering of chains leading to the formation of bundles of linear chains. **Fig. 5.10e** shows the magnified view (3.5 µm × 10 µm) of a section of **Fig. 5.10d** (indicated by the rectangle), where the presence of emulsion droplets along the linear chains was clearly seen. **Fig. 5.10f** shows a magnified view (1.8 µm × 2.0 µm) of a section (indicated by rectangle) of **Fig. 5.10e**, where the presence of the individual droplets can be

seen. It was further observed from **Fig. 5.10f** that the droplets appear slightly ellipsoidal which may be attributed to an enhancement in viscous drag during chain formation due to an increased viscosity of the agar gel. Nevertheless, AFM topography images of the emulsion droplets clearly revealed morphological intactness in tissue equivalent agar matrix with or without external field induced texturing.

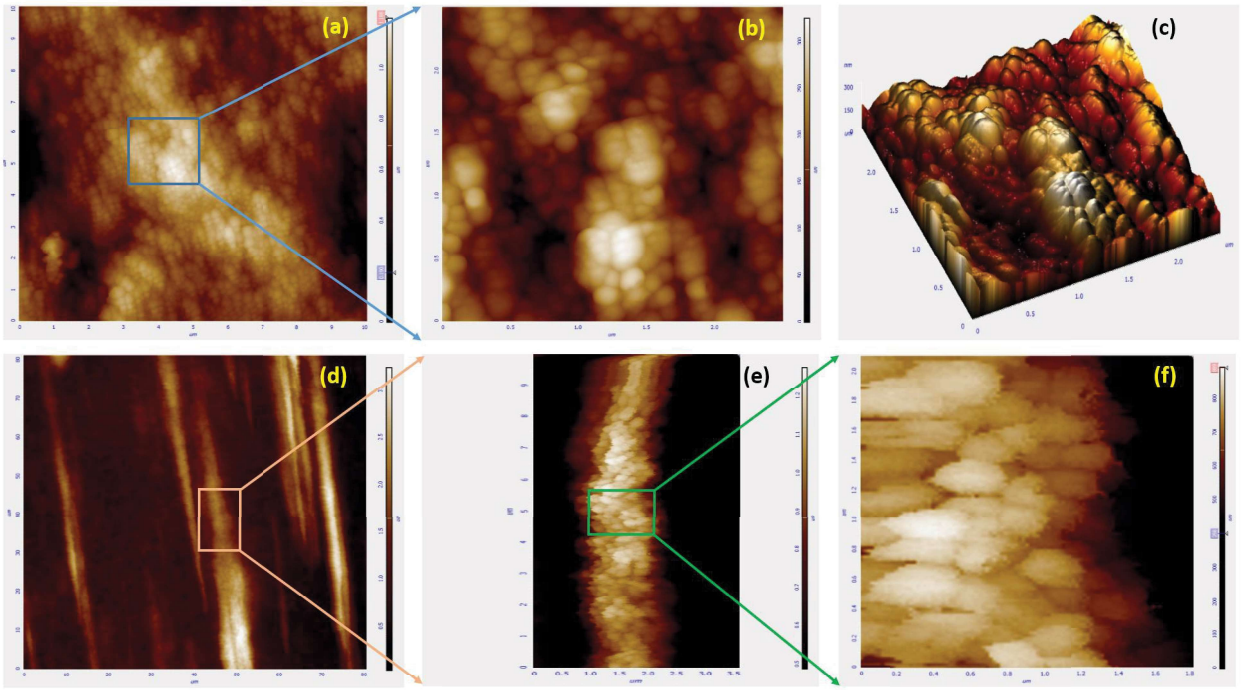


Figure 5.10: (a) AFM topography image (10 µm × 10 µm) of the emulsion droplets immobilized in an agar matrix in the absence of H_{DC}, where, the emulsion droplets are found to be randomly oriented. (b) Magnified view (2.5 µm × 2.5 µm) of a section (indicated by the blue rectangle) of Fig. 5.10a. (c) 3D surface topography of Fig. 5.10b. (d) AFM topography image showing the formation of linear chain-like structures in agar immobilized emulsion droplets under the influence of H_{DC}. (e) Magnified view (3.5 µm × 10 µm) of a section (indicated by the orange rectangle) of Fig. 5.10d. (f) Magnified view (1.8 µm × 2.0 µm) of a section (indicated by green rectangle) of Fig. 5.10e.

5.3.2.2 Effects of orientational ordering on RF-AMF induced heating efficiency

Figures 5.11a-d show typical infrared images of the emulsion sample (E) at time t = 0, 200, 400 and 600 s, respectively, during RF-AMF induced heating under an external field amplitude of 63.0 kAm^{-1}. The pseudo colour coded temperature scale is also shown along with the infrared images. The infrared images were suitably emissivity corrected to represent true temperature of the emulsion. It can be clearly seen from **Figs. 5.11a-d** that sample temperature continuously increased with time during RF-AMF induced heating. IRT based non-contact temperature monitoring enabled real time mapping of surface temperature distribution and **Fig. 5.11e** shows the horizontal line scans across the sample surface at time t = 0, 100, 200, 300, 400, 500 and 600 s during RF-AMF induced heating under an external field amplitude of 45.3 kAm^{-1}, where the maximum temperature at the end of heating phase was found to be ~ 40 ^{0}C. The flat temperature profiles (temperature variation within ± 2.5 % over the sample surface) shown in **Fig. 5.11e** indicated uniform temperature rise of the emulsion during RF-AMF induced heating.

Figures 5.12a-d show the variation of ΔT as a function of time during RF-AMF induced heating under four different external field amplitudes, viz., 63.0, 57.0, 51.4 and 45.3 kAm^{-1} for the samples E, EA, EA_{para} and EA_{per}, respectively, where the temperature was measured using IRT and average value of ΔT was obtained by spatial averaging over several locations. It can be clearly seen from **Fig 5.12** that ΔT increased with time and the initial rate of temperature rise and the maximum temperature rise at the end of heating phase (ΔT_{max}) increased with RF-AMF amplitude in all the cases.

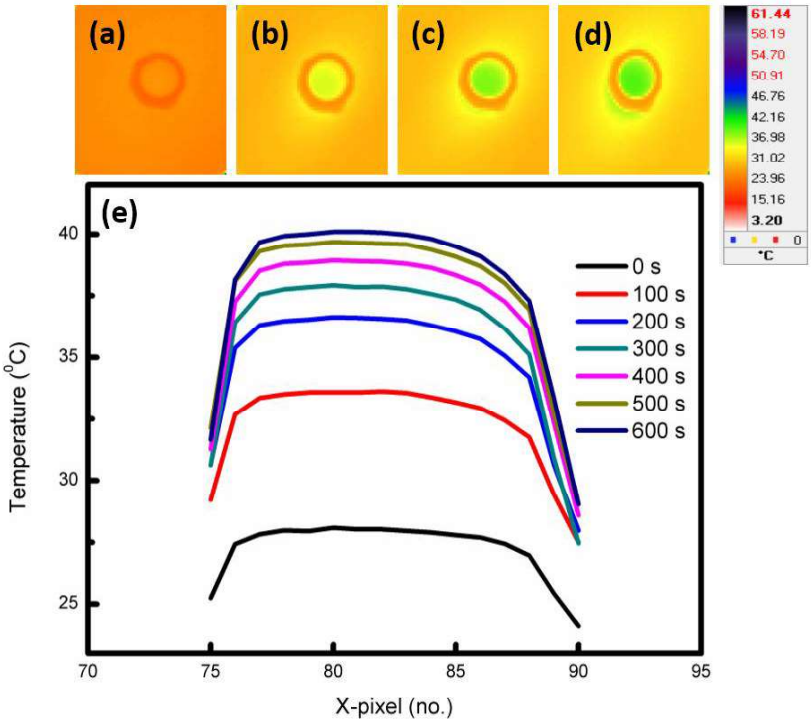


Figure 5.11: Typical infrared images of the emulsion sample (E) at time t = (a) 0, (b) 200, (c) 400 and (d) 600 s, respectively, during RF-AMF induced heating under an external field amplitude of 63.0 kAm^{-1}. The pseudo colour coded temperature scale is also shown. (e) Horizontal temperature profiles along the top surface of the sample E, during RF-AMF induced heating under an external field amplitude of 45.3 kAm^{-1} at time t = 0, 100, 200, 300, 400, 500 and 600 s.

It was further observed from **Fig. 5.12** that the values of initial rate of temperature rise and ΔT_{max} were significantly higher for the fluid based sample (E) as compared to the agar based samples (EA, EA_{para} and EA_{per}) which was attributed to the abrogation of Brownian relaxation of the emulsion droplets in the agar matrix [258, 286]. The experimentally measured temperature rise curves were adiabatically reconstructed using the procedure described in section 2.6.6 in chapter 2 and the adiabatically reconstructed temperature rise curves for the sample E, EA, EA_{para} and EA_{per} are shown in the **insets of Figs. 5.12a-d**, respectively. It can be clearly seen that $\Delta T_{adiabatic}$ was largely unaffected from thermal losses at higher time scales and the values of $\Delta T_{adiabatic}$ were found to be physically significant up to a temperature difference corresponding to ΔT_{LL} (~ 7.6 ± 0.1, 4.5 ± 0.1, 4.7 ± 0.1 and 4.2 ± 0.1

^{0}C for the samples E, EA, EA_{para} and EA_{per}, respectively), which were determined from linear regression analyses of the natural cooling curves after RF-AMF induced heating phases.

The initial rates of temperature rise were determined from linear regression analysis of the adiabatically reconstructed curves and it was observed that the adiabatically reconstructed initial rates varied linearly with the experimentally measured initial rates. The slope of the linear regression analysis was found to be ~ 1.29 ± 0.03 with an adjusted R^2 value of 0.99, which showed that the adiabatically reconstructed initial rates were on average ~ 29 (±3) % higher than the experimental values due to thermal losses.

SAR was estimated from the initial rates of temperature rise obtained from the adiabatically reconstructed temperature curves and **Fig. 5.13a** shows the variation of SAR as a function of square of the external field amplitude (H^2) for the agar based samples, viz., EA, EA_{para} and EA_{per}. It can be seen from **Fig. 5.13a** that SAR varied linearly with H^2 which was found to be in agreement with the theoretical predictions ($P \sim H^2$) [51]. The adjusted R^2 for the linear regression analyses (also shown in Fig. **5.13a**) were ~ 0.96, 0.93 and 0.86 for the samples EA, EA_{para} and EA_{per}, respectively, indicating good accuracy of the linear fits. It can be further seen from **Fig. 5.13a** that for a fixed magnetic field amplitude, SAR was highest for the sample EA_{para} ($\phi = 0^0$, where, ϕ indicates the angle between anisotropy axis, i.e., H_{DC} and applied RF-AMF), whereas, SAR was lowest for the sample EA_{per} ($\phi = 90^0$), which was attributed to an increase in effective anisotropy of the H_{DC} induced linear chain-like structures for parallel orientation ($\phi = 0^0$) [286]. The highest SAR was obtained as ~ 72.9 ± 1.6 W/g_{Fe}, for the sample EA_{para}, under an external field amplitude of 63.0 kAm^{-1}. The SAR values of the samples E, EA, EA_{para} and EA_{per}, under four different external field amplitudes, are listed in **Table 5.2**.

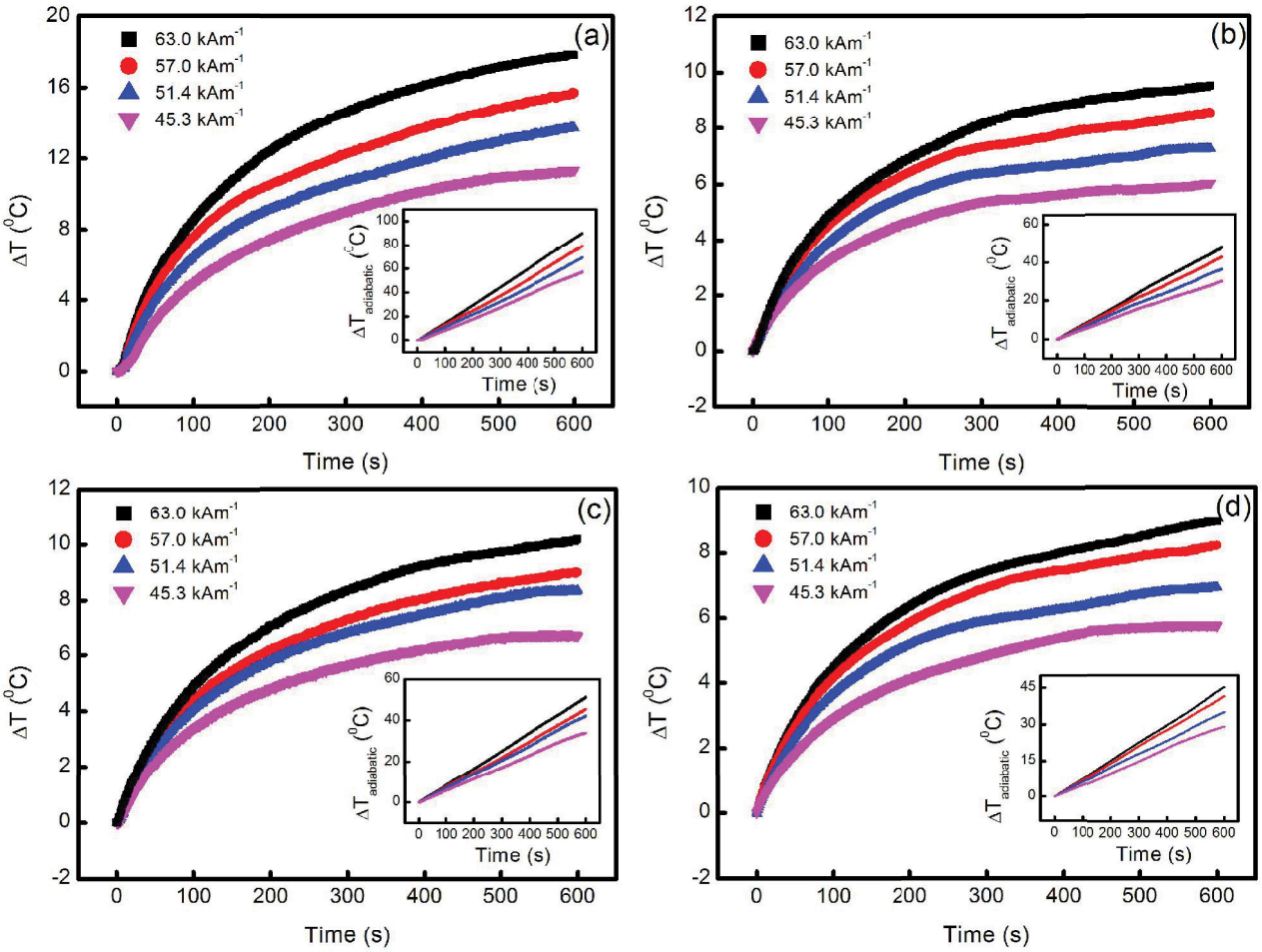


Figure 5.12: Temperature rise (ΔT) as a function of time, for the samples (a) E, (b) EA, (c) EA_{para} and (d) EA_{per}, during field induced heating under external field amplitudes of 63.0, 57.0, 51.4 and 45.3 kAm^{-1}. (Insets) Adiabatically reconstructed temperature rise as a function of time, during RF-AMF induced heating under four different external field amplitudes, for the corresponding samples.

The **inset of Fig. 5.13a** shows the variation of SAR as a function of H^2 for the emulsion sample in fluid form (sample E), where it can be seen that SAR varied linearly with H^2 (adjusted $R^2 \sim 0.88$). The highest SAR, for the sample E, was obtained as 128.32 ± 3.1 W/g_{Fe} under an external field amplitude of 63.0 kAm^{-1}, which was significantly higher than the SAR values obtained for the agar based samples due to the abrogation of Brownian relaxation of the emulsion droplets after immobilization in agar matrix [258, 286]. A comparison of the

SAR values for the sample E and EA at H = 63.0 kAm^{-1} indicates ~ 53.8 % contribution of Brownian relaxation of the oil droplets to the global SAR.

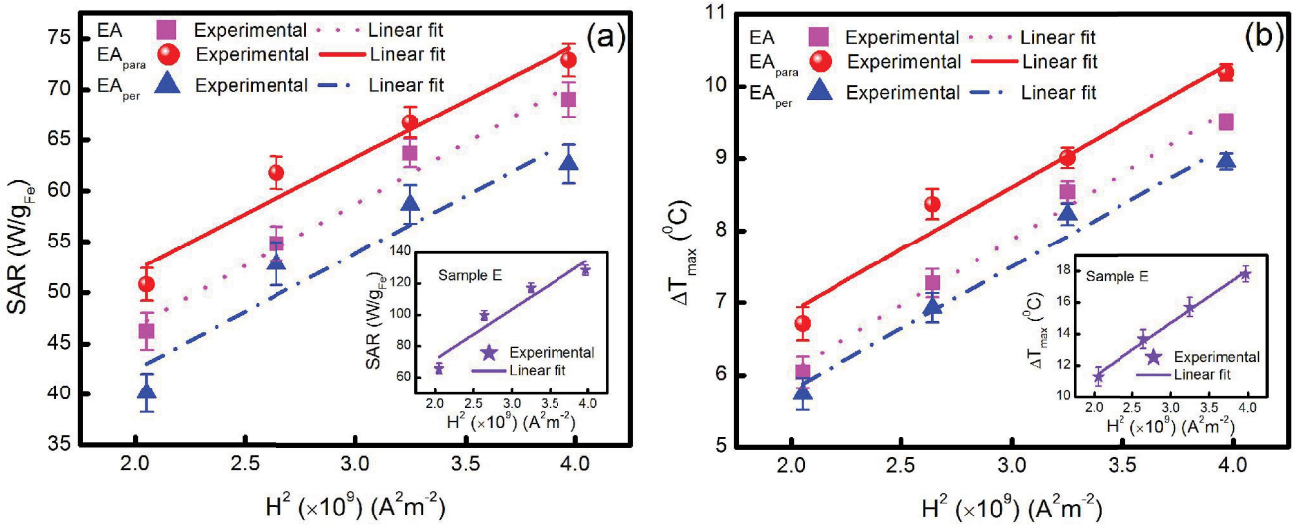


Figure 5.13: (a) Variation of SAR as a function of H^2, during RF-AMF induced heating of the agar based samples, viz., EA, EA_{para} and EA_{per}. (Inset) Linear variation of SAR as a function of H^2 for the sample E. (b) Variation of ΔT_{max} as a function of H^2, during RF-AMF induced heating of the samples EA, EA_{para} and EA_{per}. (Inset) Linear variation of ΔT_{max} as a function of H^2 for the sample E.

Table 5.2: SAR and ΔT_{max} values of the samples E, EA, EA_{para} and EA_{per}, during RF-AMF induced heating, under four different external field amplitudes.

Sample	RF-AMF amplitude (kAm^{-1})	SAR (W/g_{Fe})	ΔT_{max} (^0C)
E (fluid)	63.0	128.32 ± 3.1	17.8 ± 0.5
	57.0	117.19 ± 2.9	15.7 ± 0.6
	51.4	99.68 ± 2.9	13.7 ± 0.6
	45.3	65.95 ± 3.2	11.3 ± 0.6
EA ($H_{DC} = 0$)	63.0	69.01 ± 1.7	9.5 ± 0.1
	57.0	63.76 ± 1.4	8.5 ± 0.2
	51.4	54.85 ± 1.7	7.3 ± 0.2
	45.3	46.22 ± 1.8	6.0 ± 0.2
EA_{para} ($H_{DC} > 0$ & $\phi = 0^0$)	63.0	72.91 ± 1.6	10.2 ± 0.1
	57.0	66.76 ± 1.5	9.0 ± 0.1
	51.4	61.79 ± 1.6	8.4 ± 0.2
	45.3	50.81 ± 1.6	6.7 ± 0.2
EA_{per} ($H_{DC} > 0$ & $\phi = 90^0$)	63.0	62.69 ± 1.9	9.0 ± 0.1
	57.0	58.71 ± 1.9	8.2 ± 0.2
	51.4	52.84 ± 2.1	6.9 ± 0.2
	45.3	40.14 ± 1.9	5.7 ± 0.2

Figure 5.13b shows the variation of maximum temperature rise at the end of the heating phase (ΔT_{max}) as a function of H^2 for the agar based samples (EA, EA_{para} and EA_{per}) during RF-AMF induced heating under four different external field amplitudes, viz., 63.0, 57.0, 51.4 and 45.3 kAm^{-1}. It can be seen from **Fig. 5.13b** that ΔT_{max} [$\Delta T_{max} = \int_{t-on}^{t-off} (SAR/c_{samp})dt$] increased linearly with H^2. The adjusted R^2 values for the linear regression analyses were ~ 0.98, 0.95 and 0.99 for the samples EA, EA_{para} and EA_{per}, respectively, indicating good accuracy of the linear fits. ΔT_{max} values for the samples E, EA, EA_{para}, EA_{per}, under four different external field amplitudes, are also shown in **Table 5.2**. The maximum value of ΔT_{max} was obtained as ~ 10.2 ± 0.1 ^{0}C, for the sample EA_{para} ($\phi = 0^0$), under an external field amplitude of 63.0 kAm^{-1}. Nevertheless, it has been reported that such values of temperature rise are sufficient for multimodal therapy involving MFH along with photodynamic therapy or thermally activated drug delivery [268]. The **inset of Fig. 5.13b** shows the linear variation of ΔT_{max} (adjusted R^2 = 0.99) as a function of H^2 for the emulsion sample in fluid form (sample E).

Figure 5.14 shows a bar chart of the SAR values as a function of external field amplitude for the sample EA, EA_{para} and EA_{per}. It can be seen from **Fig. 5.14** that SAR increased with increasing RF-AMF amplitude for all the samples, which was attributed to the enhancement of electromagnetic energy density with increasing RF-AMF amplitudes (~ H^2 as shown in **Fig. 5.13a**). On the other hand, for a fixed RF-AMF amplitude, the variation of SAR for the agar based samples was attributed to the variation in effective uniaxial anisotropy energy density of the samples with changing direction of the H_{DC} induced orientational ordering with respect to the direction of RF-AMF (H). For the sample EA_{para}, the orientational ordering was parallel to the direction of H, which resulted in an enhancement of effective relaxation time due to an increase in anisotropy energy density [464]. On the other hand, for the sample

EA_{per}, RF-AMF was directed perpendicular to the anisotropy barrier leading to an effective lowering of anisotropy energy density, resulting in a comparatively lower SAR [286]. For the sample EA, with $H_{DC} = 0$ during gel formation, the emulsion droplets were randomly oriented and no orientational ordering was present, which led to intermediate values of SAR in all the cases and was comparable to the cases of linear chains oriented at 45^0, reported by Serantes et al. [286], where the anisotropy axes were randomly oriented with respect to the RF-AMF leading to insignificant (averaged out) effective contributions from anisotropy-field interactions. Similar results were reported by Muller et al. [463], where higher SAR was observed for MNP assembled (H_{DC} induced) into linear chain-like structures in solid matrix and oriented parallel to the direction of RF-AMF. The geometrical orientations of RF-AMF and H_{DC}, for the samples EA, EA_{para} and EA_{per}, are schematically shown in **Fig. 5.14** for easy comparison.

According to Stoner-Wohlfarth model [48], for an aligned structure consisting of identical and non-interacting MNP oriented towards the direction of an external DC magnetic field, the extent of magnetization rotation (under the action of RF-AMF) depends on Zeeman and anisotropic energy terms and the total energy, normalized with respect to thermal energy can be expressed as $\frac{E_t}{k_B T} = \sigma_{AT}[\sin^2(\theta_m) - 2h\cos(\phi - \theta_m)]$ (Eq. 1.21 in chapter 1), where, E_t is the total energy, $\sigma_{AT} = KV_p/k_BT$ is the ratio of anisotropy energy to thermal energy, h is the normalized magnetic field amplitude ($h = H/H_A$, where H_A is the anisotropy field amplitude), θ_m is the angle between the anisotropy axis and magnetization and ϕ is the angle between the anisotropy axis (along the direction of H_{DC}) and applied RF-AMF [18, 289]. For, $\phi = 0$, 45 or 90^0, the expression for E_t/k_BT changes significantly and section 1.7.6 (in chapter 1) shows the detailed description, where it can be seen that the energy profile changes considerably for different orientation of the anisotropy axes with respect to the direction of RF-AMF [42].

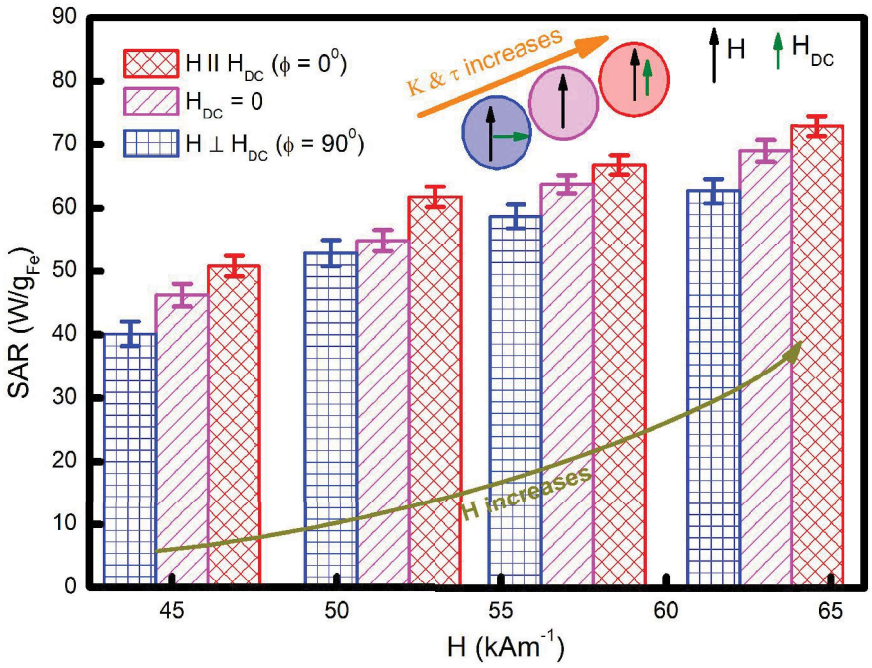


Figure 5.14: Bar chart of the SAR values, as a function of external field amplitude, for the agar based samples, viz., EA, EA_{para} and EA_{per}. It is observed that the maximum and minimum values of SAR are for the samples EA_{para} ($\phi = 0^0$) and EA_{per} ($\phi = 90^0$), respectively, and SAR values for the sample EA are intermediate in all the cases. The geometrical orientations of RF-AMF (H) and H_{DC} for the samples EA, EA_{para} and EA_{per} are schematically shown in the figure.

Assuming a half cone angle of 25^0 (half cone angle of 20^0 was used for numerical simulations by Serantes et al. [286]), the values of the effective uniaxial anisotropy energy density for the cases $\phi = 0, 90^0$ were found to be (using Eq. 1.22) ~ 26.7 and 9.6 kJm^{-3}, respectively, which were then used for calculating the effective relaxation times for the samples EA_{para} and EA_{per} during RF-AMF induced heating. **Fig. 5.15** shows the variation of Neel, Brownian and effective relaxation times, as a function of MNP diameter, for the cases when RF-AMF was applied parallel or perpendicular to the anisotropy axes. The variation of Brownian relaxation time for both cases was similar, as τ_B depends on the viscosity of the medium only. On the other hand, the Neel relaxation time scales exponentially with effective anisotropy energy density and it was observed from **Fig. 5.15** that τ_N varied significantly for $\phi = 0^0$ and 90^0. The

higher value of τ_N for $\phi = 0^0$ was attributed to the larger effective uniaxial anisotropy energy density for the sample EA_{para}. For MNP diameter up to 10 nm, the effective relaxation time was found to be Neel dominated and strong dependence of τ_N on effective uniaxial anisotropy energy density resulted in a similar trend for effective relaxation time.

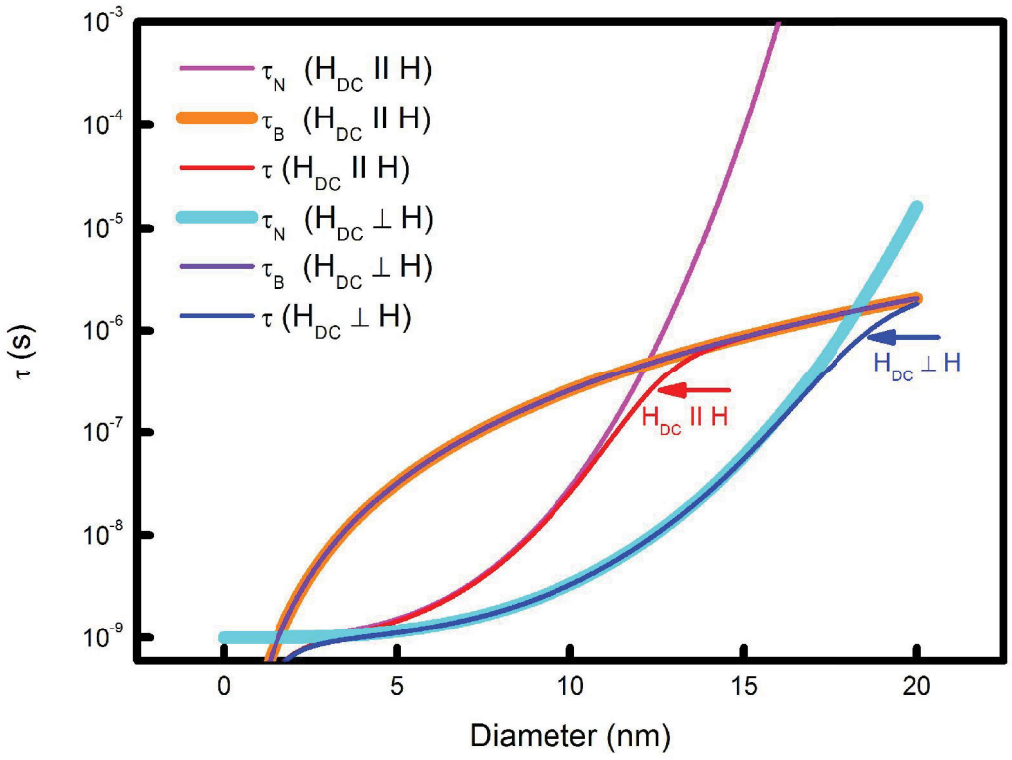


Figure 5.15: Variation of Neel, Brownian and effective relaxation time, as a function of MNP diameter, for $\phi = 0^0$ (H_{DC} parallel to H) and 90^0 (H_{DC} perpendicular to H).

Figure 5.16a shows the variation of effective relaxation time (τ) as a function of MNP diameter in the range 0-10 nm (magnified section from **Fig. 5.15**), where, it can be clearly observed that effective relaxation time was higher for $\phi = 0^0$. The dissipative power per unit volume (P) is linearly proportional to $f(\omega\tau)$, where, $f(\omega\tau) = \omega\tau/(1+ \omega^2\tau^2)$ [51] and for $\omega\tau<<1$ (in the present case, $\omega\tau \sim 4\times10^{-4}$), $f(\omega\tau) \sim \omega\tau$ [52], indicating a linear variation of SAR with effective relaxation time ($P \sim \tau$). Hence, SAR was higher for the sample EA_{para} due to larger

effective anisotropy energy density which resulted in a higher effective relaxation time. The **inset of Fig. 5.16a** shows the theoretically calculated (using a log-normal size distribution function under linear response regime approximation [51]) normalized SAR for the samples EA_{para} and EA_{per} as a function of MNP diameter, where it can be seen that SAR was indeed higher for the sample EA_{para}. For theoretical calculations, the values of viscosity, coating thickness, half cone angle between magnetization and anisotropy axes, temperature, most probable diameter, σ_{ln} and τ_0 were considered as 0.00051 Pa. s, 2 nm, 25^0, 300 K, 6.9 nm, 0.14 and 10^{-9} s, respectively.

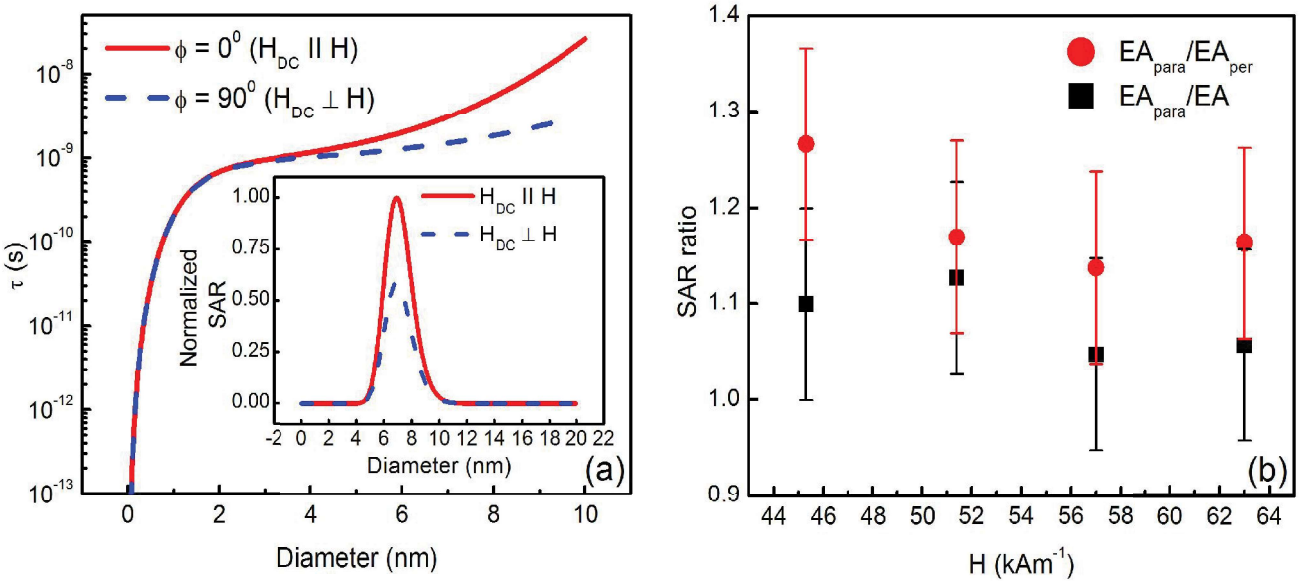


Figure 5.16: (a) Variation of effective relaxation time (τ), as a function of MNP diameter, for two different orientation of RF-AMF with respect to H_{DC}, viz., $\phi = 0^0$ and 90^0. (Inset) Theoretically calculated normalized SAR, as a function of MNP diameter, for $\phi = 0^0$ and 90^0. (b) Variation of SAR ratios (EA_{para} to EA_{per} and EA_{para} to EA) as a function of external field amplitude for the agar based samples.

The energy absorption in a system of identical MNP undergoing Neel relaxation under RF-AMF is directly proportional to the hysteresis loop area and using semi-analytical

calculations based on Stoner-Wohlfarth model [48], the hysteresis loop areas (A) for randomly oriented and aligned ($\phi = 0^0$) MNP varies according to Eq. 1.23 (in chapter 1), where, the parameter ε is defined as $\varepsilon = \frac{k_B T}{K V_p} \ln\left(\frac{k_B T}{4\mu_0 M_s H_{\max} V_p f \tau_0}\right)$ (Eq. 1.24 in chapter 1) [42]. It is evident from the above expressions that for intermediate to high dissipation limits, SAR, for the aligned MNP, is ~ 4.2 (= 4/0.96, neglecting the effect of ε) times higher than that of the randomly oriented MNP which was, very recently, experimentally shown by Beck et al. [294] by pre-orientating MNP at a very high (3 T) static magnetic field.

Figure 5.16b shows the SAR ratios (EA_{para} to EA_{per} and EA_{para} to EA) as a function of external field amplitude. The SAR ratio between the samples EA_{para} and EA was found to be ~ 1.1 for H = 63.0-45.3 kAm^{-1}, indicating ~ 10 % increase in SAR upon external DC magnetic field induced pre-orientation as compared to the randomly oriented emulsion droplets. The lower SAR ratio obtained in the present case (as compared to the calculations based on Stoner-Wohlfarth model [42, 48, 294]) was attributed to the minor loop cycling of the emulsion droplets at maximum RF-AMF amplitudes considerably lower than the anisotropy field of Fe_3O_4 (~ 160 kAm^{-1} [293]). As can be seen from the expression of ε and Eq. 1.23, a lower value of applied field amplitude leads to an enhancement of ε, where its effects cannot be neglected. The SAR ratio between the samples EA_{para} and EA_{per} varied between ~1.2-1.3 (i.e., SAR enhancement of ~ 20-30 %) for H = 63.0-45.3 kAm^{-1}, which was found to be in good agreement with the SAR ratio of 1.16 reported by Muller et al. [463] for carboxymethyl dextran coated γ-Fe_2O_3 immobilized in a solid gel.

This study clearly shows the increased efficiency of oriented magnetic nanoemulsion for RF-AMF induced heating and the findings are also in agreement with the general observations made by Mehdaoui et al. [448] that assembling MNP in chains of higher uniaxial anisotropy energy density leads to an enhancement in SAR.

5.4 Conclusions

The SAR of the MNP based nanofluid increased linearly with square of the external field amplitudes and the maximum SAR for the oil based sample was obtained as 164.4 ± 4.3 W/g_{Fe}. The RF-AMF induced heating in the MNP based nanofluid was attributed to the Neel-Brownian relaxation of the magnetic nanoparticles under the influence of a RF-AMF. On the other hand, in magnetic nanoemulsions with MNP loaded in the oil phase, the RF-AMF induced heating was due to Neel-Brownian relaxation of the MNP (length scale ~ 10 nm) and whole scale Brownian relaxation of the emulsion droplets at ~ 20 times larger length scale.

The observed SAR of the magnetic nanoemulsion with similar size (and MNP concentration) but with different polydispersity showed that the sample with lower polydispersity (σ_{ln} = 0.2) exhibited a significantly higher SAR as compared to the sample with larger polydispersity (σ_{ln} = 0.4), under identical experimental conditions. The SAR ratio between these two samples was ~ 3.3, which was comparable to the theoretical predictions. The SAR obtained for a sample with 4.6 wt. % MNP loading (with σ_{ln} = 0.4) and 1.7 wt. % MNP loading (with σ_{ln} = 0.3) were comparable, indicating that higher MNP loading does not necessarily result in a higher SAR in polydisperse system.

The contribution from whole-scale Brownian relaxation of the emulsion droplets was eliminated by immobilizing the droplets in an agar matrix (4 wt. % agar concentration). The maximum SAR for the immobilized sample was 41.7 ± 2.4 W/g_{Fe}, as compared to the significantly higher value of 111.8 ± 3.4 W/g_{Fe}, observed for the emulsion dispersed in water. The observed reduction in SAR by ~ 40-50 % in agar immobilized emulsion sample was attributed to the abrogation of Brownian relaxation. The residual SAR values of the agar immobilized droplets were compared with those obtained from the MNP based nanofluid and it was observed that the theoretically obtained SAR ratio of 0.19 (by considering emulsion

droplet induced demagnetization of the applied external field) was in good agreement with the experimental SAR ratios of 0.24-0.21.

Studies on the effect of external DC magnetic field induced orientational ordering on hyperthermia efficiency of the agar immobilized emulsion droplets showed that the formation of linear chain-like structures due to head-on aggregation of the emulsion droplets along the direction of the external DC magnetic field (confirmed using AFM) led to an increased heating efficiency. Magnetic force microscopy (MFM) studies, carried out under topography guided lift mode, clearly showed the presence of emulsion droplets from the MFM phase contrast images. Using classical point dipole approximation, residual volume magnetization of the emulsion droplets was found to be ~ 1.1×10^{-6} emu/cc, indicating the superparamagnetic nature of the emulsion droplets even after disorder-order transition under the influence of an external DC magnetic field.

For a fixed amplitude of RF-AMF, SAR was found to be higher for the sample EA_{para} due to an increase in the effective uniaxial anisotropy energy density along the chain direction, resulting in a higher effective relaxation time. Theoretical calculations of total energy (consisting of Zeeman and anisotropy energy terms) indicated an increase of effective uniaxial anisotropy energy density for the parallel orientation (~ 3 times higher than the perpendicular orientation) leading to an increase in effective relaxation time (Neel dominated) for the sample EA_{para} and a higher SAR.

The new insights obtained, from this study, on the effect of polydispersity, particle concentration, medium viscosity, cluster demagnetization field and orientational ordering will be useful for tailoring efficient MNP based nanoemulsions for practical applications. The experimental findings clearly showed an increased hyperthermia efficiency of the oriented magnetic nanoemulsion droplets, offering new possibilities for thermally triggered drug

delivery with lower doses and shorter treatment time due to availability of large amount of volume for loading with anti-cancer drug or photodynamic agents.

Chapter 6

Conclusions and recommendations for future work

Chapter 6 Conclusions and recommendations for future work

6.1 Summary and conclusions

Towards developing MFH as an alternate cancer therapy and to achieve effective heating with minimum dosage of magnetic nanoparticles, the effects of particle loading, medium viscosity, size polydispersity, orientational ordering and thermal losses on magnetically triggered heating efficiency have been studied systematically in magnetic fluids of different characteristic properties. In addition, an adiabatic reconstruction protocol was developed to minimize the uncertainties in SAR measurements. The important results are summarized below.

Various uncertainties involved in the non-adiabatic measurement of SAR during RF-AMF induced heating of magnetic nanofluids were studied. The uncertainties were classified into three categories, viz., material uncertainties (level-1), thermodynamic uncertainties (level-2) and parametric uncertainties (level-3). The material and parametric uncertainties were found to influence the SAR values estimated using data obtained from calorimetric and magnetic methods, whereas, the thermodynamic uncertainties were significant only in the case of non-adiabatic calorimetric measurements. The effects of peripheral heating, delayed heating, heat loss to sample holder, spatial variation of temperature within the sample were studied in detail and the uncertainties contributed by each of the factors were experimentally evaluated. Theoretical calculations showed that linear decay rate increased with sample area to volume ratio, which was experimentally validated using samples of different volumes. The variation of linear decay rate was studied and an adiabatic reconstruction protocol was developed for correcting the measured temperature rise curves, which was found to reduce the uncertainties by ~ 3 times.

It was observed that the field induced temperature rise curves measured using fiber optic temperature sensor and infrared thermography (IRT) were similar, except a higher initial rate of temperature rise and a lower maximum temperature at the end of the heating period in the case of IRT, which were attributed to the internal and external convection phenomena, respectively. An empirical data analysis procedure was developed for incorporating the convection phenomena and the SAR values obtained from convection corrected IRT profile were found to be in very good agreement (maximum errors were limited within ± 5 %) with those obtained from fiber optic temperature sensor. Additionally, IRT based experiments enabled surface temperature mapping, which showed a uniform and homogenous temperature rise in the magnetic fluids during RF-AMF induced heating, an essential prerequisite for practical applications. This study clearly showed the efficacy and accuracy of IRT based temperature measurement during field induced heating of water and oil based magnetic nanofluids. The advantages of IRT based measurements over conventional point measurements include non-contact and real time temperature measurement, sample contamination free measurement and visualization of surface temperature distribution. In the case of water based magnetic fluid, the highest SAR obtained was ~ 135.9 (±4.6) W/g_{Fe} for a sample concentration of 3 wt. % at an external field amplitude of 63.0 kAm^{-1}. SAR was found to decrease with increasing sample concentration due to enhanced dipolar interaction, possibly due to aggregation. On the other hand, for oil based ferrofluids, in the absence of agglomeration (confirmed from dynamic light scattering studies), enhancement of dipolar interaction was insignificant and SAR was found to increase with sample concentration due to an increase in the effective number of heat sources per unit volume. The highest SAR obtained in the case of oil based ferrofluid was ~ 75.2 (±3.4) W/g_{Fe} for a sample concentration of 23 wt. % under an external field amplitude of 57.3 kAm^{-1}.

MFH studies in water based ferrofluids, containing phosphate coated superparamagnetic Fe_3O_4 MNP, showed that SAR initially increased with sample concentration, attained a maximum at an optimum concentration and beyond that it decreased. The decrease in interparticle distance with increasing sample concentration resulted in an enhanced dipolar interaction and a decrease in the anisotropy energy barrier. For a lower anisotropy barrier height, number of spin flips increased albeit with a lower energy release per flip. The SAR was optimum when the product of number of flips per unit time and energy release per flip was maximum. For higher sample concentration, enhancement of dipolar interaction resulted in the lowering of Neel relaxation time and ensemble averaged equilibrium susceptibility, both of which contributed to the decrease in SAR. The highest SAR for the phosphate coated Fe_3O_4 MNP was ~ 11.1 ± 0.6 W/g_{MNP} for a sample concentration of 1.5 wt. %, at an external field amplitude of 57.3 kAm^{-1}. On the other hand, for phosphate coated ferromagnetic $CoFe_2O_4$ MNP, the maximum SAR was ~ 56.2 ± 3.4 W/g_{MNP} for a sample concentration of 2 wt. % at an external field amplitude of 51.4 kAm^{-1}. It was observed that SAR did not vary significantly with sample concentration for the phosphate coated $CoFe_2O_4$ MNP, which was attributed to the dominant contribution of ferromagnetic hysteresis losses to the global SAR.

In magnetic nanoemulsions with MNP loaded in the oil phase, field induced heating is due to Neel-Brownian relaxation of the MNP (length scale ~ 10 nm) and the whole scale Brownian relaxation of the emulsion droplets at ~ 20 times larger length scale. It was observed that magnetic nanoemulsion with lower polydispersity (σ_{ln} = 0.2) exhibited a significantly higher SAR as compared to the sample with larger polydispersity (σ_{ln} = 0.4) under identical experimental conditions (similar size and concentration). The SAR ratio between these two samples was ~ 3.3, in agreement with the theoretical predictions. This study also showed that the SAR values obtained for a sample with 4.6 wt. % MNP loading (with σ_{ln} = 0.4) and 1.7

wt. % MNP loading (with σ_{ln} = 0.3) were comparable, indicating that higher MNP loading does not necessarily result in a higher SAR in polydisperse system. The contribution from whole-scale Brownian relaxation of the droplets was eliminated by immobilizing the emulsion droplets in an agar matrix. The maximum SAR for the immobilized sample was ~ 41.7± 2.4 W/g_{Fe}, as compared to the significantly higher value of ~ 111.8 ± 3.4 W/g_{Fe} observed in the case of emulsion. It was observed that the SAR decreased by ~ 40-50 % due to abrogation of Brownian relaxation of the emulsion droplets in agar. The residual SAR of the agar immobilized droplets were compared with those obtained from the MNP based nanofluid and it was observed that the experimental SAR ratios of ~ 0.24-0.21 was in fairly good agreement with theoretically obtained SAR ratio of ~ 0.19. The effects of external DC magnetic field induced orientational ordering on hyperthermia efficiency of the agar immobilized emulsion droplets showed that the SAR was higher for the sample oriented parallel to the alternating magnetic field due to an increase in the effective uniaxial anisotropy energy density along the chain direction resulting in a longer relaxation time.

6.2 Recommendations for future work

A few recommendations for future work is presented below.

- Studies on the effects of shape anisotropy on magnetic fluid hyperthermia efficiency. For spherical MNP, contributions from shape anisotropy is negligible. Enhancement of effective anisotropy energy density and relaxation time by tuning shape anisotropy or orienting anisotropy axes can significantly improve heating efficiency.
- Development of larger sized magnetic nano-carriers (~ 200-250 nm) for multimodal hyperthermia coupled with thermally triggered drug delivery or photodynamic therapy. Several challenges remain on these topics, viz., optimal MNP loading,

surface modifications, selective binding of nanocarriers with cancerous tissue and achieving enhanced permeation and retention in leaky vasculature of the cancerous tissues.

- Further studies to understand the exact role of agglomeration and cluster formation on magnetically triggered heating efficiency using model systems. Here the challenges exist on tailoring model colloidal systems and experimental validation on the role of dipolar interactions, exchange coupled interactions and anisotropy-field interactions.
- Theoretical and experimental studies on the variation of attempt frequency on changes in anisotropy energy density and non-exponential relaxation mechanisms on magnetically triggered heating which is being discussed as an alternate model to the widely accepted Rosensweig's model.
- Probing the benefits of rotating magnetic field on field induced heating efficiency.
- Synthesis of superparamagnetic MNP with high saturation magnetization and anisotropy energy density; development of bio-compatible and tissue specific coating for targeted heating and *in vivo* MFH studies for efficient cancer therapy.